The Interaction Between a Propagating Coastal Vortex and Topographic Waves

Simon Wyn Parry

Thesis submitted for the award of

Doctor of Philosophy

2004

Department of Mathematics

University College London

Supervisors

Prof. E.R. Johnson

Dr N.R. McDonald

ProQuest Number: 10015699

All rights reserved

INFORMATION TO ALL USERS
The quality of this reproduction is dependent upon the quality of the copy submitted.

In the unlikely event that the author did not send a complete manuscript
and there are missing pages, these will be noted. Also, if material had to be removed,
a note will indicate the deletion.
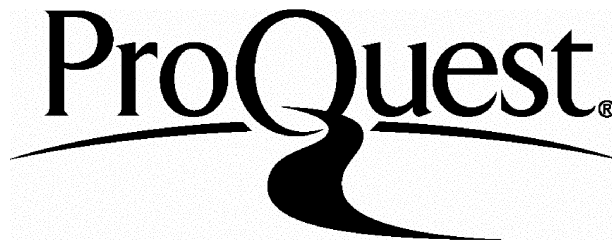
ProQuest 10015699

Published by ProQuest LLC(2016). Copyright of the Dissertation is held by the Author.

ProQuest LLC
789 East Eisenhower Parkway
P.O. Box 1346
Ann Arbor, MI 48106-1346

Abstract

This thesis investigates the motion of a point vortex near coastal topography in a rotating frame of reference at constant latitude (f-plane) in the linear and weakly nonlinear limits. Topography is considered in the form of an infinitely long escarpment running parallel to a wall. The vortex motion and topographic waves are governed by the conservation of quasi-geostrophic potential vorticity in shallow water, from which a nonlinear system of equations is derived. First the linear limit is studied for three cases; a weak vortex on- and off-shelf and a weak vortex close to the wall. For the first two cases it is shown that to leading order the vortex motion is stationary and a solution for the topographic waves at the escarpment can be found in terms of Fourier integrals. For a weak vortex close to a wall, the leading order solution is a steadily propagating vortex with a topographic wavetrain at the step. Numerical results for the higher order interactions are also presented and explained in terms of conservation of momentum in the along-shore direction.

For the second case a resonant interaction between the vortex and the waves occurs when the vortex speed is equal to the maximum group velocity of the waves and the linear response becomes unbounded at large times. Thus it becomes necessary to examine the weakly nonlinear near-resonant case. Using a long wave approximation a nonlinear evolution equation for the interface separating the two regions of differing relative potential vorticity is derived and has similar form to the BDA (Benjamin, Davies, Acrivos 1967) equation. Results for the leading order steadily propagating vortex and for the vortex-wave feedback problem are calculated numerically using spectral multi-step Adams methods.

Contents

List of Figures

Chapter 1

Introduction.

Vortices and isolated patches of vorticity form one of the most prevalent and ubiquitous structures present in the Earth's atmosphere and oceans. Atmospheric examples of these structures include the wintertime polar vortex and the associated discussions as to its involvement in the mid-latitude decline of stratospheric ozone, McIntyre [1995], or destructive tropical cyclones frequently heard about in the news. Classic oceanographic examples would be the Gulf Stream Rings (see figure (1.1)) or Agulhas rings occurring in the South Atlantic. Figure (1.1) shows a recent realization of the ocean currents off the east coast of America at a depth of approximately 1000 meters taken from GRACE data, NASA [2003], see below for more information). The colors indicate the strength of flow with red being strongest through to blue-green being weakest, the white areas are patches with no available data. A large patch of anti-cyclonic (clockwise) vorticity can be seen with smaller patches of weaker, cyclonic vorticity underneath.

Structures like these are reasonably long-lived, Reznik et al. [2000] give life-span estimates for open-ocean eddies at 130 days and oceanic rings at 650 days. They
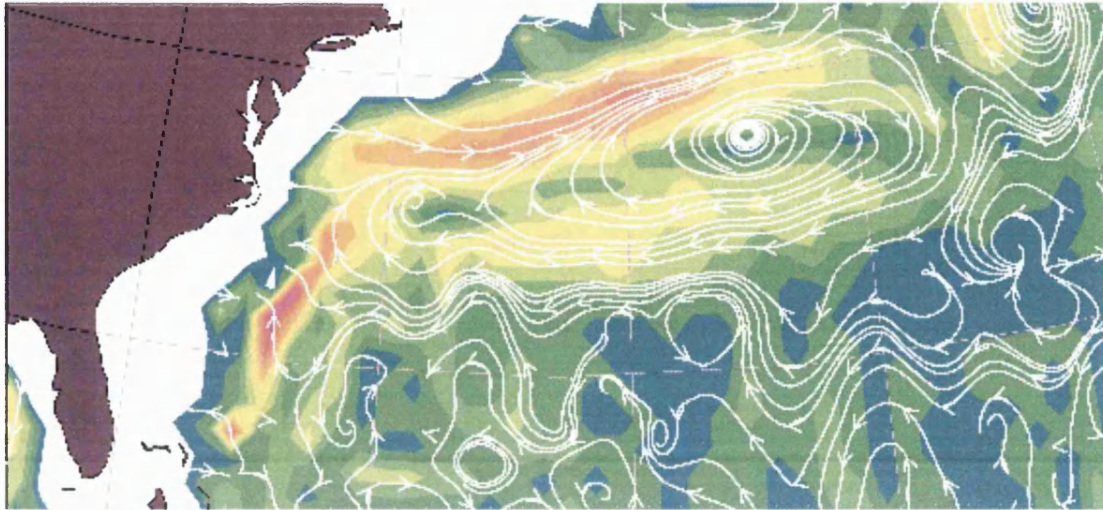
Figure 1.1: A satellite image of the Gulf Stream.

play an important role in the transport of scalars such as heat (such a structure is named the *heton*, Hogg and Stommel [1985]), salt and biota and also quantities such as momentum throughout the oceans and atmosphere. The reason being that they possess the ability to propagate either in reaction to the first effects of the curvature of the rotating Earth (the β effect) or in reaction to each other and accurately predicting these motions is an important endevour with ramifications for shipping forecasts, predicting climate change (and its consequences for industry) or simply knowing whether a particular cyclone is going to go inland causing great destruction or out to sea harming relatively little people.

Recent works on the motion of vortices on the β-plane include McDonald [1998a] who studied the effect of wave radiation due to β on eddies showing that the decay rate for oceanic cyclones was much greater than for anti-cyclones (see figure (1.1), the anti-cyclone is huge and of much greater strength than the cyclones underneath, see also examples in McWilliams [1985], Nezlin and Sutyrin [1994], Cushman-Roisin and Tang [1990]). In Reznik et al. [2000] and Reznik and Grimshaw [2001] the long-

term evolution of an intense vortex was examined and using similar techniques to those in McDonald [1998a] (see also Flierl [1984], Korotaev and Fedotov [1994], Flierl and Haines [1994]) the behavior before wave-radiation decay but after initialization was examined in detail, allowing them to give estimates on the vortex life-spans.

Naturally, one of the most important aspects of modeling these motions is that the dynamics occur on sufficiently long length-scales that the curvature and rotation of the Earth are important to the local motion. On planetary length-scales the oceans can be thought of as thin, rotating shells of fluid on a solid rotating sphere. Vertical motions can be ignored at leading order and the fluid dynamics can be taken to be 2 dimensional. This is the *shallow water* approximation and a very good description of this is given in Pedlosky [1979].

The Rossby number is a non-dimensional numbered defined

$$R_0 = \frac{U}{2\Omega L}, \qquad (1.1)$$

where L is a typical length scale (of the order of 1,000km for the Earth's oceans), U is a typical velocity (of the order of 10 m s^{-1} for the oceans) and Ω is the period of rotation of the Earth (equal to 7.3x10^{-5} s^{-1}). The Rossby number measures the importance of the Earth's rotation compared with the dynamics of the problem in question and with the figures given it is easy to see that for the Earth's oceans R_0 is small and therefore rotation is important. Further, for small Rossby numbers the leading order balance in a rotating fluid is geostrophy, which is the state whereby the vertical pressure gradient is matched by the horizontal Coriolis acceleration (akin to hydrostatic in non-rotating flows). Small departures from this state are known as quasi-geostrophic dynamics.

In addition to the self propagation properties and the effect of the rotation of the Earth, local changes in bottom topography and the presence of solid coastal barriers

also have a strong influence on vortex motion and background flow. Recent works include investigations of the so-called 'rebound' effect of a dipole-vortex from a coastal wall, Carnevale et al. [1997], due to viscous effects or inviscid β-effect. Other works include those by McDonald [1998b] and Dunn et al. [2000] for moderate and intense vortices near a topographic step. Vortices interacting with a coastally bounded shear layer are studied in Atassi et al. [1997] and Atassi [1998], these last four works are examined in more detail in the next chapter.

Figure (1.2) shows a realization of the Earth's gravity field, it and figure (1.1) were compiled from data received from the GRACE (Gravity Recovery and Climate Experiment) twin satellite mission that was launched in March 2002, NASA [2003]. These preliminary results were released in July 2003 and show the variations in the Earth's gravity field with a resolution at long & medium wavelengths that are up to 50 times more accurate than any previous Earth gravity models (i.e. from 700km resolution to 200km).

Changes in the topography of the ocean floor are quite clearly discernible (e.g. the mid-Atlantic ridge, the eastern sea-board of the United States, the Walvis Ridge off the coast of Southern Africa) as are the changes in bottom topography along the coastlines of continents, the continental shelves. It is these areas that are of relevance to this thesis.

Another important form of momentum or energy transport is that given by wave motion. Nonlinear effects such as overturning, flow reversal or blocking and ejection all contribute to mixing in the oceans and much work has been done in examining the various forms of waves that the oceans and atmosphere can support. The classic equation governing a number of different forms of wave evolution is the KdV (Korteweg-de Vries) type equation and this has been studied in various forms for
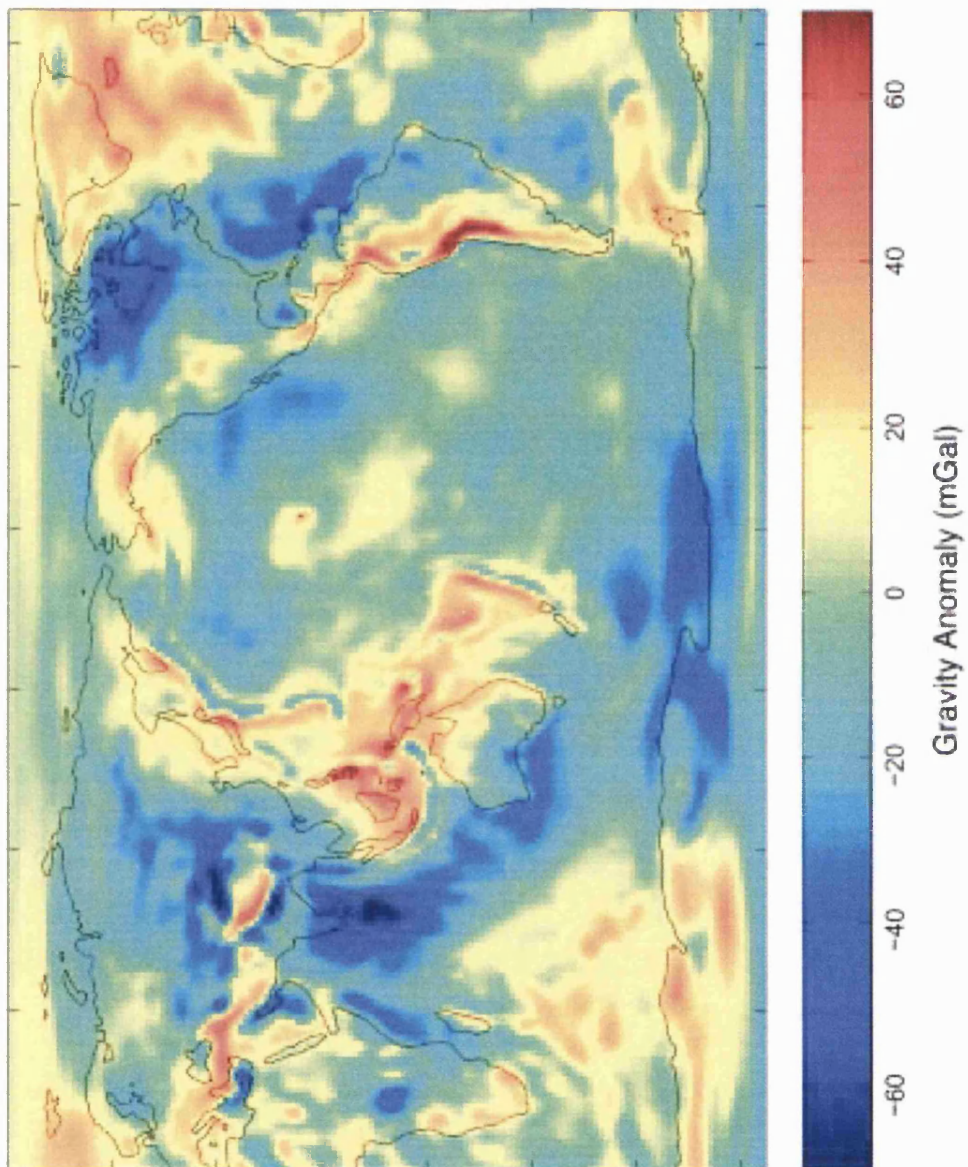
Figure 1.2: A satellite image of the the Earth's gravity field clearly showing

regions of variable bottom topography in the ocean

NASA [2003].

many situations; Akylas [1984] and Cole [1985] studied the resonant generation of water waves, internal waves have been studied in Grimshaw and Smyth [1986] and more recently in Clarke and Grimshaw [1999] and Grimshaw et al. [2002]. For rotating flows, resonant Rossby wave (see chapter 2 for definition) generation has been studied in Patoine and Warn [1982] and Malanotte-Rizzoli [1984].

Other evolution equations are also prevalent, recent work on the Camassa-Holm equation (Fokas and Fuchssteiner [1981], Camassa and Holm [1993]) and Green-Naghdi equation (Green and Naghdi [1976]) can be found in Johnson [2002] in which it is shown that the horizontal component of velocity of water waves at a specific depth is governed by the Camassa-Holm equation. Another typical equation type is the Benjamin-Ono (Benjamin [1967], Ono [1975]) or related Benjamin, Davies, Acrivos (BDA) equation (Benjamin [1967], Davies and Acrivos [1967]), this has been studied for the case of resonant generation of topographic Rossby waves in Grimshaw and Yi [1990], Clarke and Johnson [1996a] and Clarke and Johnson [1996b], as these works are of particular relevence to this thesis they are reviewed in more detail in the next chapter.

Rossby waves have also been observed in the atmospheres of other planets, in Allison et al. [1990] they claim that Saturn's polar hexagon is actually a standing Rossby wave. Tentative suggestions that Jupiter's equatorial plumes are too, Allison [1990], as is Saturn's 'ribbed' pattern, Stomovsky et al. [1983], have also been put forward.

So the general study of vortices, waves and vortex-wave dynamics is of extreme interest both on this planet and elsewhere. The choice of problems to be studied is almost overwhelming due to the multifarious nature of the topic. So whilst considerations of variable bottom topography are applicable to atmospheric flow (e.g. flows over land masses and mountains etc) the inclusion of solid boundaries only occurs

for oceanographic problems (i.e. coastlines), and the work in this thesis is primarily of oceanographic context.

This thesis is split broadly into 3 sections; the first section consists of this introduction followed by chapter 2 which is a review of the literature relevant to this study; in chapter 3 the general problem is formulated and then studied in the linear limit of weak forcing and infinitesimal disturbances at the interface. In this chapter the vortex motion is constrained to be fixed (in an appropriate frame of reference) and the short time solutions are found in terms of Fourier integrals. These are inverted numerically and compared with analytic long time solutions to ascertain which solutions remain valid for longer times. At certain vortex speeds there is a resonant interaction between the vortex and the interfacial waves which leads to the breakdown of linear theory.

In the second section, chapter 4 derives the governing evolution equation for this near-resonant case for a steadily propagating vortex. This is a long wave expansion of the general governing equation that includes weak nonlinearity. Chapter 5 describes the numerical scheme used to solve the evolution equation (and subsequent equation systems) and also discusses some of the numerical problems faced in applying the method. Chapter 6 then discusses the results of numerically integrating the weakly nonlinear evolution equation derived in chapter 4. The various flows are summarized into 5 flow types and a regime diagram is presented for the parameter space; closeness to resonance, strength of forcing (nonlinearity).

The third section then relaxes the constraint of steady vortex motion and chapter 7 considers the linear response of the vortex-wave system *including* the higher order vortex motions, in other words the vortex is free to react to the topographic waves at the step. Conservation of momentum arguments are used to explain the results

and to test the accuracy of the numerical scheme. Chapter 8 then examines the same problem but for the weakly nonlinear limit, conservation of momentum still holds and is again used to explain the dynamics and test the numerics. Finally, chapter 9 summarizes and discusses the main results of this thesis and looks ahead to extensions of this work that would be of value.

Chapter 2

Review.

The purpose of this chapter is to review some of the literature that deals with the two strands of research being used in this thesis. The first being weakly nonlinear long wave theory and the second being vortex-wave interactions near topography.

In rotating flows confined to a shallow layer, 3D turbulence is repressed and constrained by potential vorticity (PV) conservation, Stern [1991] and, further, many physical situations in rotating fluids can be considered as evolving in the horizontal plane only with piecewise continuous PV distributions. As well as surface gravity waves, a rotating fluid can also support two more surface waves, namely Poincare waves and Kelvin waves and also Rossby waves, that have as their restoring mechanism the conservation of PV. In 1932 Lamb classified these waves according to their speeds when compared to free surface, non-rotating waves. Kelvin and Poincare waves are Class 1 as they have speeds comparable to gravity waves (i.e. fast modes), they also have dependency on depth. Rossby waves are Class 2 waves as they are slow compared to gravity waves and they exhibit little or no vertical displacement.
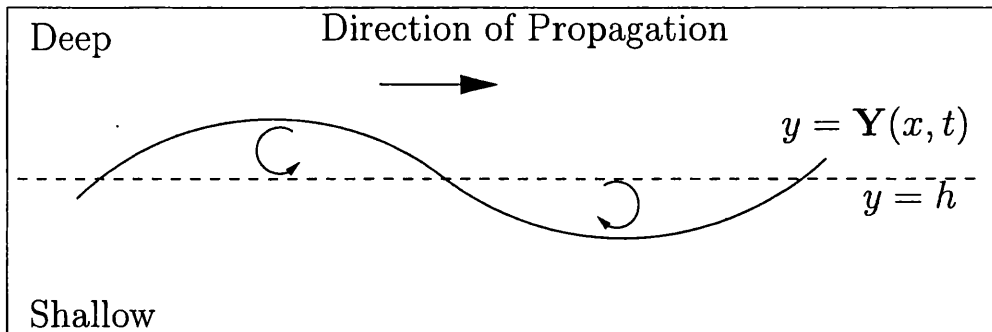
Figure 2.1: The topographic wave mechanism (viewed from above).

As remarked above they arise from changes in relative vorticity that could, for example, be due to vortex stretching (i.e. bottom topography variations) or changes in the background vorticity (i.e. shear flow, boundary layers, jets or the β-effect). Topography in the form of an infinitely long escarpment is of relevance to this study and a schematic diagram of the topographic wave generation process is shown in figure (2.1). As can be seen the line $y = h$ is the position of a step change in topography separating shallow, rotating fluid from deep, rotating fluid. Initially the line $y = \mathbf{Y}(x,t)$ (also referred to later on as the *interface*) lies directly on top i.e. $\mathbf{Y}(x,0) = h$ but this is perturbed in some manner causing fluid from the shallow side to cross into the deep side (and vice versa). Conservation of PV requires that this fluid acquires positive relative vorticity which is shown by the arrow circling in the counter-clockwise direction. The opposite occurs for fluid crossing deep to shallow and the net effect is that the wave propagates with shallow water to its right. This is always the case in the Northern Hemisphere.

2.1 Weakly Nonlinear Topographic Waves.

A natural place to start when reviewing this topic is the problem of hydraulics and hydraulic control of inviscid, homogeneous fluid passing through a long constriction or over long topography. The classical theory of the hydraulics of surface gravity waves in a non-rotating channel is studied in Baines [1995] with many extensions that carry over to rotating channel hydraulics, a review of which can be found in Pratt and Lundberg [1991]. The basis of all hydraulic theories is the observation that the nonlinear behavior of the free-surface is closely related to the wave dynamics of the free surface, Johnson and Clarke [2001], or in simpler terms that wave propagation effects can control the fluid volume flux through a system, Haynes et al. [1993]). Gill [1977] proposes a formalism for hydraulics stating that a flow is hydraulic when it can be described at any station in terms of a single variable describing the local geometry. Hydraulic control is the situation when, for a particular value of this geometric variable two flow states (or conjugate states) merge and the flow may change state. In the rotating, open-channel case the critical control condition is determined by the speed of Kelvin waves, Stern [1972]. A flow region where waves can travel back upstream is called subcritical and a flow region where all waves are swept downstream is called supercritical.

Rossby-wave hydraulics is the study of hydraulic control by another class of waves, namely the Rossby-wave, Rossby [1949]. This will occur on length scales large enough that the rotation of the earth cannot be ignored (see Pratt and Armi [1987] and Woods [1993] for examples). In their review of Rossby-wave hydraulics, Johnson and Clarke [2001] note that conservation of energy flux is not enough to determine the hydraulic solution in cases of rotating flows with varying PV distributions. They

state that some other relationship between the PV and the streamfunction is needed to reduce the problem to one that satisfies Gill's formalism and thus it is the need to circumvent the limitations of pure hydraulics (e.g. the need for shock joining theories) that leads to the development of 'unsteady' hydraulic theory and a relaxation of hydraulic conditions to include the first order effects of dispersion. These solutions retain the simplicity of hydraulic theory but exhibit many of the flow features of the fully nonlinear flows being approximated.

In his study of coastally trapped, barotropic waves Grimshaw [1987] shows that flows exhibiting critical control may also show resonant behavior, and in particular a barotropic longshore current past topography, a forcing of $O(\alpha)$ produces a response of $O(\alpha^{1/2})$, although this is not always the appropriate scaling, (c.f. Clarke and Johnson [1996a]) and resonance occurs for long waves. Grimshaw derives a forced BDA (Benjamin [1967], Davies and Acrivos [1967]) equation that describes the evolution of the wave amplitude and discusses the solutions for various values of forcing strength and dissipation. He stresses that the resonant nonlinear effects produced do not only occur at exact resonance but within a bandwidth of long wave speeds. Another important comment is that the resonant theory described therein is much more computationally efficient to solve (when compared to fully nonlinear contour dynamics, say) and so the parameter regime can be more widely examined.

Another approach is that taken by Stern [1991] in which the two-dimensional shear flow around a semi-circular cape of varying sizes is considered. Analytical results for long waves are compared against contour dynamical integrations of the fully nonlinear problem in an attempt to test the validity of steady state and long wave ap-

proximations of hydraulic theory. He claims that regions of flow reversal (blocking) indicate that refinements of hydraulic theory are necessary including time dependence and shorter length scales (i.e. dispersive effects) and concludes that the effects of barotropic shear as well as gravity should be taken into account when studying control and transitions.

Haynes et al. [1993] consider hydraulic control and upstream influence in systems that only allow Rossby-wave propagation (i.e. wave propagation with the restoring mechanism being the conservation of PV). They investigate the problem using steady, nonlinear long wave theory and also fully nonlinear, time-dependent contour integrations, Dritschel [1988] of the long wave problem. They find behavior analogous to open channel hydraulics (e.g. hydraulic control at the point of maximum forcing) but also additional behavior in the strongly subcritical case. For this case there is a critical forcing amplitude which induces the point of control to move to the leading edge of the obstacle, leaving supercritical flow over the downstream side of the forcing which leaps to another supercritical solution at the downstream edge of the forcing. This is the approach-controlled flow, Lawrence [1993], described next.

In studying the properties and flow patterns of Rossby-waves in a channel, Johnson and Clarke [1999] and Clarke and Johnson [1999] extend the work of Haynes et al. [1993] by considering the higher order effects of dispersion to the hydraulic solutions described therein. They consider the role of long finite-amplitude Rossby-waves in determining the flow evolution in a rapidly rotating channel with a varying bottom topography. The PV for the fluid region takes on one of two values and the initial value problem can be explored effectively.

In Johnson and Clarke [1999] the usual slowly-varying hydraulic solutions are found (subcritical and supercritical) but the supercritical leap described above is explored further and found to break into two flow types described as 'approach controlled (AC)' and 'twin supercritical leap (TSL)'. These are steady flows characterized by a leap from one supercritical hydraulic solution to another and they correspond to kink soliton solutions of the steady, unforced problem. To summarize, the difference between the two flows is that AC flow is really a jump from a subcritical branch of the hydraulic solution to a supercritical branch via an intermediate supercritical solution whereas the TSL is a jump from one supercritical branch to another. They go on to show that increased dispersion negates the possibility of the classic hydraulic subcritical solution and that even when dispersion is small enough that this solution is allowed the initial value problem evolves to AC flows.

The works described so far have studied waves with no restrictions on wave amplitudes, so called finite-amplitude waves. In recent work, Clarke and Johnson [2001] study the weakly nonlinear limit of the finite-amplitude waves described above. They use the weakly nonlinear (and weakly dispersive) solutions to test the validity of the steady, non-dispersive hydraulic solutions by demanding that a postulated hydraulic solution is a valid asymptotic solution of the finite-amplitude evolution equation for small forcing when it matches the corresponding weakly nonlinear flow regime. In general they find that the steady hydraulic theory matches well to equivalent steady, weakly nonlinear flows but the expected unsteady hydraulic flows need to be modified to include the possibility of supercritical leaps. This explains the behavior described above where the weakly dispersive flow evolves to AC rather that

subcritical flow.

In Clarke and Johnson [1996a] they examine the flow of constant vorticity current past coastal topography in the weakly nonlinear, long wave limit. The study marries the approach of Grimshaw [1987] described above to one of the problems studied in Stern [1991]. They first note that even though this is the weakly nonlinear limit of the problem in Grimshaw [1987], the $O(\alpha)$ forcing will not result in $O(\alpha^{1/2})$ response at the interface (this is essentially due to their problem having constant depth and this denies a balance between forcing and nonlinearity at leading order) and so the problem must first be rescaled. They then derive an evolution equation of the BDA type which is typical of the semi-infinite fluid domain. In their problem they show, using conservation of PV, that any steady, hydraulically-controlled solution with differing widths up- and down-stream always has reversed flow upstream. They also show that there are no monotonic, steady transitions between conjugate states and attribute this to the nonlocal nature of the forcing. They present solutions of the unsteady initial value problem for a range of the parameter space (topographic amplitude, downstream flux) which fall into the categories; supercritical, steady-critical, blocked (large and small amplitude) and subcritical (large and small amplitude) and finally show that in the hydraulic limit the blocked and steady-critical regimes disappear.

Clarke and Johnson [1996b] considers the finite amplitude response to the same problem, which is again governed by an evolution equation of the BDA type. The flows are classified into 5 regimes consisting of the usual supercritical (denoted **D**) and subcritical flow (denoted **U**) and 3 new near-critical flow types. These are

the critical regime (denoted **C**) which is characterized by large amplitude solitary waves that propagate upstream from the topography with a smaller amplitude wave forming at the topography. There is partial blocking of the flow downstream which is terminated by an undular bore. The next regime is the transition regime (denoted **T**) which has a quasi-steady nonlinear wavetrain downstream of the vortex with a small-amplitude solitary wave upstream of the topography. The third regime is the blocked regime (denoted **B**) which is characterized by the generation of large-amplitude waves upstream and the formation of a downstream shelf (blocking), at even stronger forcing overturning occurs (denoted **O**). They present a regime diagram showing the placements of all of these regimes for the parameter space (topographic amplitude, downstream flux) for both the finite-amplitude and weakly nonlinear responses (note, however that the overturning regime is only present in the finite-amplitude case)

2.2   Vortex-Wave Interactions.

Interfacial vorticity waves have similar properties to Rossby-waves as they arise from situations where two regions of differing but constant PV are bordered. Such PV gradients may arise physically, for example, from jets or strong currents. Bell [1989] studies the interaction of vortices and interfacial vorticity waves in a shear flow with a weak interaction assumption (arising from the fact that the vortex is situated far from the interface but would also include a weak vortex closer to the interface). He simplifies the complex feedback mechanism greatly with the observation that with a weak interaction process the vortex motions owing to the waves will be negligible at the vortex and, further, the wave amplitude will be sufficiently small to be well described by linear theory. This effectively decouples the equations of motion and

allows individual analysis of the interface and vortex motions, with the waves evolving on a much more rapid timescale than the time taken for the vortex to respond to the presence of the waves. He finds that the critical factor deciding the eventual evolution is whether a stationary interfacial wave is possible. In particular, the system is *unstable* if a lee wave wake forms since this signifies a transfer of momentum and the vortex responds by drifting towards or away from the interface i.e. the solution cannot remain steady. The situation where a steady solution occurs but without the lee wake is defined as *stable*. Bell derives an exact conservation law for the along flow-component of momentum which is valid in the linear and fully nonlinear cases and uses this to describe the drift of the vortex towards or away from the interface. He goes on to study the interaction of a vortex with many vortex strips as a first approximation to continuous PV distributions and finds that solutions can be derived using the results for one interface provided that a configuration of stable interfaces can be found.

The decoupling of vortex motions and wave motions has been used in many recent studies and similar decoupling can be done in cases where the interaction between a PV interface and a vortex is strong (the opposite limit to Bell [1989]). In McDonald [1998b] the motion of an intense, quasi-geostrophic, singular vortex near an infinitely long escarpment is studied using small and long time asymptotics and fully nonlinear contour dynamics. The word 'intense' is used here to describe motions whereby the timescale for vortex circulation is much shorter than the topographic vortex stretching time. In other words, initially the advection of fluid across the step dominates over topographic wave generation and for short time (compared with topographic wave timescale) the initial value problem can be solved without consideration of

energy release from topographic waves. The vortex drift due to the influence of fluid crossing the escarpment is found to be an order of magnitude lower and again the problem can be split into an evolution equation for the secondary circulations and their effect on the vortex drift velocity. McDonald finds that initially cyclones propagate away from deep fluid with the opposite occurring for anti-cyclones but that both eventually settle to a drift with shallow fluid to their right at constant distance from the step. He also finds that this repulsion from deep fluid of the cyclone (and vice versa for the anti-cyclone) also occurs on the longer, topographic timescale, provided the vortex is an $O(1)$ distance from the escarpment. Further, it is shown that the vortex will always resonate with the background topographic wavefield implying that energy is being lost due to wave generation and this energy transfer is used to describe the time variation of the distance from the step of the vortex. Contour dynamics are then used to verify the analytic results.

The remaining cases of the weak and moderate strength vortex in the presence of an infinitely long escarpment are studied in Dunn et al. [2000]. Analytic progress is made in the weak case through linearising the governing equations using the small parameter which is the ratio of the topographic wave timescale to the advective timescale. For times which are short compared with the advective timescale the topographic waves all propagate away from the disturbance of the interface at the vortex and have no leading order effect on the vortex motion. A steady, localised, non-dispersive disturbance forms at the vortex and this is dubbed the 'pseudoimage' of the vortex in the interface (see also Stern and Flierl [1987] and Bell [1989]). It is the cause of the driving force of the vortex parallel to the escarpment in a similar manner to a vortex near a plane wall and governs the subsequent motion

for many eddy turnover times until topographic wave radiation becomes important. This occurs on the longer timescale and large time asymptotics reveal that for vortices moving in the same direction of the topographic waves radiate non-decaying (stationary) lee waves. The vortex then drifts towards the escarpment in response to the loss of energy in a manner identical to the above discussions. A vortex moving in the opposite direction eventually reaches a steady state with the pseudoimage dominating the motion. The moderate strength vortex is not studied analytically but is investigated with contour dynamics, as is the validity of the weak case analytics. A characteristic of the moderate case is the formation of dipoles and contrary to the intense case in McDonald [1998b] both cyclonic and anti-cyclonic vortices drift eastwards at large times.

Both McDonald [1998b] and Dunn et al. [2000] note that the protean nature of a vortex patch, i.e. its ability to change shape in response to wave radiation, is not captured when considering singular vortices, as is the contributions of vortex deformation to the velocity field and advection of ambient PV. The problem of the motion of a vortex patch that is initially circular is studied in Dunn [1999]. He finds that contour dynamic integrations show that the singular vortex formulation does predict the weak vortex patch's drift well, except for eastward traveling vortices where topographic wave radiation strips the vortex patch. The intense regime has good agreement with the results for singular vortices as long as the patch remains circular and that moderate vortex patches aren't modeled well with singular vortices, however they are still characterized by the formation of dipoles.

In Atassi et al. [1997] the interaction of a point vortex with a wall-bounded shear

layer is studied in the case where the initial interaction between the two is assumed to be weak. The geometry considered consists of a layer of constant vorticity bounded below by a wall and above by inviscid, irrotational flow. Three cases are discussed; firstly the interaction with a weak point vortex that is outside the layer; secondly, a weak point vortex inside the layer and finally a point vortex inside the layer that has sufficient strength to allow it move with a large horizontal velocity, i.e it is close to the wall. They are interested in finding conditions in the two-dimensional parameter space of initial position and vortex strength that will lead to sustained unsteadiness in the flow evolution. For the first case considered the vortex moves with a horizontal speed that is slow compared with the interfacial longwave speed and the interaction does not result in any large amplitude disturbances, the system will approach a steady state at large times with the vortex having drifted toward the layer. The second case contains the possibility that the vortex can move at a horizontal speed equaling an interfacial wave's phase speed, this results in a resonant interaction and in some cases the ejection of vorticity into the outer layer. They note that in this case it is necessary to account for the off-shore displacement of the vortex in order to describe the interactions that occur. For the third case it is shown that the faster horizontal speed of the vortex precludes any strong interactions and the interfacial wave amplitude is actually independent of the vortex strength, the long time state is again that of equilibrium. Having witnessed a variety of phenomena seen in boundary layer flows including evidence of nonlinear effects such as vorticity ejection, entrainment, rollup and solitary waves in this weak vortex study, they conclude that a study of the interaction between a much stronger point vortex and a wall bounded shear layer is necessary.

This problem is considered in Atassi [1998]. He studies the nonlinear interaction

analytically and numericallly, for the linear, weakly nonlinear and fully nonlinear limits, using contour dynamics to model the fully nonlinear flows. The paper is concerned with investigating the mechanism for vortex-induced ejection of vorticity from the wall as a model for transport and mixing between rotational and irrotational flows. The transport and mixing manifest themselves as the nonlinear effects hinted at above, namely ejection of vorticity and entrainment of irrotational flow. Again it is found that a resonant interaction occurs when the vortex speed is close to that of the interfacial wave speed and that this results in ejection. Furthermore this occurs for vortices of a weaker strength whose circulation is opposite in sign to the shear layer vorticity than for vortices whose sign of circulation is the same as the shear layer. He classifies the deformation of the interface into two types; wave-like behavior which occurs when the interaction is weak and/or not sustained; otherwise strong interaction resulting from a match in the vortex / interfacial wave speed and enhanced by an opposite sign of circulation. This case leads to ejection of vorticity away from the wall and entrainment of irrotational flow towards the wall. He concludes that these areas of isolated vorticity act to transfer momentum between the irrotational outer flow and the rotational shear layer.

2.3   Relevance to the Present Work

Even though the work presented in this thesis has no hydraulic limit corresponding to long topography or forcing the literature reviewed above serves to highlight the path from steady hydraulic theory, the drawbacks of which lead to the development of unsteady, dispersive corrections to hydraulic theory. This together with near-critical long wave theory are married in Clarke and Johnson [1996a]. In this it is pointed out that even with flow over long topography there are *no smooth transi-*

tions between conjugate states in coastally bounded, semi-infinite domains.

They further add that it is the very nature of the domain that causes this lack of hydraulic control, in effect, in a semi-infinite domain there can always be found a region of influence off-shore that is of comparable length scale to the topography or forcing being considered. This off-shore flow makes its presence felt through the dispersive term (which requires information from across the whole of the fluid domain) and nullifies the existence of smooth transitions. This is not so in the rotating channel (or coastally trapped) case as the topography/forcing can be made long compared to the off-shore fluid lengthscale (which is fixed).

Therefore, with regards to the work in this thesis, nothing has been lost in choosing a forcing that is short(i.e. a point vortex) and exists in a domain that is semi-infinite (i.e. coastal flow). The methods set out in the literature reviewed above can be applied, with some other parameter that describes a long lengthscale (in this case the wavelength of the topographic waves), leading, interestingly to qualitatively similar flow regimes to those described in Clarke and Johnson [1996a] and Clarke and Johnson [1996b]. An interesting problem (not considered here) would be the effect of a point vortex in a channel, the closed nature of the flow domain would imply a governing wave equation of the KdV type, which has locally determined dispersion.

Chapter 3

Problem Formulation and Linear Analysis.

3.1 Introduction.

In this chapter the linear dynamics of a weak point vortex in the presence of coastal topography are examined. The governing equations that describe wave generation and horizontal vortex motions are derived and it is shown that the leading order solution for a vortex that is initially an order one distance from the wall is simply a stationary vortex on- or off-shelf with transient, topographic waves generated at the step. For the case of a vortex that is initially close to the wall (and therefore on-shelf) the leading order solution is a steadily propagating vortex with topographic waves at the step. The speed and direction of propagation of the vortex depends on its strength and sign of circulation and its distance from the wall and it is shown that there are three typical responses; subcritical, supercritical and resonant when compared to the maximum group velocity of the waves.

3.2 Formulation.

Quasi-geostrophic motion on an f-plane is governed by the conservation of potential vorticity q say. In dimensional form this can be expressed as,

$$\frac{\partial q}{\partial t} + J(\psi, q) = 0. \tag{3.1}$$

Where ψ is the streamfunction and the operator $J(.)$ is the nonlinear Jacobian term defined $J(f, g) = f_x g_y - g_x f_y$. Consider the geometry shown in figure (3.1) which comprises of a thin layer of homogeneous, inviscid fluid which is rotating at a constant rate about a vertical axis z and has a rigid lid. A point vortex of circulation strength Γ is at the point $(X(t), Y(t))$ and there is a step in the bottom topography $z = h_B(y)$ along the line $y = h$. For quasi-geostrophy to hold the change in step height must be small, in other words the ratio $(D - d)/D \ll 1$. Non-dimensionalise the variables as follows; q on Q (where Q is some scale for the PV which will be specified later), (x, y) on h (an $O(1)$ length scale) and t on Q^{-1}. Therefore the streamfunction scales as QL^2.

The PV q is comprised of relative vorticity contributions due to the velocity field and the bottom topography, this can be written

$$q = \nabla^2 \psi + \frac{f\delta}{Q} h_B(y). \tag{3.2}$$

Where f is the Coriolis parameter and $\delta = (D-d)/D$ is a non-dimensional parameter describing the scale height of the topography. Setting the as yet undetermined PV scale Q as $f\delta$ gives the non-dimensional PV

$$q = \nabla^2 \psi + h_B(y), \tag{3.3}$$

(a)

(b)
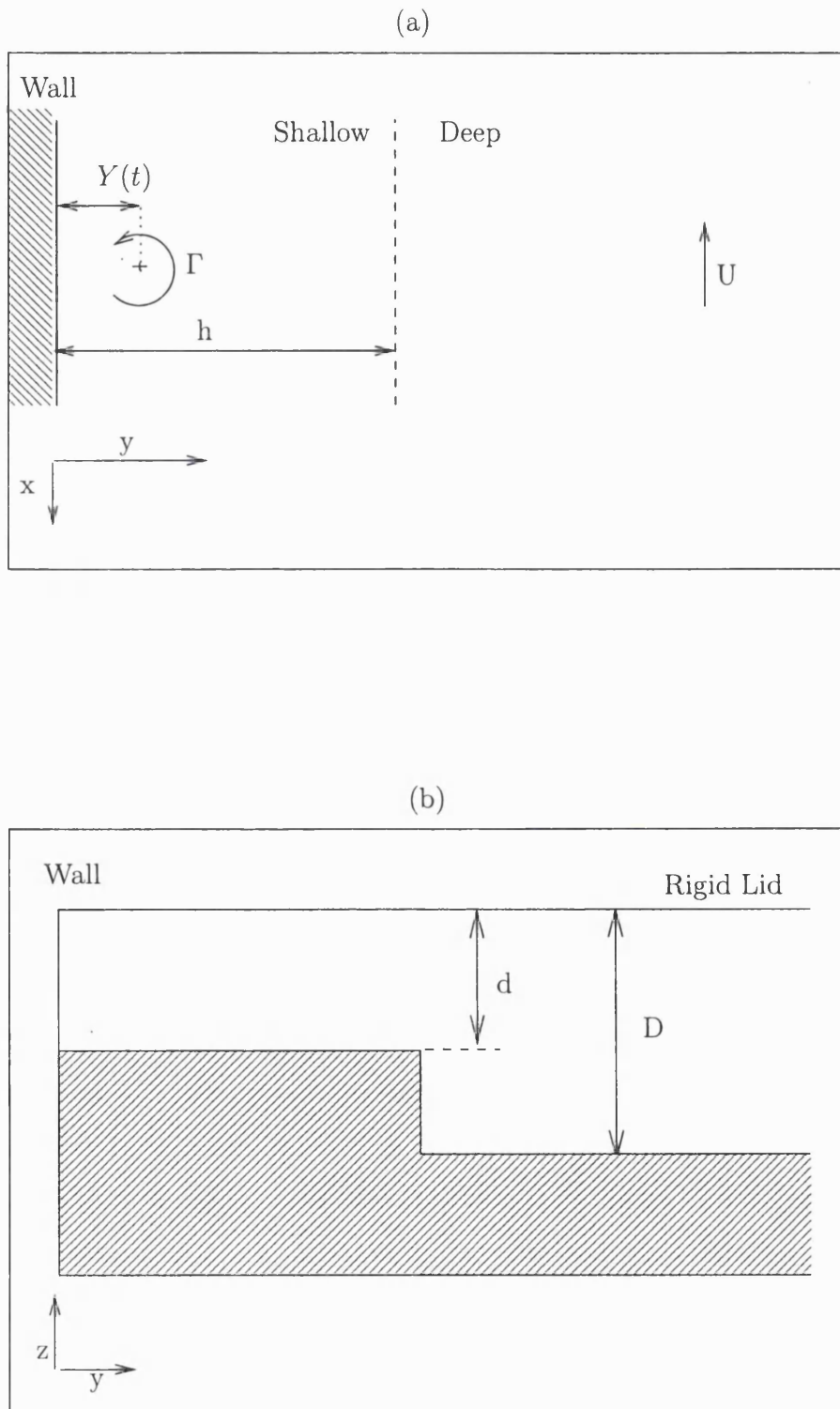
Figure 3.1: Schematic diagram of the domain of interest. Figure (a) shows the top view and (b) shows the side view.

and the non-dimensional governing equation (3.2) becomes

$$\frac{\partial}{\partial t}(\nabla^2 \psi) + J(\psi, \nabla^2 \psi) + \frac{\partial \psi}{\partial x}\frac{\partial h_B}{\partial y} = 0. \tag{3.4}$$

Equation (3.4) can be linearised for small disturbances, assume ψ takes the form

$$\psi = \varepsilon \psi_0 + \varepsilon^2 \psi_1 + O(\varepsilon^3), \tag{3.5}$$

where $0 < \varepsilon \ll 1$ is a small parameter (to be specified later). The governing equation (3.4) becomes

$$\varepsilon\left(\frac{\partial}{\partial t}(\nabla^2 \psi_0) + \frac{\partial \psi_0}{\partial x}\frac{\partial h_B}{\partial y}\right) + \varepsilon^2\left(\frac{\partial}{\partial t}(\nabla^2 \psi_1) + \frac{\partial \psi_1}{\partial x}\frac{\partial h_B}{\partial y} + J(\psi_0, \nabla^2 \psi_0)\right) = 0. \tag{3.6}$$

Then the $O(\varepsilon)$ terms of (3.6) form a linear forced topographic wave equation

$$\frac{\partial}{\partial t}(\nabla^2 \psi_0) + \frac{\partial \psi_0}{\partial x}\frac{\partial h_B}{\partial y} = 0. \tag{3.7}$$

The solution to (3.7) without any bottom topography (and in fact (3.4)) gives the forcing to the problem which is a standard log vortex positioned at $(X(t), Y(t))$ in the presence of a wall at $y = 0$ (see figure (3.2)).

$$\Psi = \frac{\Gamma}{4\pi}\log\left((x - X(t))^2 + (y - Y(t))^2\right) - \frac{\Gamma}{4\pi}\log\left((x - X(t))^2 + (y + Y(t))^2\right). \tag{3.8}$$

This is simply the sum of a point vortex Ψ_v of circulation strength $\Gamma \sim O(1)$ and its image in the wall Ψ_i. The sign of Γ gives the sense of the circulation, for $\Gamma < 0$ the sense is clockwise. The equations of motion for the vortex center are
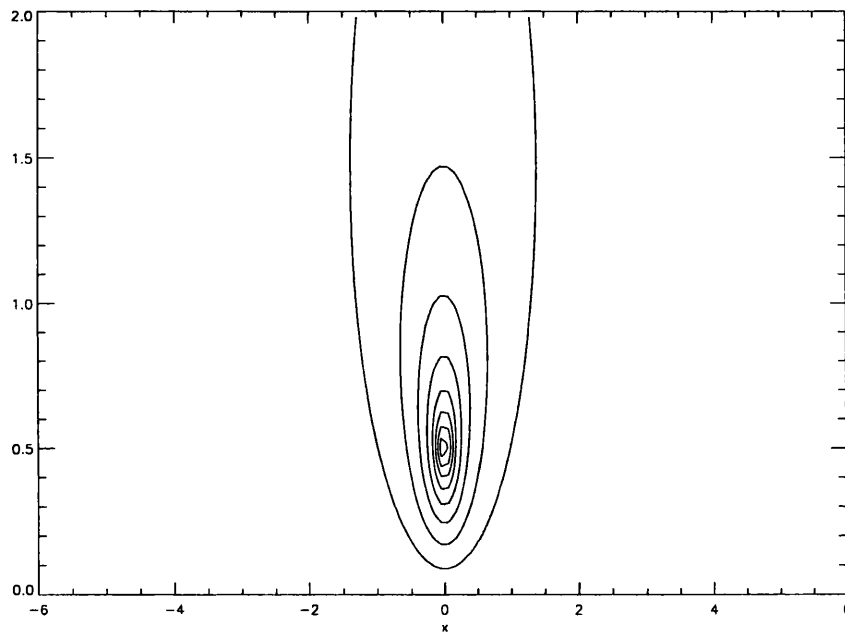
Figure 3.2: Streamfunction contours for a standard *Log* vortex, at $(X, Y) = (0, 0.5)$ with a wall along $y = 0$. The strength of the vortex is $\Gamma = 1$.

$$\frac{dX}{dt} = -\frac{\partial \psi}{\partial y}\Big|_{X,Y}, \tag{3.9}$$

$$\frac{dY}{dt} = \frac{\partial \psi}{\partial x}\Big|_{X,Y}, \tag{3.10}$$

and implicit in this is the assumption that there is no self-advection of the vortex, only the image Ψ_i contributes to the right-hand side.

In the absence of topography the vortex is advected purely by its reaction to the image vortex in the wall and so

$$\frac{dX}{dt} = \frac{\varepsilon \Gamma}{4\pi Y(0)}, \tag{3.11}$$

$$\frac{dY}{dt} = 0. \tag{3.12}$$

So now it is clear that the translational velocity of the vortex will have two components, one due to its interaction with topography which is (for linear theory to be valid) at most $O(\varepsilon)$, and a drift due to the action of the image vortex in the wall, which from (3.11) is of $O(\varepsilon/Y(0))$.

Thus there are two cases for $Y(0)$ to consider. In Section 3.4.1 it will be shown that starting the vortex at $Y(0) \sim O(1)$ distance from the wall results in $O(\varepsilon)$ forcing at the topography and will induce an $O(\varepsilon)$ background drift due to the wall, meaning that for $O(1)$ timescales the vortex is stationary and positioned at $(0, Y(0))$. Then in section 3.4.4, choosing $Y(0) \sim O(\varepsilon)$ results in $O(\varepsilon^2)$ forcing at the topography, but (3.11) implies an $O(1)$ drift speed parallel to the wall and it will be shown that the possibility of a resonant interaction between the vortex and the topographic waves may arise in this case.

Before the interaction of a vortex and topographic waves is studied in detail, the freewave (i.e. in the absence of forcing by a vortex) dispersion relation for linear

topographic waves is derived and it is shown that they have an $O(1)$ maximum group velocity which occurs for the longest wave. This is also the wave with the maximum phase velocity.

3.3   The Free Wave Dispersion Relation.

To derive the free wave dispersion relation consider wave-like solutions to the unforced form of (3.7) i.e.

$$\psi_0 = \phi_0(y)e^{i(kx-\omega t)} \tag{3.13}$$

with bottom topography given by

$$h_B(y) = -H(y-h). \tag{3.14}$$

Here $H(y-h)$ is the Heaviside step function defined as

$$H(y-h) = \begin{cases} 1 & y-h > 0 \\ 0 & y-h < 0. \end{cases} \tag{3.15}$$

Therefore

$$\frac{\partial h_B}{\partial y} = -\delta(y-h). \tag{3.16}$$

With $\delta(y-h)$ the Dirac-Delta function, which has the sampling property

$$\int_{-R}^{R} \delta(y)F(y)\mathrm{d}y = F(0), \tag{3.17}$$

for any function F and any value $R > 0$. Away from $y = h$ the governing equation becomes

$$\frac{\partial}{\partial t}(\nabla^2 \psi_0) = 0. \tag{3.18}$$

However in the linear limit any disturbance at the interface is infinitesimal and therefore the line $y = h$ approximates the position of the material contour over

which a jump in PV occurs. This jump is due to the change in depth at the step and therefore the relative vorticity due to the velocity field is constant and equal to zero everywhere. So for all (x, y) except $y = h$,

$$\nabla^2 \psi_0 = 0. \tag{3.19}$$

Jump conditions at $y = h$ can be derived from (3.7) by integrating across the step i.e.

$$\int_{h-d}^{h+d} \nabla^2 \psi_{0t} \mathrm{d}y - \int_{h-d}^{h+d} \psi_{0x} \delta(y - h) \mathrm{d}y = 0, \tag{3.20}$$

for vanishingly small d. Now ψ_{0xx} is continuous at $y = h$ so denoting $[f(y)] = \lim_{d \to 0} \left(f(h + d) - f(h - d) \right)$ the jump in f, (3.20) becomes

$$[\psi_{0yt}] - \psi_{0x}(x, h) = 0. \tag{3.21}$$

Since ψ_{0x} is also continuous at $y = h$,

$$[\psi_0] = 0. \tag{3.22}$$

The final system of equations to be solved is

$$\nabla^2 \psi_0 = 0, \tag{3.23}$$

everywhere, with boundary conditions;

$$\psi_0 = 0 \quad \text{on} \quad y = 0, \tag{3.24}$$

$$\psi_0 \to 0 \quad \text{as} \quad y, \to \infty. \tag{3.25}$$

and the jump conditions at $y = h$,

$$[\psi_0] = 0, \tag{3.26}$$

$$[\psi_{0yt}] - \psi_{0x} = 0. \tag{3.27}$$

The condition (3.24) represents no normal flow at the wall $y = 0$ and (3.25) says that the flow becomes quiescent at large distances from the wall. For $y < h$. The solution of (3.23) satisfying (3.24) and (3.25) is

$$\phi = 2A \sinh(ky). \tag{3.28}$$

Using the first jump condition (3.26) gives for $y > h$

$$\phi = 2A \sinh(kh)e^{|k|(h-y)}, \tag{3.29}$$

where A is some constant.

The second jump condition (3.27) then gives the dispersion relation as,

$$\omega = \frac{k \sinh(kh)}{|k| \sinh(kh) + k \cosh(kh)} = \sinh(kh)e^{-|k|h}. \tag{3.30}$$

The group velocity C_g and phase velocity C_p are defined

$$C_g = \frac{\partial \omega}{\partial k} = he^{-2|k|h}, \tag{3.31}$$

$$C_p = \frac{\omega}{k} \quad \frac{\sinh(kh)e^{-|k|h}}{k}. \tag{3.32}$$

Both the phase and group velocities have a maximum of h at $k = 0$ and both vanish as $k \to \infty$ (figure (3.3)), hence the longest wave travels the fastest. Also $C_g > 0$ and $C_p > 0$ for all k which means that the waves travel with shallow water to their right (in the Northern Hemisphere) as described in chapter 2.

For future reference the longwave limit $k \to 0$ of the dispersion relation (3.30) is

$$\omega = kh - h^2 k|k| + \frac{2}{3}k^3 h^3 + ... \tag{3.33}$$

So the frequency given by (3.30) is bounded as $k \to \infty$ for in that limit $\omega \to 1/2$ whereas in the longwave limit the dispersion relation (3.33) allows waves of all frequencies. The linear problem should not have waves of frequency higher than 1/2
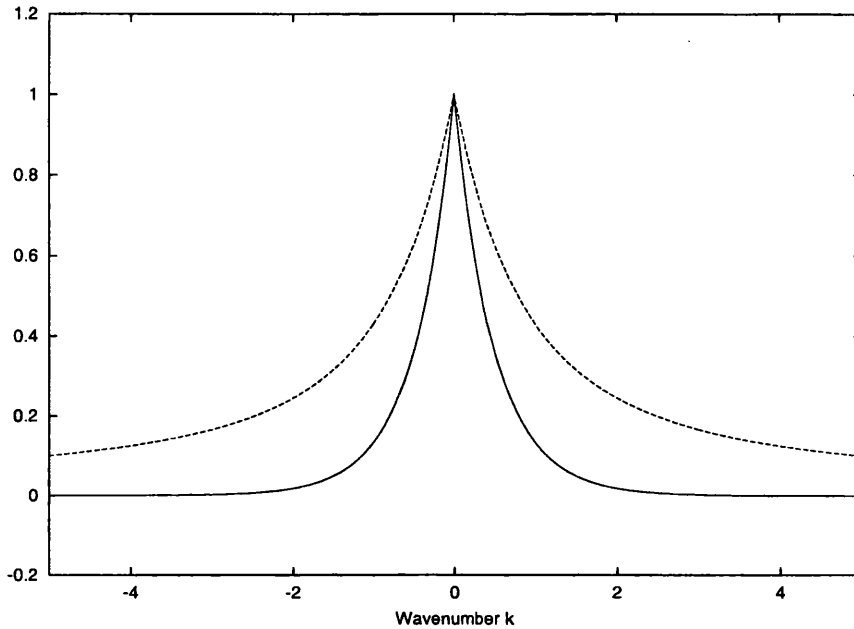
Figure 3.3: Phase velocity (dashed line) and group velocity (solid line) with $h = 1$.

whereas waves of all frequency are permitted in the longwave case, this becomes important only in a numerical sense and is dealt with further in chapter 5.

It is noted for later use that (3.33) is equivalent to a wave equation of the form, Whitham [1974]

$$\frac{\partial \psi}{\partial t} = -h\frac{\partial \psi}{\partial x} + h^2 \mathbb{B}\left(\frac{\partial \psi}{\partial x}\right) + \frac{2}{3}h^3\frac{\partial^3 \psi}{\partial x^3}. \tag{3.34}$$

The $\mathbb{B}$ operator is defined as

$$\mathbb{B}(\psi) = \frac{1}{2\pi}\int_{-\infty}^{\infty}\hat{\psi}|k|e^{ikx}dk = \frac{1}{\pi}\frac{\partial}{\partial x}\int_{-\infty}^{\infty}\frac{\psi(y)}{x-y}dy, \tag{3.35}$$

and the Hilbert integral in the second form for $\mathbb{B}$ is a Cauchy Principal Value (Benjamin [1967], Davies and Acrivos [1967]).

3.4 The Forced Linear Response.

In this section consider the linear response at the interface due to the motion of a point vortex with circulation $\varepsilon\Gamma$.

Let the maximum group velocity be rescaled to unity so that $h = 1$, in this section a full solution for the short time linear problem is derived in terms of Fourier integrals. These integrals are examined in various asymptotic limits and the validity for large times of such solutions discussed.

Equation (3.11) showed that the along-shore drift of the vortex due to the wall was $O(\varepsilon/Y)$ so there are two cases to consider, first, when $Y \sim O(1)$ it is shown that at leading order the vortex is stationary and, second, for $Y \sim O(\varepsilon)$ to leading order the vortex moves at a fixed distance from the wall at a constant speed $U \sim O(1)$.

3.4.1 $Y \sim O(1)$:

In this case the forcing at the escarpment is clearly $O(\varepsilon)$. The presence of the vortex *and* coastal topography will induce $O(\varepsilon)$ secondary motions ϕ. Hence the streamfunction is decomposed as $\psi = \varepsilon\psi_0 + O(\varepsilon^2)$, where

$$\psi_0 = \Psi + \phi. \tag{3.36}$$

Here $\Psi = \Psi_v + \Psi_i$ represents the vortex and its image and ϕ the streamfunction due to the topographic waves. Equations (3.9) for the vortex center reduce to

$$\frac{\mathrm{d}X}{\mathrm{d}t} = -\varepsilon\frac{\partial\phi}{\partial y}\bigg|_{X,Y} - \varepsilon\frac{\partial\Psi_i}{\partial y}\bigg|_{X,Y}, \tag{3.37}$$

$$\frac{\mathrm{d}Y}{\mathrm{d}t} = \varepsilon\frac{\partial\phi}{\partial x}\bigg|_{X,Y} + \varepsilon\frac{\partial\Psi_i}{\partial x}\bigg|_{X,Y}, \tag{3.38}$$

where

$$\Psi_i = -\frac{\Gamma}{4\pi}\log\left((x - X(t))^2 + (y + Y(t))^2\right). \tag{3.39}$$

So equations (3.37) and (3.38) simplify to

$$\frac{dX}{dt} = -\varepsilon\frac{\partial\phi}{\partial y}\Big|_{X,Y} + \frac{\varepsilon\Gamma}{4\pi Y(t)}, \tag{3.40}$$

$$\frac{dY}{dt} = \varepsilon\frac{\partial\phi}{\partial x}\Big|_{X,Y}. \tag{3.41}$$

Without the presence of bottom topography the vortex would drift at a constant horizontal speed of $U = \varepsilon\Gamma/4\pi Y(0)$ at a fixed distance $y = Y(0)$ from the wall. Therefore set

$$X = Ut + \varepsilon X_1(t) + \ldots, \tag{3.42}$$

$$Y = y_0 + \varepsilon Y_1(t) + \ldots, \tag{3.43}$$

with $y_0 = Y(0) \sim O(1)$. Equations (3.40) give

$$U + \varepsilon\frac{dX_1}{dt} \simeq -\varepsilon\phi_y(X_0, Y_0) + \varepsilon\frac{\Gamma}{4\pi y_0} + O(\varepsilon^2), \tag{3.44}$$

$$\varepsilon\frac{dY_1}{dt} = \varepsilon\phi_x(X_0, Y_0). \tag{3.45}$$

So choosing $U = \varepsilon\Gamma/4\pi y_0$ gives the horizontal drift of the vortex as $O(\varepsilon)$ and so to leading order the vortex remains at $(0, y_0)$ for times $t \ll O(\varepsilon^{-1})$.

Taking Ψ to be the leading order forcing

$$\Psi = \frac{\Gamma}{4\pi}\log\left(\frac{x^2 + (y - y_0)^2}{x^2 + (y + y_0)^2}\right). \tag{3.46}$$

The equations of motion become;

$$\nabla^2\phi = 0, \tag{3.47}$$

everywhere except $y = 1$ and at the vortex. The boundary conditions are

$$\phi = 0 \quad\quad \text{on} \quad\quad y = 0, \tag{3.48}$$

$$\phi \to 0 \quad\quad \text{as} \quad\quad x^2 + y^2 \to \infty, \tag{3.49}$$

and the jump conditions at $y = 1$ now become,

$$[\phi] = 0, \tag{3.50}$$

$$[\phi_{yt}] - \phi_x = \Psi_x. \tag{3.51}$$

The initial condition for this problem is that at time $t = 0$ the topography is 'switched on' near a pre-existing point vortex, this process is assumed to occur on a timescale that is much faster than the topographic wave speed and so at $t = 0$

$$\phi = 0, \tag{3.52}$$

Define the Fourier transform $\hat{\phi}(k, y, t)$ of $\phi(x, y, t)$ by

$$\hat{\phi} = \int_{-\infty}^{\infty} \phi e^{-ikx} dx, \tag{3.53}$$

with the inverse transform

$$\phi = \frac{1}{2\pi} \int_{-\infty}^{\infty} \hat{\phi} e^{ikx} dk. \tag{3.54}$$

Taking Fourier transforms of $(3.47) - (3.51)$ gives;

$$\hat{\phi}_{yy} - k^2 \hat{\phi} = 0, \tag{3.55}$$

with boundary conditions

$$\hat{\phi} = 0 \qquad \text{on} \qquad y = 0, \tag{3.56}$$

$$\hat{\phi} \to 0 \qquad \text{as} \qquad x^2 + y^2 \to \infty, \tag{3.57}$$

and the jump conditions at $y = 1$,

$$[\hat{\phi}] = 0, \tag{3.58}$$

$$[\hat{\phi}_{yt}] - ik\hat{\phi} = ik\hat{\Psi}(k, 1). \tag{3.59}$$

With the Fourier transform of (3.46) $\hat{\Psi}(k, y)$ is found to be (see appendix A)

$$
\hat{\Psi}(k, y) = \begin{cases} -\frac{\Gamma}{k} \sinh(ky) e^{-|k|y_0} & 0 < y < y_0, \\[2ex] -\frac{\Gamma}{k} \sinh(ky_0) e^{-|k|y} & y_0 < y. \end{cases} \tag{3.60}
$$

The general solution of equation (3.55) satisfying (3.56) and (3.57) is

$$
\hat{\phi} = \begin{cases} 2A(t) \sinh(ky) & 0 < y < 1, \\[2ex] B(t) e^{-|k|y} & 1 < y, \end{cases} \tag{3.61}
$$

for some undetermined functions A, B. Matching at $y = 1$ using condition (3.58) and (3.59) gives

$$
-|k| B_t e^{-|k|} - 2A_t k \cosh(k) - 2ikA \sinh(k) = ik\hat{\Psi}(k, 1), \tag{3.62}
$$

$$
B = 2A \sinh(k) e^{|k|}. \tag{3.63}
$$

Equations (3.62) and (3.63) combine to give

$$
2\frac{\partial}{\partial t}\left(A e^{i\omega t}\right) = -i\hat{\Psi}(k, 1) e^{i\omega t - |k|}, \tag{3.64}
$$

where $\omega(k) = \sinh(k) e^{-|k|}$ is the dispersion relation. Solving (3.64) gives

$$
A = -\frac{\hat{\Psi}(k, 1) e^{-|k|}}{2\omega} + C e^{-i\omega t}, \tag{3.65}
$$

for some constant $C(k)$. The initial condition $\hat{\phi} = 0$ at $t = 0$ means

$$
A = -\frac{\hat{\Psi}(k, 1) e^{-|k|}}{2\omega}\left(1 - e^{-i\omega t}\right), \tag{3.66}
$$

$$
B = -\frac{\hat{\Psi}(k, 1) \sinh(k)}{\omega}\left(1 - e^{-i\omega t}\right) \tag{3.67}
$$

So

$$
\hat{\phi}(k, y, t) = -\frac{\hat{\Psi}(k, 1) W(k, y)}{\omega}\left(1 - e^{-i\omega t}\right), \tag{3.68}
$$

where

$$W(k,y) = \begin{cases} \sinh(ky)e^{-|k|} & 0 < y < 1, \\ \\ \sinh(k)e^{-|k|y} & 1 < y. \end{cases} \tag{3.69}$$

The solution is therefore composed of three parts, the forcing term Ψ defined as before, a steady term ϕ_s and an unsteady wavelike term ϕ_w

$$\psi_0 = \Psi + \phi_s + \phi_w, \tag{3.70}$$

i.e.

$$\phi_s = -\frac{1}{2\pi} \int_{-\infty}^{\infty} \frac{\hat{\Psi}(k,1)W(k,y)}{\omega} \ e^{ikx}\mathrm{d}k, \tag{3.71}$$

$$\phi_w = \frac{1}{2\pi} \int_{-\infty}^{\infty} \frac{\hat{\Psi}(k,1)W(k,y)}{\omega} \ e^{i(kx-\omega t)}\mathrm{d}k. \tag{3.72}$$

(a)

(b)
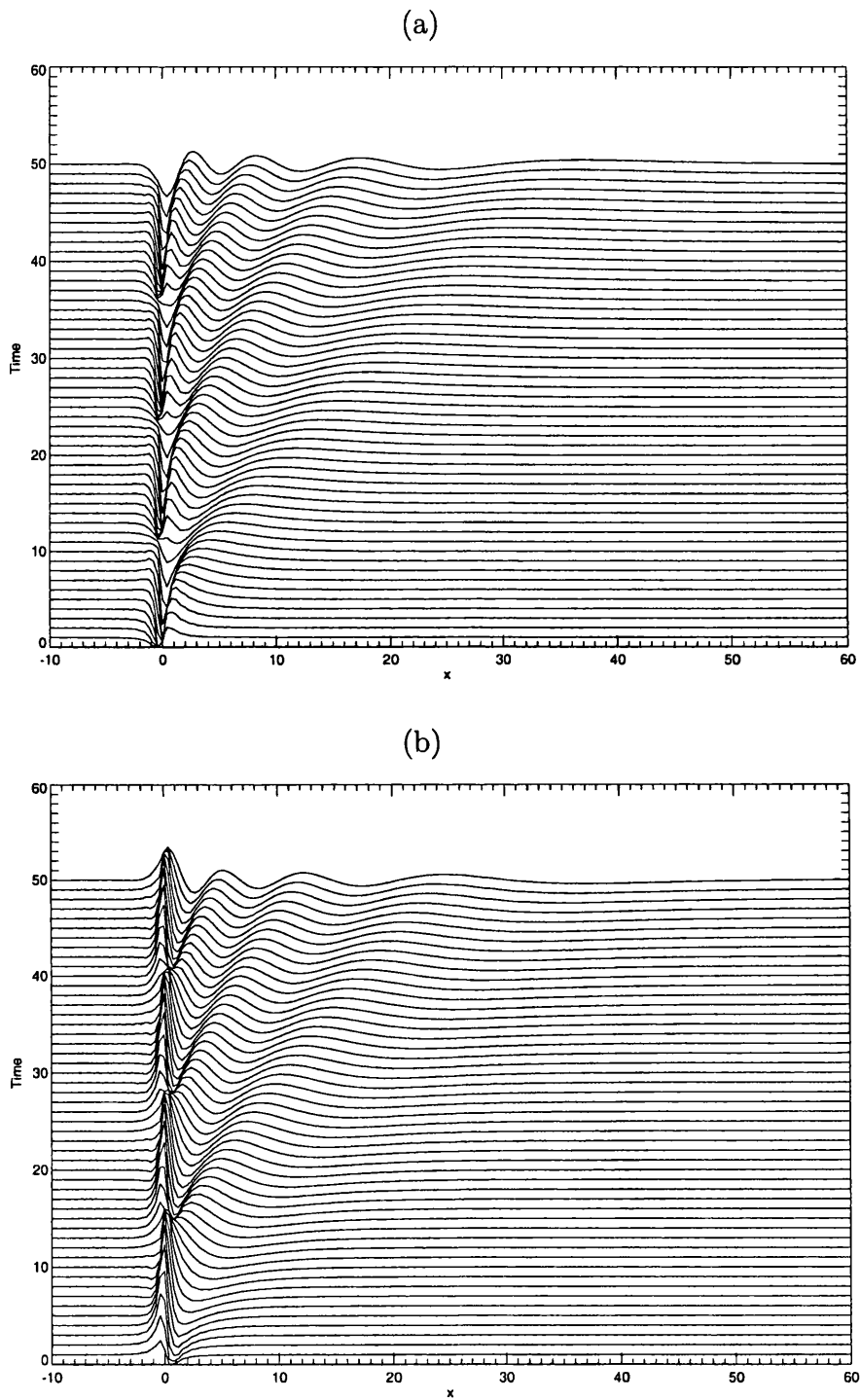
Figure 3.4: Evolution of $\eta(x,t)$ for an on-shelf vortex (a) $y_0 = 0.5$ and $\Gamma = 1$, (b) $y_0 = 0.5$ and $\Gamma = -1$.

(a)

(b)
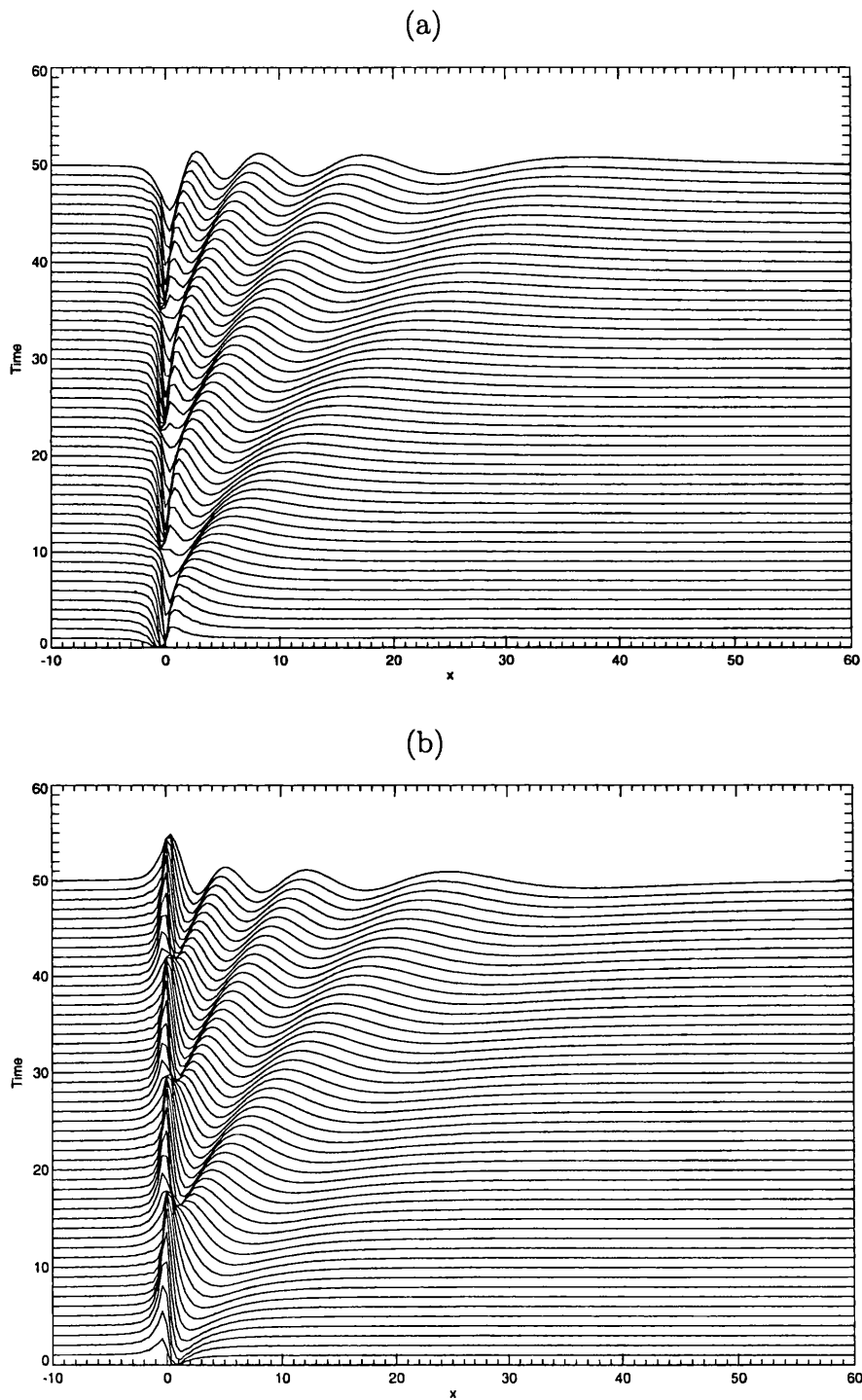
Figure 3.5: Evolution of $\eta(x, t)$ for an off-shelf vortex (a) $y_0 = 1.5$ and $\Gamma = 1$, (b) $y_0 = 1.5$ and $\Gamma = -1$.

The interface displacement in the linear limit is related to the streamfunction ψ_0 by

$$\eta_t = \psi_{0x},\tag{3.73}$$

along the line $y = 1$. Taking Fourier transforms of (3.73) with respect to x gives,

$$\hat{\eta}_t = ik\hat{\psi}_0(k, 1, t),\tag{3.74}$$

which can be written

$$\hat{\eta}_t = ik\hat{\Psi}(k, 1)e^{-i\omega t}.\tag{3.75}$$

Performing the integration with respect to t and using the initial condition $\hat{\eta} = 0$ at $t = 0$ gives that the Fourier transform of the interface is

$$\hat{\eta} = \frac{\hat{\Psi}(k, 1)}{C_p(k)}\left(1 - e^{-i\omega t}\right).\tag{3.76}$$

Equation (3.76) is to be inverted using the Fast Fourier Transform (FFT) method of Cooley and Tukey [1965], as are the other Fourier integrals of this chapter.

Figure (3.4a) illustrates the case of an on-shelf ($y_0 = 0.5$) cyclonic ($\Gamma = 1$, counterclockwise circulation) vortex by plotting the response of the interface at various time levels. Initially the contour is flat, the vortex is introduced and pulls fluid from the deep side to the shallow side (and vice-versa). A topographic wave forms and propagates with shallow water to the right as expected. The fastest wave is also the longest wave and is traveling at speed unity. Eventually the transient waves will disperse leaving the solitary 'hump' solution corresponding to a vortex and its image in the step, this has been dubbed the ' pseudoimage' (Stern and Flierl [1987], Bell [1989], Dunn et al. [2000]) and will be described in the next two sections.

Figure (3.4b) is the on-shelf ($y_0 = 0.5$) anti-cyclonic case ($\Gamma = -1$), the initially flat contour is deformed by the presence of the vortex which pushes fluid from the

shallow side to the deep side (and vice-versa). The topographic wave is formed and propagates to the right, this will eventually decay leaving the steady, pseudoimage solution above the vortex.

An explanation of whether the pseudoimage solution corresponds to fluid that has been pushed off the shelf or fluid that has been pulled onto the shelf is simple. An on-shelf cyclonic vortex will produce an off-shelf *anti-cyclonic* pseudoimage in the interface, this corresponds to a patch of negative vorticity on the deep side of the escarpment which is exactly what a permanent deformation of the interface from deep to shallow is, so the on-shelf cyclonic vortex 'pulls' the interface towards it. The exact opposite occurs for the on-shelf, anti-cyclonic vortex which 'pushes' the interface away as this is the only manifestation of the 'extra' positive vorticity present off-shelf.

This is seen again in figure (3.5) where (3.5a) is the off-shelf, cyclonic vortex ($\Gamma = 1$, $y_0 = 1.5$) and (3.5b) is the off-shelf, anti-cyclonic vortex ($\Gamma = -1$, $y_0 = 1.5$). Unsurprisingly there is no appreciable difference in the wave dynamics, the topographic waves just propagate with shallow water to their right. However now the off-shelf, cyclonic vortex 'pushes' the interface onto the shelf where-as the off-shelf, anti-cyclonic vortex 'pulls' the interface off the shelf.

There is no real difference between the on- and off- shelf vortex cases in this leading order approximation as the vortices are stationary, however when the higher order effects of the topographic waves are considered the response is very different (see chapter 7).

3.4.2 The Unsteady Response.

Note that, for small k, (3.60) and (3.69) are

$$\hat{\Psi}(k,y) \approx \begin{cases} -\Gamma y & 0 < y < y_0, \\ -\Gamma y_0 & y_0 < y. \end{cases} \qquad (3.77)$$

$$\frac{W(k,y)}{\omega(k)} \approx \begin{cases} y & 0 < y < 1, \\ 1 & 1 < y. \end{cases} \qquad (3.78)$$

So both integrals (3.71) and (3.72) have no poles and the long time asymptotic behavior of ϕ_w is dominated by points $k = \pm k_s$ of stationary phase where $x - C_g(k_s)t = 0$. Splitting the integral up into 5 sections;

1. $k = [-\infty, -k_s - \delta]$.

2. $k = [-k_s - \delta, -k_s + \delta]$.

3. $k = [-k_s + \delta, k_s - \delta]$.

4. $k = [k_s - \delta, k_s + \delta]$.

5. $k = [k_s + \delta, \infty]$.

With δ small all but integrals 2 and 4 will decay like t^{-1} as they contain no points of stationary phase. So for large times the maximum contribution to the integral comes from the immediate neighborhood of $k = \pm k_s$ and so $\phi_w \sim I_2 + I_4$ given by

$$\phi_w \sim \int_{-k_s-\delta}^{-k_s+\delta} \frac{\hat{\Psi}(k,1)W(k,y)}{2\pi\omega} e^{i(kx-\omega t)} dk + \int_{k_s-\delta}^{k_s+\delta} \frac{\hat{\Psi}(k,1)W(k,y)}{2\pi\omega} e^{i(kx-\omega t)} dk.$$

$$(3.79)$$

Examining the second integral I_4 in (3.79), this can be split further

$$I_4 = I_- + I_+ = \int_{k_s-\delta}^{k_s} \frac{\hat{\Psi}(k,1)W(k,y)}{2\pi\omega} e^{i(kx-\omega t)} dk + \int_{k_s}^{k_s+\delta} \frac{\hat{\Psi}(k,1)W(k,y)}{2\pi\omega} e^{i(kx-\omega t)} dk.$$

$$(3.80)$$

Consider the second integral of (3.80), $I_+(x, y, t)$, expand the phase $kx - \omega t$ about $k = k_s > 0$

$$kx - \omega(k)t = k_s x - \omega(k_s)t + (x - \omega'(k_s)t)(k - k_s) - \omega''(k_s)t\frac{(k - k_s)^2}{2} + \ldots, \quad (3.81)$$

where the dash represents differentiation with respect to k.

Utilising the method of Stationary Phase (see Bender and Orszag [1978]), at large times only the immediate neighborhood of $k = k_s$ will contribute to the integral in (3.81) thus,

$$I_+(x, y, t) \sim \frac{\hat{\Psi}(k_s, 1)W(k_s, y)}{2\pi\omega(k_s)} e^{i(k_s x - \omega(k_s)t)} \int_{k_s}^{k_s + \delta} \exp(-itC_g'(k_s)(k - k_s)^2/2)dk.$$

$$(3.82)$$

Define α and α_s as;

$$\alpha(k) = \begin{cases} (k - k_s)\left(\frac{t}{2}|C_g'(k_s)|\right)^{1/2} e^{-i\frac{\pi}{4}} & C_g'(k_s) > 0, \\ (k - k_s)\left(\frac{t}{2}|C_g'(k_s)|\right)^{1/2} e^{i\frac{\pi}{4}} & C_g'(k_s) < 0, \end{cases}$$

$$\alpha_s = \alpha(k_s + \delta). \quad (3.83)$$

Note that

$$C_g'(k) = -2\,\text{sgn}(k)e^{-2|k|}. \quad (3.84)$$

So $\text{sgn}(C_g'(k)) = -\text{sgn}(k)$. This gives, as $t \to \infty$

$$I_+(x, y, t) \sim \frac{\sqrt{2}\hat{\Psi}(k_s, 1)W(k_s, y)}{2\pi\omega(k_s)\sqrt{t|C_g'(k_s)|}} \exp(i(k_s x - \omega(k_s)t - \pi/4)) \int_0^\infty e^{-i\alpha^2}d\alpha. \quad (3.85)$$

Where the error in extending the integral to ∞ decays like t^{-1}. Using the integral representation of the gamma function $\gamma(1/2)$

$$\gamma(1/2) = 2\int_0^\infty e^{-i\alpha^2}d\alpha = 2\sqrt{\pi}. \quad (3.86)$$

So for large times,

$$I_+(x,y,t) \sim \frac{\sqrt{2}\hat{\Psi}(k_s,1)W(k_s,y)}{\omega(k_s)\sqrt{\pi t|C_g'(k_s)|}}e^{i\left(k_s x - \omega(k_s)t - \pi/4\right)}. \qquad (3.87)$$

An identical analysis can be done for I_- and the equivalent form for (3.85) is, as $t \to \infty$

$$I_-(x,y,t) \sim \frac{\sqrt{2}\hat{\Psi}(k_s,1)W(k_s,y)}{2\pi\omega(k_s)\sqrt{t|C_g'(k_s)|}} \exp\left(i(k_s x - \omega(k_s)t - \pi/4)\right) \int_{-\infty}^{0} e^{-i\alpha^2}\mathrm{d}\alpha. \qquad (3.88)$$

Swapping the dummy variable of integration in (3.88) from $\alpha \to -\alpha$ reverts (3.88) back to (3.85) and so

$$I_4(x,y,t) \sim t^{-\frac{1}{2}}\frac{2\sqrt{2}\hat{\Psi}(k_s,1)W(k_s,y)}{\omega(k_s)\sqrt{\pi|C_g'(k_s)|}}e^{i\left(k_s x - \omega(k_s)t - \pi/4\right)}. \qquad (3.89)$$

The analysis for I_2 is very similar, note that the function

$$\frac{\hat{\Psi}(k,1)W(k,y)}{\omega(k)}, \qquad (3.90)$$

is even in k and so the result is just quoted as

$$I_2(x,y,t) \sim t^{-\frac{1}{2}}\frac{2\sqrt{2}\hat{\Psi}(k_s,1)W(k_s,y)}{\omega(k_s)\sqrt{\pi|C_g'(k_s)|}}e^{-i\left(k_s x - \omega(k_s)t - \pi/4\right)}. \qquad (3.91)$$

Therefore

$$\phi_w(x,y,t) \sim \frac{t^{-\frac{1}{2}}}{\sqrt{\pi}}\frac{4\hat{\Psi}(k_s,1)W(k_s,y)}{\omega(k_s)e^{-|k_s|}}\cos\left(k_s x - \omega(k_s)t - \frac{\pi}{4}\right). \qquad (3.92)$$

So for large times the unsteady response decays as $t^{-1/2}$ (see figure (3.6)).

3.4.3 The Steady Response.

In this section it is shown that the long term asymptotic behavior of the vortex is that it regards the step in the bottom topography as a plane wall, so the off-shelf
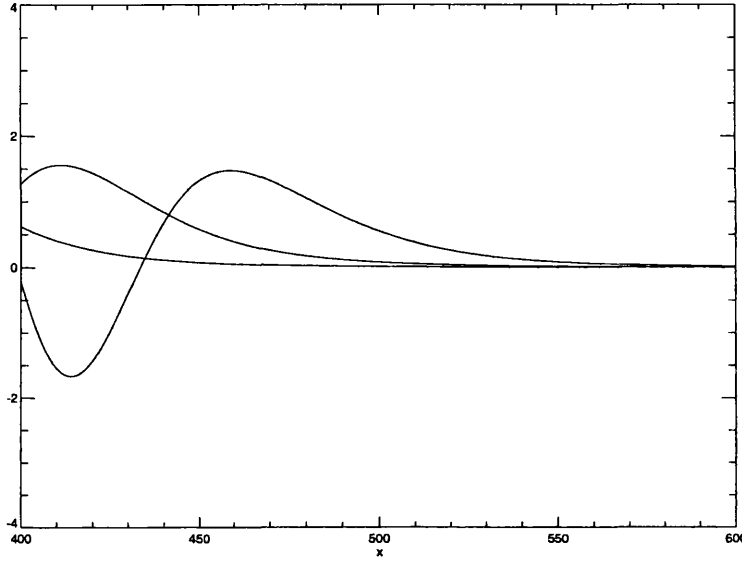
Figure 3.6: Close up of the wavefront decay for $\Gamma = 2\pi$, $y_0 = 1.5$ (off-shelf). The times shown are at $t = 400, 450, 500$.

vortex becomes equivalent to a vortex plus its image in the step where-as the on-shelf vortex becomes an infinite series of images in the wall and the step, i.e. a vortex in a channel. There are two cases to consider

Case A: $y_0 > 1$.

This is the off-shelf vortex. As $t \to \infty$

$$\psi_0 \to \Psi + \phi_s. \tag{3.93}$$

Where ψ_0 can be written

$$\psi_0(x,y) = \begin{cases} 0 & 0 < y < 1 \\[2ex] \frac{\Gamma}{2\pi} \int_{-\infty}^{\infty} e^{|k|(1-y_0)} \frac{\sinh[k(1-y)]}{k} e^{ikx} dk & 1 < y < y_0 \\[2ex] \frac{\Gamma}{2\pi} \int_{-\infty}^{\infty} e^{|k|(1-y)} \frac{\sinh[k(1-y_0)]}{k} e^{ikx} dk & y_0 < y. \end{cases} \quad (3.94)$$

Substitute

$$y_0 - 1 = \bar{y}_0, \qquad (3.95)$$

$$y - 1 = \bar{y}. \qquad (3.96)$$

Therefore

$$\psi_0(x,\bar{y}) = \begin{cases} -\frac{\Gamma}{2\pi} \int_{-\infty}^{\infty} e^{-|k|\bar{y}_0} \frac{\sinh[k\bar{y}]}{k} e^{ikx} dk & 0 < \bar{y} < \bar{y}_0 \\[2ex] -\frac{\Gamma}{2\pi} \int_{-\infty}^{\infty} e^{-|k|\bar{y}} \frac{\sinh[k\bar{y}_0]}{k} e^{ikx} dk & \bar{y}_0 < \bar{y}. \end{cases} \quad (3.97)$$

Now it is clear by referring back to (3.60) that equations (3.97) are the response at $(x, \bar{y})$ of a vortex at $(0, \bar{y}_0)$ So for this case:

$$\psi_0(x,\bar{y}) = \frac{\Gamma}{4\pi} \log \left(\frac{x^2 + (\bar{y} - \bar{y}_0)^2}{x^2 + (\bar{y} + \bar{y}_0)^2} \right). \qquad (3.98)$$

A vortex and its image shifted above $y = 1$, see figure (3.7).
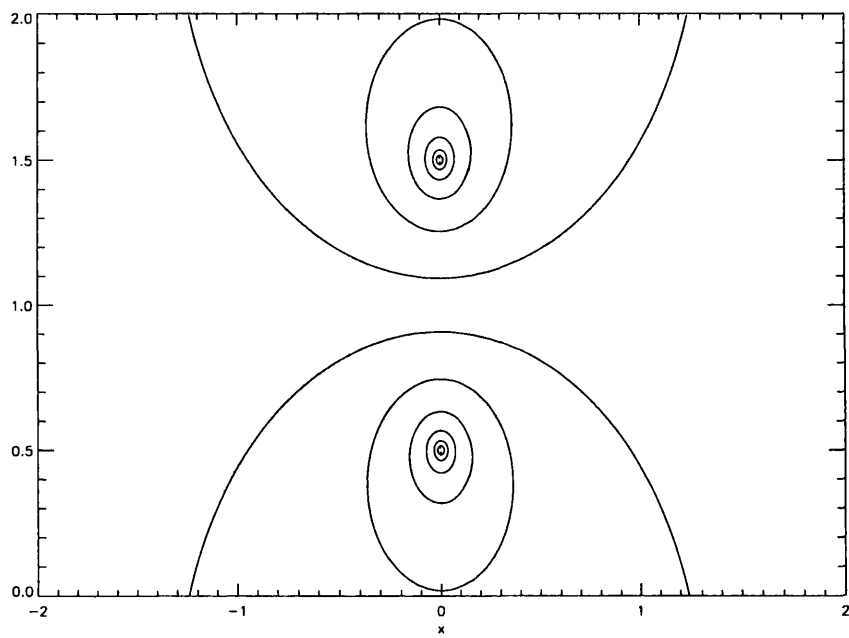
Figure 3.7: Streamfunction contours for a vortex and its image shifted above $y = 1$ with $y_0 = 1.5$ and $\Gamma = 1$.

Case B: $y_0 < 1$.

This is the on-shelf vortex. As $t \to \infty$

$$\psi_0 \to \Psi + \phi_s. \tag{3.99}$$

$$\psi_0(x, y) = \begin{cases} \frac{\Gamma}{2\pi} \int_{-\infty}^{\infty} \frac{\sinh(k(y_0-1))\sinh(ky)}{k\sinh(k)} e^{ikx} \mathrm{d}k & 0 < y < y_0 \\[2em] \frac{\Gamma}{2\pi} \int_{-\infty}^{\infty} \frac{\sinh(ky_0)\sinh(k(y-1))}{k\sinh(k)} e^{ikx} \mathrm{d}k & y_0 < y < 1 \\[2em] 0 & 1 < y. \end{cases} \tag{3.100}$$

So there is no response off-shelf, the step is acting like a plane wall. Differentiating (3.100) once with respect to y gives

$$\frac{\partial \psi_0}{\partial y} = \begin{cases} \frac{\Gamma}{2\pi} \int_{-\infty}^{\infty} \frac{\sinh(k(y_0-1))\cosh(ky)}{\sinh(k)} e^{ikx} \mathrm{d}k & 0 < y < y_0 \\[2em] \frac{\Gamma}{2\pi} \int_{-\infty}^{\infty} \frac{\sinh(ky_0)\cosh(k(y-1))}{\sinh(k)} e^{ikx} \mathrm{d}k & y_0 < y < 1 \\[2em] 0 & 1 < y. \end{cases} \tag{3.101}$$

Consider the first of the two integrals in (3.101) above, this can be written as the sum

$$\frac{\partial \psi_0}{\partial y} = \frac{\Gamma}{4\pi} \int_{-\infty}^{\infty} \left[\frac{\sinh[k(y_0 + y - 1)]}{\sinh(k)} + \frac{\sinh[k(y_0 - y - 1)]}{\sinh(k)} \right] e^{ikx} \mathrm{d}k. \tag{3.102}$$

Only the even part of the integrand will be non-zero i.e.

$$\frac{\partial \psi_0}{\partial y} = \frac{\Gamma}{2\pi} \mathrm{Re} \int_{0}^{\infty} \left[\frac{\sinh[k(y_0 + y - 1)]}{\sinh(k)} + \frac{\sinh[k(y_0 - y - 1)]}{\sinh(k)} \right] e^{ikx} \mathrm{d}k. \tag{3.103}$$

Note that because $y < y_0 < 1$

$$\mathrm{Re}(1 \pm (y_0 \pm y - 1)) > 0. \tag{3.104}$$

So performing the integration gives (see Gradshteyn and Rhysik [1980]: 3.541.2)

$$\frac{\partial \psi_0}{\partial y} = \frac{\Gamma}{4\pi} \mathbf{Re}\left[\varphi\left(\frac{y_0 + y - ix}{2}\right) \; - \; \varphi\left(\frac{2 - y_0 - y - ix}{2}\right) + \right.$$
$$\left. \varphi\left(\frac{y_0 - y - ix}{2}\right) \; - \; \varphi\left(\frac{2 - y_0 + y - ix}{2}\right)\right]. \qquad (3.105)$$

Where φ is the *psi* function (defined in Gradshteyn and Rhysik [1980]: 8.36). Using the series representation (described in Gradshteyn and Rhysik [1980]: 8.362.1) the difference of two *psi* functions can be expressed as

$$\varphi(x) - \varphi(y) = \sum_{j=0}^{\infty} \frac{1}{y+j} - \frac{1}{x+j}, \qquad (3.106)$$

and so

$$\frac{\partial \psi_0}{\partial y} = \frac{\Gamma}{2\pi} \mathbf{Re} \sum_{j=0}^{\infty} \left[\left(\frac{1}{2(1+j) - (y+y_0) - ix}\right) \; - \; \left(\frac{1}{2j + y + y_0 - ix}\right) + \right.$$
$$\left. \left(\frac{1}{2(1+j) + y - y_0 - ix}\right) \; - \; \left(\frac{1}{2j - (y - y_0) - ix}\right)\right].$$
$$(3.107)$$

Taking the real part gives

$$\frac{\partial \psi_0}{\partial y} = \frac{\Gamma}{2\pi} \sum_{j=0}^{\infty} \left[\left(\frac{2(1+j) - (y+y_0)}{(2(1+j) - (y+y_0))^2 + x^2}\right) \; - \; \left(\frac{2j + y + y_0}{(2j + y + y_0)^2 + x^2}\right) + \right.$$
$$\left. \left(\frac{2(1+j) + y - y_0}{(2(1+j) + y - y_0)^2 + x^2}\right) \; - \; \left(\frac{2j - (y - y_0)}{(2j - (y - y_0))^2 + x^2}\right)\right].$$
$$(3.108)$$

Integrating with respect to y gives the steady response for $0 < y < y_0$ as

$$\psi_0(x,y) = \frac{\Gamma}{4\pi} \sum_{j=0}^{\infty} \log\left(\frac{x^2 + (y - [y_0 - 2(1+j)])^2}{x^2 + (y + y_0 - 2(1+j))^2}\right) + \log\left(\frac{x^2 + (y - [y_0 + 2j])^2}{x^2 + (y + y_0 + 2j)^2}\right).$$

$$(3.109)$$

A similar analysis reveals that for $y_0 < y < 1$

$$\psi_0(x,y) = \frac{\Gamma}{4\pi} \sum_{j=0}^{\infty} \log\left(\frac{x^2 + (y - [y_0 + 2(1+j)])^2}{x^2 + (y + y_0 + 2j)^2}\right) + \log\left(\frac{x^2 + (y - [y_0 - 2j])^2}{x^2 + (y + y_0 - 2(j+1))^2}\right).$$

$$(3.110)$$

Which is the sum of an infinite number of image vortices, as expected for a vortex at $y = y_0$ in a channel of unit width.

3.4.4 $Y \sim O(\varepsilon)$:

The forcing now becomes $O(\varepsilon^2)$ as it can be approximated to a dipole, to see this write

$$\bar{\Psi} = \frac{\varepsilon\Gamma}{4\pi} \log\left(\frac{(x - X(t))^2 + (y - Y(t))^2}{(x - X(t))^2 + (y + Y(t))^2}\right). \qquad (3.111)$$

and so

$$\bar{\Psi} = -\frac{\varepsilon\Gamma}{4\pi}\Big(F(Y) - F(-Y)\Big). \qquad (3.112)$$

Here

$$F(Y) = \log\left((x - X(t))^2 + (y + Y(t))^2\right). \qquad (3.113)$$

Hence for $Y \sim O(\varepsilon)$

$$F(Y) - F(-Y) \simeq 2Y\frac{\mathrm{d}F(0)}{\mathrm{d}Y}. \qquad (3.114)$$

So

$$\bar{\Psi} \simeq \frac{-\varepsilon\Gamma Y y}{\pi((x - X)^2 + y^2)}, \qquad (3.115)$$

and since $Y \sim O(\varepsilon)$, $\bar{\Psi} \sim O(\varepsilon^2)$ but note that Ψ_v and Ψ_i are still $O(\varepsilon)$. Therefore the secondary motions ϕ will come in at $O(\varepsilon^2)$ and the streamfunction should be written

$$\psi = \varepsilon^2 \psi_1, \tag{3.116}$$

$$\psi_1 = \Psi + \phi, \tag{3.117}$$

with Ψ defined as

$$\Psi = \frac{-\Gamma(Y/\varepsilon)y}{\pi((x-X)^2 + y^2)}. \tag{3.118}$$

The governing equation for ψ_1 is still the linear forced topographic wave equation by virtue of the fact that $\psi_0 = 0$. The $O(\varepsilon^2)$ terms of (3.6) give that

$$\frac{\partial}{\partial t}(\nabla^2 \psi_1) + \frac{\partial \psi_1}{\partial x}\frac{\partial h_B}{\partial y} = 0. \tag{3.119}$$

Consider now the motion of the vortex center $(X(t), Y(t))$. Write

$$X(t) = Ut + \varepsilon X_1(t) + \varepsilon^2 X_2(t) + \ldots, \tag{3.120}$$

$$Y(t) = \varepsilon Y_0(t) + \varepsilon^2 Y_1(t) + \ldots, \tag{3.121}$$

then equations (3.40) give the vortex motions as

$$U + \varepsilon\frac{dX_1}{dt} + \varepsilon^2\frac{dX_2}{dt} \simeq \frac{\Gamma}{4\pi Y_0(t)} - \frac{\varepsilon\Gamma Y_1(t)}{4\pi Y_0^2(t)} - \varepsilon^2 \phi_y(X, Y), \tag{3.122}$$

$$\varepsilon\frac{dY_0}{dt} + \varepsilon^2\frac{dY_1}{dt} = \varepsilon^2 \phi_x(X, Y). \tag{3.123}$$

A balance can be found if Y_0 is constant, so set $y_0 = Y_0(0)$ and therefore $U = \Gamma/4\pi y_0 \sim O(1)$. The leading order solution is a steadily propagating vortex at $(Ut, \varepsilon y_0)$ and the leading order forcing is

$$\Psi = \frac{-\Gamma y_0 y/\pi}{(x - Ut)^2 + y^2}. \tag{3.124}$$

The system described by (3.47) - (3.52) still holds so taking Fourier transforms of (3.47) - (3.52) gives;

$$\hat{\phi}_{yy} - k^2\hat{\phi} = 0,$$ (3.125)

with boundary conditions as before

$$\hat{\phi} = 0 \qquad \text{on} \qquad y = 0,$$ (3.126)

$$\hat{\phi} \to 0 \qquad \text{as} \qquad x^2 + y^2 \to \infty,$$ (3.127)

and the jump conditions at $y = 1$,

$$[\hat{\phi}] = 0,$$ (3.128)

$$[\hat{\phi}_{yt}] - ik\hat{\phi} = ik\hat{\Psi}(k,1)e^{-ikUt}.$$ (3.129)

Here $\hat{\Psi}(k,1)$ is given from the transform of (3.118)

$$\hat{\Psi}(k,1) = -\Gamma y_0 e^{-|k|}.$$ (3.130)

The initial condition is

$$\hat{\phi}(k,y,0) = 0.$$ (3.131)

The analysis is identical to the stationary case except that the presence of the background drift U gives rise to the possibility of stationary lee waves and a resonant interaction between the propagating vortex and the topographic waves. The solution is just quoted and is again composed of three parts, the forcing term Ψ defined as before, a quasi-steady term ϕ_s and an unsteady wavelike term ϕ_w

$$\psi_1 = \Psi + \phi_s + \phi_w,$$ (3.132)

where, defining $\zeta = x - Ut$,

$$\phi_s = -\frac{1}{2\pi} \int_{-\infty}^{\infty} \frac{\hat{\Psi}(k,1)W(k,y)}{\omega - kU} \, e^{ik\zeta} \mathrm{d}k,$$ (3.133)
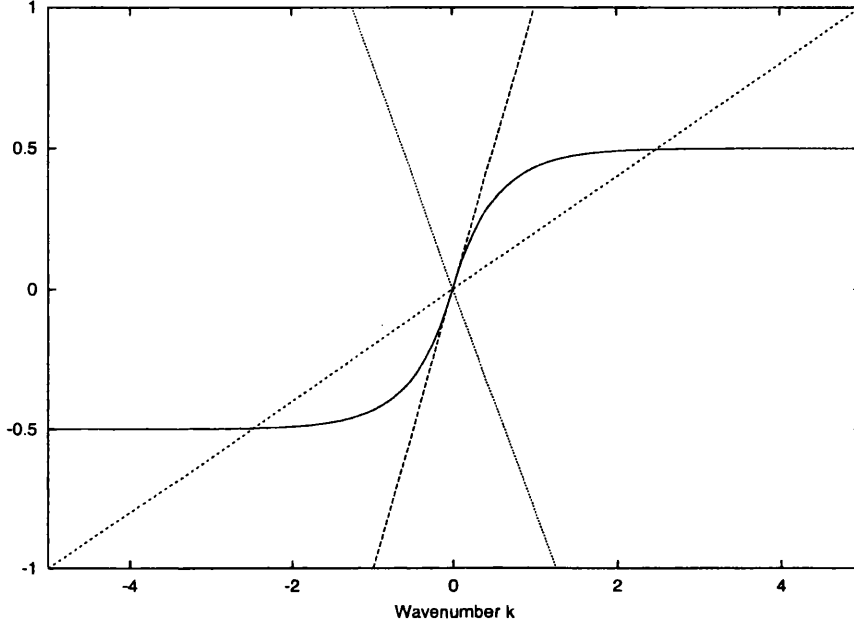
Figure 3.8: The dispersion $\omega(k)$ (solid line) against kU for $U = -0.8$ (dotted line),

$U = 1$ (long dashed) and $U = 0.2$ (small dashed).

$$\phi_w = \frac{1}{2\pi} \int_{-\infty}^{\infty} \frac{\hat{\Psi}(k,1)W(k,y)}{\omega - kU} \; e^{ik\zeta - it(\omega - Uk)} \mathrm{d}k. \tag{3.134}$$

Here $W(k,y)$ and $\hat{\Psi}(k,1)$ are defined by (3.69) and (3.130). The interface displacement can again be found by integrating (3.74) with respect to time, the result is

$$\hat{\eta} = \frac{k\hat{\Psi}(k,1)e^{-ikUt}}{\omega - kU} \left(1 - e^{-it(\omega - kU)}\right). \tag{3.135}$$

The long time solutions for ϕ_s and ϕ_w can be found using contour integration. The integrands in (3.133) and (3.134) will have singularities whenever $\omega(k) = kU$ at $k = \pm k_p$ (see figure (3.8)), however for $U \neq 1$ the singularity at $k = 0$ is removable, to see this write

$$I(k,y) = \frac{\hat{\Psi}(k,1)W(k,y)}{\omega - kU}, \tag{3.136}$$

and expanding (3.136) for small k gives

$$I(k,y) \simeq -\frac{\Gamma y y_0}{1-U},$$
(3.137)

which is analytic at $k = 0$ as long as $U \neq 1$. Figure (3.8) shows $\omega - kU$ for three different values of U, if $U > 1$ or $U < 0$ (dotted line) then there is only the one intersection at $k = 0$ which is removable and there are no poles so the inversion contour can lie along the real line. If $0 < U < 1$ (small dashed) then there are two more intersections apart from at the origin, these are poles of the integrands in (3.133) and (3.134) and a suitable contour must be found (i.e. that satisfies the radiation condition, see Appendix B) and there will be a residue contribution from each of the poles. If $U = 1$ (long dashed) then there is only one intersection which is at $k = 0$ but this is no longer removable, $U = 1$ is the resonant case and the main contribution to (3.133) and (3.134) comes from the behavior at this pole, Akylas [1984].

This leads to three cases

i. $U > 1, U < 0$.

The response at large times for ϕ_w will be dominated by points $k = k_s$ of stationary phase where the phase $k\zeta - (\omega - kU)t$ has a zero first derivative

$$x - C_g(k_s)t = 0.$$
(3.138)

Writing $\Theta = \omega - kU$ and noting that W/Θ is even in k, the unsteady term (3.134) can be written

$$\phi_w = \frac{1}{2\pi} \int_{-\infty}^{\infty} \frac{\hat{\Psi}(k,1)W(k,y)}{\Theta} \, e^{i(kx-\Theta t)} \mathrm{d}k.$$
(3.139)

Stationary phase analysis identical to that of section 3.4.2 can now be applied to (3.139) and the result is just quoted as

$$\phi_w(x,y,t) \sim \frac{t^{-\frac{1}{2}}}{\sqrt{\pi}} \frac{4\hat{\Psi}(k_s,1)W(k_s,y)}{\Theta(k_s)e^{-|k_s|}} \cos{(k_s\zeta - \Theta(k_s)t - \frac{\pi}{4})}. \tag{3.140}$$

So for large times the unsteady response decays as $t^{-1/2}$ leaving the quasi-steady term and the steadily propagating vortex

$$\psi_1 \to \Psi(\zeta,y,t) + \phi_s(\zeta,y,t). \tag{3.141}$$

The steady response of the streamfunction at the step corresponding to the vortex can be examined further, at $y = 1$

$$\psi_1 = \Psi(\zeta,1,t) + \phi_s(\zeta,1,t), \tag{3.142}$$

and so

$$\psi_1 = \frac{1}{2\pi}\int_{-\infty}^{\infty} \hat{\Psi}(k,1)\Big(\frac{1}{1 - C_p(k)/U}\Big)e^{ik\zeta}dk. \tag{3.143}$$

A binomial expansion can be used on the integrand for those values of k where $|C_p(k)|/U < 1$. Note that $0 < C_p < 1$ and so this valid for all k when $|U| > 1$. To leading order,

$$\psi_1 \simeq \frac{1}{2\pi}\int_{-\infty}^{\infty} \hat{\Psi}(k,1)(1 + \frac{C_p}{U})e^{ik\zeta}dk. \tag{3.144}$$

Which, using (3.32) and (3.130) can be written as

$$\psi_1 \simeq \frac{1}{2\pi}\int_{-\infty}^{\infty} \Big(\hat{\Psi}(k,1) - \frac{\Gamma y_0}{Uk}\sinh(k)e^{-2|k|}\Big)e^{ik\zeta}dk. \tag{3.145}$$

This integrates to (c.f. Gradshteyn and Rhysik [1980]: 3.551.6)

$$\psi_1 \simeq \Psi(\zeta, 1) - \frac{\Gamma y_0}{2U\pi} \mathrm{Re}\left\{\ln\left(\frac{3 - i\zeta}{1 - i\zeta}\right)\right\}. \tag{3.146}$$

Written explicitly this is

$$\psi_1(\zeta, 1) \simeq -\frac{\Gamma y_0}{\pi}\left\{\frac{1}{1 + \zeta^2} + \frac{1}{4U}\ln\left(\frac{9 + \zeta^2}{1 + \zeta^2}\right)\right\}. \tag{3.147}$$

Equation (3.147) represents a steady, symmetric 'hump' of fluid that is localised about the vortex, this is the pseudoimage of the vortex in the step. This behavior is shown in figures (3.9) and (3.10) for pure supercritical and subcritical flows. The diagrams are plots of the time evolution of the interface displacement η (calculated using FFT inversions of (3.135)) with the results plotted in a frame of reference moving with the vortex drift speed U. The transient waves can clearly seen to be leaving behind the quasi-steady pseudoimage solution $\Psi + \phi$ which remains above the vortex for all time. In this frame of reference the slowest wave (speed zero) travels with velocity $-U$ and the fastest wave (speed $C_g = 1$) travels with velocity $1 - U$. Figure (3.9) demonstrates this, for $U = 1.5$ the slowest wave appears to have traveled to the left a distance 40 units in time 60. Likewise the longest wave has traveled to the left a distance 50 units in time 100.

ii. $0 < U < 1$.

For this case there are two poles lying on the real axis at $k = \pm k_p$ and the inversion contour must be indented to pass below them in order to satisfy the radiation condition (Lighthill [1974], see appendix B). The poles satisfy

$$\omega(k_p) - k_p U = 0, \tag{3.148}$$
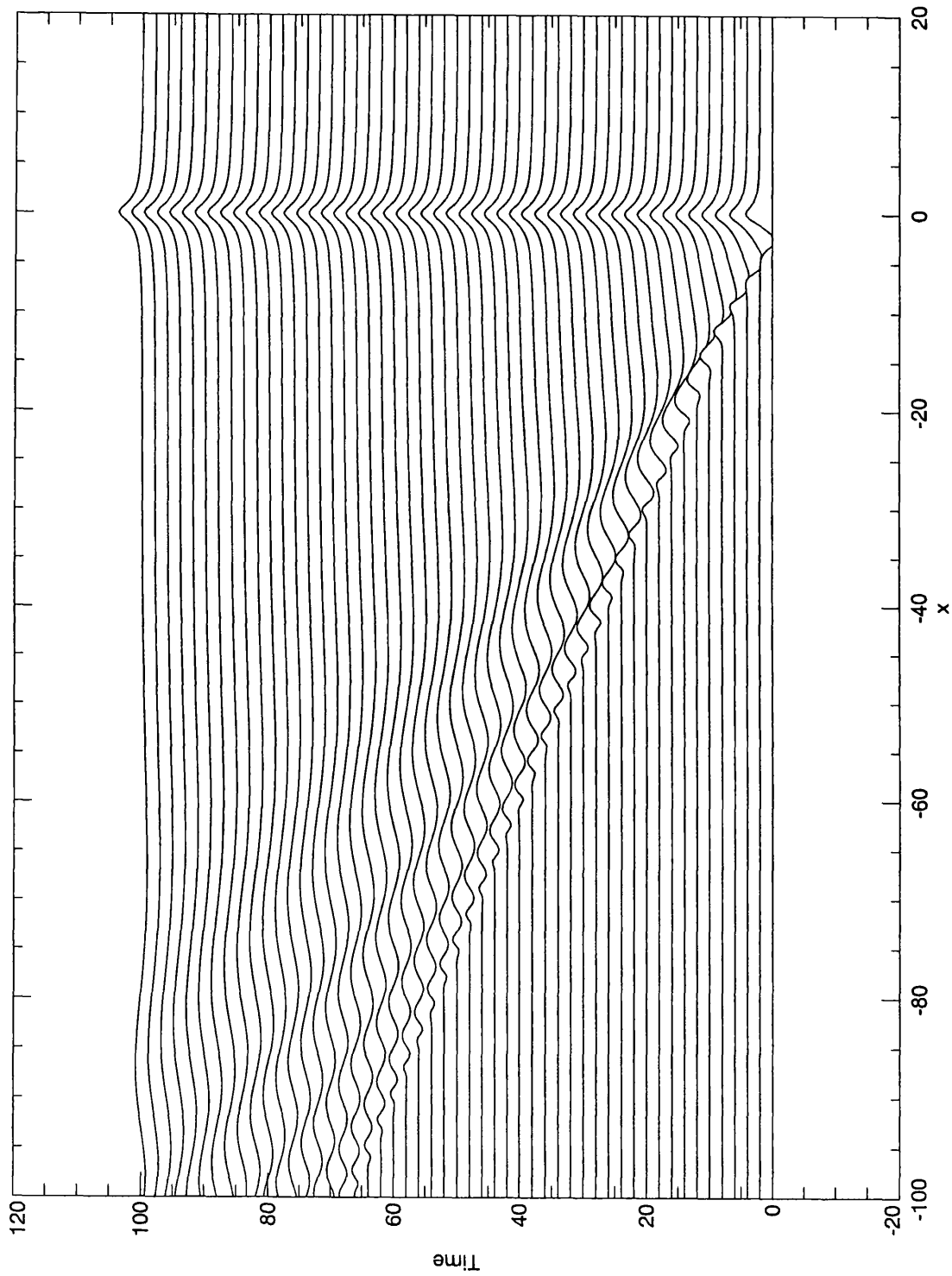
Figure 3.9: Supercritical response for $U = 1.5$ and $\Gamma = 2\pi$.
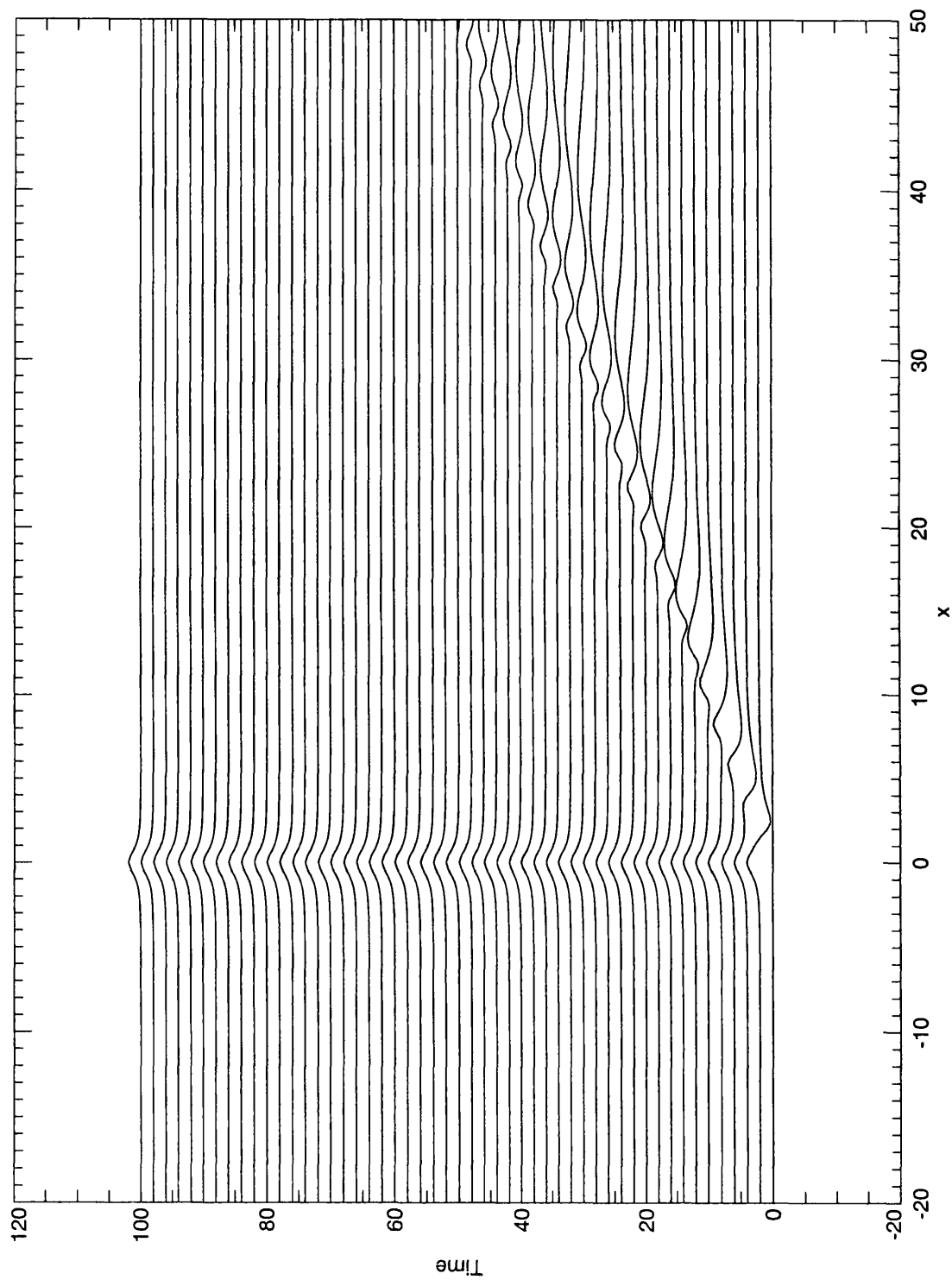
Figure 3.10: Subcritical response for $U = -1$ and $\Gamma = -2\pi$.

for $k_p \neq 0$. The presence of poles in both integrals indicates that the large time response will consist of a stationary lee wave trailing the vortex. At the interface $y = 1$ the quasi-steady response ϕ_s and the wave-like response ϕ_w become

$$\phi_s = -\frac{1}{2\pi} \int_C \frac{kU\hat{\Psi}(k,1)}{\omega - kU} \; e^{ik\zeta} dk, \tag{3.149}$$

$$\phi_w = \frac{1}{2\pi} \int_C \frac{\omega\hat{\Psi}(k,1)}{\omega - kU} \; e^{ik\zeta - it(\omega - Uk)} dk, \tag{3.150}$$

where the integration is performed around the contour C (see Appendix B). Using the residue theorem the quasi-steady term becomes

$$\phi_s = \mathbf{Re}\left(-\frac{i\hat{\Psi}(k_p,1)k_pU}{c_g(k_p) - U}e^{ik_p\zeta}H(\zeta) + \frac{i\hat{\Psi}(k_p,1)k_pU}{c_g(k_p) - U}e^{-ik_p\zeta}H(\zeta) \right), \tag{3.151}$$

which simplifies to

$$\phi_s = \frac{2\hat{\Psi}(k_p,1)k_pU}{c_g(k_p) - U}\sin(k_p\zeta)H(\zeta). \tag{3.152}$$

Next consider the wave-like term ϕ_w. Define a function $G(k)$ such that

$$G(k) = \omega(k) - kU. \tag{3.153}$$

Expand about a pole $k = \pm k_p$ where $G(\pm k_p) = 0$

$$G(k) \simeq (k \mp k_p)G'(\pm k_p), \tag{3.154}$$

and therefore

$$\omega(k) - kU = kC_g(k_p) \mp k_pC_g(k_p) - kU \pm k_pU. \tag{3.155}$$

So the dispersion $\omega(k)$ can be written

$$\omega(k) \simeq kC_g(k_p) \mp k_pC_g(k_p) \pm k_pU. \tag{3.156}$$

Expanding expression (3.150) for ϕ_w about $k = \pm k_p$ gives

$$\phi_w = \frac{\hat{\Psi}(\pm k_p, 1)}{2\pi} \int_C \frac{kC_g(k_p) \mp k_pC_g(k_p) \pm k_pU}{(k \mp k_p)(C_g(k_p) - U)} \quad \exp\left(ik\bar{\zeta} \pm ik_pt(C_g(k_p) - U)\right)dk,$$

$$(3.157)$$

where $\bar{\zeta} = x - C_g(k_p)t$.

So when $\bar{\zeta} > 0$ exponential decay is achieved when the contour is closed off in the upper half-plane and the poles contribute. When $\bar{\zeta} < 0$ the converse is true and the poles do not contribute. The residue theorem thus gives

$$\phi_w = \mathbf{Re}\left(\frac{i\hat{\Psi}(k_p, 1)k_pU}{c_g(k_p) - U}(e^{ik_p\bar{\zeta}} - e^{-ik_p\bar{\zeta}})H(\bar{\zeta})\right),$$

$$(3.158)$$

which simplifies to

$$\phi_w = -\frac{2\hat{\Psi}(k_p, 1)k_pU}{c_g(k_p) - U}\sin(k_p\bar{\zeta})H(\bar{\zeta}),$$

$$(3.159)$$

which is similar to (3.152). Combining (3.152) and (3.159) shows that the long time response consists of the vortex traveling at speed U with a lee wavetrain between the points $x/t = C_g(k_p)$ and $x/t = U$, for points outside of this envelope the interface η is flat.

$$\psi_1 = \Psi(x - Ut, y) - \frac{2\hat{\Psi}(k_p, 1)k_pU}{c_g(k_p) - U}\sin(k_p(x - Ut))\left(H(x - C_g(k_p)t) - H(x - Ut)\right).$$

$$(3.160)$$

This is valid whenever $C_g(k_p) \neq U$.

Figures (3.11) and (3.12) show the subcritical time evolution of the interface displacement η calculated through numerical FFT inversions of (3.135) at each time level. The parameters for the flow are $U = 0.5$ and $\Gamma = 2\pi$, figure (3.11) shows the evolution up to time $t = 500$ and the response quite clearly consists of a large-amplitude, linear wavetrain in the lee of the vortex. It is quasi-steady as there are slight modulations in the amplitudes of the standing waves. Upstream of the vortex
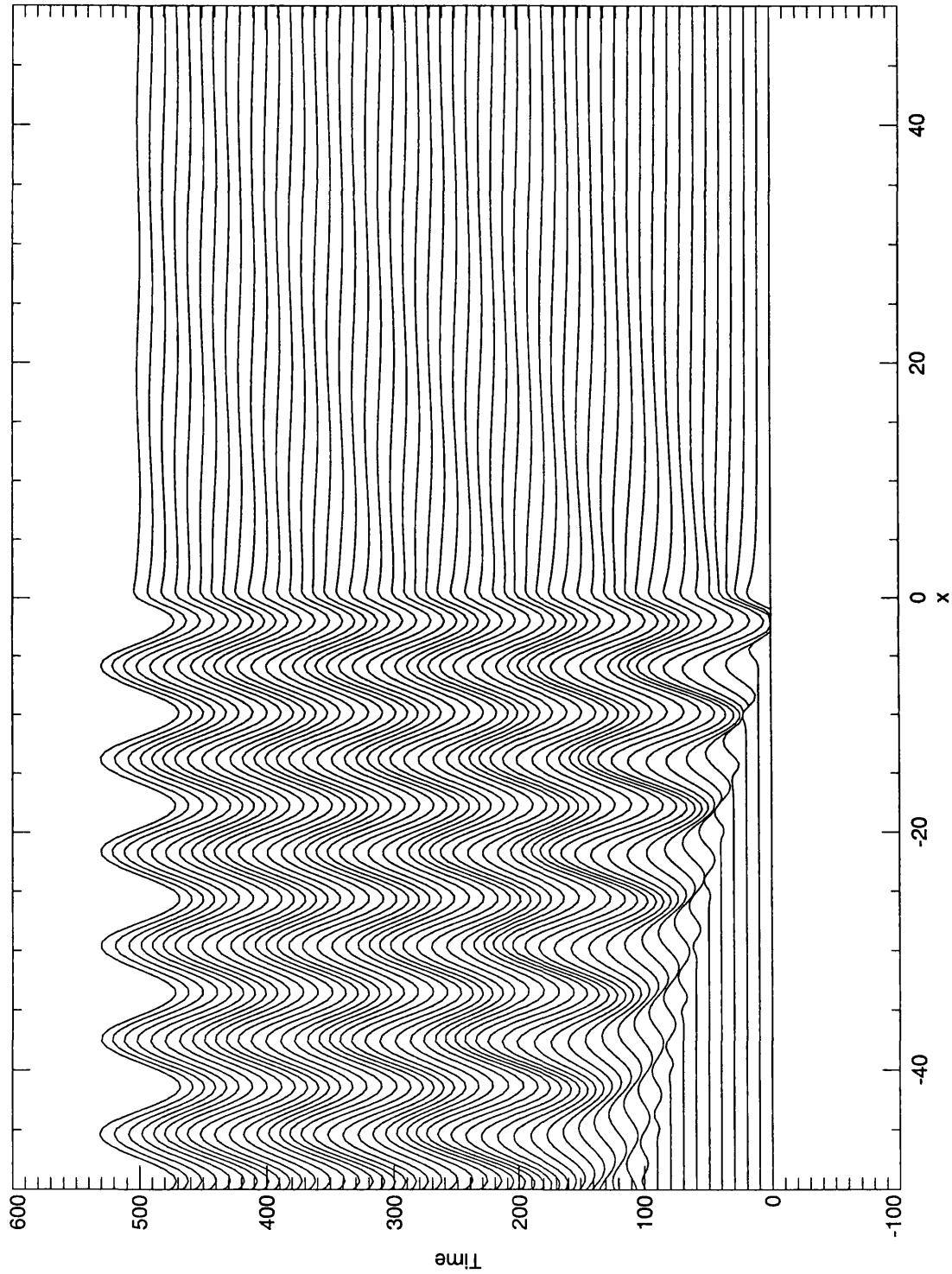
Figure 3.11: Subcritical response for $U = 0.5$ and $\Gamma = 2\pi$.
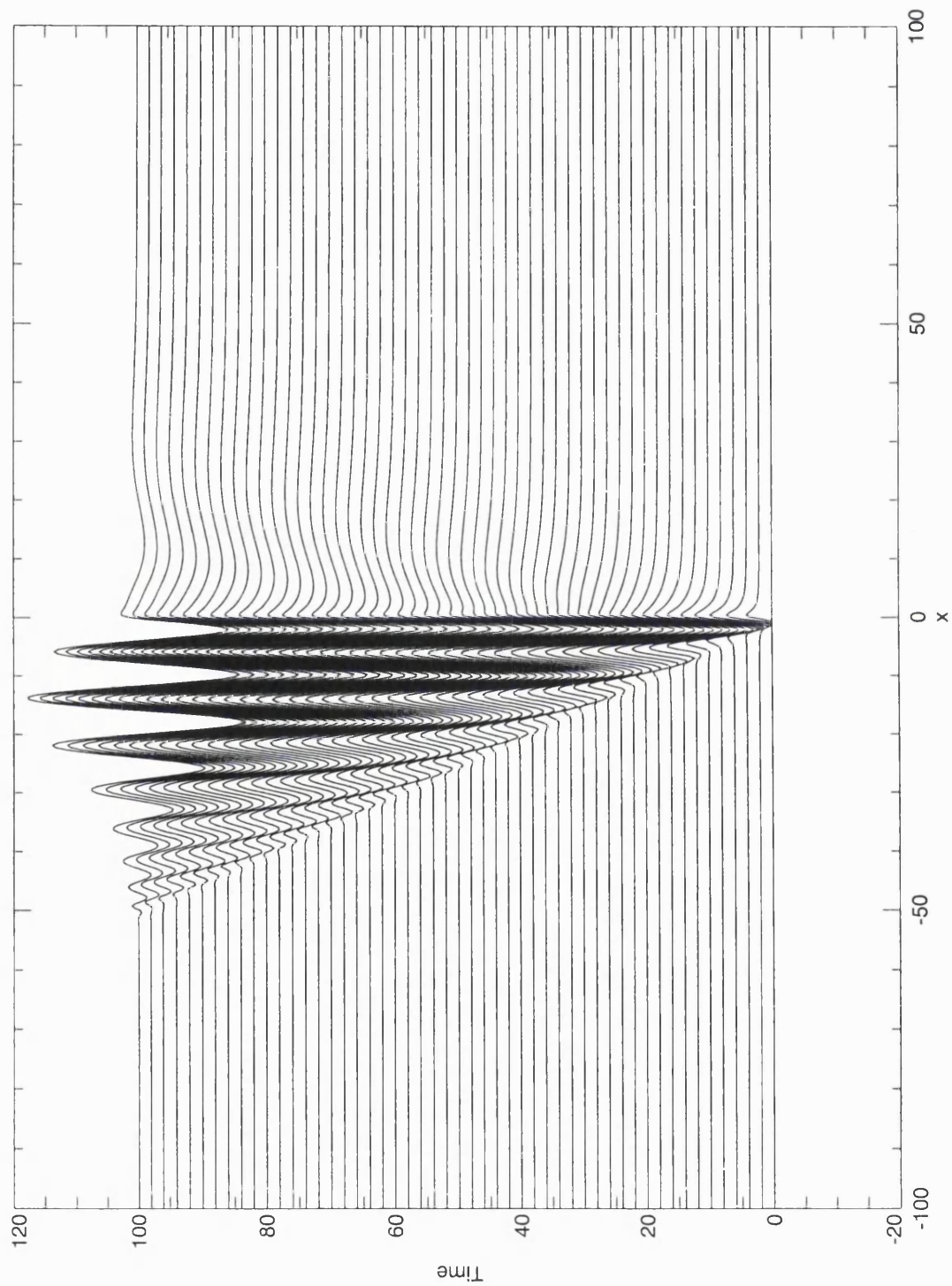
Figure 3.12: Close up of initial subcritical response for $U = 0.5$ and $\Gamma = 2\pi$.

there are small-amplitude waves that travel upstream (in this frame of reference) at a speed $C_{g\,max} - U = 1 - 0.5$, this is easier to discern in figure (3.12) which shows a close up of the same flow for times up to $t = 100$. At time $t = 100$ the fastest longwave has just reached $x = 50$ whereas the slowest wave (traveling at speed $-U$ in this frame of reference) has reached $x = -50$. Equation (3.160) says that eventually the upstream waves vanish leaving just the vortex (at the origin, in this frame of reference) and the lee wave between (in this frame of reference) the two points $x/t = C_g(k_p) - U$ and $x/t = 0$, the origin.

iii. $U = 1$.

For this case the integrands in (3.133) and (3.134) will have singularities whenever $\omega(k) = k$. This occurs at one value of k only, namely $k = 0$, the longest wave. At $k = 0$

$$C_p(0) = C_g(0) = 1. \tag{3.161}$$

Both the group velocity and phase velocity are at a maximum and the point $k = 0$ is a pole of the integral and the point of stationary phase. The vortex is traveling at the speed of the maximum group velocity and therefore the energy of the waves becomes 'trapped' and the response at the origin becomes unbounded, this is a common occurrence. Akylas [1984], for example, discusses a similar situation for surface waves generated by a moving pressure distribution. Figure (3.13) shows the resonant interaction, in a frame of reference moving with the vortex it can be seen clearly that the waves are trapped by the vortex (which remains at the origin in this frame of reference) as there are no upstream traveling waves. All the energy is trapped between the points $x = -Ut$ (shortest and slowest waves) and $x = 0$, the longwaves. Figure (3.14) shows the growth of the response at the vortex over a

much greater period of time, this figure shows $\log t$ against $\log \eta(0, 1, t)$ and therefore the gradient will give the growth rate of η as a power of t. Firstly, it is positive, implying that the linear response becomes unbounded and therefore invalid at large times. Akylas [1984] predicts that for a moving pressure distribution the resonant growth rate goes like $O(t^{1/3})$ for large t, this graph is predicting a growth rate of something slightly less than $O(t^{1/5})$ which is slower, but certainly increasing.

The response for $U = 1$ is therefore ultimately nonlinear and a new theory is needed which examines the longwave, near-resonant interaction of the weak vortex and the interfacial waves. In chapter 4 this interaction is studied for the leading order case of a steadily propagating vortex.
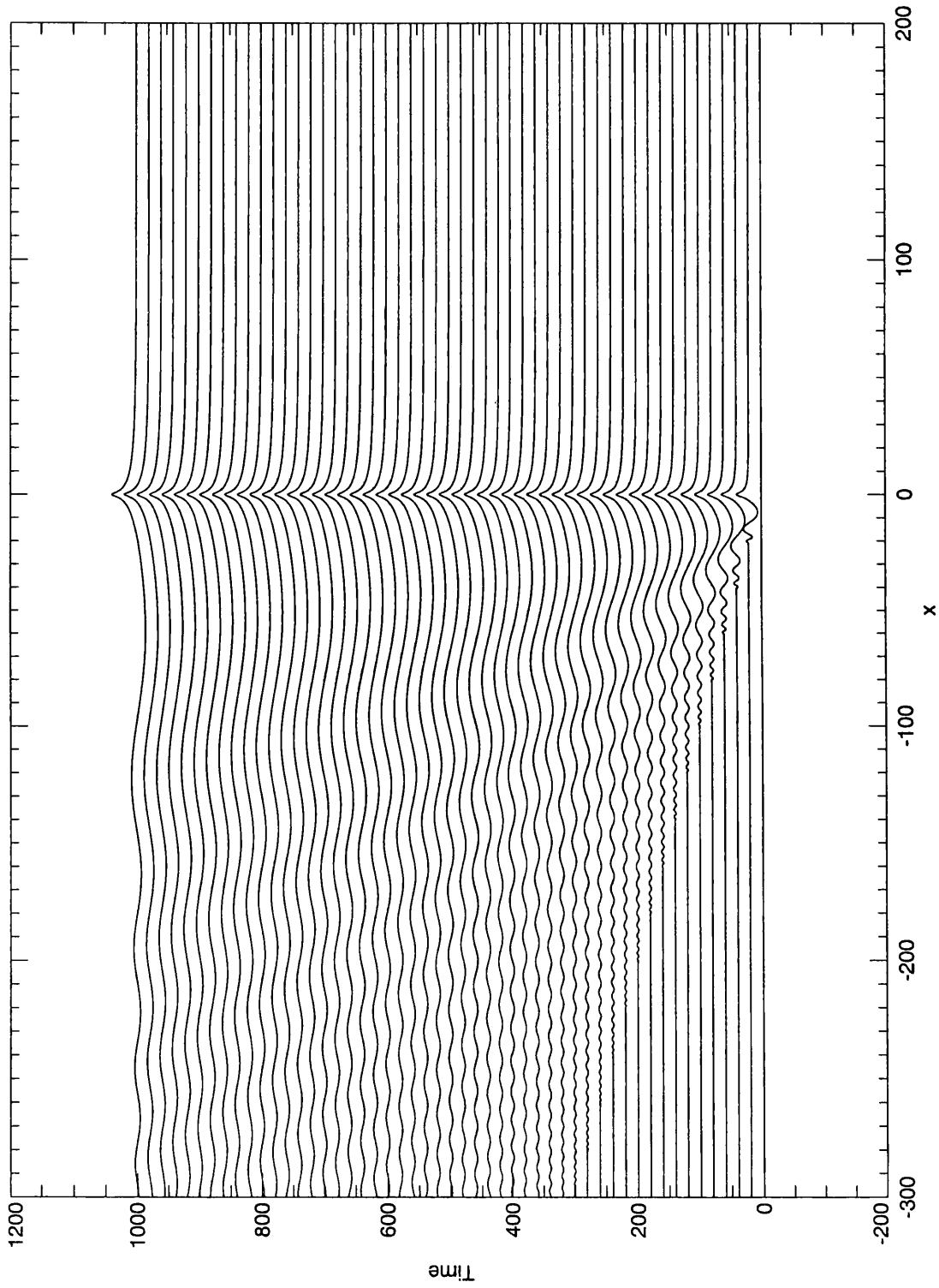
Figure 3.13: Resonance $U = 1$, $\Gamma = 2\pi$ and $y_0 = 0.5$.
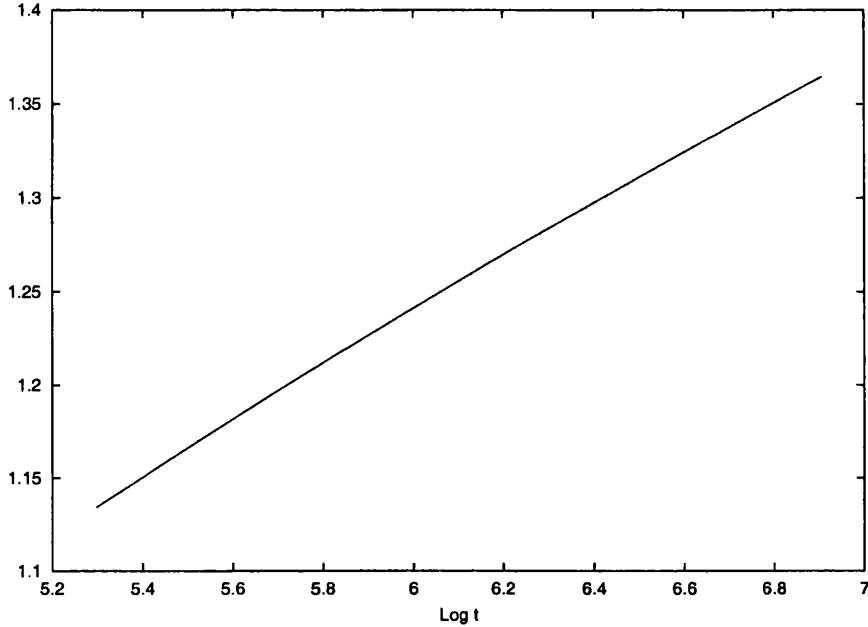
Figure 3.14: Resonant growth at vortex for $U = 1$, $\Gamma = 2\pi$ and $y_0 = 0.5$. This plot is showing $\text{Log}(t)$ against $\text{Log}(\text{Max}(\eta))$.

3.5 Discussion.

In this chapter the linear response was examined in the two cases of a weak vortex situated (i) an order one distance from coastal topography and (ii) an order ε from the coastal wall. The vortex creates linear waves at the interface between deep and shallow fluid. These waves are topographic Rossby waves with the conservation of PV acting as the restoring mechanism. The waves are dispersive and always travel with shallow fluid to their right and the full dispersion relation has been obtained analytically. Longwaves travel fastest and have a maximum group velocity h (the distance from the wall to the step), a longwave expansion was also derived for later reference.

For the forced problem (i.e. with the vortex present) the leading order motion for a weak vortex situated an order one distance from the wall was simply a stationary

vortex, the response at the interface was written in terms of Fourier integrals and long time asymptotics revealed that the step eventually starts to act like a plane wall and analytic expressions of the streamfunction or the interfacial displacement were derived for the on-shelf and off-shelf cases. The on-shelf response became identical to a vortex in a channel and the off-shelf case became a vortex by a wall at $y = 1$. When the vortex was placed an order ε distance from the wall the leading order motion was an order one drift speed whose direction parallel to the wall depended on the sign of the vortex circulation and whose speed varied as the ratio of the strength to the distance from the wall. The interfacial waves still have a maximum finite group velocity which can be normalised to unity and so the response could be divided in to supercritical, subcritical and resonant, depending on the drift speed of the vortex.

For supercritical flow the vortex drift speed $U > 1$ and the response at the interface is a packet of transient waves that get left behind by the vortex with a steady 'hump' of positive PV fluid localised about the vortex position. This is the pseudoimage of the vortex in the step and an expression for this was found analytically.

The subcritical response can be divided further into steady and unsteady flows for when the vortex drift speed $U < 0$ the response is similar to the supercritical with transient waves that travel ahead of the vortex, the long time response of the vortex is then its reaction to its image in the wall and the pseudoimage in the step, for $U < -1$ an analytic expression for this longtime response was calculated. For subcritical flow with $0 < U < 1$ the vortex and wavepacket travel together and thus the longwaves protrude ahead of the vortex and the shortest waves get left behind, thus energy can escape and the response remains linear but unsteady with time. An approximation for the long time response was found using contour integration.

For the resonant case the vortex is constrained to travel at exactly the maximum

group velocity and so energy cannot escape and the response becomes unbounded at large times and linear theory is not valid for $U = 1$. This means that a new nonlinear theory is needed to examine the near-resonant limit $U \simeq 1$. This is the subject of chapter 4
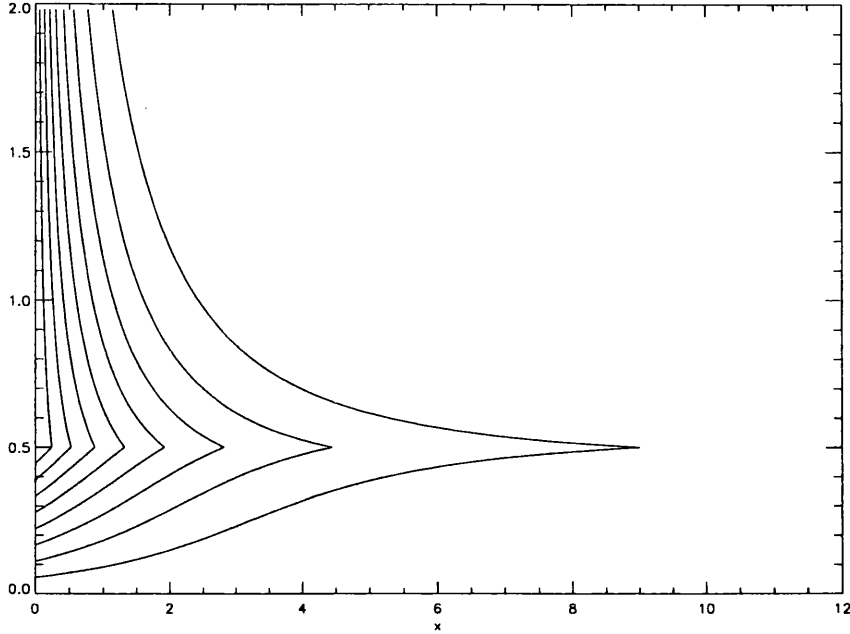
Figure 3.15: Transform of the *log* vortex forcing

3.6 APPENDIX A: The Transform of the Forcing Term

In this appendix it is shown that the forcing term of a vortex at $(0, Y(t))$

$$\Psi(x,y) = \frac{\Gamma}{4\pi} \log \left(\frac{x^2 + (y - Y(t))^2}{x^2 + (y + Y(t))^2} \right), \tag{A-1}$$

transforms to $\hat{\Psi}$ where, see figure (3.15)

$$\hat{\Psi}(k,y) = \begin{cases} -\frac{\Gamma}{k} \sinh(ky) e^{-|k|Y} & 0 < y < Y, \\ \\ -\frac{\Gamma}{k} \sinh(kY) e^{-|k|y} & Y < y. \end{cases} \tag{A-2}$$

Proof

$$\hat{\Psi}(k,y) = \frac{\Gamma}{4\pi} \int_C \log \left(\frac{x^2 + (y - Y(t))^2}{x^2 + (y + Y(t))^2} \right) e^{-ikx} dx. \tag{A-3}$$

For the contour C shown in figure (3.16), exponential decay is achieved for $k < 0$ $(k > 0)$ when the contour is closed off in the upper (lower) half plane. Now consider $\hat{\Psi}_y = I_1 - I_2$ where

$$\hat{\Psi}_y = \frac{\Gamma}{2\pi} \int_C \left(\frac{y - Y(t)}{x^2 + (y - Y(t))^2} - \frac{y + Y(t)}{x^2 + (y + Y(t))^2} \right) e^{-ikx} dx. \tag{A-4}$$

The integrand for I_1 shown above has simple poles situated at

$$x = \pm i|y - Y|. \tag{A-5}$$

The residues at these poles are

$$\text{Res}(I_1, \pm i|y - Y|) = \begin{cases} \frac{\text{sgn}(y-Y)\, e^{-k|y-Y|}}{2i} & k > 0, \\ \\ \frac{\text{sgn}(y-Y)\, e^{k|y-Y|}}{2i} & k < 0. \end{cases} \tag{A-6}$$

Cauchy's Residue Theorem gives

$$I_1 = \frac{\Gamma}{2} \text{sgn}(y - Y)\, e^{-|k||y-Y|}. \tag{A-7}$$

Similarly, the integrand for I_2 has simple poles at

$$x = \pm i(y + Y). \tag{A-8}$$

With the residues at these poles given by

$$\text{Res}(I_2, \pm i(y + Y)) = \begin{cases} \frac{e^{-k(y+Y)}}{2i} & k > 0, \\ \\ \frac{e^{k(y+Y)}}{2i} & k < 0. \end{cases} \tag{A-9}$$

So

$$I_2 = \frac{\Gamma}{2} e^{-|k|(y+Y)}. \tag{A-10}$$

Therefore

$$\hat{\Psi}_y(k, y) = \frac{\Gamma}{2}\left[\operatorname{sgn}(y - Y)\,e^{-|k||y-Y|} - e^{-|k|(y+Y)}\right].$$

(A-11)

Equation (A-11) can also be written

$$\hat{\Psi}_y(k, y) = \begin{cases} -\Gamma\,\cosh(|k|y)e^{-|k|Y} & 0 < y < Y, \\\\ \Gamma\,\sinh(|k|Y)e^{-|k|y} & Y < y. \end{cases}$$

(A-12)

Integrating (A-12) once gives the required result

$$\hat{\Psi}(k, y) = \begin{cases} -\frac{\Gamma}{k}\,\sinh(ky)e^{-|k|Y} & 0 < y < Y, \\\\ -\frac{\Gamma}{k}\,\sinh(kY)e^{-|k|y} & Y < y. \end{cases}$$

(A-13)

In performing the last integration the boundary conditions of zero forcing at the wall $y = 0$ and in the far-field $y \to \infty$ have been used. Also note that for all k,

$$\frac{\sinh(|k|)}{|k|} = \frac{\sinh(k)}{k}.$$

(A-14)
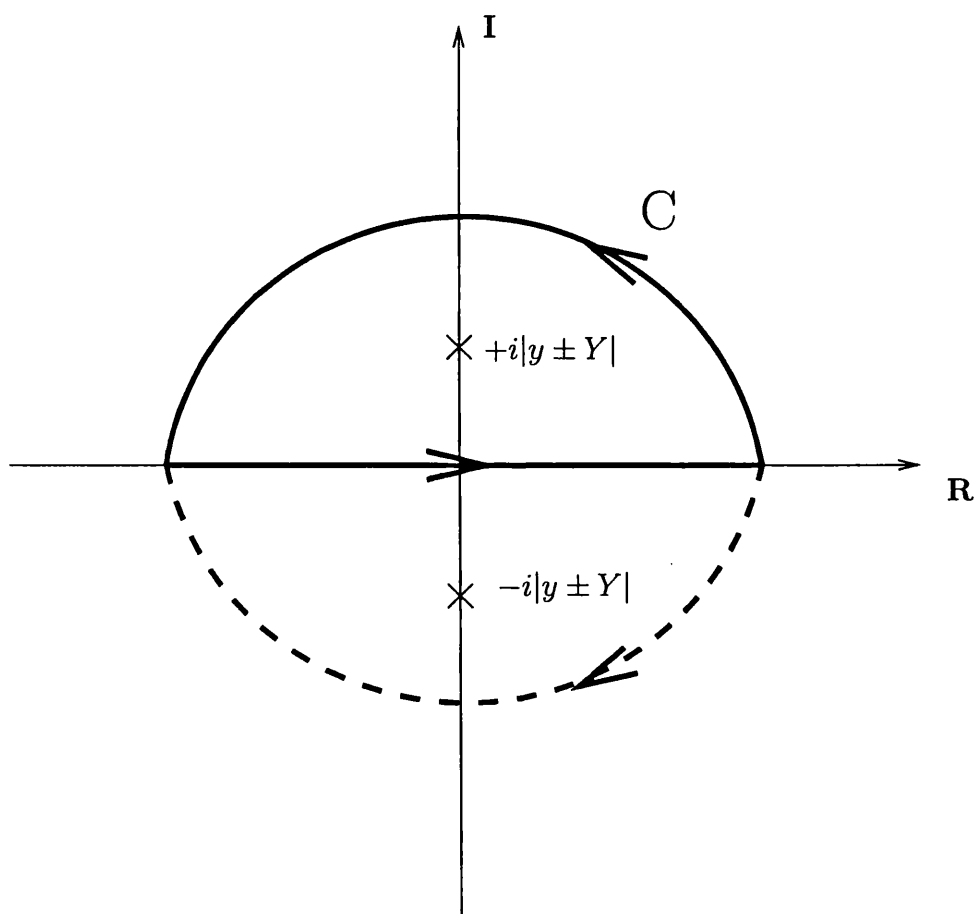
Figure 3.16: Contour of integration for transforming the forcing term Ψ.

3.7 APPENDIX B: The Radiation Condition

To determine which waves can stand in the free stream it is helpful to consider an alternate but equally valid form of forcing, Lighthill [1974], let

$$\Psi_v = \Psi_v e^{\varepsilon t}, \tag{B-1}$$

for some $\varepsilon > 0$. Then the governing equations become,

$$\nabla^2 \phi = 0, \tag{B-2}$$

everywhere except $y = 1$ and at the vortex. The boundary conditions are still;

$$\phi = 0 \quad \text{on} \quad y = 0 \tag{B-3}$$

$$\phi = 0 \quad \text{as} \quad x^2 + y^2 \to \infty. \tag{B-4}$$

but the jump conditions at $y = 1$ now become,

$$[\phi] = 0. \tag{B-5}$$

$$[\phi_{yt}] - \phi_x = \Psi_{vx} e^{\varepsilon t}. \tag{B-6}$$

and the initial condition,

$$\phi = 0, \tag{B-7}$$

at $t = 0$.

Fourier analysis can be used to determine the response along the interface $y = 1$,

$$\psi = \frac{1}{2\pi} \int_{-\infty}^{\infty} \frac{\hat{\Psi}(k,1)}{G(k) - i\varepsilon} \left(\omega(k) e^{i(kx - \omega(k)t)} - (kU + i\varepsilon) e^{ik(x - Ut) + \varepsilon t} \right) dk,$$

$$G(k) = \omega(k) - kU. \tag{B-8}$$

For small ε the poles in the integrand above will be close to $k = k_p$ where $G(k_p) = 0$ but offset from the real axis, Whitham [1974]. It remains to determine on which side of the real axis to complete the contour of integration. Near a pole $k = k_p + i\delta$,

$$G(k_p + i\delta) \simeq i\delta G'(k_p) = i\delta(C_g(k_p) - U).$$
(B-9)

for group velocity $C_g(k)$. Consider the denominator of the integrand shown above, there are poles whenever

$$G(k_p + i\delta) - i\varepsilon = 0.$$
(B-10)

Giving the offset of the poles from the real axis as

$$\delta = \frac{\varepsilon}{G'(k_p)}.$$
(B-11)

So

$$\text{sgn}(\delta) = \text{sgn}(G'(k_p)) = \text{sgn}(C_g(k_p) - U).$$
(B-12)

Now it is true that $C_g(k) \leq C_p(k)$ the group velocity is less than the phase velocity for all k (see figure (3.3)) and so

$$C_g(k) - U \leq C_p(k) - U$$
(B-13)

for all k. However at $k = k_p$

$$C_p(k_p) - U = 0$$
(B-14)

and so

$$C_g(k_p) - U \leq 0.$$
(B-15)

Therefore the offset of the original poles is

$$\delta \leq 0.$$
(B-16)
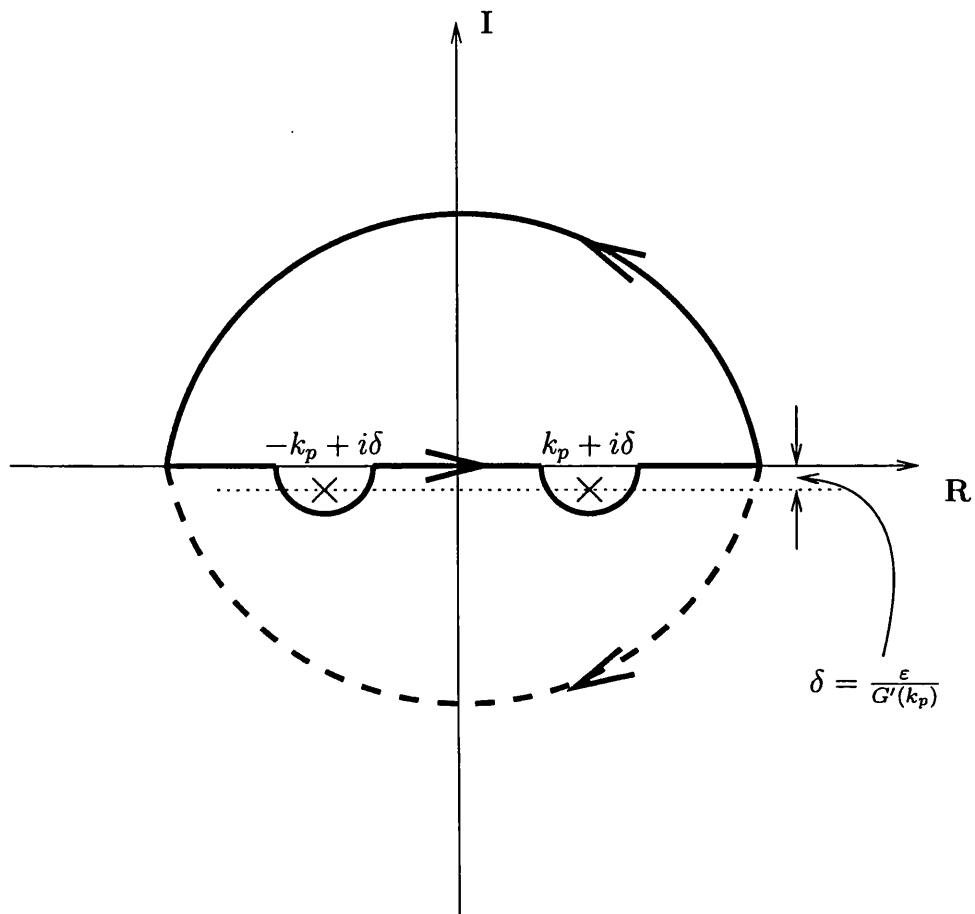
Figure 3.17: Contour of integration showing the offset of the poles.

The poles have shifted below the real axis and so the contour must pass below the poles as shown (see figure (3.17)).

Chapter 4

The Weakly Nonlinear Response: Formulation.

4.1   Introduction.

In chapter 3 it was shown that the linear response of the PV interface due to a point vortex, that is initially situated close to the coastal wall, becomes unbounded at large times whenever the vortex is compelled to travel with a velocity matching the maximum group velocity of the topographic waves. The waves that travel with this maximum group velocity are the longest waves and in this near-critical regime nonlinear effects become important and a new theory is needed to explain the behavior. In this chapter the weakly nonlinear response is examined in the long wave limit for a point vortex that is propagating parallel to and close to an infinitely long wall at $y = 0$, with a step in the bottom topography which is situated at $y = h \sim O(1)$. In this chapter the vortex is still constrained to move steadily, parallel to the coastal wall and thus can be considered fixed to leading order, in a suitable reference frame.

At the moment the effects of the small amplitude waves at the interface are ignored, this assumption is relaxed in later chapters and the linear and weakly-nonlinear response (and contribution) to the vortex motion at higher orders is examined.

The analysis follows Clarke and Johnson [1996a] who used the resonant longwave theory in Grimshaw [1987] to study the weakly nonlinear response of a shear flow past a coastal, topographic feature. They show that in the hydraulic limit (i.e. steady flow and topography becoming long, compared to its own offshore scale) no smooth transitions between conjugate states can exist (i.e. hydraulically controlled flow), and attribute this to the unbounded nature of the fluid domain. With this in mind, it is of interest to apply the resonant, longwave theory to the case of point vortex forcing with the knowledge that hydraulic solutions will not be present. Instead a long wave parameter μ can be derived from the wavelength of the wave response of the PV interface at the topographic step and in the limit that the response becomes long, the point vortex becomes a δ-function (see figure (4.1)).

Problems involving longwave theory with δ-function forcing have been discussed previously in the context of the Korteweg-de Vries (KdV) equation Akylas [1984] who uses it to derive jump conditions for the discontinuous slope of the interface displacement at the forcing, however, in the semi-infinite case of coastal flow which is unbounded as $y \to \infty$ the dispersive term in the evolution equation becomes, as will be shown, the familiar Benjamin-Ono dispersion and the evolution equation is a forced-BDA (Benjamin [1967], Davies and Acrivos [1967]) type equation. The BDA type integro-differential equation is of a more complicated form than the KdV equation (which is a purely *differential* equation) and it is not easy to integrate twice and obtain an 'energy' equation as in Clarke and Johnson [1999] but the flow patterns of the initial value problem are qualitatively similar to the channel flows

and numerical results are presented for a wide region of the parameter space.

4.2 Formulation.

Using the scalings of chapter 3 the conservation of PV can be written

$$\frac{\partial q}{\partial t} + J(\psi, q) = 0. \tag{4.1}$$

Where ψ is the streamfunction, the operator $J(.)$ is the nonlinear Jacobian term defined $J(f, g) = f_x g_y - g_x f_y$. The alongshore coordinate is x and offshore coordinate is y. The nondimensional PV q is

$$q = \nabla^2 \psi + h_B(y). \tag{4.2}$$

The PV comprises of the changes in relative vorticity due to the flow field ψ and contributions from the bottom topography $h_B(y)$ shown in figure (3.1), which, as before, is given by,

$$h_B(y) = -2H(y - h), \tag{4.3}$$

where $h \sim O(1)$ and $H(.)$ the Heaviside Step function. The near resonant response occurs when the vortex propagates with a velocity matching the topographic waves maximum group velocity, $C_{g\text{max}} = h$, and since such topographic Rossby waves travel with shallow water to their right this corresponds to the case of a point vortex with weak positive circulation that is situated close to the wall. For a vortex of strength Γ situated at $(0, y_0)$ with y_0 and Γ small, the vortex and its image are approximated as a dipole

$$\Psi \simeq \frac{-\Gamma y_0 y}{\pi (x^2 + y^2)}. \tag{4.4}$$

To leading order this will remain at $x = 0$ if it is placed in an opposing stream $\psi = Uy$, where

$$U = \frac{\Gamma}{4\pi y_0}. \tag{4.5}$$

Let $y = \mathbf{L}(x, t)$ be the line which initially lies along $y = h$ (i.e. $\mathbf{L}(x, 0) = h$). This is a material contour which separates the two regions of differing PV. If it is perturbed in some manner then fluid crossing from shallow to deep (deep to shallow) will acquire positive (negative) relative PV and so

$$\nabla^2 \psi = H(y - h) - H(y - \mathbf{Y}(x, t)), \tag{4.6}$$

as shown in figure (2.1). For coastal topography the far field conditions are that far offshore the flow is a free stream as described by (4.5). In both directions alongshore the contour $\mathbf{Y}$ tends to the unperturbed value $y = h$ as $|x| \to \infty$. There is no flow through any solid walls and the initial condition is that the topography is 'switched on' near a pre-existing vortex in a free stream.

The kinematic condition at the interface $y = \mathbf{Y}(x, t)$ that relates the cross-step velocity v to the time rate of change of $\mathbf{Y}$ is, Grimshaw and Yi [1990]

$$\mathbf{Y}_t = \frac{\mathrm{d}}{\mathrm{d}x}\psi(x, \mathbf{Y}, t). \tag{4.7}$$

Writing the streamfunction ψ as

$$\psi = Uy + \Psi + \phi. \tag{4.8}$$

gives a set of equations to solve for the secondary motions ϕ and hence through (4.7) the contour $\mathbf{Y}(x, t)$. Now, when $x \neq 0$ and $y \neq y_0$

$$\nabla^2 \phi = H(y - h) - H(y - \mathbf{Y}(x, t)), \tag{4.9}$$

$$\lim_{|x| \to \infty} \mathbf{Y}(x, t) = h, \tag{4.10}$$

$$\phi(x, 0, t) = 0, \tag{4.11}$$

$$\mathbf{Y}_t = \frac{d}{dx}(U\mathbf{Y} + \Psi(x, \mathbf{Y}) + \phi(x, \mathbf{Y}, t)). \tag{4.12}$$

The fluid domain is split into two regions. The first region, the 'inner' region, is that defined by $0 < y < L$ where L is some $O(1)$ quantity with $0 < \max(1, \mathbf{Y}(x, t)) < L$. The 'outer' region is that defined by $L < y < \infty$ and the problem is completed with the far-field condition

$$\lim_{y \to \infty} \phi = 0. \tag{4.13}$$

The 'inner' and 'outer' asymptotic expansions for ϕ can be matched by invoking continuity of ϕ and ϕ_y across the line $y = L$.
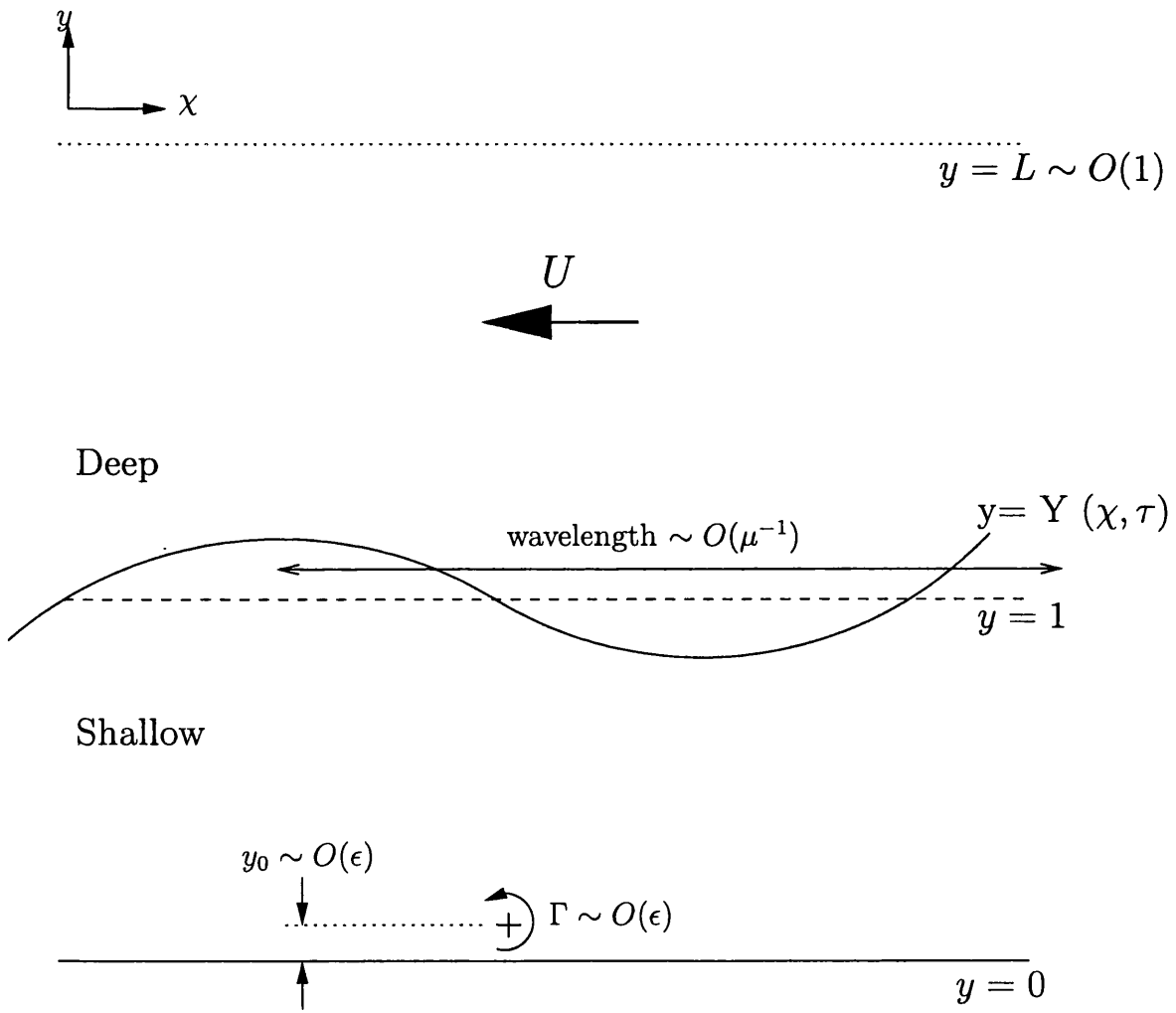
Figure 4.1: Schematic diagram of the domain of interest.

4.3   Coastal Flow.

Taking, without loss of generality, $h = 1$, so the maximum group velocity is unity the equations to be solved are

$$\nabla^2 \phi = H(y - 1) - H(y - \mathbf{Y}(x, t)), \tag{4.14}$$

$$\lim_{y \to \infty} \phi = 0, \tag{4.15}$$

$$\lim_{|x| \to \infty} \mathbf{Y}(x, t) = 1, \tag{4.16}$$

$$\phi(x, 0, t) = 0, \tag{4.17}$$

$$\mathbf{Y}_t = \frac{d}{dx}(U\mathbf{Y} + \Psi(x, \mathbf{Y}) + \phi(x, \mathbf{Y}, t)). \tag{4.18}$$

4.3.1   The 'Inner' Region.

Introduce the small parameter $\mu \ll 1$ defined by

$$\varepsilon = \mu^{1/2}, \tag{4.19}$$

where ε was the small parameter of linearisation in chapter 3. There it was shown that a vortex of strength $\Gamma \sim O(\varepsilon)$ an $O(\varepsilon)$ distance from the wall produces a $O(\varepsilon^2)$ response at the interface, and that at resonance this will eventually become unbounded. In this chapter, μ will be the small parameter and so the interface disturbances will be $O(\mu)$ and the longwave assumption demands that a typical wavelength at the interface is taken to be $O(\mu^{-1})$. Take $y < L$ and using the longwave approximation, the along shore response is $O(\mu^{-1})$, however the domain is bounded in the offshore direction so for the 'inner' solution rescaling is necessary in x but not in y. Equation (4.14) with the stretched coordinate $\chi = \mu x$ can be written,

$$\phi_{yy} + \mu^2 \phi_{\chi\chi} = H(y - 1) - H(y - \mathbf{Y}), \tag{4.20}$$

with $\phi = 0$ at $y = 0$. Another feature of the weakly nonlinear response is that it occurs on a slower timescale (Akylas [1984], Clarke and Johnson [1996a]), it will become clear later on that an appropriate scaling is given by $\tau = \mu^2 t$ as this enables the correct balance to be found at leading order in the evolution equation. The interface condition (4.18) is now

$$\mu \mathbf{Y}_\tau = \frac{\partial}{\partial \chi}(U\mathbf{Y} + \Psi(\chi, \mathbf{Y}) + \phi(\chi, \mathbf{Y}, \tau)). \tag{4.21}$$

Expand ϕ in terms of the small parameter μ;

$$\phi = \phi^0 + \mu^2 \phi^1 + \ldots \tag{4.22}$$

Substituting (4.22) into (4.20) gives

$$\phi^0_{yy} = H(y - 1) - H(y - \mathbf{Y}), \tag{4.23}$$

which, upon integrating with respect to y twice and using the condition(4.17) gives,

$$\phi^0 = \frac{1}{2}(y - 1)^2 H(y - 1) - \frac{1}{2}(y - \mathbf{Y})^2 H(y - \mathbf{Y}) + Ay. \tag{4.24}$$

At the next order,

$$\phi^1_{yy} = -\phi^0_{\chi\chi}. \tag{4.25}$$

Differentiation of (4.24) with respect to χ gives

$$\phi^0_{\chi\chi} = H(y - \mathbf{Y})\Big((y - \mathbf{Y})\mathbf{Y}_{\chi\chi} - \mathbf{Y}^2_\chi\Big) + A_{\chi\chi}y. \tag{4.26}$$

So, integrating (4.26) twice with respect to y and using (4.17) now gives,

$$\phi^1 = \frac{\mathbf{Y}^2_\chi}{2}(y - \mathbf{Y})^2 H(y - \mathbf{Y}) - \frac{\mathbf{Y}_{\chi\chi}}{6}(y - \mathbf{Y})^3 H(y - \mathbf{Y}) - \frac{A_{\chi\chi}y^3}{6} + By. \tag{4.27}$$

Note that

$$\frac{\mathbf{Y}^2_\chi}{2}(y - \mathbf{Y})^2 H(y - \mathbf{Y}) - \frac{\mathbf{Y}_{\chi\chi}}{6}(y - \mathbf{Y})^3 H(y - \mathbf{Y}) - \frac{A_{\chi\chi}y^3}{6}$$

$$= \frac{1}{12}\frac{\partial^2}{\partial\chi^2}(\frac{1}{2}(y - \mathbf{Y})^4 H(y - \mathbf{Y}) - 2Ay^3). \tag{4.28}$$

Finally the inner perturbation to the streamfunction to $O(\mu^2)$ is, using (4.22), (4.24) and (4.27),

$$\phi = \frac{1}{2}((y-1)^2 H(y-1) - (y-\mathbf{Y})^2 H(y-\mathbf{Y})) + y(A + \mu^2 B) +$$

$$\frac{\mu^2}{12}\frac{\partial^2}{\partial \chi^2}(\frac{1}{2}(y-\mathbf{Y})^4 H(y-\mathbf{Y}) - 2Ay^3). \qquad (4.29)$$

Let ϕ at $y = L$ be $F = F(\chi, \tau)$, and so putting these values into (4.29) gives that

$$F = \frac{1}{2}((L-1)^2 - (L-\mathbf{Y})^2) + L(A + \mu^2 B) + \frac{\mu^2}{12}\frac{\partial^2}{\partial \chi^2}(\frac{(L-\mathbf{Y})^4}{2} - 2AL^3), \qquad (4.30)$$

and let ϕ_y at $y = L$ be $G = G(\chi, \tau)$, the derivative of (4.29) with respect to χ, gives

$$G = \mathbf{Y} - 1 + A + \mu^2 B + \frac{\mu^2}{12}\frac{\partial^2}{\partial \chi^2}(2(L-\mathbf{Y})^3 - 6AL^2). \qquad (4.31)$$

4.3.2 The 'Outer' Region.

For $y > L > \max(\mathbf{Y}, 1)$ both the along and off-shore regions have the same length scale of $O(\mu^{-1})$. Hence the alongshore coordinate is scaled as before but now let $\eta = \mu y$ and now the governing equation (4.14) becomes

$$\phi_{\chi\chi} + \phi_{\eta\eta} = 0 \qquad (4.32)$$

with $\phi = 0$ as $y \to \infty$.

Taking the Fourier transform of (4.32) with respect to χ gives

$$\hat{\phi}_{\eta\eta} - k^2\hat{\phi} = 0. \qquad (4.33)$$

The general solution satisfying (4.13) is

$$\hat{\phi} = Ae^{-|k|\eta}, \qquad (4.34)$$

for $A(k, \tau)$ to be found. Let $\hat{F}(k, \tau)$ be the transform of the boundary conditions at the edge of the outer region $\eta = \mu L$ and so

$$\hat{F} = Ae^{-|k|\mu L}. \qquad (4.35)$$

Putting (4.35) into (4.34) and taking the inverse transform gives

$$\phi = \frac{1}{2\pi} \int_{-\infty}^{\infty} \hat{F}(k, \tau)e^{ik\chi + \mu|k|(L-y)}dk. \qquad (4.36)$$

Note that for small μ

$$\hat{F}(k, \tau)e^{\mu|k|(L-y)} \simeq \hat{F}(k, \tau)\Big(1 + \mu|k|(L - y) +$$

$$\frac{1}{2}\mu^2 k^2(L - y)^2 + \frac{1}{6}\mu^3 k^2|k|(L - y)^3\Big). \qquad (4.37)$$

Equation (4.37) can be written

$$\hat{F}(k,\tau)e^{\mu|k|(L-y)} \simeq \hat{F} + \mu|k|(L-y)\hat{F} -$$

$$\frac{1}{2}\mu^2(L-y)^2\hat{F}_{xx} - \frac{1}{6}\mu^3|k|(L-y)^3\hat{F}_{xx}. \tag{4.38}$$

Therefore (4.36) can be written

$$\phi = F + \mu(L-y)\mathbb{B}(F) - \frac{1}{2}\mu^2(L-y)^2 F_{xx} - \frac{1}{6}\mu^3(L-y)^3\mathbb{B}(F_{xx}), \tag{4.39}$$

Where the operator $\mathbb{B}$ is defined as (Benjamin [1967], Davies and Acrivos [1967])

$$\mathbb{B}(F) = \frac{1}{\pi}\frac{\partial}{\partial\chi}\int\frac{F(y,t)}{y-\chi}dy = \frac{1}{2\pi}\int_{-\infty}^{\infty}|k|\hat{F}e^{ikx}dk. \tag{4.40}$$

The first form of the integral in (4.40) is a Cauchy Principal Value.

4.3.3 Matching.

The continuity of ϕ and ϕ_y across $y = L$ can be used to specify the unknown quantities $A + \mu^2 B$ and F in terms of $\mathbf{Y}$. Equations (4.29) and (4.39) give, for the continuity of ϕ

$$F = \frac{1}{2}((L-1)^2 - (L-\mathbf{Y})^2) + L(A + \mu^2 B)$$

$$+\mu^2\Big(\frac{\mathbf{Y}_\chi^2}{2}(L-\mathbf{Y})^2 - \frac{\mathbf{Y}_{xx}}{6}(L-\mathbf{Y})^3 - \frac{A_{xx}L^3}{6}\Big). \tag{4.41}$$

Note that the left hand side of (4.41) is exact as putting $y = L$ into (4.39) gives that $\phi = F$ exactly. Differentiating (4.29) and (4.39) with respect to y and using the continuity of the alongshore velocity at $y = L$ gives

$$-\mu\mathbb{B}(F) = \mathbf{Y} - 1 + A + \mu^2 B + \mu^2\Big(\mathbf{Y}_\chi^2(L-\mathbf{Y}) - \frac{\mathbf{Y}_{xx}}{2}(L-\mathbf{Y})^2 - \frac{A_{xx}L^2}{2}\Big), \tag{4.42}$$

and again the left hand side of (4.42) is exact. It remains now to find expressions for the unknown functions $A + \mu^2 B$ and F so expanding for small μ,

$$F = F_0 + \mu F_1 + \mu^2 F_2 + \mu^3 F_3 + ..., \tag{4.43}$$

$$A + \mu^2 B = A_0 + \mu A_1 + \mu^2 (A_2 + B_0) + \mu^3 (A_3 + B_1) + ... \tag{4.44}$$

Now putting (4.43) and (4.44) in (4.41) and (4.42) and writing

$$\mathbf{Y} = 1 + \mu \Theta_1 + \mu^2 \Theta_2, \tag{4.45}$$

gives to $O(\mu^3)$, (see Appendix C for details of this calculation)

$$A + \mu^2 B = -\mu \Theta_1 - \mu^2 (\Theta_2 + \mathbb{B}(\Theta_1)) + \frac{\mu^3}{2} \left(\Theta_{1\chi\chi} + \mathbb{B}(\Theta_1^2) \right), \tag{4.46}$$

and

$$F = -\mu \Theta_1 + \mu^2 \left(L\mathbb{B}(\Theta_1) - \frac{\Theta_1^2}{2} \right) - \mu^3 \left(\Theta_2 + \Theta_1 \Theta_2 - \frac{\Theta_{1\chi\chi}}{6}(1 - L^3) + L^2 \mathbb{B}^2(\Theta_1) + \frac{L}{2} \mathbb{B}(\Theta_1^2) \right). \tag{4.47}$$

The interface condition (4.21) becomes, in the weakly nonlinear limit (and using the $\mathbf{Y}$ notation briefly again for brevity),

$$\mu^2 \Theta_\tau = \frac{\partial}{\partial \chi} \left(U \mathbf{Y} + \Psi(\chi, \mathbf{Y}, \tau) + \phi(\chi, \mathbf{Y}, \tau) \right). \tag{4.48}$$

The 'inner' expression for ϕ was given by (4.29) and so $\phi(\chi, \mathbf{Y}, \tau)$ is given by,

$$\phi = \frac{1}{2}(\mathbf{Y} - 1)^2 H(\mathbf{Y} - 1) + (A + \mu^2 B)\mathbf{Y} - \frac{\mu^2}{6}(A + \mu^2 B)_{\chi\chi} \mathbf{Y}^3. \tag{4.49}$$

Taking the derivative of (4.49) with respect to χ gives

$$\frac{\partial}{\partial \chi} \phi(\chi, \mathbf{Y}, \tau) = (\mathbf{Y} - 1)\mathbf{Y}_\chi H(\mathbf{Y} - 1) + (A + \mu^2 B)\mathbf{Y}_\chi + (A + \mu^2 B)_\chi \mathbf{Y}$$

$$- \frac{\mu^2}{6}(A + \mu^2 B)_{\chi\chi\chi} \mathbf{Y}^3 - \frac{\mu^2}{2}(A + \mu^2 B)_{\chi\chi} \mathbf{Y}^2 \mathbf{Y}_\chi. \tag{4.50}$$

On putting (4.45) back into (4.50) there are two things to note, firstly

$$H(\mu\Theta_1 + \mu^2\Theta_2) \simeq H(\Theta_1), \qquad (4.51)$$

and secondly the last term of (4.50) is $O(\mu^4)$.

Putting (4.50) into (4.48) and using (4.45) and (4.46) gives,

$$\mu^2\Theta_{1\tau} + \mu^3\Theta_{2\tau} = \frac{\partial}{\partial\chi}\Big(\Psi_v(\chi, 1+\mu\Theta_1+\mu^2\Theta_2,\tau)\Big) + \mu\Theta_{1\chi}(U-1) + \mu^2\Theta_{2\chi}(U-1)$$

$$-\mu^2\Theta_1\Theta_{1\chi}(2-H(\Theta_1)) + \mu^2\mathbb{B}(\Theta_{1\chi}) - \frac{\mu^3}{2}(\Theta_1\Theta_2)_\chi(2-H(\Theta_1))$$

$$+\frac{2\mu^3}{3}\Theta_{1\chi\chi\chi} - \mu^3\Theta_{1\chi}\mathbb{B}(\Theta_1) + \frac{\mu^3}{2}\Big[\mathbb{B}(\Theta_1^2)\Big]_\chi.$$

$$(4.52)$$

At leading order (i.e. ignoring terms of order μ) equation (4.52) is a forced BDA-type equation. Note that the triple derivative, KdV-type dispersion comes in at higher order. Dividing (4.52) by μ^2 and ignoring terms of $O(\mu)$, (4.52) can be written as

$$\Theta_{1\tau} - \Big(\frac{U-1}{\mu}\Big)\Theta_{1\chi} - (U-1)\Theta_{2\chi} + \Theta_1\Theta_{1\chi}(2-H(\Theta_1)) - \mathbb{B}(\Theta_{1\chi}) =$$

$$\frac{1}{\mu^2}\frac{\partial}{\partial\chi}(\Psi(\chi, 1+\mu\Theta_1+\mu^2\Theta_2,\tau)). \qquad (4.53)$$

The near-resonant limit corresponds to $U \simeq 1$ so writing $\Delta = (U-1)/\mu$ with $\Delta \sim O(1)$ as the detuning parameter gives that $U-1 \sim O(\mu)$ and therefore Θ_2 drops out of the leading order problem entirely (see Appendix E for forcing considerations). Writing $\Theta_1 = \Theta$ gives the equation of motion governing the evolution of the interface as

$$\Theta_\tau - \Delta\Theta_\chi + \Theta\Theta_\chi(2-H(\Theta)) - \mathbb{B}(\Theta_\chi) = -\frac{\kappa^2/4\pi}{1+\mu\Delta}\delta_\chi(\chi), \qquad (4.54)$$

for

$$\Gamma = \mu^{1/2}\kappa, \qquad (4.55)$$

with $\kappa \sim O(1)$ and

$$y_0 = \frac{\mu^{1/2}\kappa}{4\pi(1+\mu\Delta)}.$$

(4.56)

Observe that the linear long wave problem mentioned at the end of section 3.3 can be recovered from the linear terms of (4.52). For this problem the interface $\mathbf{Y} = 1 + \mu\Theta$ (recall that $\mu = \varepsilon^2$) and so $\Theta_2 = 0$, there is no forcing so $U = 0$ and the time τ has to be rescaled appropriately to the faster timescale $\tau' = \tau/\mu$. Rescaling (4.52) and dividing through by μ gives that

$$\Theta_{\tau'} = -\Theta_\chi + \mu\mathbb{B}(\Theta_\chi) + \frac{2\mu^2}{3}\Theta_{\chi\chi\chi}.$$

(4.57)

and (3.34) is recovered.

4.4 Discussion

Having derived the governing equation of the evolution of the interface (4.54) it is first prudent to side-step slightly and discuss the numerical scheme used to solve this equation (or rather its equivalent in Fourier space) and the subsequent systems of ordinary differential equations in the later chapters on the feedback problem (chapters 7 and 8). In the next chapter the chosen numerical method will be expounded and some of the computational problems that arise during application will be discussed, not all of which refer to this chapter, some are considerations for chapter 8, however it is natural to place them together. Then the results of the test equations are shown, demonstrating the accuracy and efficiency of the chosen method. After this brief segue into the numerics is completed the results of chapter 4 are presented.

4.5   APPENDIX C: Derivation of (4.46) and (4.47).

Putting (4.43) and (4.44) in (4.41) and (4.42) gives,

$$
\begin{aligned}
F_0 + \mu F_1 + \mu^2 F_2 + \mu^3 F_3 &= \frac{1}{2}(-2L + 1 + 2L\mathbf{Y} - \mathbf{Y}^2) \\
&+ L(A_0 + \mu A_1 + \mu^2(A_2 + B_0) + \mu^3(A_3 + B_1)) \\
&+ \frac{\mu^2 \mathbf{Y}_\chi^2}{2}(L - \mathbf{Y})^2 - \frac{\mu^2 \mathbf{Y}_{xx}}{6}(L - \mathbf{Y})^3 \\
&- \frac{\mu^2 L^2}{2}(A_0 + \mu A_1 + \mu^2(A_2 + B_0) + \mu^3(A_3 + B_1))_{\chi\chi},
\end{aligned} \tag{C-1}
$$

and

$$
\begin{aligned}
-(\mu \mathbb{B}(F_0) + \mu^2 \mathbb{B}(F_1) + \mu^3 \mathbb{B}(F_2)) &= \mathbf{Y} - 1 \\
&+ A_0 + \mu A_1 + \mu^2(A_2 + B_0) + \mu^3(A_3 + B_1) \\
&+ \mu^2 \mathbf{Y}_\chi^2(L - \mathbf{Y}) - \frac{\mu^2 \mathbf{Y}_{xx}}{2}(L - \mathbf{Y})^2 \\
&- \frac{\mu^2 L^2}{2}(A_0 + \mu A_1 + \mu^2(A_2 + B_0) + \mu^3(A_3 + B_1))_{\chi\chi}.
\end{aligned} \tag{C-2}
$$

Putting $\mathbf{Y} = 1 + \mu \Theta_1(\chi, \tau) + \mu^2 \Theta_2(\chi, \tau)$ gives that

$$
\mu^2 \mathbf{Y}_\chi^2 \sim O(\mu^4), \tag{C-3}
$$

which is at a higher order than is required. Note also that

$$
\mu^2 \mathbf{Y}_{xx} \sim O(\mu^3), \tag{C-4}
$$

which means that only the $O(1)$ quantities of the terms in (C-1) and (C-2) multiplying (C-4) are required i.e.

$$(L - \mathbf{Y})^2 \simeq (L - 1)^2, \tag{C-5}$$

and

$$(L - \mathbf{Y})^3 \simeq (L - 1)^3. \tag{C-6}$$

Now (C-1) and (C-2) can be simplified to

$$F_0 + \mu F_1 + \mu^2 F_2 + \mu^3 F_3 = \mu \Theta_1 (L - 1) + \mu^2 (L \Theta_2 - \frac{\Theta_1^2}{2}) - \mu^3 \Theta_2 (1 + \Theta_1)$$

$$+ L(A_0 + \mu A_1 + \mu^2 (A_2 + B_0) + \mu^3 (A_3 + B_1))$$

$$- \frac{\mu^3 \Theta_{1xx}}{6}(L - 1)^3 - \frac{\mu^2 L^2}{2}(A_0 + \mu A_1)_{xx}, \tag{C-7}$$

and

$$-(\mu \mathbb{B}(F_0) + \mu^2 \mathbb{B}(F_1) + \mu^3 \mathbb{B}(F_2)) = \mu \Theta_1 + \mu^2 \Theta_2$$

$$+ A_0 + \mu A_1 + \mu^2 (A_2 + B_0) + \mu^3 (A_3 + B_1)$$

$$- \frac{\mu^3 \Theta_{1xx}}{2}(L - 1)^2 - \frac{\mu^2 L^2}{2}(A_0 + \mu A_1)_{xx}, \tag{C-8}$$

to $O(\mu^3)$.

Equating powers of μ in (C-7) and (C-8) gives that at $O(1)$,

$$A_0 = F_0 = 0. \tag{C-9}$$

Then at $O(\mu)$,

$$A_1 = F_1 = -\Theta_1, \tag{C-10}$$

at $O(\mu^2)$,

$$
\begin{aligned}
A_2 + B_0 &= -\Theta_2 + \mathbb{B}(\Theta_1), \\
F_2 &= -\frac{\Theta_1^2}{2} + L\mathbb{B}(\Theta_1),
\end{aligned}
\tag{C-11}
$$

and at $O(\mu^3)$

$$
\begin{aligned}
A_3 + B_1 &= \Theta_{1xx}(\frac{1}{2} - L) - L\mathbb{B}^2(\Theta_1) + \frac{1}{2}\mathbb{B}(\Theta_1^2), \\
F_3 &= -\Theta_2 - \Theta_1\Theta_2 + \frac{\Theta_{1xx}}{6}(1 - L^3) - L^2\mathbb{B}^2(\Theta_1) + \frac{L}{2}\mathbb{B}(\Theta_1^2). \tag{C-12}
\end{aligned}
$$

Note that (C-12) can be simplified further using (see Appendix D)

$$
\mathbb{B}^2(\Theta) = -\Theta_{xx}.
\tag{C-13}
$$

Finally putting (C-9)-(C-12) together as described by (4.43) and (4.44) gives that

$$
A + \mu^2 B = -\mu\Theta_1 - \mu^2(\Theta_2 + \mathbb{B}(\Theta_1)) + \frac{\mu^3}{2}\left(\Theta_{1xx} + \mathbb{B}(\Theta_1^2)\right),
\tag{C-14}
$$

and

$$
F = -\mu\Theta_1 + \mu^2\left(L\mathbb{B}(\Theta_1) - \frac{\Theta_1^2}{2}\right) - \mu^3\left(\Theta_2 + \Theta_1\Theta_2 - \frac{\Theta_{1xx}}{6}(1 - L^3) + L^2\mathbb{B}^2(\Theta_1) + \frac{L}{2}\mathbb{B}(\Theta_1^2)\right),
\tag{C-15}
$$

which are (4.46) and (4.47).

4.6 APPENDIX D: The BDA Operator.

In this appendix it is shown that

$$\mathbb{B}^2(\Theta) = -\Theta_{xx}. \tag{D-1}$$

Consider the Fourier transform of the $\mathbb{B}$ operator

$$\mathcal{F}[\mathbb{B}(\Theta)] = |k|\hat{\Theta}, \tag{D-2}$$

Hence, operating on Θ twice gives

$$\mathcal{F}\left[\mathbb{B}(\mathbb{B}(\Theta))\right] = |k|\,\mathcal{F}[\mathbb{B}(\Theta)] = k^2\hat{\Theta}, \tag{D-3}$$

which is equivalent to

$$\mathcal{F}[\mathbb{B}^2(\Theta)] = -\mathcal{F}[\Theta_{xx}]. \tag{D-4}$$

Taking inverse transforms gives the required result

$$\mathbb{B}^2(\Theta) = -\Theta_{xx}. \tag{D-5}$$

4.7 APPENDIX E: Forcing considerations for equation (4.53).

Without any preconceptions of how close to the wall the vortex is placed or on what length scale the problem is being explored, the vortex forcing can be represented by (3.46) which is

$$\Psi = \frac{\Gamma}{4\pi} \log \left(\frac{x^2 + (y - y_0)^2}{x^2 + (y + y_0)^2} \right). \tag{E-1}$$

Now for the weakly nonlinear problem studied in chapter 4, which is given by (4.53) the leading order terms of (E-1) need to be found for the long wave limit $x = \chi/\mu$, at the interface $y = 1 + \mu\Theta_1 + \mu^2\Theta_2$ and with y_0 small. Putting these values into (E-1) gives

$$\Psi = \frac{\Gamma}{4\pi} \log \left[\frac{(\chi\mu^{-1})^2 + (1 - y_0)^2 + 2(1 - y_0)(\mu\Theta_1 + \mu^2\Theta_2) + (\mu\Theta_1 + \mu^2\Theta_2)^2}{(\chi\mu^{-1})^2 + (1 + y_0)^2 + 2(1 + y_0)(\mu\Theta_1 + \mu^2\Theta_2) + (\mu\Theta_1 + \mu^2\Theta_2)^2} \right]. \tag{E-2}$$

This is the difference of two log functions both of the form

$$L_\mp = \log \left[\left((\chi\mu^{-1})^2 + (1 \mp y_0)^2 \right) \left(1 + \frac{2(1 \mp y_0)(\mu\Theta_1 + \mu^2\Theta_2) + (\mu\Theta_1 + \mu^2\Theta_2)^2}{(\chi\mu^{-1})^2 + (1 \mp y_0)^2} \right) \right], \tag{E-3}$$

or

$$L_\mp = \log[F_\mp(\chi)] + \log[1 + G_\mp(\chi, \tau)], \tag{E-4}$$

for

$$F_\mp(\chi) = (\chi\mu^{-1})^2 + (1 \mp y_0)^2, \tag{E-5}$$

$$G_\mp(\chi, \tau) = \frac{2(1 \mp y_0)(\mu\Theta_1 + \mu^2\Theta_2) + (\mu\Theta_1 + \mu^2\Theta_2)^2}{(\chi\mu^{-1})^2 + (1 \mp y_0)^2}. \tag{E-6}$$

Since $|G| < 1$,

$$\log[1 + G_\mp] \simeq G_\mp, \tag{E-7}$$

and so

$$L_{\mp} = \log[F_{\mp}(\chi)] + O(\mu), \qquad (\text{E-8})$$

where-upon (E-2) becomes

$$\Psi \simeq \frac{\Gamma}{4\pi} \log \left(\frac{(\chi\mu^{-1})^2 + (1 - y_0)^2}{(\chi\mu^{-1})^2 + (1 + y_0)^2} \right). \qquad (\text{E-9})$$

Equation (E-9) can again be approximated to a dipole for small y_0 (c.f. Section 3.4.4)

$$\Psi \simeq -\frac{\Gamma y_0/\pi}{1 + (\chi/\mu)^2}. \qquad (\text{E-10})$$

However in the longwave limit the forcing to (4.54) appears as the derivative of a δ-function as demonstrated below, for $\mu \to 0$

$$-\frac{\Gamma y_0}{\mu^2} \frac{\partial}{\partial \chi} \left(\frac{\mu^2}{\pi(\mu^2 + \chi^2)} \right) = -\frac{\Gamma y_0}{\mu} \delta_\chi(\chi). \qquad (\text{E-11})$$

Choosing

$$\Gamma = \mu^{1/2} \kappa, \qquad (\text{E-12})$$

with $\kappa \sim O(1)$ gives that

$$y_0 = \frac{\mu^{1/2} \kappa}{4\pi(1 + \mu\Delta)}. \qquad (\text{E-13})$$

This is consistent with chapter 3 as $\mu = \epsilon^2$. Therefore (4.54) remains uniformly valid in the limit $\mu \to 0$.

Chapter 5

The Numerical Method.

5.1 Introduction.

Having derived the evolution equation for the topographic longwaves generated in steady flow past a stationary vortex (for a particular choice of reference frame) it is now appropriate to devote some discussion to the numerical method used throughout this thesis to solve the evolution equation. The method used is a spectral method based on Fornberg [1999]. In their paper they point out the need for high computational efficiency which implies the use of high-order methods in time that can bypass the severe stability conditions for systems of stiff differential equations. They achieve this with the innovation of using different multi-step methods at different wavenumbers.

Their method applies to differential equations for $\Theta = \Theta(x, t)$ of the form

$$\Theta_t = N(\Theta, \Theta_x, \ldots) + L(\Theta). \tag{5.1}$$

where the function N is the nonlinear part and can include inhomogeneous forcing terms $f(x, t)$ say. The function L is the linear part and takes the general form

$L(\Theta) = c(t)i^{m+1}(\partial^m\Theta/\partial x^m)$ or a sum of such terms, for some real function $c(t)$ and $i = \sqrt{-1}$. On taking Fourier transforms the linear operator L will become a polynomial in wavenumber k of degree max(m). The transform of the nonlinear part is not generalisable.

5.2   Linearly Implicit Multi-step Methods

To numerically solve the system:

$$\frac{dy}{dt} = f(t,y),\tag{5.2}$$

where f can be separated into a nonlinear (N) and linear (L) part,

$$f(t,y) = N(t,y) + L(t,y),\tag{5.3}$$

one can employ the technique of linear multi-step methods, of which the Adams' type are an easily implementable sub-family. They comprise of both explicit (Adams-Bashforth) and implicit (Adams-Moulton) schemes.

The family of k-step Adams-Bashforth (ABk) methods are summarised thus (see Fröberg [1970] for details):

$$y_{n+1} - y_n = h\sum_{j=0}^{k-1}\gamma_j^*\nabla^j f_n\tag{5.4}$$

They are order k and have error constant $C_{k+1} = \gamma_k^*$.

Here ∇ is the backward difference operator, defined by:

$$\nabla F_n = F_n - F_{n-1},\tag{5.5}$$

$$\nabla^2 F_n = \nabla(F_n - F_{n-1}) = F_n - 2F_{n-1} + F_{n-2}\quad\text{etc.}\tag{5.6}$$

The constants γ_j^* are defined:

$$\gamma_j^* + \frac{\gamma_{j-1}^*}{2} + \frac{\gamma_{j-2}^*}{3} + \ldots + \frac{\gamma_0^*}{j+1} = 1. \tag{5.7}$$

and

$$\gamma_0^* = 1$$

For future reference the first few are,

$$\gamma_0^* = 1, \quad \gamma_1^* = 1/2, \quad \gamma_2^* = 5/12, \quad \gamma_3^* = 9/24.$$

The family of k-step Adams-Moulton (AMk) methods are:

$$y_{n+1} - y_n = h \sum_{j=0}^{k} \gamma_j \nabla^j f_{n+1} \tag{5.8}$$

They are order $k + 1$ and have error constant $C_{k+2} = \gamma_{k+1}$.

Here, the γ_j are defined:

$$\gamma_j + \frac{\gamma_{j-1}}{2} + \frac{\gamma_{j-2}}{3} + \ldots + \frac{\gamma_0}{j+1} \quad = \quad 1 \quad j = 0$$
$$= \quad 0 \quad \text{otherwise.} \tag{5.9}$$

The first few are,

$$\gamma_0 = 1, \quad \gamma_1 = 1/2, \quad \gamma_2 = 1/12, \quad \gamma_3 = 1/24, \quad \gamma_4 = 19/720, \quad \gamma_5 = 3/160$$

5.2.1 Stiffness

A system of differential equations is *stiff* if variations with respect to the independent variable can occur on widely different scales of magnitude. A classic example is given in Fröberg [1970] whereby the system

$$\frac{dy}{dx} = -12y + 9z, \tag{5.10}$$
$$\frac{dz}{dx} = 11y - 10z,$$

is solved using a Runga-Kutta scheme. The solution to (5.10) is

$$y = 9e^{-x} + 5e^{-21x}, \qquad (5.11)$$

$$z = 11e^{-x} - 5e^{-21x}.$$

Using initial values of $x = 1$, $y = 3.3111$ and $z = 4.0469$ with a step-size of 0.2 gives an error of over 150% after only 8 steps. Stiff equations can be solved by normal 'non-stiff' methods (i.e. Runga-Kutta) but they would require an extremely small time-step size and thus are impractical. For equations of the form (5.1) it is the linear part at high wavenumbers that is creating the stiffness.

5.2.2 Stability

The stability of a numerical method is concerned with the behavior of a perturbed solution as calculated using the method under examination. There are various forms of stability; a method is zero-stable if for two different perturbations to the system/initial values the method can calculate the same answer for vanishingly small time-step size. Another more elaborate definition of zero-stability is that the roots of the characteristic polynomial must all have a modulus less than unity. It is well known that all Adams-methods are zero-stable but Fornberg [1999] are concerned with Absolute stability, or A-stability, as they phrase it. This is the condition that stability occurs for a fixed, non-zero timestep.

Hairer and Wanning [1996] show that no multi-step method of order greater than 2 can be A-stable and this is restrictive of the timestep size (again due to the linear part). Fornberg [1999] point out that at low wavenumbers stability is not an issue and that the equations for different wavenumbers can be treated with different multi-step solvers, as multi-step methods do not need information from all modes, as can

the linear and nonlinear parts of the equation.

They summarise their basic concept as: Use explicit methods on the nonlinear part, for the linear part and a time step h, use a higher-order scheme for as high wavenumber as stability will allow and elsewhere use an A-stable, implicit multi-step method. Implicitness usually increases the stable step size for stiff problems and the implicitness of the method is not a problem computationally as it is only being applied to the linear part (i.e. the linear operator matrix can be inverted to give an explicit solution).

Now using the notation 'method A/method B' to denote that the nonlinear part is to be solved by method A and the linear part by method B, and denoting the solution at n time-steps of length h by

$$L_n = L(y_n),$$

Fornberg [1999] propose the following combinations of Adams' methods:

5.2.3   AB4/AM2* for high wavenumbers.

This combination uses a modified AM2 scheme for the linear part,

$$y_{n+1} - y_n = \frac{h}{24}(55N_n - 59N_{n-1} + 37N_{n-2} - 9N_{n-3}) + \frac{h}{4}(3L_{n+1} + L_{n-1}). \quad (5.12)$$

Re-arranging to give the explicit form,

$$y_{n+1} = \left(1 - \frac{3h}{4}L\right)^{-1}\left(y_n + \frac{h}{24}(55N_n - 59N_{n-1} + 37N_{n-2} - 9N_{n-3}) + \frac{h}{4}L_{n-1}\right). \quad (5.13)$$

5.2.4   AB4/AM6 for medium wavenumbers.

For this combination,

$$y_{n+1} - y_n = \frac{h}{24}\left(55N_n - 59N_{n-1} + 37N_{n-2} - 9N_{n-3}\right)$$

$$+\frac{h}{1440}\Big(475L_{n+1} + 1427L_n - 798L_{n-1} + 482L_{n-2} - 173L_{n-3} + 27L_{n-4}\Big). \quad (5.14)$$

Which can be written explicitly as

$$y_{n+1} = \Big(1 - \frac{475h}{1440}L\Big)^{-1}\Big(y_n + \frac{h}{24}(55N_n - 59N_{n-1} + 37N_{n-2} - 9N_{n-3})$$
$$+\frac{h}{1440}(1427L_n - 798L_{n-1} + 482L_{n-2} - 173L_{n-3} + 27L_{n-4})\Big). \quad (5.15)$$

5.2.5 AB4/AB4 for low wavenumbers.

This is just the usual AB4 scheme applied to both,

$$y_{n+1} = y_n + \frac{h}{24}\Big(55(L+N)_n - 59(L+N)_{n-1} + 37(L+N)_{n-2} - 9(L+N)_{n-3}\Big). \quad (5.16)$$

The boundaries between these regions of wavenumber space are given in

Fornberg [1999] and it is noted here that increasing the boundaries' cutoff points

in wavenumber space will increase accuracy and will therefore help towards dealing

with any activity at higher wavenumbers (as opposed to say filtering them out,

Canuto et al. [1988]) whereas decreasing the cutoff points (if necessary) must be

done with care.

5.3 Considerations for the Present Numerical Experiments.

In Fourier space (E-10) transforms to

$$\hat{\Psi} = -\frac{ik\Gamma y_0}{\mu}e^{-\mu|k|}. \quad (5.17)$$

Therefore taking Fourier transforms of (4.54) with respect to χ gives

$$\hat{\Theta}_\tau = (\Delta + |k|)ik\hat{\Theta} - \mathcal{F}[\Theta\Theta_\chi(2 - H(\Theta))] - \frac{ik\Gamma y_0}{\mu}e^{-\mu|k|}, \qquad (5.18)$$

where $\mathcal{F}(.)$ denotes the Fourier transform. Taking $\Gamma y_0 \sim O(\mu)$ gives a well defined problem for the limit $\mu \to 0$. As such Γ is written

$$\Gamma = \mu^{1/2}\kappa, \qquad (5.19)$$

for $\kappa \sim O(1)$. Therefore (4.5) gives an expression for y_0 which is

$$y_0 = \frac{\mu^{1/2}\kappa}{4\pi(1 + \mu^2\Delta)}. \qquad (5.20)$$

This is in agreement with the scalings in chapter 3 where an $O(\epsilon)$ strength vortex and $O(\epsilon)$ distance from the wall produces an $O(\epsilon^2)$ response at the interface. Here $\epsilon = \mu^{1/2}$ and $y_0 \sim \Gamma \sim O(\mu^{1/2})$ with the interface displacement $Y \sim O(\mu)$.

5.3.1   Small Time Solution:

The numerical method used to integrate (5.18) is basically an interpolation and so time-stepping $\hat{\Theta}$ from $\tau_i \to \tau_{i+1}$ requires knowledge of the values of $\hat{\Theta}$ at previous times. Therefore in order to start the integrations some initial conditions are required. These can be found analytically by expanding $\hat{\Theta}$ for small τ up to $O(\tau^3)$, let $\hat{\Theta}$ be written

$$\hat{\Theta}(k, \tau) = \tau\hat{\Theta}_1(k) + \tau^2\hat{\Theta}_2(k) + \tau^3\hat{\Theta}_3(k) + \ldots \qquad (5.21)$$

Putting (5.21) into (5.18) and equating powers of τ gives,

$$\hat{\Theta}_1 = -\frac{\Gamma y_0}{\mu}ike^{-\mu|k|}, \qquad (5.22)$$

$$\hat{\Theta}_2 \;\; = \;\; \frac{ik\hat{\Theta}_1}{2}(\Delta + |k|), \tag{5.23}$$

$$\hat{\Theta}_3 \;\; = \;\; -\frac{k^2\hat{\Theta}_1}{2}(\Delta + |k|)^2 - \mathbb{F}[\Theta_1\Theta_1'(2 - H(\Theta))]. \tag{5.24}$$

Here the dash represents differentiation with respect to χ. Now Θ_1 and its derivative are given by

$$\Theta_1 \;\; = \;\; \frac{\Gamma y_0}{\pi}\frac{2\chi}{(\mu^2 + \chi^2)^2}, \tag{5.25}$$

$$\Theta_1' \;\; = \;\; \frac{\Gamma y_0}{\pi(\mu^2 + \chi^2)^3}\left(2(\mu^2 + \chi^2) - 8\chi^2\right). \tag{5.26}$$

The error associated with this expansion is $O(\tau^4)$ and so for a timestep of size 10^{-3} the numerical error is approximately 10^{-12}.

5.3.2   Forcing

One of the interesting things about this choice of problem is that in the longwave limit the vortex forcing becomes the infinitely narrow δ-function forcing. This is in contrast to other works which utilise longwave theory to investigate unsteady deviations to hydraulic behavior where the longwave limit results in long forcing. Numerically the difficulties arising from narrow forcing show up in the spectral representation of the evolution equation, the forcing in (5.18) is of the form

$$iCke^{-\mu|k|}, \tag{5.27}$$

where C is an O(1) constant given by

$$C = -\frac{\Gamma y_0}{\mu}. \tag{5.28}$$

Figure (5.1) shows this function for various values of the small parameter μ. The limit that the present work is concerned with is that of small μ and it can be seen that as μ is getting smaller the forcing term gets larger at its maximum and approaches zero at higher and higher wavenumber ($k \sim 100$ for $\mu = 0.1$). In order to avoid aliasing problems with the Discrete Fourier Transform it is necessary to extend the wavenumber range to these higher wavenumbers, the relationship between the number of points (n), the maximum wavenumber (k_m) and the length of the domain in real space (χ_m) is given by

$$\chi_m k_m = \frac{\pi n}{2}.$$
(5.29)

So true realization of the forcing for $\mu = 0.1$ with $k_m = 100$ and $\chi_m = 200$ (say) requires that $n > 12000$. It will be seen that for the stationary vortex case considered first, it is not imperative to use such high wavenumbers as the results for differing values of μ are checked and are qualitatively similar. However in the chapters concerning the feedback problem the role of the forcing as the derivative of a δ-function is more important and thus needs to be more accurately described. In the limit $\mu \rightarrow 0$

$$iCke^{-\mu|k|} \rightarrow ik,$$
(5.30)

which is the transform of the derivative of the δ-function. It will be seen that this limit plays an important part in modeling the conservation of momentum in the alongshore direction that is inherent in the feedback problem, Bell [1989]. The problem concerning the stationary vortex does not contain that particular momentum conservation and this is due to the unrealistic nature of the *stationary* vortex forcing.
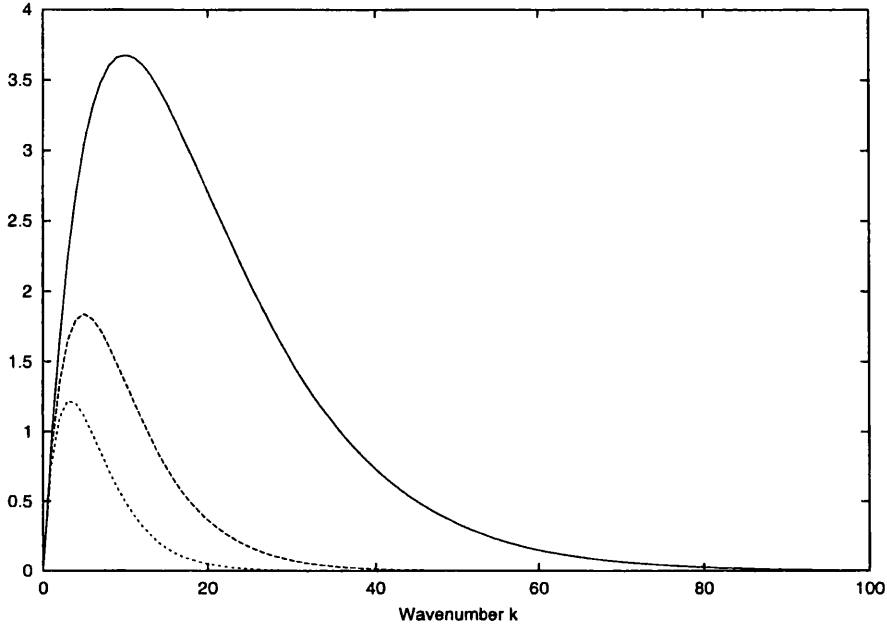
Figure 5.1: The weakly nonlinear forcing term for $\mu = 0.3$ (dotted line), $\mu = 0.2$ (dashed line) and $\mu = 0.1$ (solid line).

5.3.3 Dispersion

As was mentioned before in chapter 3, the longwave dispersion relation causes some difficulties as it allows waves of all frequencies. In the weakly nonlinear limit of the near resonant case considered in chapter 4, the dispersion ω is given by (5.18)

$$\omega(k) = -k(\Delta + |k|). \tag{5.31}$$

This is the near resonant equivalent of the longwave expansion (3.33). A plot of (5.31) is shown in figure (5.2) along with the linear dispersion ω_L given by

$$\omega_L(k) = \sinh(k)e^{-|k|}. \tag{5.32}$$

It is easy to see that in the weakly nonlinear case, waves of high wavenumber have a large frequency whereas in the linear case all waves of high wavenumber have a frequency of $1/2$. This presents itself as a numerical problem in the weakly nonlinear
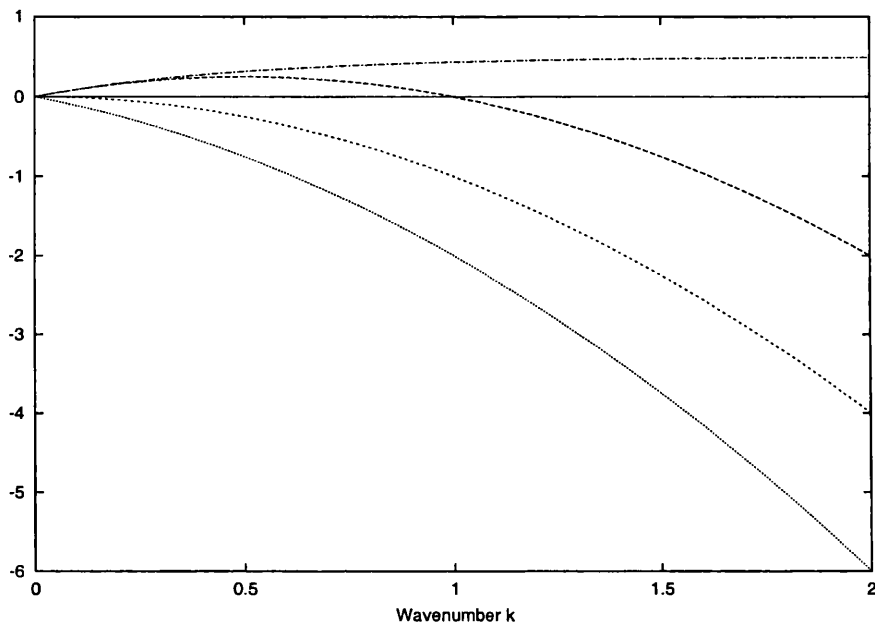
Figure 5.2: The linear dispersion (dash-dotted) and weakly nonlinear, longwave dispersion for subcritical $\Delta = -1$ (long dashes), resonant $\Delta = 0$ (short dashes) and supercritical $\Delta = 1$ (dots).

case as the waves of high frequency end up 'wrapping' around the finite computational domain. One solution is to make sure that the domain is large enough to contain all of the wavetrain without any wrap around interference. Another solution is applying a filter to knock out the higher wavenumbers (see Canuto et al. [1988]), however it was felt that as this is a non-dissipative (dissipative terms do not occur at leading order), non-viscous (the near-critical limit corresponds to *long* waves) model, filtering could not be justified physically and would add falsities to the results. The first solution (extending the domain) is easily implementable and because the numerical method is very efficient (as compared with contour dynamics, say) there doesn't have to be any equivalent loss in resolution. In addition, the numerical method itself uses different methods at different wavenumbers and it is always possible to change the boundaries between methods so that the high wavenumber solver takes more responsibility, thus making the method more stable without much computational cost.

5.3.4 Nonlinearity

The nonlinear term $\mathbf{N}(\Theta, \Theta_\chi)$ of (4.54) is

$$\mathbf{N}(\Theta, \Theta_\chi) = \Theta\Theta_\chi(2 - H(\Theta)), \qquad (5.33)$$

where $H(.)$ is the Heaviside step-function. Therefore $\mathbf{N}$ is discontinuous as Θ changes sign (i.e. wavelike responses) and for cases where Θ is of one sign (i.e. blocked regions, flat regions) the nonlinearity reverts back to the well-known form of some constant multiplying

$$\mathbf{N} = \frac{\partial \Theta^2}{\partial \chi}. \qquad (5.34)$$

The ability of the method to deal with this seemingly harsh problem was tested by firstly artificially removing the nonlinear term which reverted the problem back to the forced, linear, longwave problem described in section 3.3. This problem then illustrated that the high wavenumber waves were being generated by the longwave dispersion. This was then tested further by reinstating the nonlinear term but artificially inserting the full linear dispersion defined by (3.30) instead of the longwave dispersion. The lack of high wavenumber response showed further that the high wavenumbers were being generated by the dispersive terms and not by the discontinuity in the nonlinear coefficient.

Subsequent integrations of (4.54) at weak forcing compared well with the equivalent linear FFT inversions of chapter 3 (see chapter 4) and then the integrations of the vortex-wave feedback problem in chapter 8 showed errors of $10e - 8$ (see chapter 8 for definition of error measure and results).

The numerical method is therefore thought to be sound and accurate, with the main computational difficulties arising from the forcing term and the dispersion. No further action was taken concerning the nonlinear term as it appears well behaved, however an algorithm dealing more thoroughly with these types of discontinuities can be found in Driscoll and Fornberg [2001].

5.3.5 Interpolation for interior points

This section really refers to technical points that arise in the later chapters on the feedback problem. The feedback problem is concerned with modeling the higher order motions of the vortex that are due to the back reaction of the small amplitude topographic waves on the vortex. It therefore becomes necessary to calculate the interface displacement and its derivative exactly at the vortex and this means that

an interpolation procedure is required for calculations at points interior to those of the discrete Fourier Transforms. Two types of interpolation are used, namely trigonometric interpolation and the sampling property of the δ-function.

Trigonometric Interpolation

An interpolation of a real function $f(x)$ is a polynomial of the form

$$f(x) = c_0 + c_1\zeta(x) + c_2\zeta(x)^2 + \ldots + c_{n-1}\zeta(x)^{n-1}. \tag{5.35}$$

This calculates the function $f(x)$ at any point in the domain, not just grid points, it only remains to find the quantities c_k for $k = 0, \ldots, n - 1$. One such example of a trigonometric interpolation is

$$f(x) = c_0 + c_1 e^{ix} + c_2(e^{ix})^2 + \ldots + c_{n-1}(e^{ix})^{n-1}, \tag{5.36}$$

it still remains to find the coefficients c_k. A sensible way to proceed would be to use the coefficients of the Discrete Fourier Transform of $f(x_j)$ where the function has been discretised at evenly spaced points, spaced $\mathrm{d}x$ apart

$$x_j = j\mathrm{d}x, \tag{5.37}$$

for $j = 0, n - 1$. These coefficients are given by

$$c_k = \frac{1}{\sqrt{n}} \sum_{j=0}^{n-1} f(x_j)\left(e^{-i\frac{2\pi k}{n}}\right)^j. \tag{5.38}$$

(See NAG C06FAF documentation & Brigham [1973]).

However now the trigonometric interpolant takes on a slightly different form

$$f(x) = c_0 + c_1 e^{i\Theta(x)} + c_2(e^{i\Theta(x)})^2 + \ldots + c_{n-1}(e^{i\Theta(x)})^{n-1}. \tag{5.39}$$

The real function $\Theta(x)$ needs to be found. It has the property that at grid points $x_j = j\mathrm{d}x$ the quantity $f_j = f(x_j)$ are the inverse Discrete Fourier Transforms

$$f_j = \frac{1}{\sqrt{n}} \sum_{k=0}^{n-1} c_k \left(e^{i\frac{2\pi j}{n}} \right)^k. \qquad (5.40)$$

So choosing

$$\Theta(x) = e^{i2\pi x/n\mathrm{d}x}, \qquad (5.41)$$

gives the required result at grid points

$$\Theta(x_j) = e^{i2\pi j/n}, \qquad (5.42)$$

and (5.39) gives $f(x)$ for $x = [0, (n-1)\mathrm{d}x]$. Finally to shift the domain of interest to $x = [-(n/2)\mathrm{d}x, (n/2-1)\mathrm{d}x]$ so that the grid points are given by

$$x_j = -\frac{n}{2}\mathrm{d}x + j\mathrm{d}x, \qquad (5.43)$$

it is noted that

$$\Theta(x) = e^{i(\pi + 2\pi x/n\mathrm{d}x)} \qquad (5.44)$$

will again give the required interpolation variable

$$\Theta(x_j) = e^{i2\pi j/n}. \qquad (5.45)$$

Sampling using δ-function.

Another way to calculate the values of a discretised function at interior points would be to utilise the sampling property of the δ-function, for a continuous function $F(x)$

$$\int_{-\infty}^{\infty} F(x)\delta(x - x_0)\mathrm{d}x = F(x_0). \qquad (5.46)$$

Discretising F at evenly spaced grid points x_j for $j = 0, ..., n-1$, spaced a distance dx apart and using the δ sequence

$$\lim_{\mu \to 0} \frac{\mu/\pi}{\mu^2 + (x - x_0)^2} = \delta(x - x_0), \qquad (5.47)$$

gives that

$$F(x_0) \simeq \sum_{j=0}^{n-1} \frac{F(x_j)\mu/\pi}{\mu^2 + (x_j - x_0)^2} dx. \qquad (5.48)$$

5.3.6   Scaling the BDA operator

The Fourier transform of a derivative can be expressed:

$$\mathcal{F}_1(\Theta_{x_1}) = ik_1\mathcal{F}_1(\Theta). \qquad (5.49)$$

Here the subscript on the $\mathcal{F}$ is referring to the independent variable k_1 not the dummy variable of integration. Rescaling gives:

$$x_1 = ax_2 \qquad (5.50)$$

for positive constant a. Now,

$$\mathcal{F}_1(\Theta_{x_1}) = \int_{-\infty}^{\infty} (\Theta_{x_1})e^{-ik_1 x_1} dx_1, \qquad (5.51)$$

becomes

$$\mathcal{F}_1(\Theta_{x_1}) = \int_{-\infty}^{\infty} \frac{\Theta_{x_2}}{a} e^{-ik_1 a x_2} a dx_2, \qquad (5.52)$$

$$\mathcal{F}_1(\Theta_{x_1}) = \int_{-\infty}^{\infty} \Theta_{x_2} e^{-ik_2 x_2} dx_2. \qquad (5.53)$$

So

$$\mathcal{F}_1(\Theta_{x_1}) \rightarrow \mathcal{F}_2(\Theta_{x_2}) = ik_2\mathcal{F}_2(\Theta), \tag{5.54}$$

with $x_1 = ax_2$ and $k_2 = ak_1$. The BDA operator has the form:

$$\mathbb{B}(\Theta_{x_1}) = \frac{1}{2\pi} \int_{-\infty}^{\infty} |k_1|\mathcal{F}_1(\Theta_{x_1})e^{ik_1x_1}\mathrm{d}k_1. \tag{5.55}$$

Rescaling $x_1 = ax_2$ gives:

$$\mathbb{B}(\Theta_{x_1}) = \frac{1}{2\pi} \int_{-\infty}^{\infty} \frac{|k_2|}{a}ik_2\mathcal{F}_2(\Theta)e^{ik_2x_2}\frac{\mathrm{d}k_2}{a}. \tag{5.56}$$

Therefore,

$$\mathbb{B}(\Theta_{x_1}) = \frac{\mathbb{B}(\Theta_{x_2})}{a^2}, \tag{5.57}$$

for $x_1 = ax_2$.

5.4 Tests using analytic solutions of similar evolution equations.

Two test equations are used; firstly the Korteweg-de Vries (KdV) equation with a two-soliton solution to try and mimic the results in Fornberg [1999]. Secondly, the Benjamin-Ono (BO) equation with a stationary soliton solution. The results of integrating (F-1) with the initial condition given by (F-4) at $t = 0$ are shown in figure (5.3) for $\alpha_1 = 2$, $\Theta_1 = -20$ and $\alpha_2 = 1$, $\Theta_2 = 0$. The associated error is
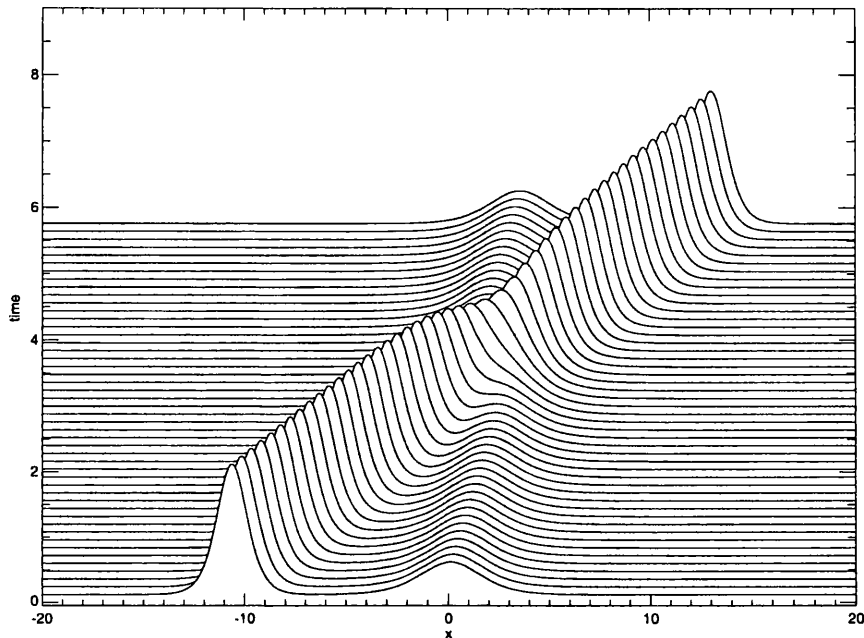
Figure 5.3: Two-Soliton test solution for KdV.

plotted in figure (5.4). The error measure $E(t)$ used for this analysis is

$$E(t) = \sqrt{\frac{\sum_{i=0}^{n-1} (A_i(t) - B_i(t))^2}{n}}, \qquad (5.58)$$

for two arrays A, B of length n. The numerical parameters used for this experiment were a spatial discretisation over $n = 1024$ points with $\delta x = \delta k = 7.854e - 2$. The timestep $\delta t = 0.0001$. The results of integrating (4.54) with the initial condition given by (G-6) for $c = -0.4$ are shown in figure (5.5). The numerical parameters for this experiment are $n = 100000$ points with $\delta x = 0.2$, $\delta k = 3.14e10 - 4$. The timestep $\delta t = 0.0001$. The error (given by (5.58)) is shown in figure (5.6).
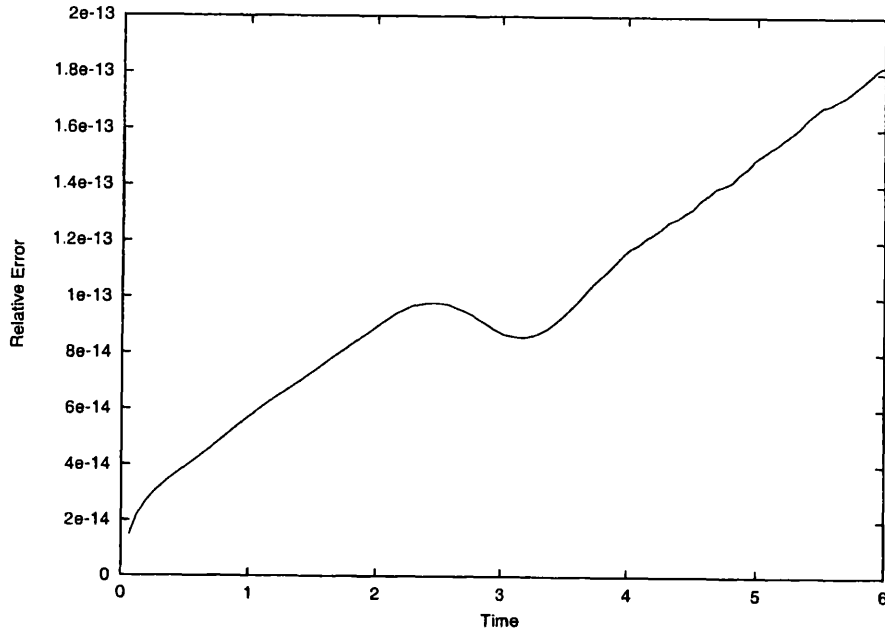
Figure 5.4: Error of test solution for KdV.
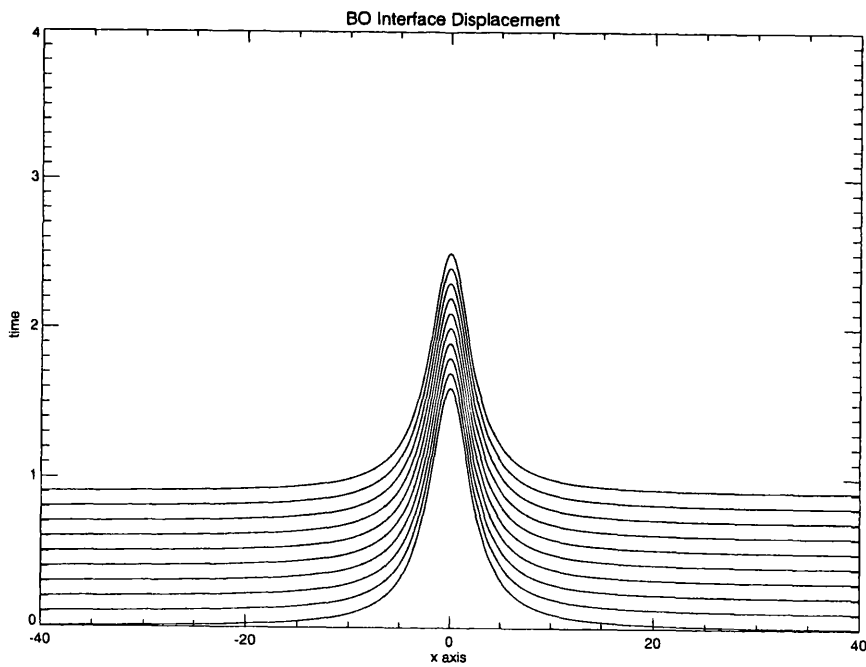
Figure 5.5: One-Soliton test solution for BO.
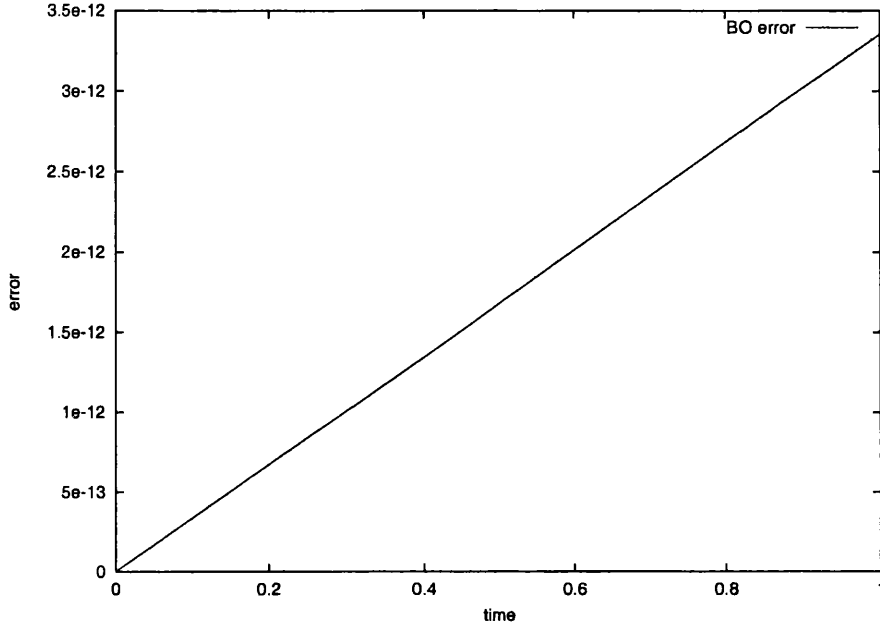
Figure 5.6: Error of test solution for BO.

5.5 APPENDIX F: Two Soliton Solution of the KdV Equation.

One of the canonical forms of the KdV is given by

$$\eta_t + 6\eta\eta_x + \eta_{xxx} = 0, \tag{F-1}$$

and this admits traveling soliton solutions. A single solitary wave has the form

$$\eta = \frac{1}{2}\alpha^2 \text{sech}^2 \frac{\Theta - \Theta_0}{2}, \tag{F-2}$$

where

$$\Theta = \alpha x - \alpha^3 t. \tag{F-3}$$

Here α and Θ_0 are parameters. The peak of the soliton is at $\alpha^2/2$, it moves with velocity α^2 and has position $\Theta_0/\alpha + \alpha^2 t$. Whitham [1974] derives the analytic result for n traveling solitons interacting. The result for two solitons is

$$\frac{\eta}{2} = \frac{\alpha_1^2 f_1 + \alpha_2^2 f_2 + 2(\alpha_2 - \alpha_1)^2 f_1 f_2 + \{(\alpha_2 - \alpha_1)/(\alpha_2 + \alpha_1)\}^2 (\alpha_2^2 f_1^2 f_2 + \alpha_1^2 f_1 f_2^2)}{(1 + f_1 + f_2 + \{(\alpha_2 - \alpha_1)/(\alpha_2 + \alpha_1)\}^2 f_1 f_2)^2},$$

(F-4)

where

$$f_j = \exp\{-\alpha_j \left(x - \frac{\Theta_j}{\alpha_j} \right) + \alpha_j^3 t\}.$$

(F-5)

Again α_j and Θ_j are parameters.

5.6   APPENDIX G: The BO Equation with one-soliton solution.

The BO equation is an integro-differential equation of the form

$$u_t + cu_x + uu_x + \mathbb{H}(u_{xx}) = 0, \tag{G-1}$$

where c is a translation parameter (speed of background flow) and $\mathbb{H}$ is the Hilbert operator defined by

$$\mathbb{H}(u(x,t)) = \frac{1}{\pi} \int \frac{u(y,t)}{y-x} dy. \tag{G-2}$$

The integral is a Cauchy Principal Value and in terms of Fourier integrals this can be written

$$\mathbb{H}(u(x,t)) = \frac{1}{2\pi} \int_{-\infty}^{\infty} i \operatorname{sgn}(k)\, \hat{u}(k,t)\, e^{ikx} dk. \tag{G-3}$$

The BDA operator is defined, again in terms of a Cauchy Principal Value

$$\mathbb{B}(u(x,t)) = \frac{1}{\pi} \frac{\partial}{\partial x} \int \frac{u(y,t)}{y-x} dy, \tag{G-4}$$

and thus the BO equation and BDA equation can be interchanged as

$$\mathbb{H}(u_{xx}) = -\mathbb{B}(u_x). \tag{G-5}$$

This is easier to see when considered in Fourier space. Equation (G-1) admits stationary, solitary waves of the form, Drazin and Johnson [1989]

$$u = \frac{4c}{1 + c^2 x^2}. \tag{G-6}$$

Chapter 6

The Weakly Nonlinear Response: Results.

6.1 Introduction

The results of the numerical integrations of (4.54) are presented in the next five sections for a wide range of the parameter space (Δ, κ). The parameter space is two dimensional for fixed μ, this is illustrated in figures (6.1a), (6.1b) and (6.1c). The plot shows three integrations for $\mu = 0.01, 0.05, 0.1$ but with $\Delta = -0.2$ and $\kappa = 3$. It can be seen that qualitatively the behaviors are the same, however note that variations in μ will cause changes in the absolute strength of the vortex Γ and the flow speed U.

Note also that $\kappa > 0$ always, as this near-resonant study requires that the vortex be traveling at a velocity close to the maximum group velocity of the waves and in particular the waves can only travel in one direction, namely with shallow water to their right. There is no reason however why (4.54) cannot be solved for negative

(a)

(b)

(c)
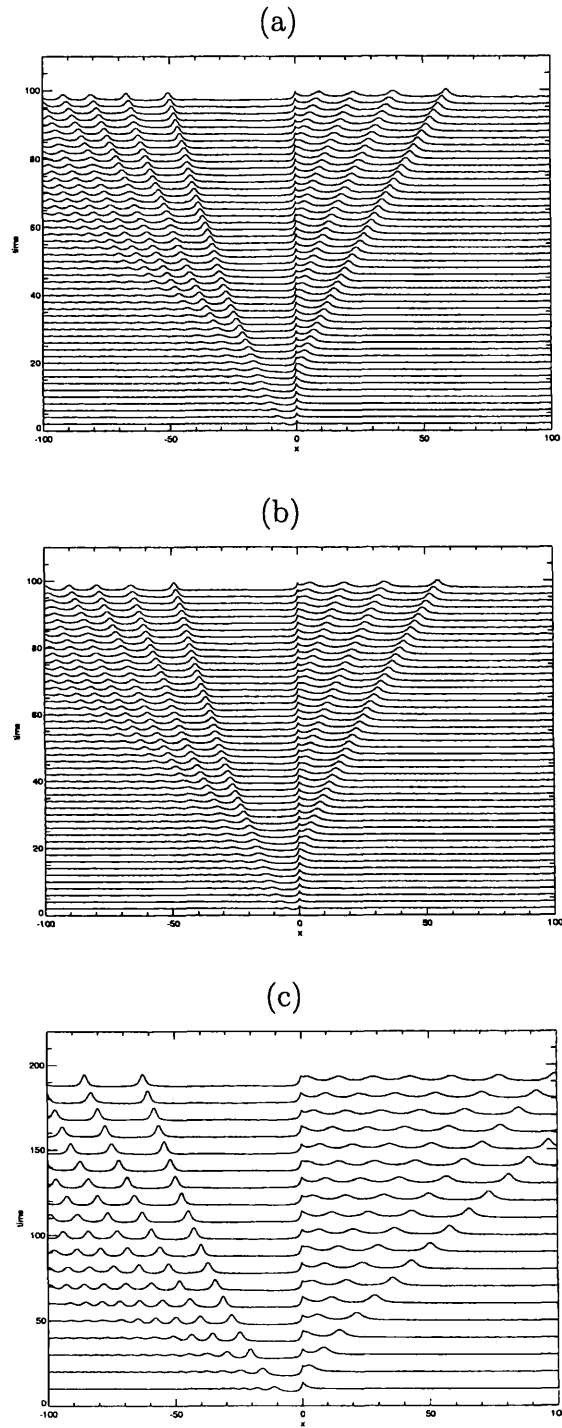
Figure 6.1: Evolution of Θ for (a) $\mu = 0.01$, (b) $\mu = 0.05$ and (c) $\mu = 0.1$ with $\Delta = -0.2$ and $\kappa = 3$.

κ and this would correspond to a vortex that is stationary in a stream of strength $U < 0$, in other words from left to right. The behavior for negative κ would therefore fall into the linear, subcritical regime as was described in chapter 3 and is not shown here.

As the chosen value of μ only makes a difference to the boundaries of the different flow regimes and not to the qualitative behavior of the flow evolution, its value will be fixed at $\mu = 0.1$ from here on.

6.2 Small κ Behavior.

Firstly the small κ (i.e. weak forcing) behavior is shown in figures (6.2) - (6.4) these being the nonlinear equivalents of the earlier linear results of chapter 3. The behavior is not greatly changed in this regime by the addition of weak nonlinearity, except exactly at resonance. For Δ away from zero the results are either subcritical ($\Delta < 0$) or supercritical ($\Delta > 0$) and the agreement with linear theory is very precise. The error in figures (6.2b) - (6.4b) is calculated with the usual error measure defined by (5.58) i.e.

$$E(t) = \sqrt{\frac{\sum_{i=0}^{n-1} \left(\Theta_i(t) - \eta_i(t) \right)^2}{n}}, \qquad (6.1)$$

where Θ_i are the values of the interface calculated from the weakly nonlinear evolution and η_i are the FFT inversions of (3.135) for the same parameter values Δ, κ.

The supercritical example figure (6.2a) consists of an isolated wave that propagates with the vortex. Also there is a transient, dispersive wavetrain which is rapidly washed downstream. It will be seen later that a larger value of κ produces a larger isolated disturbance at the vortex but the general behavior is still pure supercritical. Waves of a much higher wavenumber are also seen and this is due to the weakly

nonlinear dispersion relation having no upper bound. Since the forcing is so weak the amplitude has had to be scaled up by a factor of 60000.

On the subcritical side the solutions are analogous to the small-amplitude subcritical solutions of Clarke and Johnson [1996a], an example is shown in figure (6.3a), this graph has been scaled by 30000. An isolated wave appears at the vortex with a weakly nonlinear, quasi-steady, lee wave train propagating downstream. Waves can travel upstream and these can be seen as a very faint disturbance upstream of the vortex. Linear theory shows that these upstream waves do eventually decay to zero but at stronger forcing, weakly nonlinear effects become important and the subcritical regime must be altered.

Figure (6.4) shows a weakly forced resonant example (scaled by 30000) and it is very similar to that of the linear case with the growth of the solution at the vortex and the distinctive long, trailing lee waves. Dispersion acts to continually stretch out the wavetrain with the longest wave remaining the fastest (seen just downstream of the vortex). One difference with the added nonlinearity is the allowance of upstream disturbances. In the linear case the fastest wave (the longest) had a maximum speed equal to the vortex propagation speed and so couldn't pass upstream of the vortex. Energy could not escape upstream and consequently the linear approximation broke down. In this case nonlinearity becomes important and allows the energy to escape in some form, since nonlinearity allows the waves to have a speed greater than the linear long wave speed.

(a)

(b)
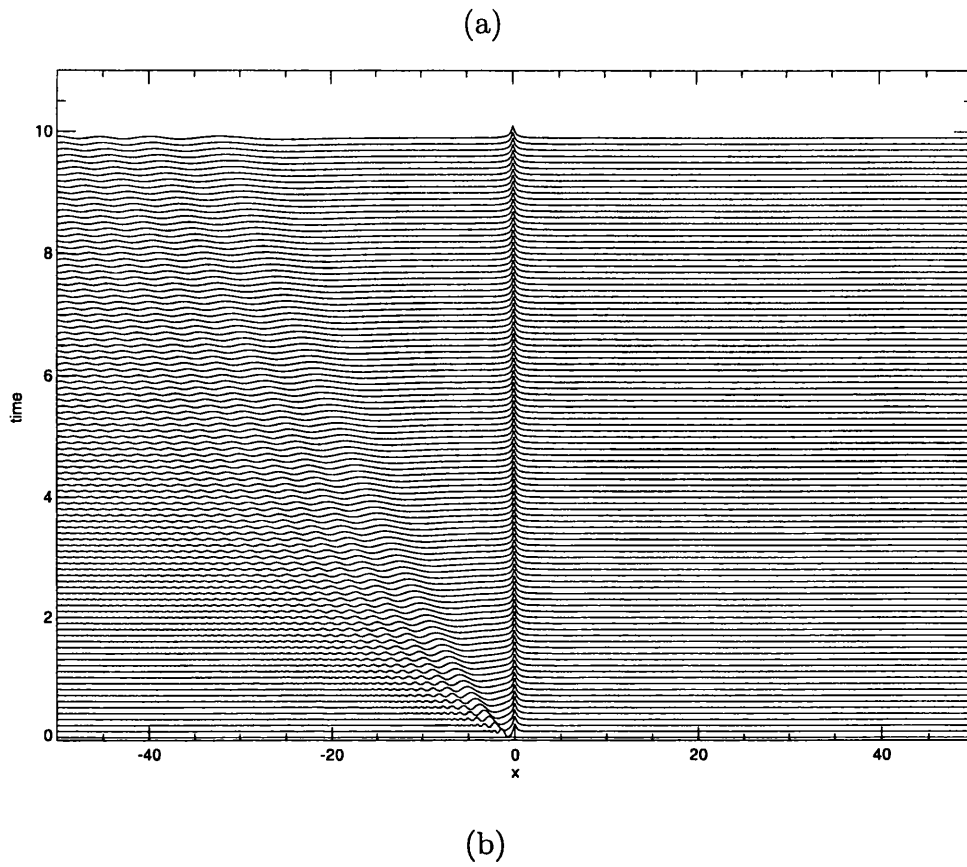
Figure 6.2: (a) A supercritical example with $\Delta = 2$ and $\kappa = 0.01$ and (b) the error when compared with the equivalent linear response.

(a)
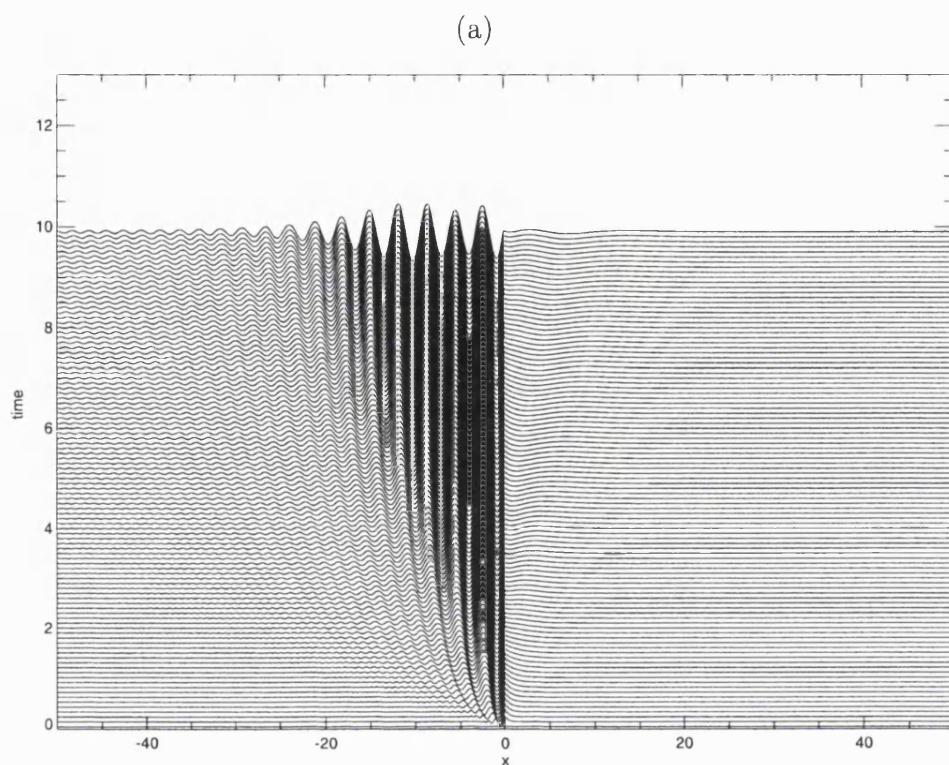
(b)
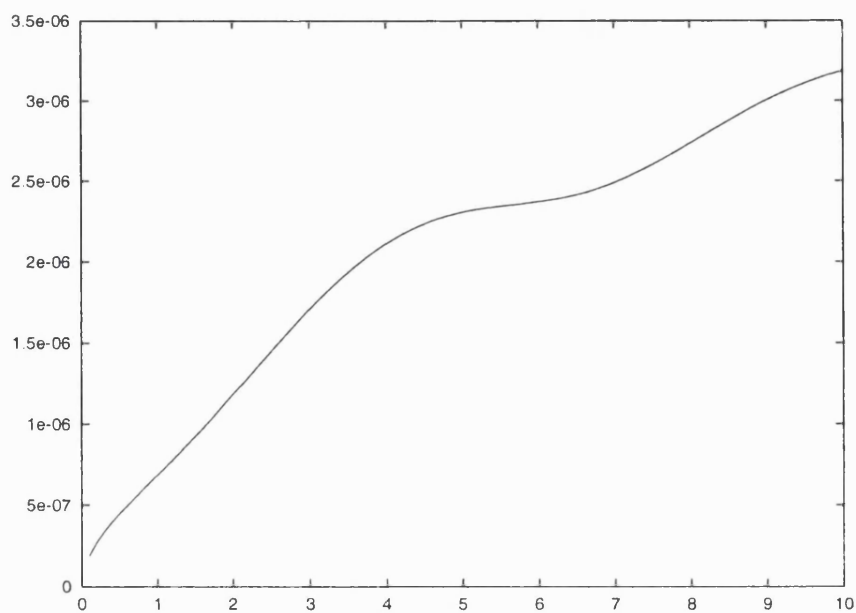
Figure 6.3: (a) A subcritical example with $\Delta = -2$ and $\kappa = 0.01$ and (b) the error when compared with the equivalent linear response.

(a)

(b)
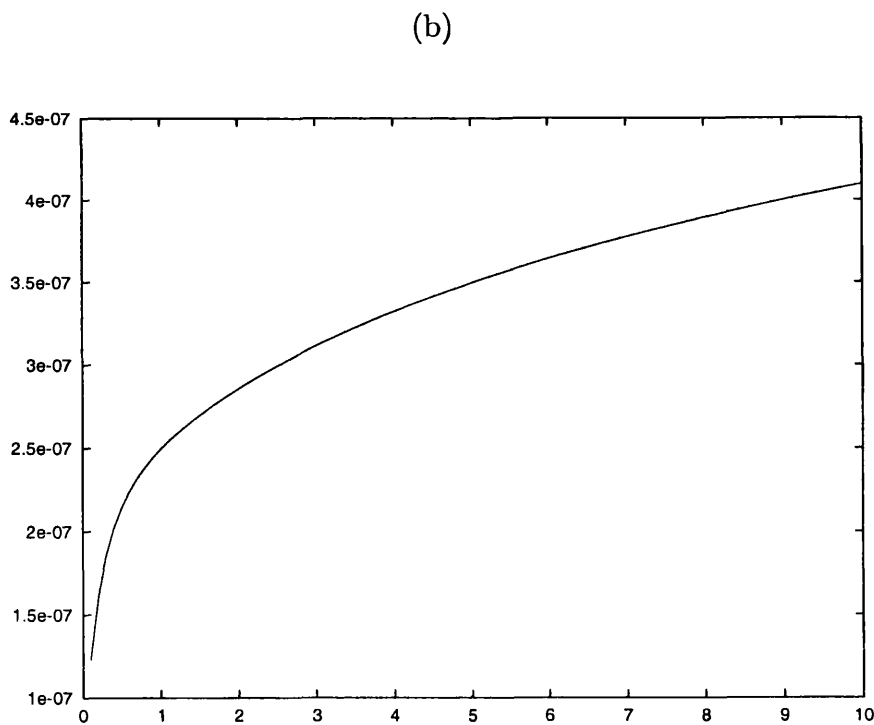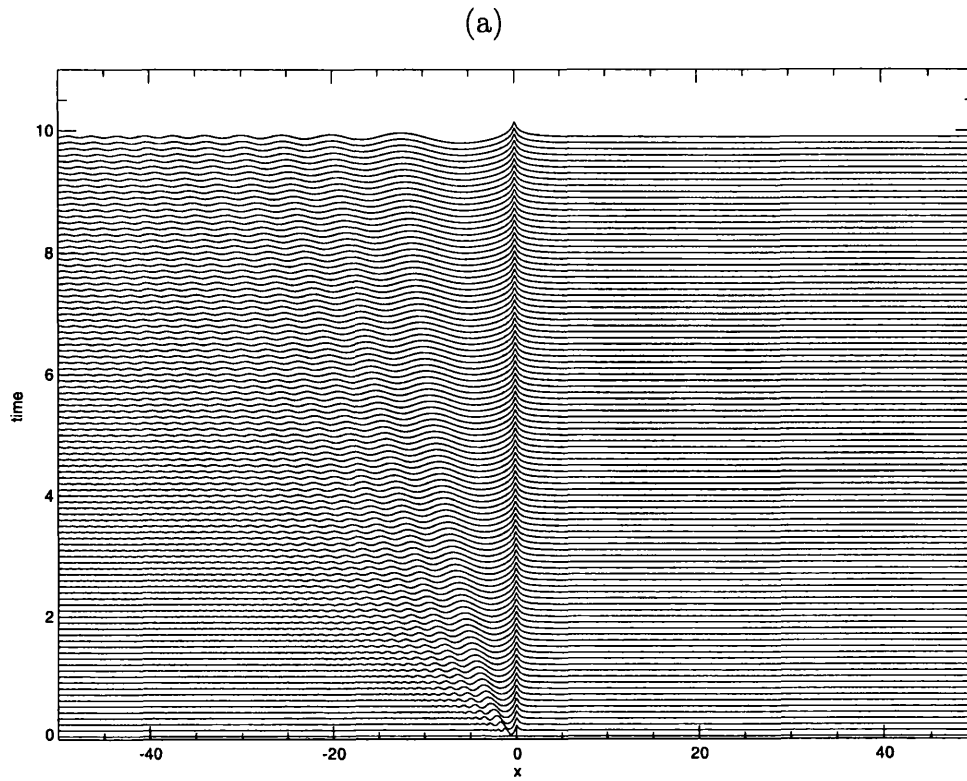
Figure 6.4: (a) A resonant example with $\Delta = 0$ and $\kappa = 0.01$ and (b) the error when compared with the equivalent linear response.

(a)

(b)
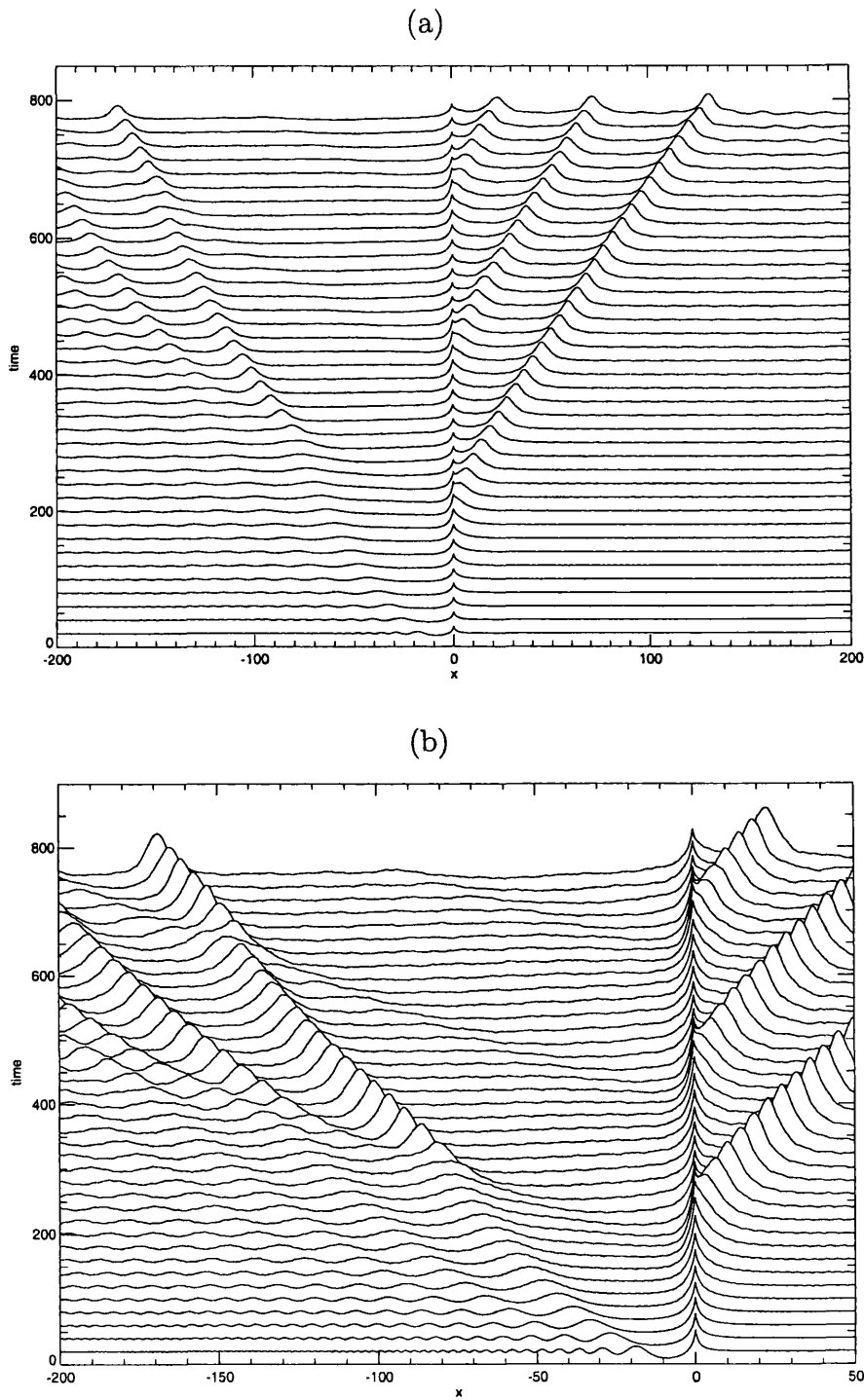
Figure 6.5: At stronger forcing the nonlinear resonant behavior is modified. (a) $\Delta = 0$, $\kappa = 1.8$ scaled by 30, (b) close up of downstream waves, scaled by 100.

6.3 Resonant Examples with Stronger Forcing.

The flow shown in figure (6.5) is for $\Delta = 0$, $\kappa = 1.8$ and it demonstrates new resonant behavior due to nonlinear effects, this is analogous to the flow region **C** in Clarke and Johnson [1996b]. Initially, as in the linear case, the response at the vortex grows with time because the long waves cannot escape upstream and energy accumulates at the vortex. In the linear case this marks the breakdown of linear theory but after a certain time (approximately $\tau = 200$) nonlinear effects come into play and a soliton-like wave is released upstream. The presence of solitons indicate a balance between nonlinearity and dispersion and hence the amplitude of the response near the vortex builds up until the nonlinear effects become as important as dispersion and then a soliton is released. This is coupled with a release of small amplitude, dispersive waves downstream and the response at the vortex diminishes and the process begins again. Figure (6.6) shows a close up of this process for $\Delta = 0$, $\kappa = 2.3$.

The interface on the upstream side of the vortex is always greater than or equal to zero (indicating weak blocking of the flow) and so the step function in the nonlinear part of (4.54) will equal one and so away from the vortex with $\chi > 0$, (4.54) becomes

$$\Theta_\tau + \Theta\Theta_\chi - \mathbb{B}(\Theta_\chi) = 0. \tag{6.2}$$

This has soliton solutions of the form (Benjamin [1967], Davies and Acrivos [1967]),

$$\Theta = \frac{1}{1 + (\chi - c\tau)^2}. \tag{6.3}$$

From figure (6.5) an estimate of the speed c of the first soliton is 5.

Bearing in mind that in the limit $\kappa \to 0$ the weakly nonlinear behavior returns to the linear case one question to ask is whether the modified resonant case occurs for all
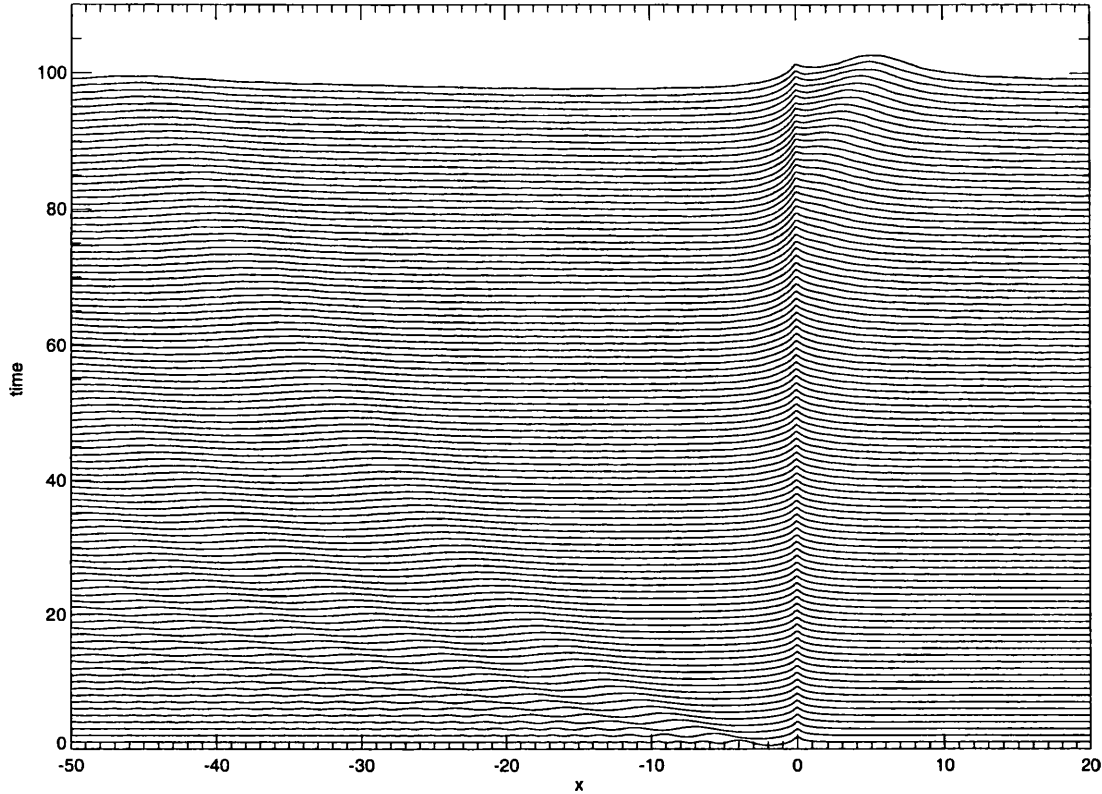
Figure 6.6: A closer view of the nonlinear resonant behavior. $\Delta = 0$, $\kappa = 2.3$

finite values of κ i.e. given sufficient time, does the production of upstream traveling solitons always occur? It is argued that since the response at the vortex is always growing with time, eventually nonlinear effects will balance dispersion and a soliton will release upstream. The growth at the vortex is shown in figure (6.7) which is a plot of $\mathrm{Log}(\tau)$ against $\mathrm{Log}(\Theta(0, \tau))$ for $\kappa = 0.5$. At this strength of forcing it was not possible to integrate equation (4.54) numerically for a sufficiently long time to see a soliton emerging, however it is believed that this will eventually be the case as the growth in amplitude near the vortex is quite apparent.
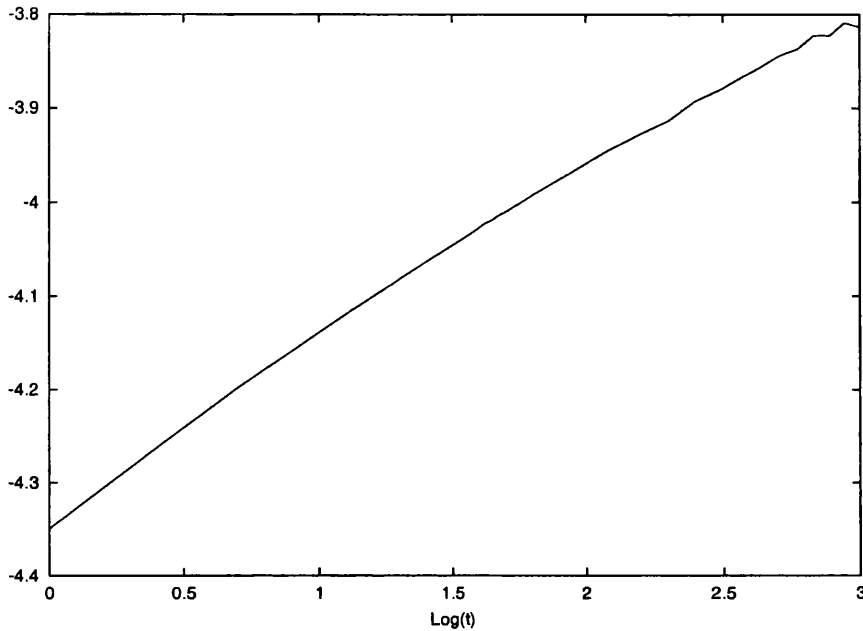
Figure 6.7: A plot of Log(τ) against Log($\Theta(0, \tau)$) for $\Delta = 0$, $\kappa = 0.5$.

6.4 Near-resonant (Subcritical) Solutions: blocking.

Figure (6.8) shows a near resonant solution for $\Delta = -0.3$, $\kappa = 3$. At these values the response is in the blocked subcritical regime which is characterised by an intial disturbance which is carried downstream as a train of separated solitary waves. The response at the vortex increases as for the resonant case until a solitary wave is released upstream (see figure (6.8) $\tau = 30$), however there is no equivalent small-amplitude wave response downstream as this occurs. Instead a shelf forms downstream indicating that the energy balance is restored through blocking, Stern [1991], rather than transient wave generation. Since there is now an imbalance of contour amplitudes upstream and downstream of the vortex the next upstream wave is ejected much sooner than for the resonant case and by $\tau = 50$ it has broken away creating

stronger blocking of the flow. This process repeats and the flow becomes steady and flat downstream with an unsteady, blocked response upstream. It is thought that this will remain the case for larger times as by $\tau = 190$ the upstream waves have reached a constant amplitude and are not decaying, indeed this would indicate a hydraulic solution that jumps from subcritical upstream to supercritical downstream which can't be so.

Figure (6.9) shows a similar solution with $\Delta = -0.5$ and $\kappa = 2.9$ so this is further from resonance but the forcing is approximately the same. It also has been integrated for a shorter time but it still clearly shows the mechanism for blocking of the flow. After the initial transient disturbance has propagated downstream the fluid gradually builds up on the upstream side of the vortex and reduces on the downstream side, this can't be sustained smoothly and a wave is released upstream. The energy loss is compensated for with a reduction in amplitude downstream and the process repeats but in a shorter time than previously, resulting in continuous generation of nonlinear waves upstream and a flat, supercritical response downstream.

This behavior is analogous to that described as region **B** in Clarke and Johnson [1996b], however overturning is never going to occur in the weakly nonlinear limit studied here.

6.5 Transition (Subcritical) Solutions: steady downstream wake.

The downstream response shown in figure (6.9) shows a wave packet of solitary waves and these can be seen to be slowing down. A natural inference from this observation is that there should be a region of (Δ, κ) space where the downstream
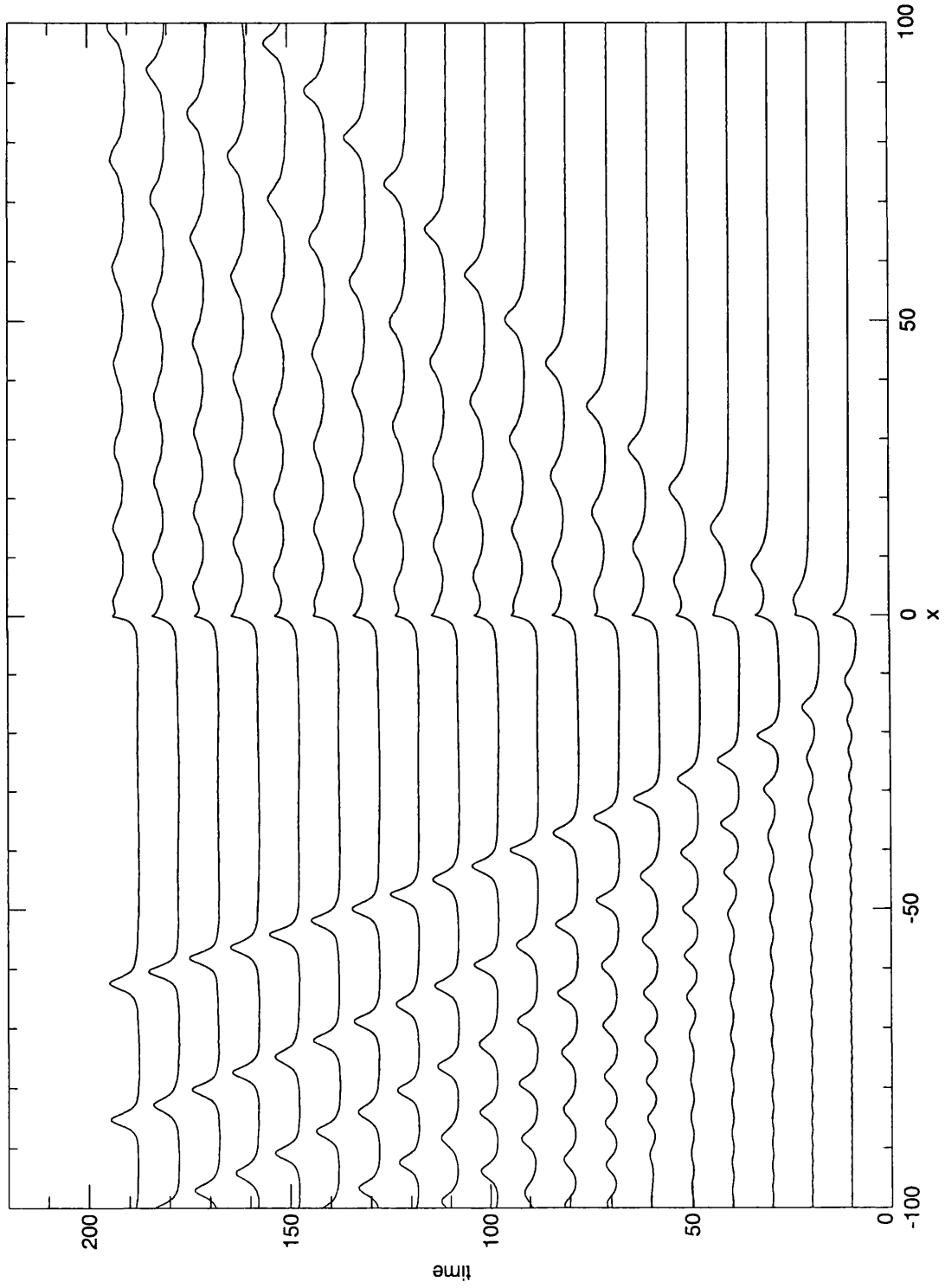
Figure 6.8: $\Delta = -0.3$ and $\kappa = 3$.
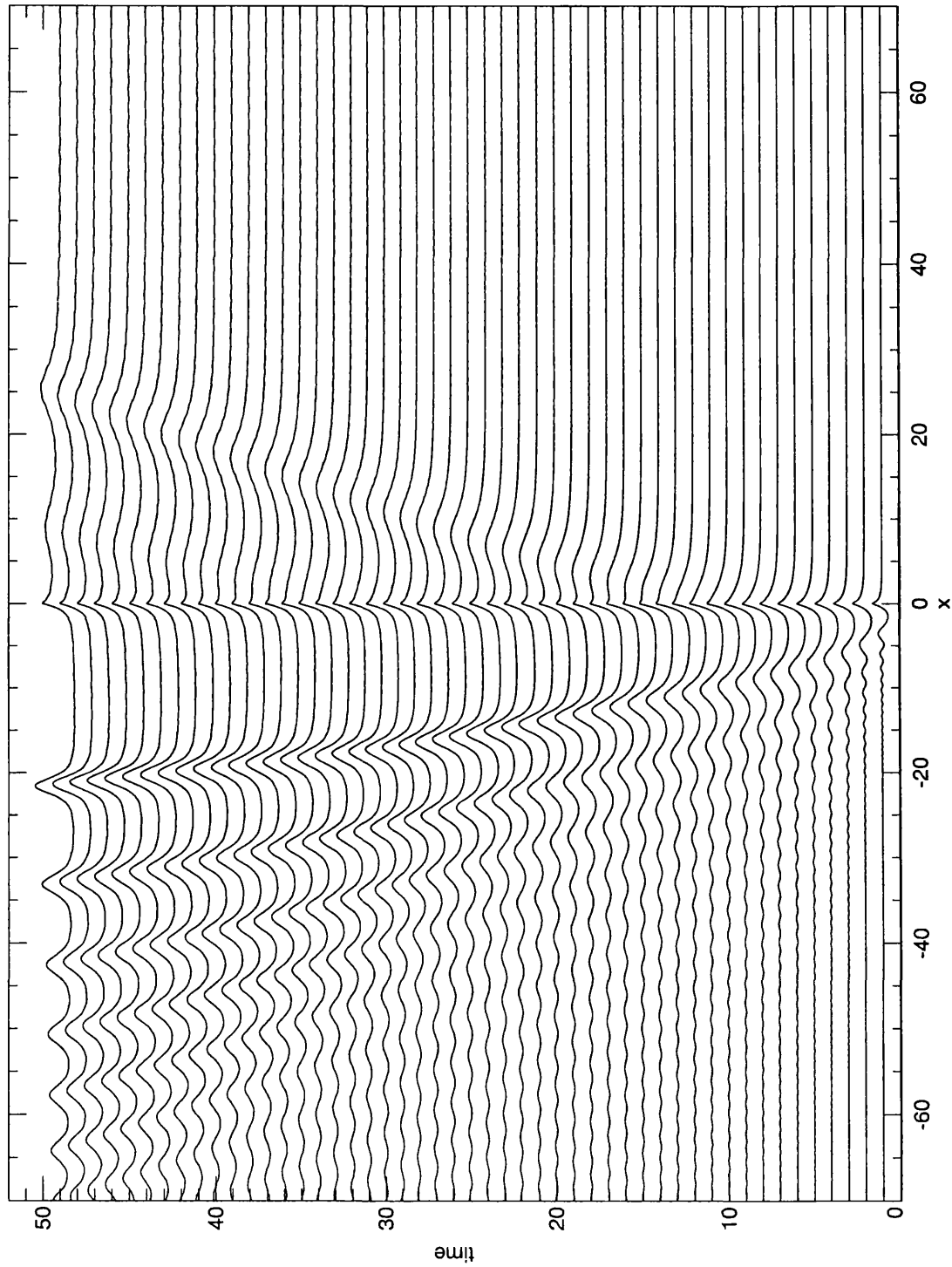
Figure 6.9: $\Delta = -0.5$ and $\kappa = 2.9$.

response becomes steady and a standing wave is formed. This is certainly the case although the region in the parameter space is very narrow. Figure (6.10) shows one such example for $\Delta = -0.8$ and $\kappa = 2.9$, the initial conditions rapidly disperse into a train of solitary waves downstream of the vortex leaving a peaked, isolated disturbance at the vortex. The downstream side of this is the flat, smaller amplitude fluid and upstream the fluid is blocked and unsteady due to the nonlinear, upstream traveling waves that are generated by the vortex. The energy balance is being achieved through blocking as before but now the initial conditions are such that the downstream solitary wave train can stand in the free stream. As the solitary waves separate they speed up and increase in magnitude until finding a steady form. The lead wave is traveling the fastest in this frame of reference. For this value of (Δ, κ) the lead solitary wave has become steady by $\tau = 60$ with the other, slower waves following suit so that by the end of the experiment $\tau = 250$ there is a whole wavetrain of steadily propagating solitary waves. It is believed that they will remain in this configuration for all time, although that cannot be demonstrated here due to numerical limitations.

This behavior is analogous to that described as **T** in Clarke and Johnson [1996b] but it is interesting to note that it occurs on the other side of the blocked regime. In other words the transition regime described here is a transition between subcritical and blocked, subcritical flow. The blocked, subcritical flow then becomes resonant nearer $\Delta = 0$ whereas in Clarke and Johnson [1996b] the blocked, subcritical flows go through a steady, transition regime and then approach criticality as $\Delta \rightarrow 0$.
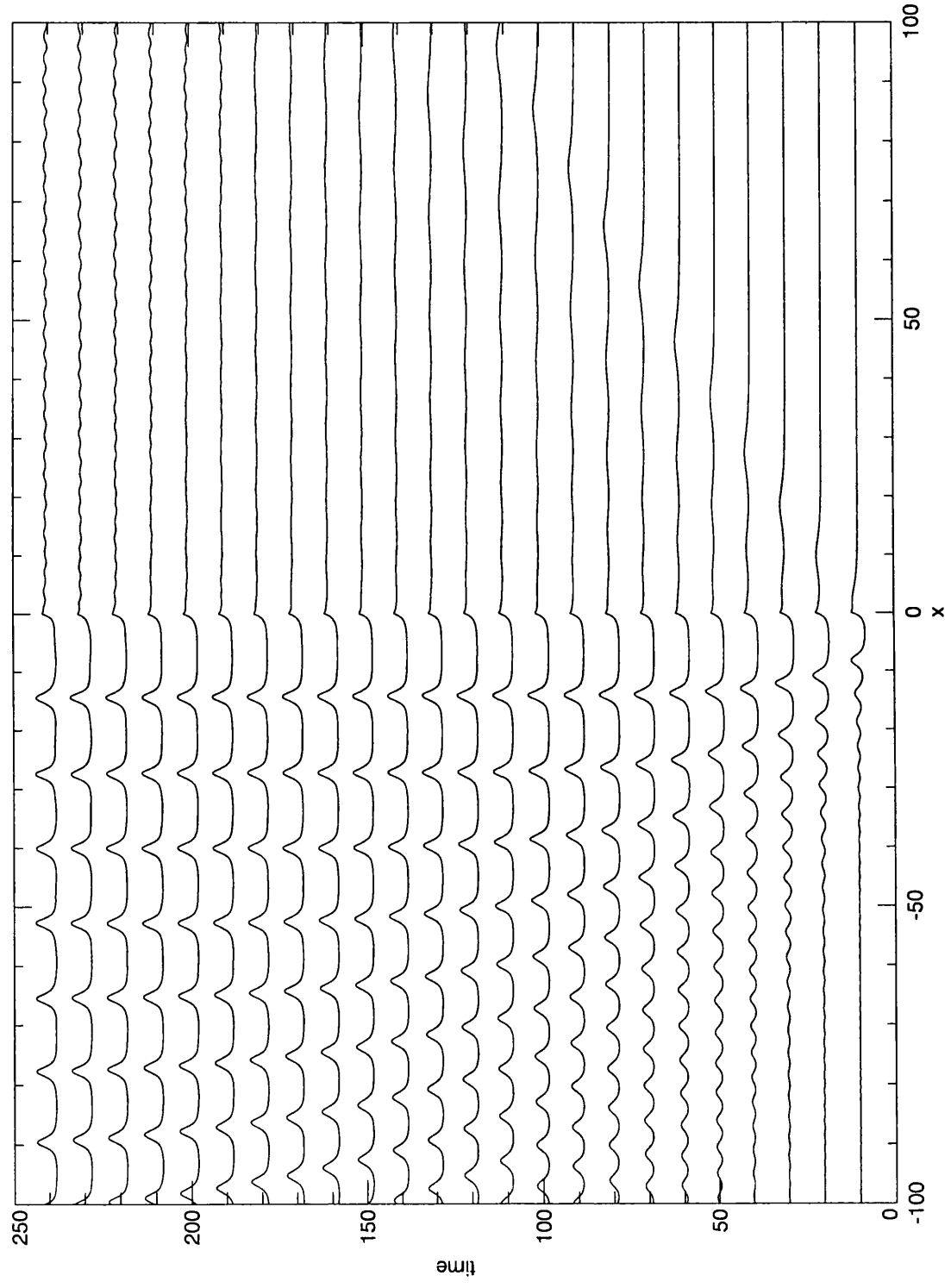
Figure 6.10: $\Delta = -0.8$ and $\kappa = 2.9$, scaled by 2.

6.6 Near-resonant (Supercritical) Solutions: weak blocking.

The near-resonant response in the supercritical region is also modified with the inclusion of weak nonlinearity although for a very small region of (Δ, κ) space $(\Delta > 0)$. Figure (6.11) shows a near-resonant supercritical solution for $\Delta = 0.24$ and $\kappa = 3$ for times up to $\tau = 390$. Again the initial disturbance is washed downstream as small amplitude transient waves and the flow becomes supercritical upstream and downstream of the vortex. However the response at the vortex grows with time as this is a near-resonant case and at time $\tau = 100 - 110$ a solitary wave breaks off and propagates upstream. There is also an associated transient wave response that propagates downstream accompanying each solitary wave breakaway, and a very weak blocking of the flow. This blocking can be more easily seen in figure (6.12) which shows a close-up of the mechanism for the values $\Delta = 0.1$ and $\kappa = 2.7$. The fluid either side of the upstream solitary wave is at different widths implying that as the wave travels upstream it is altering the width of the fluid and likewise the widths either side of the vortex are unequal. This can be also seen in figure (6.11) because the time taken between the first and second solitary wave release has got smaller implying that some extra energy is already at the vortex and thus the build up of fluid required to generate the upstream disturbance takes less time. This is again the case for the third time it occurs (c.$\tau = 290$). So for the near-resonant supercritical case the energy balance is achieved through both downstream wave generation and weak blocking of the flow. It is thought that this process will repeat indefinitely as the vortex is constrained to stay in the same position and has constant strength, (the case when the vortex is free to respond is addressed in chapters 7 and 8).

Figure (6.13) shows another close up for $\Delta = 0.1$ and $\kappa = 3$ for times up to $\tau = 100$. The blocking and downstream wave response can be seen clearly. Also note that the initial downstream wave response is very small and quickly decays whereas the subsequent downstream response due to the solitary wave generation grows in magnitude, slowing down and dispersing as it does so until it reaches some constant amplitude at the lead.
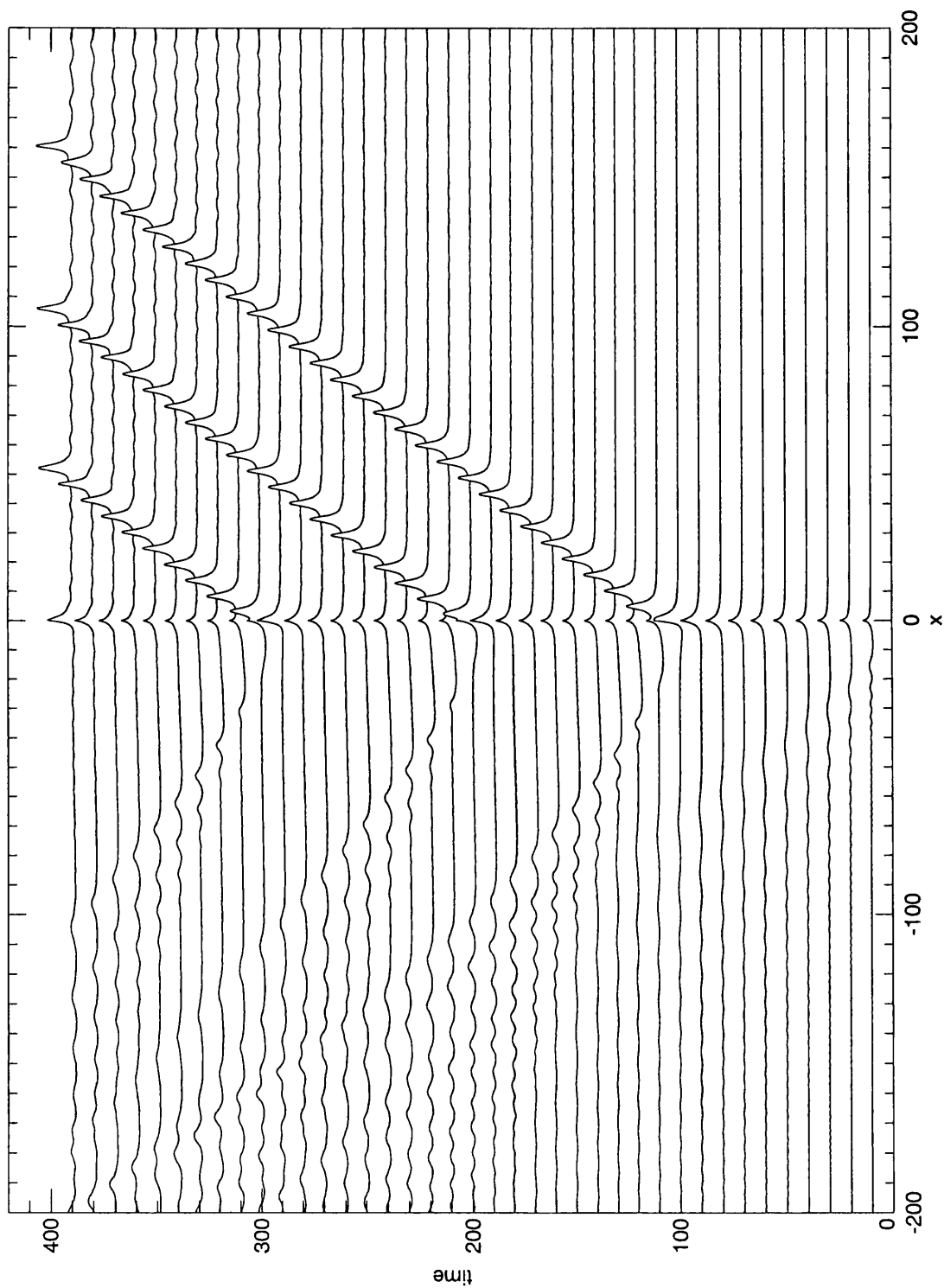
Figure 6.11: Supercritical response with $\Delta = 0.24$ and $\kappa = 3$, this plot has been scaled up by a factor 5.
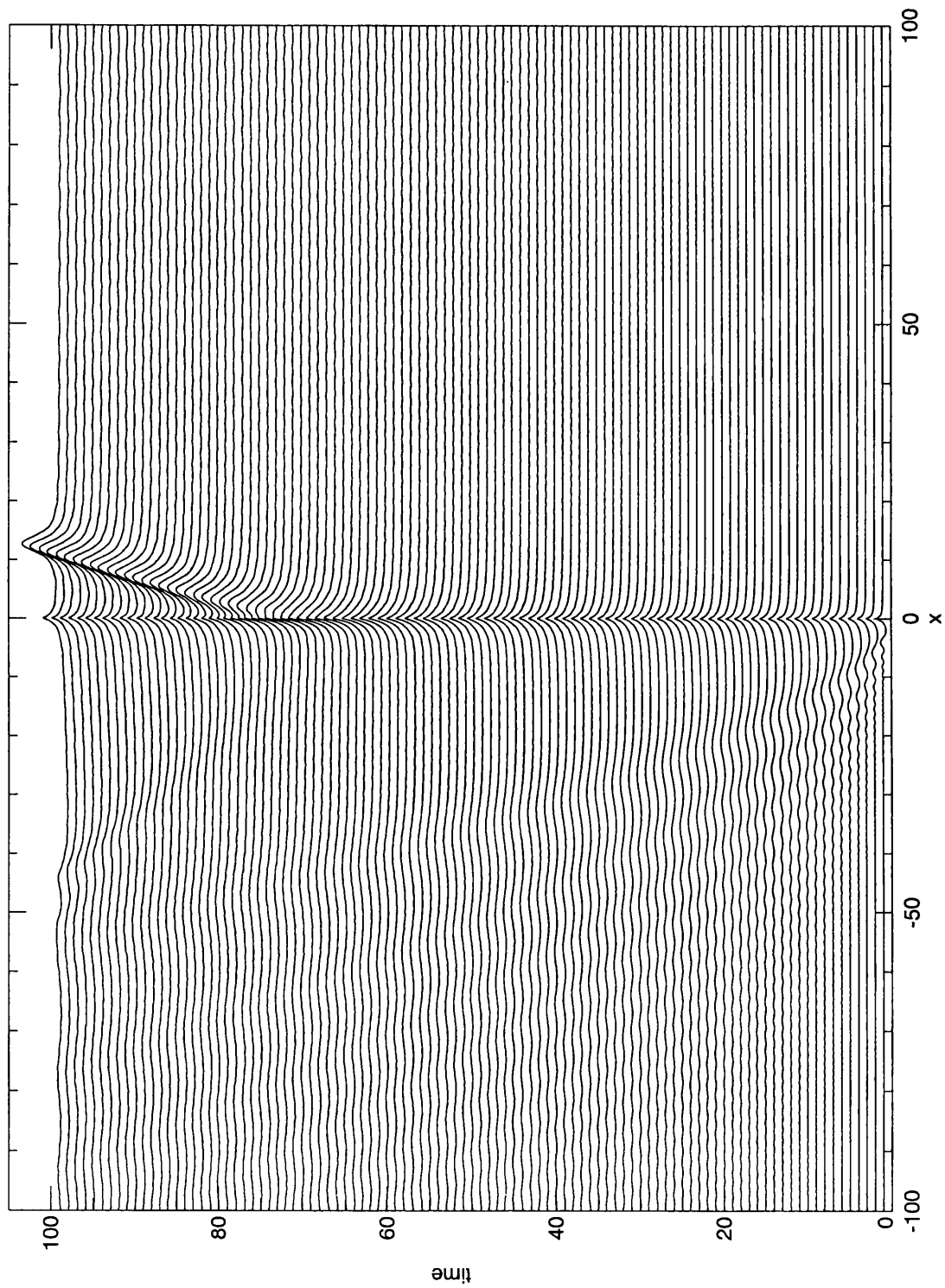
Figure 6.12: Supercritical response with $\Delta = 0.1$ and $\kappa = 2.7$, this plot has been scaled up by a factor 2.
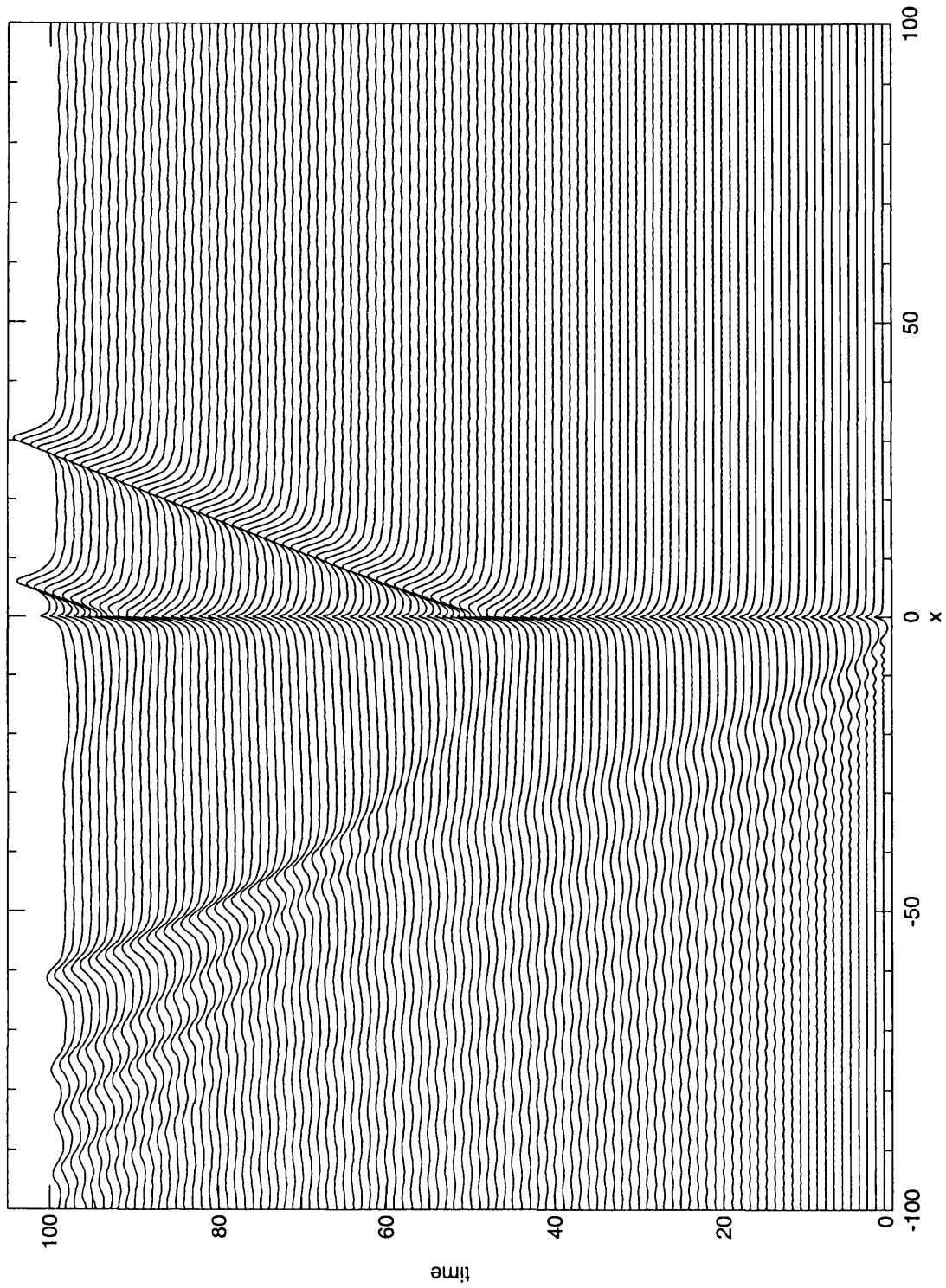
Figure 6.13: Supercritical response with $\Delta = 0.1$ and $\kappa = 3$, this plot has been scaled up by a factor 2.

6.7 Regime Diagram.

Figure (6.14) shows the regime diagram summarising all of the flow states found for the waves produces by the steadily propagating vortex. As the analysis is focused around the near-resonant case the sign of the forcing is always positive. There are then 5 regimes to consider.

1. **Downstream Propagating (D)**: This is the weakly nonlinear version of the subcritical solutions found in chapter 3 for $1 < U < 0$. It extends back for $\Delta < 0$ (as long as $\Delta \sim O(1)$) and so any vortex of strength κ can be placed at such a position that it will deliver a subcritical response such that there is a modulating, downstream-propagating wavetrain and a smaller amplitude, upstream propagating wavetrain. The error when comparing the weakly forced nonlinear version to the equivalent linear version is good but this is not necessarily so for a stronger forcing (at fixed Δ) as then the flow becomes

2. **Blocked, Steady Flow (BS)**: This is very thin region of (Δ, κ) space that is characterised with a steady wake downstream of the vortex, slight blocking of the flow at the vortex and small amplitude waves upstream of the vortex (that do not disturb the downstream wake). As the forcing becomes stronger (for a fixed Δ) the effects of nonlinearity come into play, weak blocking occurs to balance nonlinearity and dispersion but conditions are such that the downstream wake can stand in the free stream but Δ is still far enough away from resonance that the upstream waves are small and do not disturb matters downstream. As critically is approached (for fixed κ now) the flow changes into the

3. **Blocked, subcritical Flow (B)**: This is also characterised by a steady flow downstream and an unsteady wavetrain upstream but now the waves caused by the initial conditions are free to propagate away downstream, leaving a flat interface that is at a lower y position. The downstream waves in both BS and B are interesting as they are solitary-type waves whereas the upstream wavetrain is a 'spreading' wave more akin to a sum of sinusoids (as in the linear case). This is a larger sized region of the parameter space than BS and more easy to identify. Keeping κ fixed and increasing Δ more leads to the third regime

4. **Resonant flow (R)**: Approaching criticality ($\Delta = 0$) from a very small region either side is the modified, resonant regime. Here the extra effects of nonlinearity due to resonance come into play and manifest themselves as both blocking of the flow and the periodic release of upstream propagating, solitary waves. The amplitude of these solitary waves is large enough to preclude any steady state downstream as each release sends small amplitude, transient waves downstream that disturb the flat wake of the stronger initial transients. Naturally it is quite difficult to distinguish between the end of region B and the start of region R and so it has been drawn along the line $\Delta = 0$, however there is a small region of $\Delta < 0$ where the upstream waves are neither solitary nor strictly 'spreading' and there are very faint disturbances downstream. It is easier to see on the $\Delta > 0$ side and there is a very definite protrusion of the resonant regime into the supercritical regime, which is denoted by

5. **Downstream propagating (D)**: This is the weakly nonlinear equivalent of the supercritical flows of the linear response studied in chapter 3. The change between region R and region D is very abrupt although this is due in part to
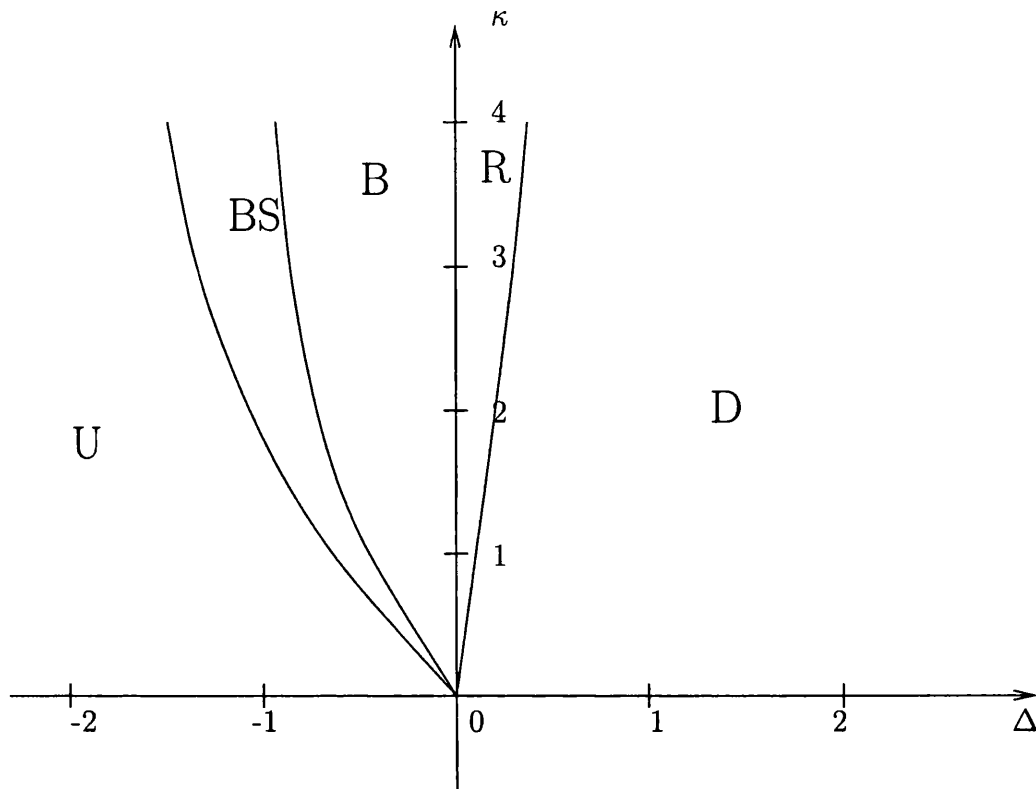
Figure 6.14: The regime diagram, D is the Downstream propagating, subcritical

flow, BS is the Blocked, Steady subcritical flow, B is the Blocked, subcritical flow,

R is the Resonant flow, U is the Upstream propagating, supercritical flow.

numerical limitations, figure (6.11) does not reveal itself to be belonging to

region R until $\tau > 100$. The supercritical regime is characterised by a steady

'hump' of fluid that doesn't grow in size and remains steadily propagating with

the vortex, this is the pseudoimage of the vortex in the interface. All other

transient waves are washed downstream and there is no blocking or upstream

influence.

6.8 Discussion.

The weakly nonlinear response of a PV front to a stationary vortex (in a particular frame of reference) has been examined in the long wave limit. The vortex was situated an $O(\mu^{1/2})$ distance from the wall and has a strength $O(\mu^{1/2})$. The action of its image on it induces a leading order drift $O(1)$ and so it can be made stationary if placed in a free stream of strength $U \sim O(1)$. The response of the interface is shown to be $O(\mu)$. If the vortex then travels at a speed matching the free topographic waves' maximum group velocity a resonant response occurs leading to the breakdown of linear theory and a need to consider nonlinear effects.

The technique used to derive the evolution equation for the interface is based on Grimshaw [1987], Clarke and Johnson [1996a] who consider resonant flow past long topographic features as a means of investigating the transition from hydraulic to unsteady, dispersive behavior and the validity of such solutions in the hydraulic limit. Clarke and Johnson [1996a] found that, even in the long obstacle limit, there was no smooth transitions between conjugate states (i.e. subcritical to supercritical etc) and therefore no hydraulic description. In this chapter the along shore length scale parameter μ is based on the topographic waves' wavelength which is assumed to be long and the point vortex forcing takes on the role of the coastal out-crop, with the major difference that in the limit $\mu \to 0$ the forcing becomes a δ-function. Due to the semi-infinite nature of the domain the governing evolution equation is a forced BDA-type, integro-differential equation and thus analytic progress is difficult. If the fluid domain were bounded above then the equation would be of the KdV type and thus, easier to integrate and it is thought that analytical techniques of the kind in Clarke and Johnson [2001], Johnson and Clarke [1999] could be used to derive expression for the nonlinear waves produced.

The nonlinear wave equation (4.54) is investigated numerically for a large range of the parameter space (Δ, κ) which are, respectively, the nondimensional detuning parameter representing closeness to resonance and the nondimensional strength of the vortex. The solution regime breaks into 5 regions:

1. Pure supercritical (U) and subcritical (D) flows: these are nonlinear equivalents to the linear solutions described in chapter 3,

2. Blocked, steady downstream subcritical flow (BS): which has weak blocking and small amplitude, upstream propagating waves, with a steady downstream train of waves,

3. Blocked subcritical flow (B): which is characterised by an unsteady, blocked upstream response and a steady, flat response downstream at a lower level to compensate for the blocking of upstream fluid,

4. Near-resonant flow (R): consisting of both pure resonant flow which has upstream solitary waves but the initial downstream transients cannot separate from the vortex and get stretched out due to dispersion and a weakly-blocked supercritical regime where, periodically, solitary waves propagate upstream along with downstream transient waves and a slight blocking of the fluid.

A somewhat unrealistic restriction was that of assuming a fixed vortex, in the next two chapters the feedback problem concerning the higher order motions of the vortex due to the motion of the interface are examined in both the linear and weakly nonlinear limits.

Chapter 7

Linear Wave-Vortex Interactions.

7.1 Introduction

As discussed in the previous chapter the fixed vortex condition is restrictive and unrealistic and although it may be true in the long term that the vortex will settle down to some steady state, the short term response needs to allow for secondary vortex motions. Fortunately, as discussed in the review chapter the equations of motion governing the evolution of the interface can be considered separately from that of the vortex motion, Bell [1989]. This is extremely useful as it allows the equations to be solved separately with the vortex reacting at each timestep to a fixed interface and then the interface reacting to the new vortex position. This chapter is concerned with the linear response, starting with a vortex which is placed initially an $O(1)$ distance from the wall (either on-shelf or off-shelf). This is followed by the linear response of a vortex placed very close to the wall. After deriving the equations of motion they are solved using a modified version of the numerical method described in 5 and conservation of momentum in the x direction is used as a test of

159
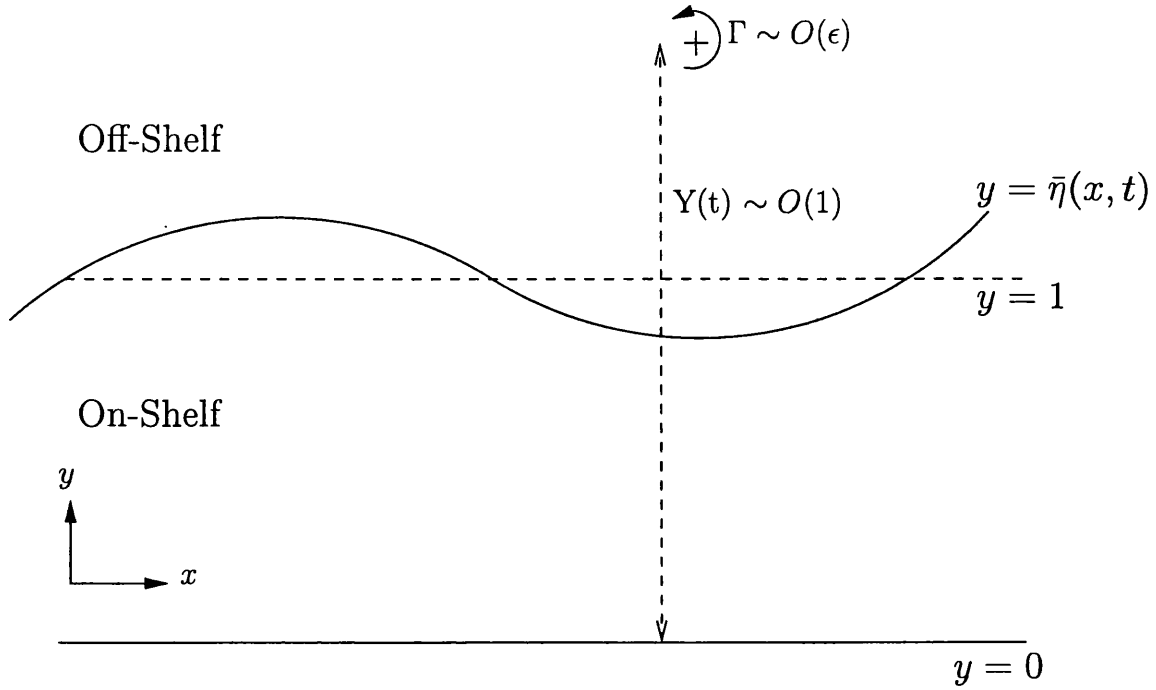
Figure 7.1: Schematic diagram for the linear feedback problem.

the accuracy of the results. A schematic diagram of the domain of interest is shown in figure (7.1).

In this section the higher order terms for the motion of the vortex center are included in the governing equations i.e. the vortex motion is computed according to the (small) velocity field owing to the presence of the topographic waves. There are two cases to consider.

7.2 $Y \sim O(1)$.

For $Y \sim O(1)$ the vortex is located an $O(1)$ distance from the wall and is also assumed to be $O(1)$ distance from the shelf, naturally it can be either on- or off-shelf initially but the present analysis assumes that it will not stray too close to

the shelf at $y = 1$ so as to avoid nonlinear effects at the step. The strength of the vortex is $O(\varepsilon)$ and in chapter 3 it was shown that this produces an $O(\varepsilon)$ response at the interface η that separates shallow and deep fluid. Previously it was also shown that an $O(\varepsilon)$ strength vortex positioned an $O(1)$ distance from a plane wall will experience an $O(\varepsilon)$ constant drift horizontally to the wall together with some higher order motions, it is the purpose of this chapter to investigate those motions.

7.2.1   Derivation of Governing Equations

The streamfunction is written

$$\psi = \varepsilon\psi_0, \tag{7.1}$$

where $\psi_0 \sim O(1)$. The vortex is located at $(X(t), Y(t))$ where

$$X = \varepsilon X_1(t) + \ldots, \tag{7.2}$$

$$Y = y_0 + \varepsilon Y_1(t) + \ldots. \tag{7.3}$$

At $t = 0$ the initial position is $(0, y_0)$ and so

$$X_1(0) = 0, \tag{7.4}$$

$$Y_1(0) = 0. \tag{7.5}$$

The streamfunction ψ_0 is separated into contributions from the vortex, denoted Ψ and secondary motions, ϕ and is written

$$\psi_0 = \phi + \Psi. \tag{7.6}$$

The forcing term $\Psi(x, y, t)$ now contains the undetermined coordinates for the vortex center

$$\Psi = \frac{\Gamma}{4\pi} \log \left(\frac{(x - X(t))^2 + (y - Y(t))^2}{(x - X(t))^2 + (y + Y(t))^2} \right). \tag{7.7}$$

Here, the vortex strength is $\varepsilon\Gamma$ and $\Gamma \sim O(1)$.

The governing equations, boundary conditions and initial conditions are identical to (3.47) - (3.52) and standard Fourier analysis reveals that the transform $\hat{\phi}$ of the secondary motions $\phi(x, y, t)$ are given by

$$\hat{\phi} = \begin{cases} 2A(t)\sinh(ky) & 0 < y < 1, \\ 2A(t)\sinh(k)e^{|k|(1-y)} & 1 < y, \end{cases} \tag{7.8}$$

for some undetermined function $A(t)$. The second of the jump conditions given by (3.51) determines an evolution equation for the unknown function $A(t)$,

$$\frac{dA}{dt} + i\omega A = -\frac{i\hat{\Psi}(k, 1)}{2} e^{-ikX(t) - |k|}. \tag{7.9}$$

Now $\hat{\Psi}(k, y)$ is defined

$$\hat{\Psi}(k, y) = \begin{cases} -\frac{\Gamma}{k}\sinh(ky)e^{-|k|Y(t)} & 0 < y < Y(t), \\ \\ -\frac{\Gamma}{k}\sinh(kY(t))e^{-|k|y} & Y(t) < y. \end{cases} \tag{7.10}$$

Equation (3.44) gives the higher order vortex motions as

$$\frac{dX_1}{dt} = -\phi_y(X, Y) + \frac{\Gamma}{4\pi y_0}, \tag{7.11}$$

$$\frac{dY_1}{dt} = \phi_x(X, Y). \tag{7.12}$$

The linearised kinematic condition relates the cross-step velocity at $y = 1$ to the interface displacement $\bar{\eta}$ (see diagram) through

$$\frac{\partial}{\partial t}\bar{\eta}(x,t) = \frac{\partial}{\partial x}\psi_0(x,1,t). \qquad (7.13)$$

Now $\bar{\eta} = 1 + \varepsilon\eta(x,t)$ and writing (7.13) in Fourier space gives

$$\varepsilon\hat{\eta}_t = ik\hat{\psi}_0(k,1,t), \qquad (7.14)$$

which can be written

$$\hat{\eta}_t = ik(\hat{\phi}(k,1,t) + \hat{\Psi}(k,1,t)e^{-ikX(t)}), \qquad (7.15)$$

where $\hat{\phi}$ is given by (7.8) and $\hat{\Psi}$ by (7.10).

Progress can be made by numerically integrating this system of equations. The algorithm used to do this is the following.

Suppose at time $t = t_i$ the functions A_i, $(\phi_x)_i$, $(\phi_y)_i$ and (X_i, Y_i) are known and let the inverse Fourier transform be denoted by $\mathcal{F}^{-1}$,

1. Time-step forward (7.11) & (7.12) from $(X_1, Y_1)_i \rightarrow (X_1, Y_1)_{i+1}$ and calculate $(X, Y)_{i+1}$.

2. Time-step forward (7.9) from $A_i \rightarrow A_{i+1}$.

3. Calculate $\hat{\phi}(k,1)_{i+1}$ and $\hat{\Psi}(k,1)_{i+1}e^{-ikX_{i+1}}$.

4. Time-step forward (7.15) from $\hat{\eta}_i \rightarrow \hat{\eta}_{i+1}$.

5. Using (7.8) calculate $\mathcal{F}^{-1}(ik\hat{\phi})_{i+1}$ and $\mathcal{F}^{-1}(\hat{\phi}_y)_{i+1}$ at $(X, Y)_{i+1}$.

6. Now have known functions A_{i+1}, $(\phi_x)_{i+1}$, $(\phi_y)_{i+1}$ and $(X, Y)_{i+1}$ at time t_{i+1} so repeat.

The time-stepping for (7.9) is done using the combinations of Adam's methods as described in chapter 5. Here the linear part at time-level ndt, L_n, is given by

$$L_n = -i \sinh (k) e^{-|k|}, \qquad (7.16)$$

which is recognised as the time-independent dispersion relation ω multiplied by $-i$. Referring back to chapter 5 in which it is noted that the nonlinear part N_n can also include any forcing terms of the equation being integrated, the 'nonlinear' term for these integrations would only consist of the forcing term of (7.9), which is

$$N_n = -\frac{i \hat{\Psi}(k, 1)}{2} e^{-ikX(t)-|k|}. \qquad (7.17)$$

The equations describing the vortex motions (7.11) & (7.12) and the linearised kinematic condition at the interface (7.15) are all integrated using the AB4 method (see chapter 5), this is fourth-order accurate and also A-stable. So with minimal effort the method used to calculate the weakly nonlinear response can be manipulated to solve the linear, vortex-wave feedback response.

7.2.2 Momentum Conservation

Based on global conservation arguments of momentum and energy, Bell [1989] derives an expression for the cross-stream velocity (i.e. perpendicular to the PV interface) of a point vortex in a shear layer. In doing so he derives an argument showing that the angular momentum in the x direction is conserved, not only in the linear case but in the fully nonlinear case too. As was pointed out in previous chapters his study considers the motion of a vortex in a shear layer responding to interfacial vorticity waves that separate regions of constant but differing PV. The system studied here should also obey the same conservation law and that even though the

equations governing the secondary motions of the vortex have already been found by different means, the conservation of momentum in the x-direction can be used as an indicator of the accuracy of the results.

The momentum P in the x direction is given by the integral over space of the product of PV ζ and y, Bell [1989],

$$P = \int \zeta \, y \, \mathrm{d}A. \tag{7.18}$$

The momentum is made up of a contribution due to the vortex and contributions due to the waves, i.e.

$$P(t) = \int y \varepsilon \Gamma \delta(x - X(t), y - Y(t)) \, \mathrm{d}A + \int y \nabla^2 \psi \, \mathrm{d}A \tag{7.19}$$

Using the sampling property of the δ-function on the first integral and noting that $\nabla^2 \psi$ is only non-zero in regions where fluid has crossed the escarpment gives

$$P(t) = \varepsilon \Gamma Y(t) + \int_{-\infty}^{\infty} \int_{1}^{\bar{\eta}(t)} y \, \mathrm{d}y \mathrm{d}x. \tag{7.20}$$

Performing the integration with respect to y gives

$$P(t) = \varepsilon \Gamma Y(t) + \frac{1}{2} \int_{-\infty}^{\infty} (\bar{\eta} - 1)^2 \, \mathrm{d}x. \tag{7.21}$$

Setting $\bar{\eta} = 1 + \varepsilon \eta$ gives,

$$P(t) = \varepsilon \Gamma Y(t) + \frac{\varepsilon^2}{2} \int_{-\infty}^{\infty} \eta^2 \, \mathrm{d}x. \tag{7.22}$$

As $P(t)$ is conserved analytically it can be used as an indicator of how accurate the numerical integrations are. Define the error $E(t)$ as

$$E(t) = \left| \frac{P(t) - P(0)}{P(0)} \right|. \tag{7.23}$$

Equation (7.22) also gives some restrictions on the motion $Y(t)$ of the vortex. At $t = 0$ there are no waves and so $\eta = 0$ and hence

$$P(0) = \varepsilon \Gamma Y(0). \tag{7.24}$$

As t increases the integral term of (7.22) can only increase as it is always positive. This leads to two cases,

Case 1: $\Gamma > 0$

In order to conserve momentum the vortex must initially move closer to the wall (towards decreasing y) and can never return to a position further from the wall than its initial position, in other words

$$Y(t) < Y(0), \tag{7.25}$$

for all time.

Case2: $\Gamma < 0$

In this case the converse is true and initially the vortex must move away from the wall (towards increasing y) and can never return to a position nearer to the wall than its initial position,

$$Y(t) > Y(0), \tag{7.26}$$

for all time.

This doesn't mean to say that $\dot{Y}(t)$ is only of one sign, the vortex can bob up and down and this corresponds to fluctuations in the amplitude of the interfacial waves. To summarise, an anticyclone ($\Gamma > 0$) initially situated on the shelf will be compelled towards the wall and thus gain velocity in the along-shore direction (since it moves closer to the wall). A cyclone ($\Gamma < 0$) will move away from the wall and, in contrast, will lose horizontal drift velocity. An anticyclone located off-shelf will initially move towards the escarpment, where-as a cyclone will move away from the escarpment. This behavior is, of course, a direct consequence of Bell's conservation of momentum and has been observed in other systems, for example Dunn et al. [2000] who find that the short-time vortex trajectory of a cyclone/anticyclone is to drift away/toward shallow water.

7.3 Linear Response for an Off-Shelf vortex

7.3.1 Small Time Solution

As was explained in section (5.3.1) the numerical method requires knowledge of the values of the system being integrated four time-steps previous to the present time-level in order to calculate the next time-step. So a small time expansion is needed for the initial four time-steps, for the off-shelf vortex the system to be solved is

$$\hat{\phi}(k, y) = 2A(t)\sinh(k)e^{|k|(1-y)}, \tag{7.27}$$

$$\frac{\mathrm{d}A}{\mathrm{d}t} + i\omega A = -\frac{i\hat{\Psi}(k, 1)}{2}e^{-ikX(t) - |k|}, \tag{7.28}$$

$$\hat{\Psi}(k, 1) = -\frac{\Gamma}{k}\sinh(k)e^{-|k|Y(t)}, \tag{7.29}$$

$$\hat{\eta}_t = ik(\hat{\phi}(k,1,t) + \hat{\Psi}(k,1,t)e^{-ikX(t)}). \tag{7.30}$$

With the vortex coordinates given by (these are true for the on-shelf case too)

$$X = \varepsilon X_1(t) + \ldots, \tag{7.31}$$

$$Y = y_0 + \varepsilon Y_1(t) + \ldots, \tag{7.32}$$

$$\frac{dX_1}{dt} = -\phi_y(X,Y) + \frac{\Gamma}{4\pi y_0}, \tag{7.33}$$

$$\frac{dY_1}{dt} = \phi_x(X,Y). \tag{7.34}$$

Expand all time dependent variables in a Taylor series up to $O(t^3)$

$$X_1(t) = X_{1a}t + X_{1b}t^2 + X_{1c}t^3 + \ldots,$$

$$Y_1(t) = Y_{1a}t + Y_{1b}t^2 + Y_{1c}t^3 + \ldots,$$

$$A(t) = A_1 t + A_2 t^2 + A_3 t^3 + \ldots,$$

$$\hat{\psi}(t) = \hat{\psi}_1 t + \hat{\psi}_2 t^2 + \hat{\psi}_3 t^3 + \ldots,$$

$$\hat{\eta}(t) = \hat{\eta}_1 t + \hat{\eta}_2 t^2 + \hat{\eta}_3 t^3 + \ldots \tag{7.35}$$

It has been assumed that all of the above quantities are zero at $t = 0$. Substitution of (7.31) into (7.33) show that

$$X_{1a} = \frac{\Gamma}{4\pi y_0}, \tag{7.36}$$

$$X_{1b} = -\frac{1}{2}\mathbb{F}^{-1}(\hat{\phi}_{1y}), \tag{7.37}$$

$$X_{1c} = -\frac{1}{3}\mathbb{F}^{-1}(\hat{\phi}_{2y}), \tag{7.38}$$

$$Y_{1a} = 0, \tag{7.39}$$

$$Y_{1b} = \frac{1}{2}\mathbb{F}^{-1}(ik\hat{\phi}_1), \tag{7.40}$$

$$Y_{1c} = -\frac{1}{3}\mathbb{F}^{-1}(ik\hat{\phi}_2). \tag{7.41}$$

Where all of the above inverse transforms are to be calculated at the interior points $(\varepsilon X_{1a}t, y_0)$. Equations (7.36) - (7.41) are also valid for the on-shelf case although the form of $\hat{\phi}$ will be different.

Before further substitutions are calculated certain terms need to be expanded first, it is found that for $U = \varepsilon X_{1a}$

$$e^{-ikX(t)} \simeq 1 - ikUt - t^2(ikX_{1b} + \frac{k^2U^2}{2}) + t^3(\frac{ik^3U^3}{6} - k^2UX_{1b} - ikX_{1c}),$$

(7.42)

$$e^{-|k|Y} \simeq e^{-|k|y_0}(1 - \varepsilon|k|Y_{1b}t^2 - \varepsilon|k|Y_{1c}t^3),$$

(7.43)

$$\sinh(kY) \simeq \sinh(ky_0) + \cosh(ky_0)(\varepsilon kY_{1b}t^2 + \varepsilon kY_{1c}t^3).$$

(7.44)

Substitution of (7.42) and (7.43) into (7.28) gives

$$A_1 = \frac{i\Gamma}{2k}\sinh(k)e^{-|k|(1+y_0)},$$

(7.45)

$$A_2 = -\frac{iA_1}{2}(\omega + kU),$$

(7.46)

$$A_3 = -\frac{1}{3}\left(\omega A_2 + A_1(ikX_{1b} + \frac{k^2U^2}{2} + \varepsilon Y_{1b}|k|)\right).$$

(7.47)

Now $\hat{\phi}(k, y, t)$ can be found using (7.27). It remains to find $\hat{\eta}$. To do this substitute (7.45) - (7.47) into (7.27) to calculate $\hat{\phi}(k, 1, t)$ and then use this and (7.42) to expand (7.30) which gives,

$$\hat{\eta}_1 = 0,$$

(7.48)

$$\hat{\eta}_2 = -\frac{\Gamma}{2}\sinh(k)e^{-|k|y_0}(kU + \omega), \tag{7.49}$$

$$\hat{\eta}_3 = \frac{i\Gamma}{3}\sinh(k)e^{-|k|y_0}\left(\varepsilon|k|Y_{1b} + ikX_{1b} + \frac{k^2U^2}{2} + \frac{\omega^2 + kU\omega}{2}\right). \tag{7.50}$$

7.3.2 Results of Numerical Experiments

The results in this section will be shown in three groups. The free parameters for these experiments are the strength of the vortex $\varepsilon\Gamma$ ($\Gamma \sim O(1)$ which can be positive and negative) and the initial position of the vortex y_0. The first group are the results for a vortex initially located far off-shelf , the second are the results from starting the vortex an $O(1)$ distance from the step and the third are the results from starting the vortex close to the step. In each group a variety of vortex strengths have been used.

There is a weak $O(\varepsilon)$ background drift of the vortex due to its image in the wall but since this is so small the plots have been shown in a static frame of reference (unlike previous results which have been plotted in a frame of reference moving with the vortex).

The value of ε used in all of these experiments (and the on-shelf cases too) was $\varepsilon = 0.1$.

Case 1. $y_0 = 3$

Figure (7.2) shows the evolution of the interface contour, vortex trajectory and error for the case $y_0 = 3$ and $\Gamma = 3.5$. The errors in the rest of the experiments in this

chapter never got higher than $\sim O(10^{-5})$ and in most cases were $\sim O(10^{-6})$, as such they have not been shown. Upon initialisation the vortex immediately drifts towards the interface as expected by conservation of momentum for positive vortex circulation ($\Gamma > 0$), this pushes fluid onto the shelf and the depression in the contour corresponding to the vortex pseudoimage grows until the vortex motion in the y-direction vanishes. The presence of this extra negative vorticity and the vortex's closer proximity to the wall cause it to drift in the horizontal towards increasing x, after some small oscillations in the off-shore direction the system reaches equilibrium and the vortex motion consists of just an $O(\varepsilon)$ drift with the interface evolution behaving similarly to the stationary vortex off-shelf response calculated in chapter 3.

Figure (7.3) shows the case for $\Gamma = -2.5$. The difference for the anti-cyclonic vortex is that conservation of momentum requires the vortex to initially drift away from the interface and the manifestation of the pseudoimage in the contour is that fluid is pulled off the shelf from shallow to deep, this fluid acquires positive vorticity and thus the image of the vortex in the wall and its pseudoimage in the contour act in tandem to propel the vortex towards decreasing x and again the system balances out to a steady state. The topographic wave dynamics are very similar to those described in chapter 3 for the stationary vortex.

Case 2. $y_0 = 1.5$

If the vortex is initialised closer to the interface then naturally the interface deformations are going to be larger in magnitude and thus the effect on the vortex will be more marked. Figure (7.4) shows the interface evolution and vortex trajectory for $y_0 = 1.5$ and $\Gamma = -0.5$. The initial response of the anti-cyclonic vortex is to

(a)

(b)
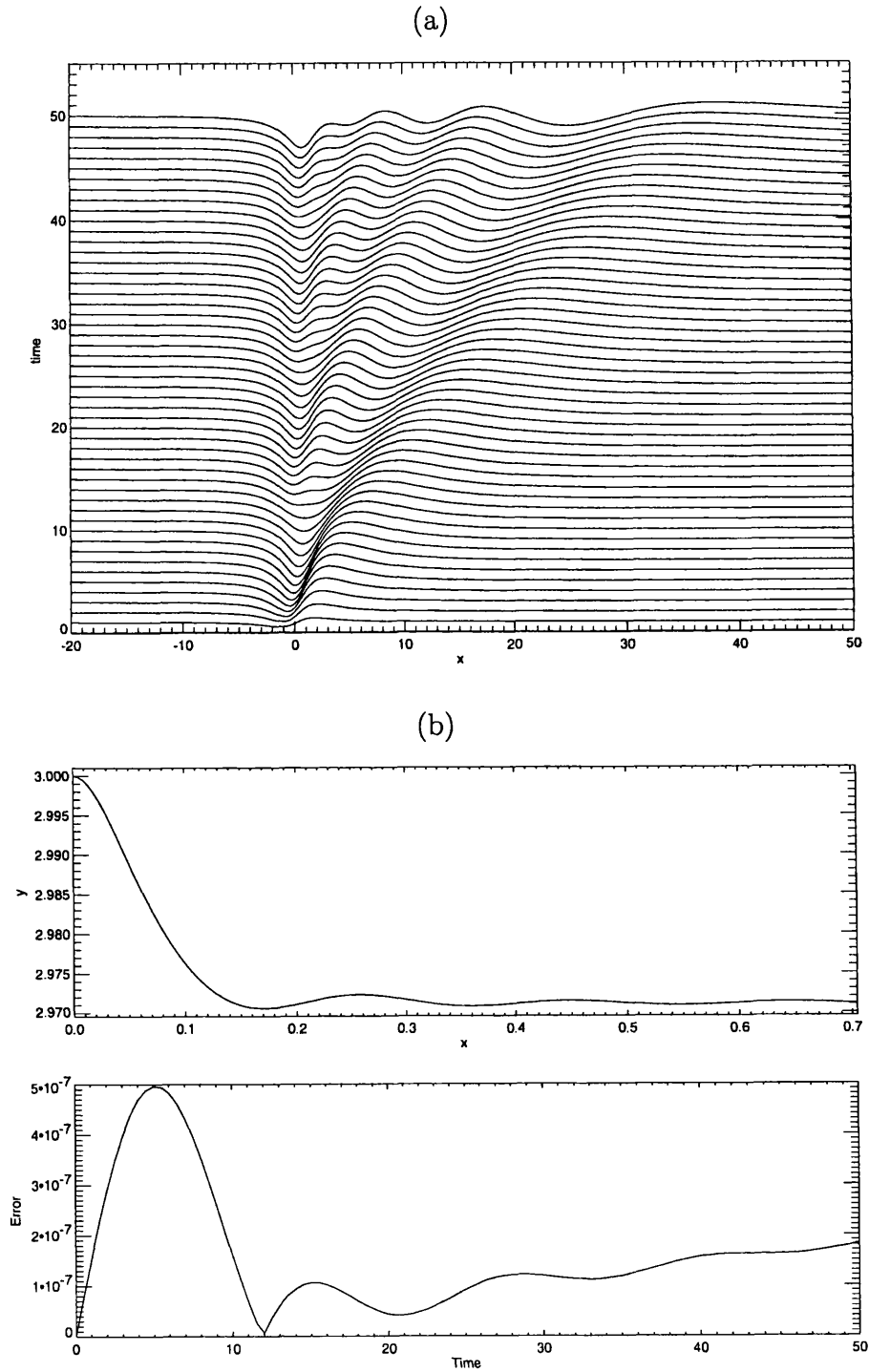
Figure 7.2: (a) The interface displacement for $y_0 = 3$ and $\Gamma = 3.5$, scaled by 5, (b) the vortex trajectory and error.

(a)

(b)
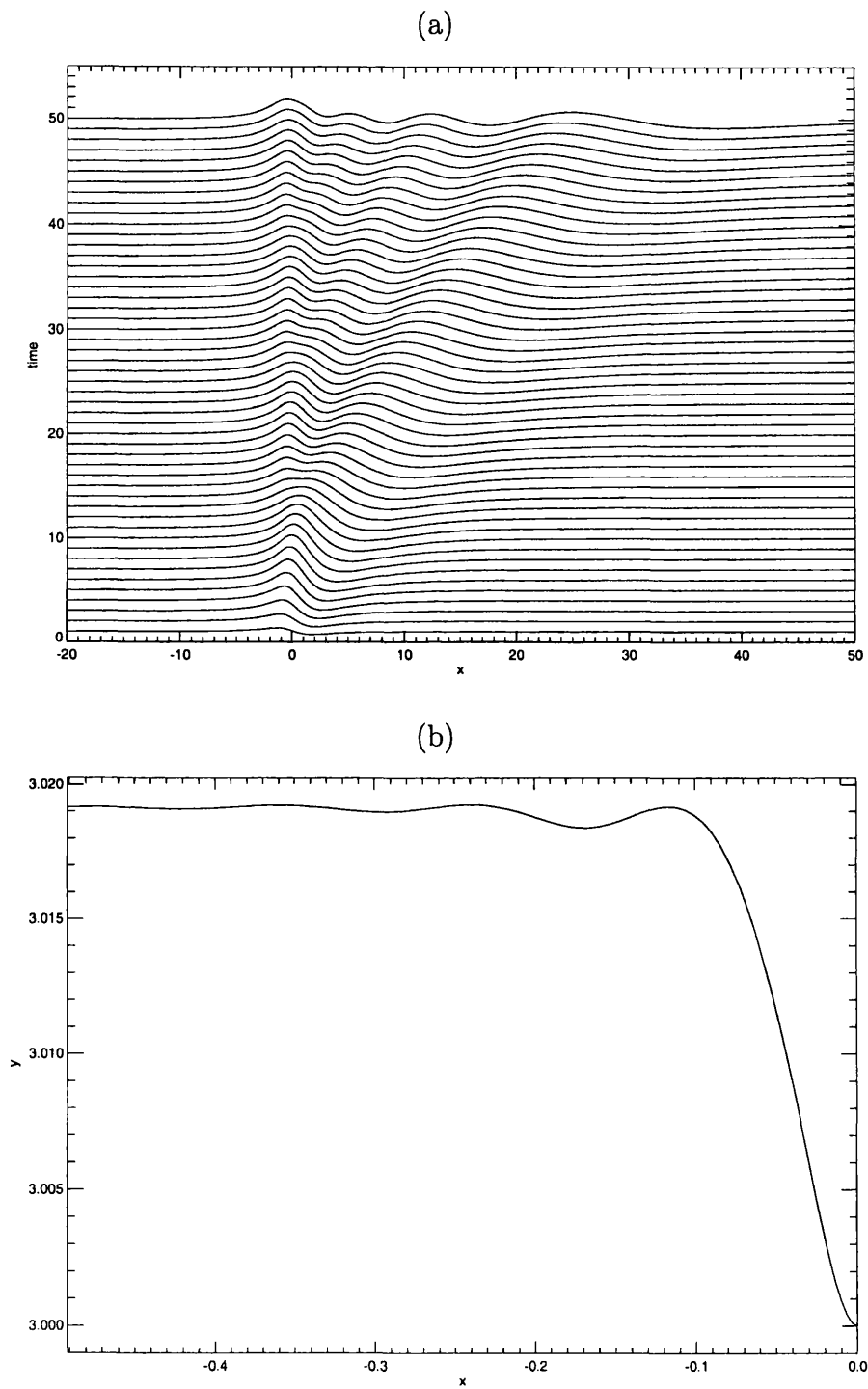
Figure 7.3: (a) The interface displacement for $y_0 = 3$ and $\Gamma = -2.5$, scaled by 5,

(b) the vortex trajectory.

move away from the interface and towards decreasing x. This is expected as conservation of momentum requires that the vortex move towards increasing y and the associated deformation of the interface at the vortex position consists of cyclonic vorticity which moves the vortex towards decreasing x. The motion of the vortex in y depends upon the local gradient of the secondary streamfunction motions (c.f. equation 7.12) and as the vortex moves horizontally, this will change sign. The vortex then starts drifting back towards the interface which responds by releasing a wave upstream, this process repeats when the vortex is close enough to pull more fluid back from shallow to deep, however the vortex oscillation is smaller than the previous one as some energy has been sent upstream in the topographic wave. This is in contrast to the analytic results in Bell [1989] which ignore energy loss and so the oscillations in y do not decay.

Eventually the system approaches a steady state. This is also shown in figure (7.5) for $y_0 = 1.5$ and $\Gamma = -3.5$. For this stronger vortex the drift parallel to the coast of the vortex is greater causing it to move away from the area of topographic wave motion much sooner than the previous example of a weaker vortex. When this happens the vortex-wave interaction consists solely of the vortex plus its pseudoimage in the interface plus a weak contribution from its image in the wall.

Figure (7.6) shows the corresponding plots for a weak cyclonic vortex with $y_0 = 1.5$ and $\Gamma = 0.5$. The situation is exactly analogous to that of figure (7.4) but now the pseudoimage is a depression in the contour and the vortex initially moves towards the interface. This has interesting consequences at larger forcing. Figure (7.7) shows the response for $y_0 = 1.5$ and $\Gamma = 2.5$ and at this strength of forcing the vortex is pulled onto the interface and the linear theory breaks down. This is mirrored in the response at the interface which is seen to be an ever-growing, nondispersive

depression in the contour.

Case 3. $y_0 = 1.2$

The final case examines the response for a weak vortex placed close to the interface. Anticyclonic vortices pose no problem. This can be seen in figures (7.8) for $y_0 = 1.2$ and $\Gamma = -2.5$ and figure (7.9) for $y_0 = 1.2$ and $\Gamma = -0.5$. Both cases show the initial response of the vortex moving away from the interface and then settling down to a steady horizontal drift after a series of oscillations in y. Unsurprisingly the case for $y_0 = 1.2$ and $\Gamma = 0.5$ immediately breaks down as even at this weak value of Γ the vortex is instantly pulled over the escarpment. The response at the interface is again a growing, nondispersive depression of negative vorticity, this is illustrated in figure (7.10).

Summary

Off-shelf cyclones are pulled towards the interface increasing the amplitude of the contour deformations and thus nonlinear effects will become important at larger times. They also accelerate towards increasing x due to the combined effects of the vortex image in the wall and the pseudoimage in the interface.

Off-shelf anti-cyclones move away from the interface and accelerate towards decreasing x. Thus, if initially linearity is a good assumption it will remain so for longer times. In both cases the pseudoimage induces a velocity which reinforces that induced by the vortex wall image and also at large times the step behaves as if it were a wall (Johnson [1985], Dunn et al. [2000]) and so the velocity along-shore must be greater as the vortex is now closer to the 'wall'.

(a)

(b)
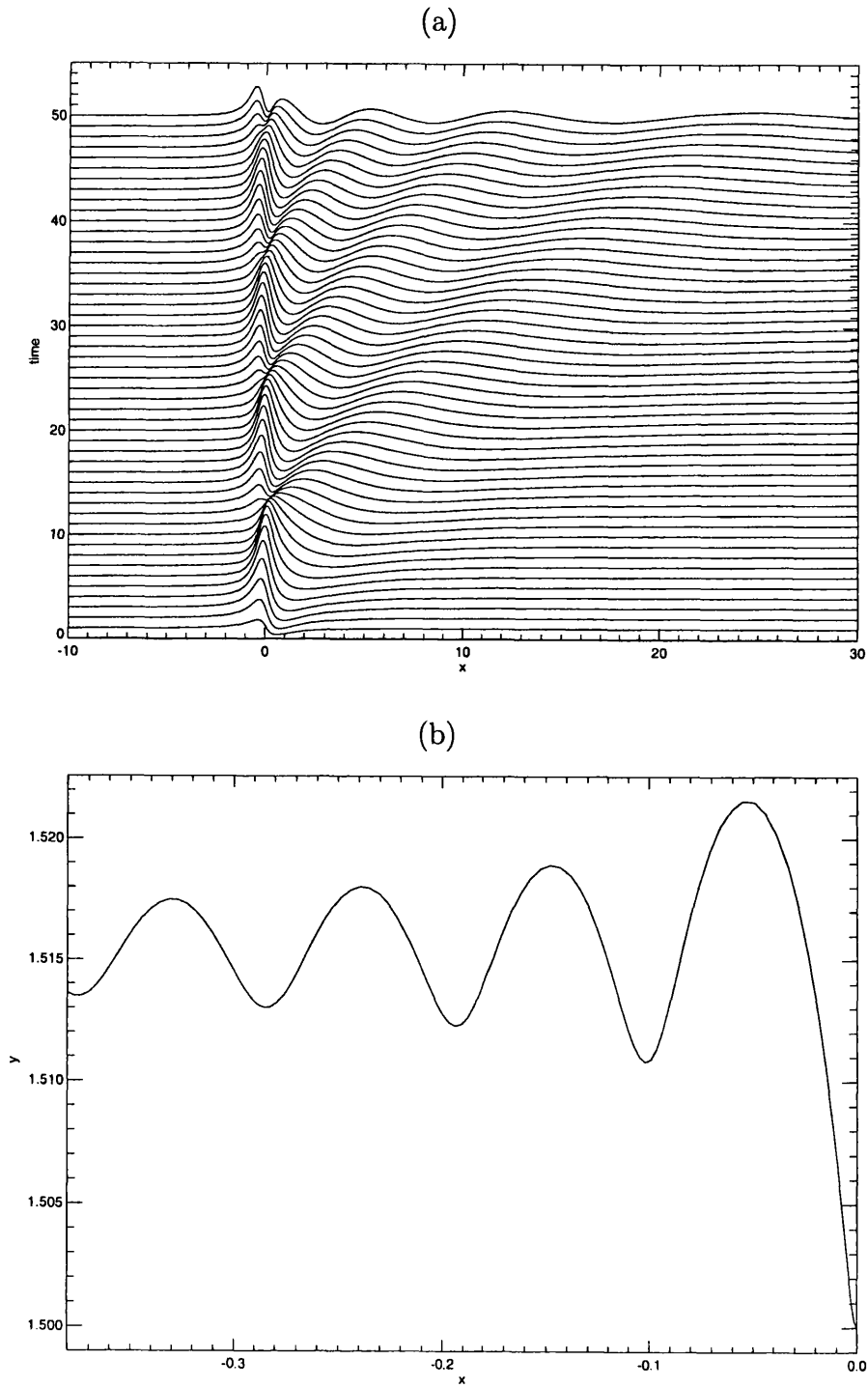
Figure 7.4: (a) The interface displacement for $y_0 = 1.5$ and $\Gamma = -0.5$, scaled by 10,

(b) the vortex trajectory.

(a)

(b)
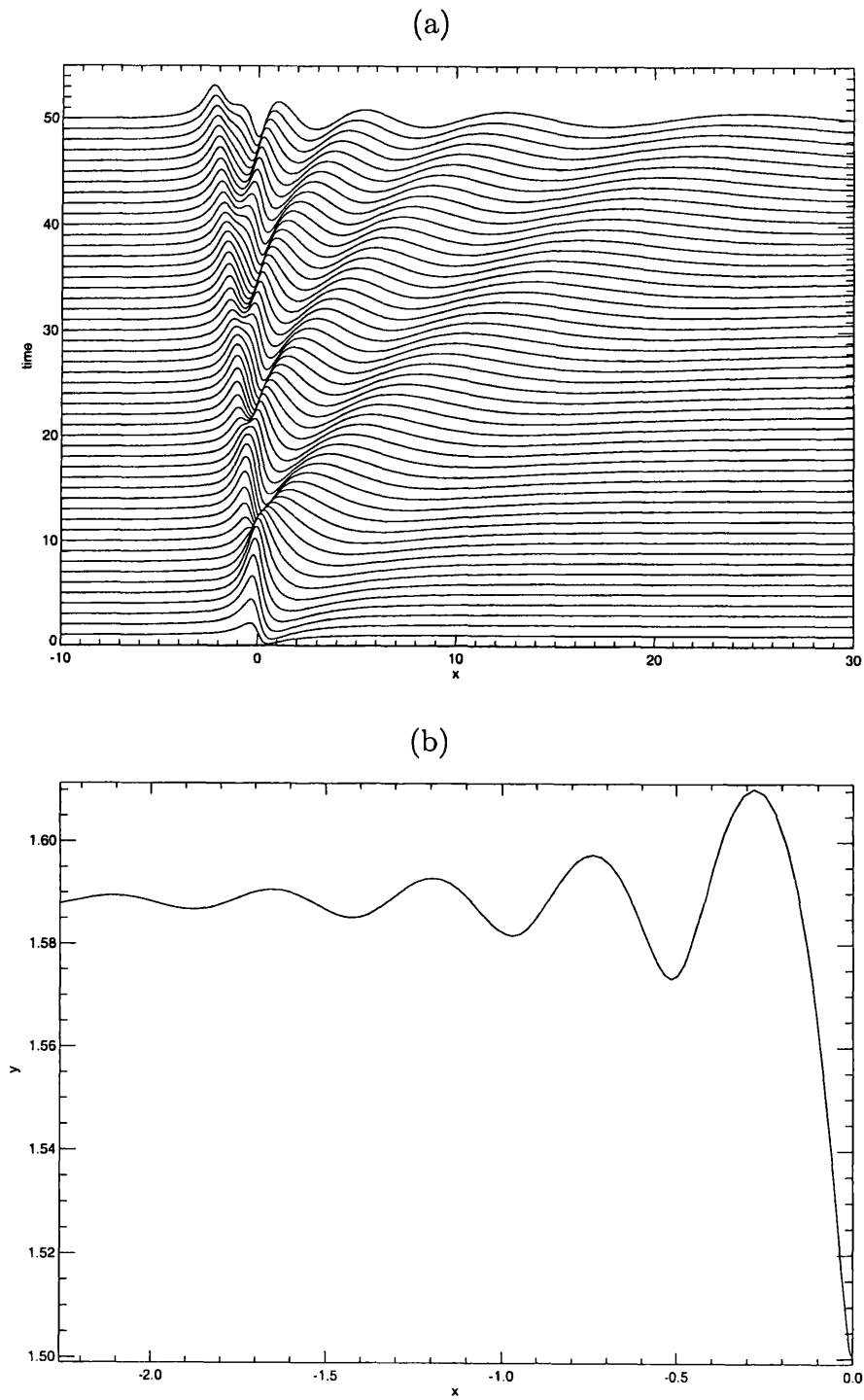
Figure 7.5: (a) The interface displacement for $y_0 = 1.5$ and $\Gamma = -3.5$, scaled by 2, (b) the vortex trajectory.

(a)

(b)
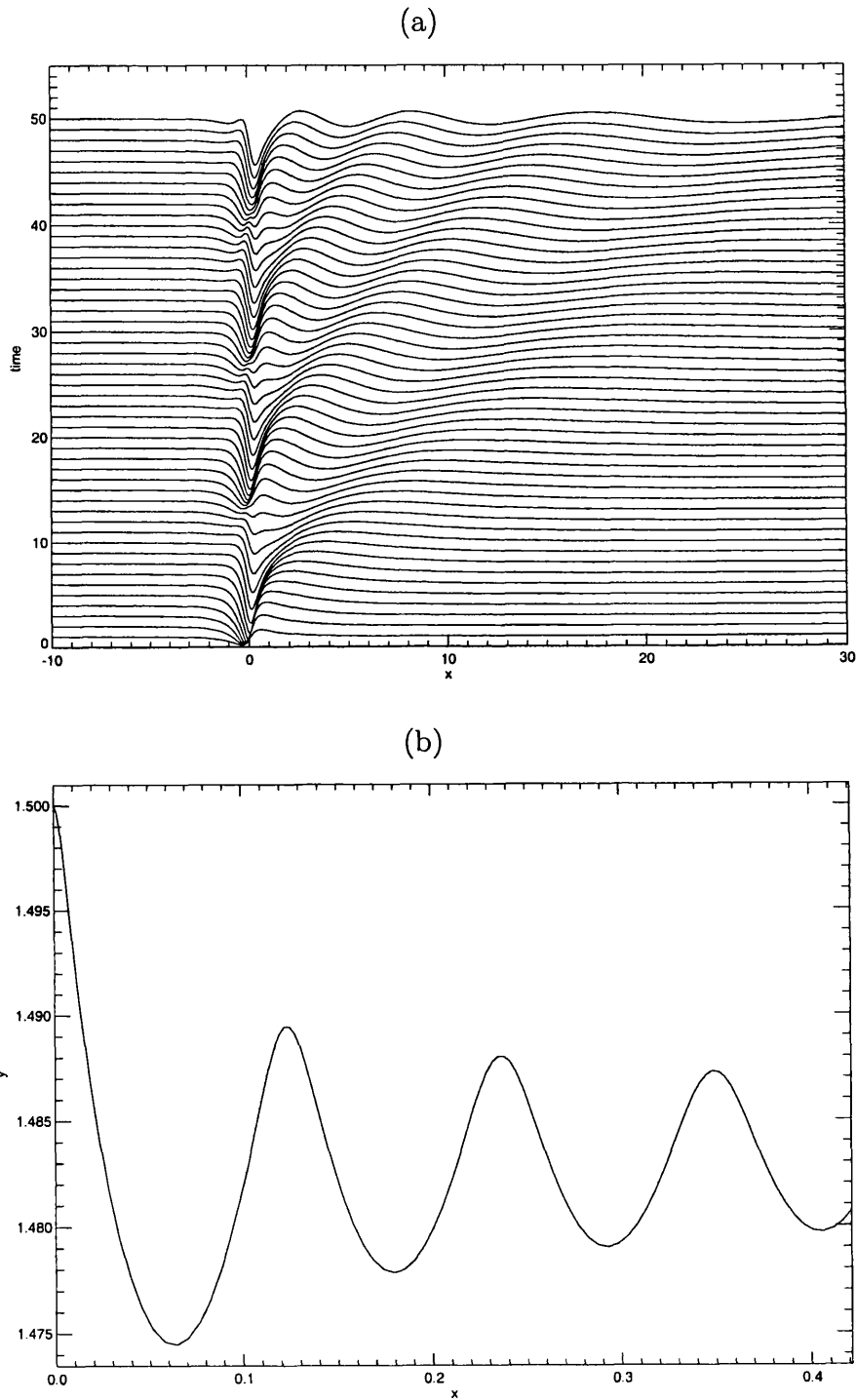
Figure 7.6: (a) The interface displacement for $y_0 = 1.5$ and $\Gamma = 0.5$, scaled by 10,

(b) the vortex trajectory.

(a)

(b)
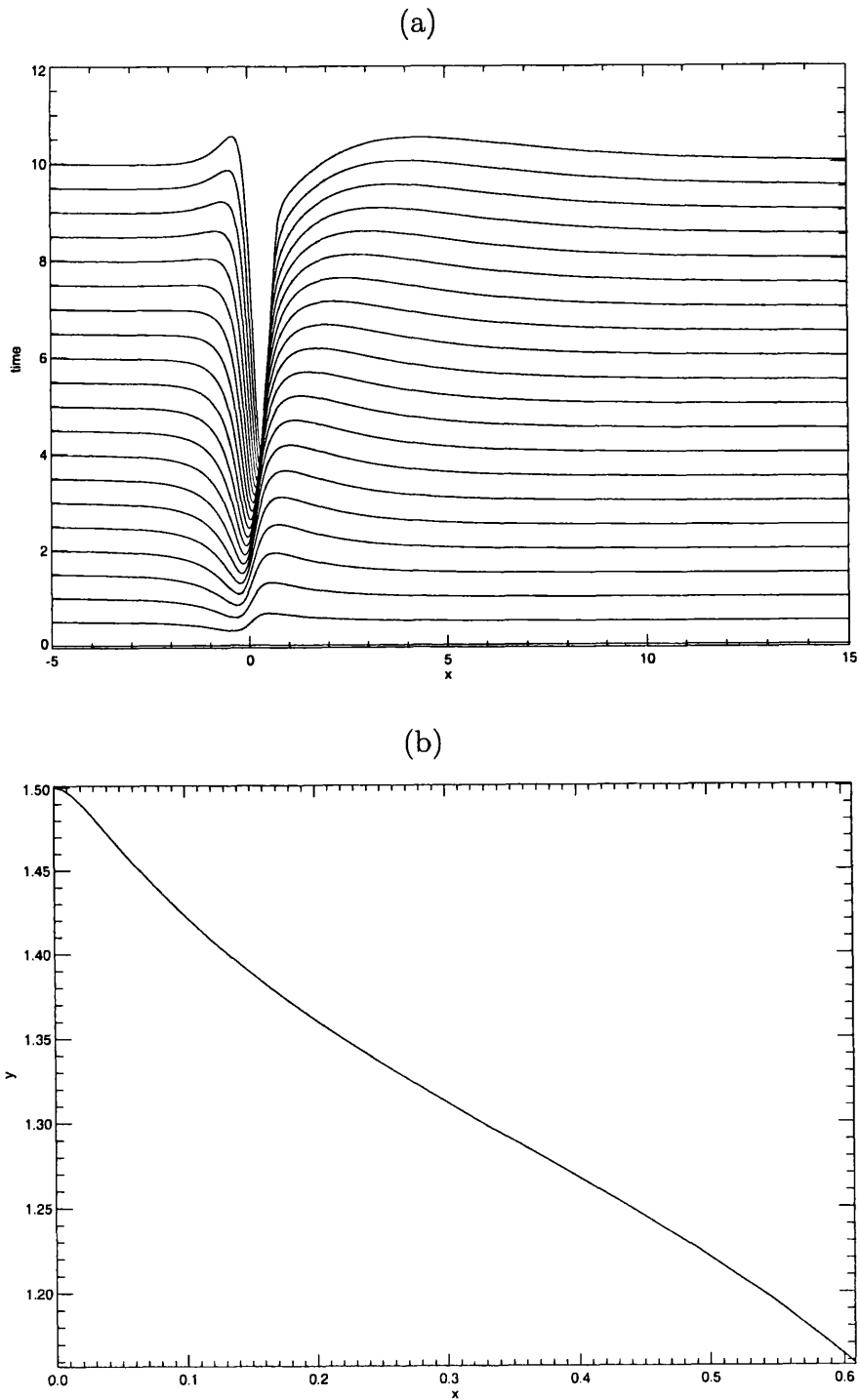
Figure 7.7: (a) The interface displacement for $y_0 = 1.5$ and $\Gamma = 2.5$, (b) the vortex

trajectory.

(a)

(b)
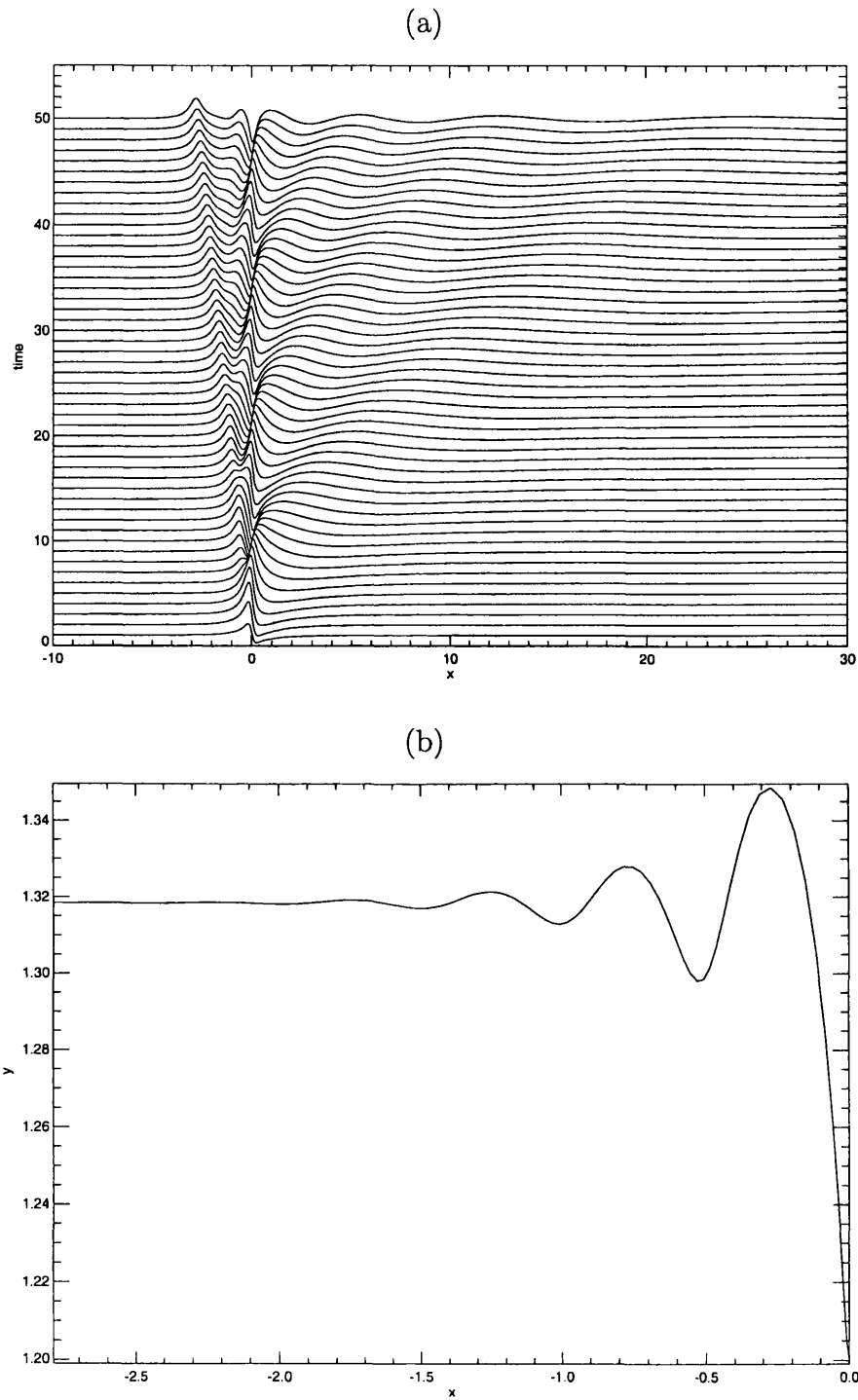
Figure 7.8: (a) The interface displacement for $y_0 = 1.2$ and $\Gamma = -2.5$, (b) the vortex trajectory.

(a)

(b)
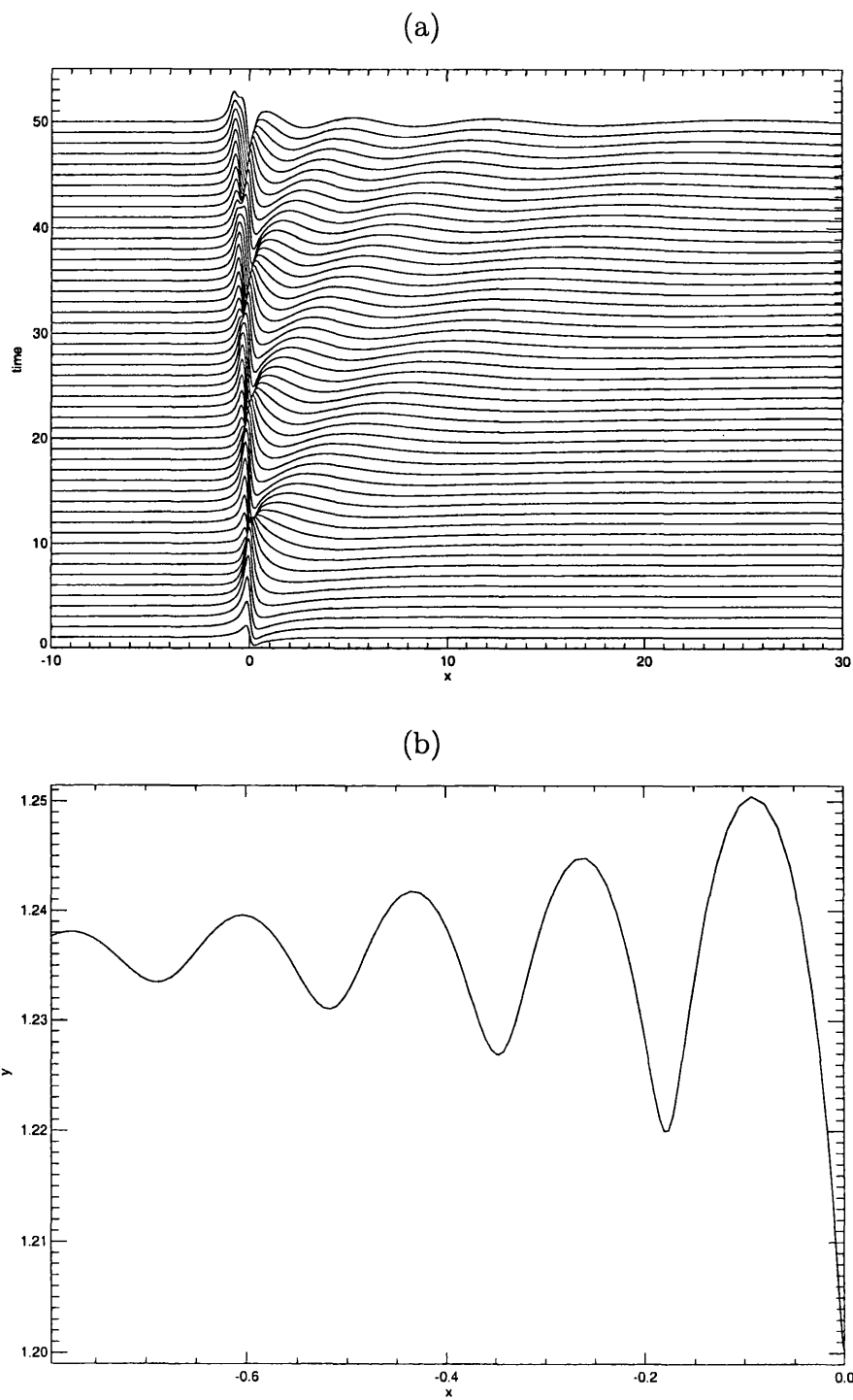
Figure 7.9: (a) The interface displacement for $y_0 = 1.2$ and $\Gamma = -0.5$, scaled by 5,

(b) the vortex trajectory.

(a)

(b)
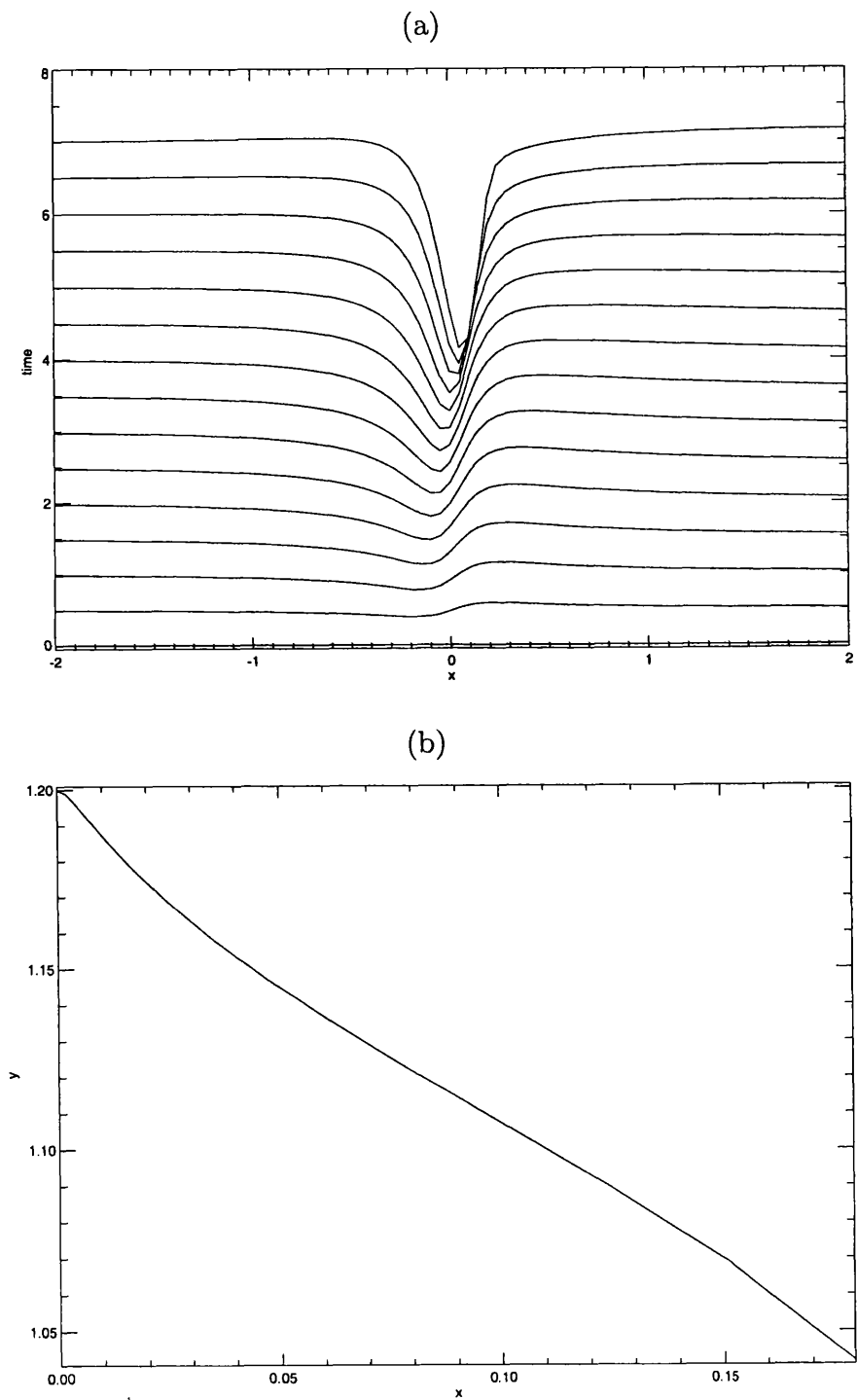
Figure 7.10: (a) The interface displacement for $y_0 = 1.2$ and $\Gamma = 0.5$, (b) the vortex trajectory.

7.4 Linear Response for an On-Shelf vortex

7.4.1 Small Time Solution

The analysis is very similar to the small time solution for the off-shelf case, the difference lies in changes in the forcing term $\hat{\Psi}$ and the secondary motions $\hat{\phi}$. The system to be solved is

$$\hat{\phi}(k, y) = 2A(t)\sinh(k), \tag{7.51}$$

$$\frac{\mathrm{d}A}{\mathrm{d}t} + i\omega A = -\frac{i\hat{\Psi}(k, 1)}{2}e^{-ikX(t)-|k|}, \tag{7.52}$$

$$\hat{\Psi}(k, 1) = -\frac{\Gamma}{k}\sinh(kY(t))e^{-|k|}, \tag{7.53}$$

$$\hat{\eta}_t = ik(\hat{\phi}(k, 1, t) + \hat{\Psi}(k, 1, t)e^{-ikX(t)}). \tag{7.54}$$

Substitution of (7.42) and (7.44) into (7.52) gives

$$A_1 = \frac{i\Gamma}{2k}\sinh(ky_0)\exp^{-2|k|}, \tag{7.55}$$

$$A_2 = -\frac{iA_1}{2}(\omega + kU), \tag{7.56}$$

$$A_3 = -\frac{A_1}{3}\left(\frac{k^2U^2}{2} - ikX_{1b}\right) + \frac{i\varepsilon\Gamma}{6}e^{-2|k|}Y_{1b}\cosh(ky_0) - \frac{i\omega A_2}{2}. \tag{7.57}$$

Now $\hat{\phi}(k, y, t)$ can be found using (7.51). It remains to find $\hat{\eta}$. To do this substitute (7.55) - (7.57) into (7.51) to calculate $\hat{\phi}(k, 1, t)$ and then use this and (7.42) and (7.44) to expand (7.54) which gives,

$$\hat{\eta}_1 = 0, \tag{7.58}$$

$$\hat{\eta}_2 = -\frac{\Gamma}{2}\sinh(ky_0)e^{-|k|}(kU + \omega), \tag{7.59}$$

$$\hat{\eta}_3 = \frac{kA_1}{3}\sinh(k)(kU + \omega) - \frac{i\Gamma}{3}e^{-|k|}\left(\varepsilon k Y_{1b}\cosh(ky_0) - \sinh(ky_0)(ikX_{1b} + \frac{k^2U^2}{2})\right). \tag{7.60}$$

7.4.2 Results of Numerical Experiments

Case 1. $y_0 = 0.8$

Continuing the trend of ever decreasing values of y_0, figure (7.11) is for $y_0 = 0.8$ and $\Gamma = 3.5$. This is the on shelf equivalent for flow forced by a vortex close to the interface. The opposite case to section 7.3.2 now occurs as a vortex with positive circulation will initally move away from the interface, towards the wall in order to conserve momentum. This is also shown in figure (7.12) for a weaker vortex: $y_0 = 0.8$ and $\Gamma = 0.5$. In both cases the motion is dominated by the vortex response to the deforming of the contour and not the image vortex in the wall, this is clearly the case as both vortices, after initially moving towards increasing x (which is the case for a cyclonic vortex near a wall) loop back and the predominant motion is towards decreasing x with oscillations in y that decay with time. After $t = 50$ the strongly forced example is clearly settling to a steady state of constant horizontal drift towards decreasing x that is due purely to the pseudoimage vortex in the interface. The weaker example has not yet settled down to a steady state but it too, will eventually do so.

Figure (7.13) shows the response for $y_0 = 0.8$ and $\Gamma = -0.5$ which is the weakly forced, anti-cyclonic case. Conservation of momentum now acts to propel the vortex towards the interface and even at this weak value of Γ the vortex gets sufficiently close to the interface to invalidate linear theory. Again the motion is dominated by the effect of the pseudoimage of the vortex in the interface.

Case 2. $y_0 = 0.5$

At middle values of y_0 the influence of the vortex image in the wall will be exactly comparable with vortex pseudoimage in the interface, this is readily apparent in figures (7.14) - (7.21) which show the linear response for $y_0 = 0.5$ and a variety of vortex strengths. A common aspect of the behavior of vortex trajectories is a looping motion. The figures are presented in the order of decreasing strength, first for the anticyclonic vortex, with figures (7.14) - (7.17) showing the response for $\Gamma = -3.5, -2.5, -1.5, -0.5$ respectively. Then figures (7.17) - (7.21) show the equivalent responses for the cyclonic vortex with $\Gamma = 3.5, 2.5, 1.5, 0.5$.

The results can be explained by examining the roles of momentum conservation (which governs the motion of the vortex in y) and the image/pseudoimage effect (which primarily govern the horizontal vortex motion). For an anti-cyclonic vortex ($\Gamma < 0$) momentum conservation requires that if the interface displacement grows in magnitude ($|\eta|$ increases) then $Y(t)$ must also increase and vice versa. Both the vortex image and the vortex pseudoimage will have positive circulation, in other words anti-clockwise circulation and so the image vortex will push the vortex towards decreasing x and the pseudoimage will push it towards increasing x. The exact opposite is true for a cyclonic vortex, the wall image pushes it towards increasing x and the pseudoimage towards decreasing x.

(a)

(b)
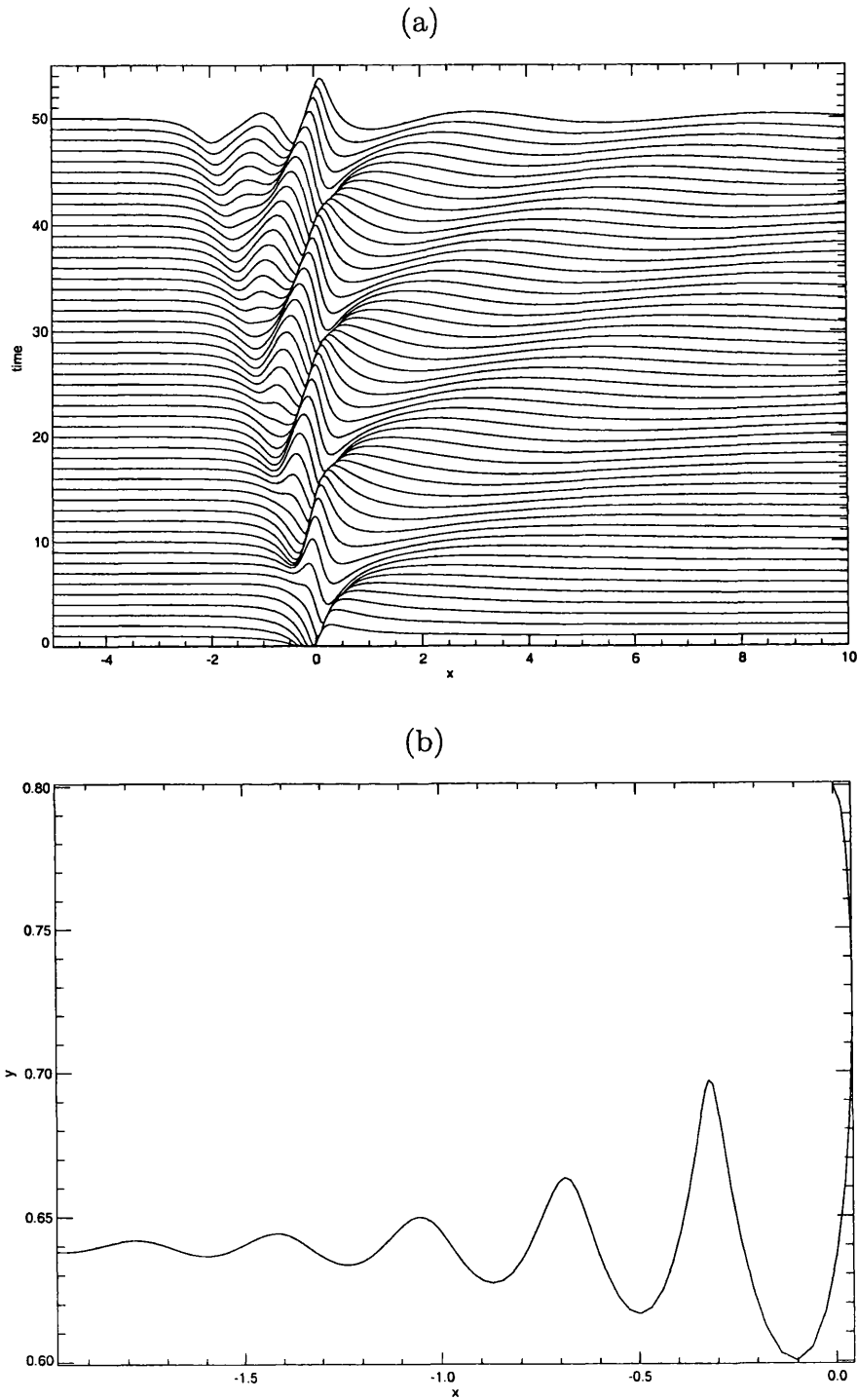
Figure 7.11: (a) The interface displacement for $y_0 = 0.8$ and $\Gamma = 3.5$, (b) the

vortex trajectory.

(a)

(b)
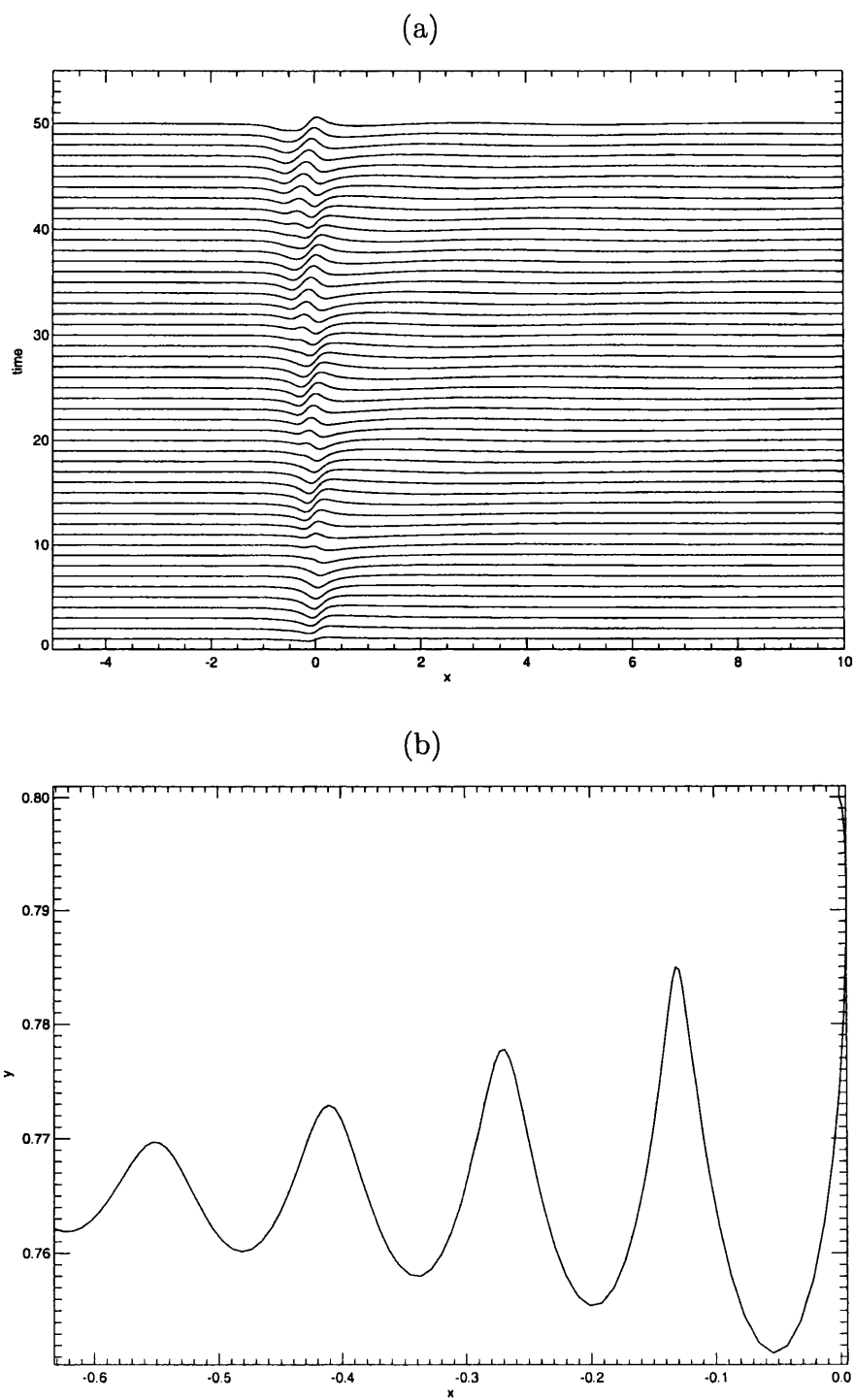
Figure 7.12: (a) The interface displacement for $y_0 = 0.8$ and $\Gamma = 0.5$, (b) the vortex trajectory.

(a)

(b)
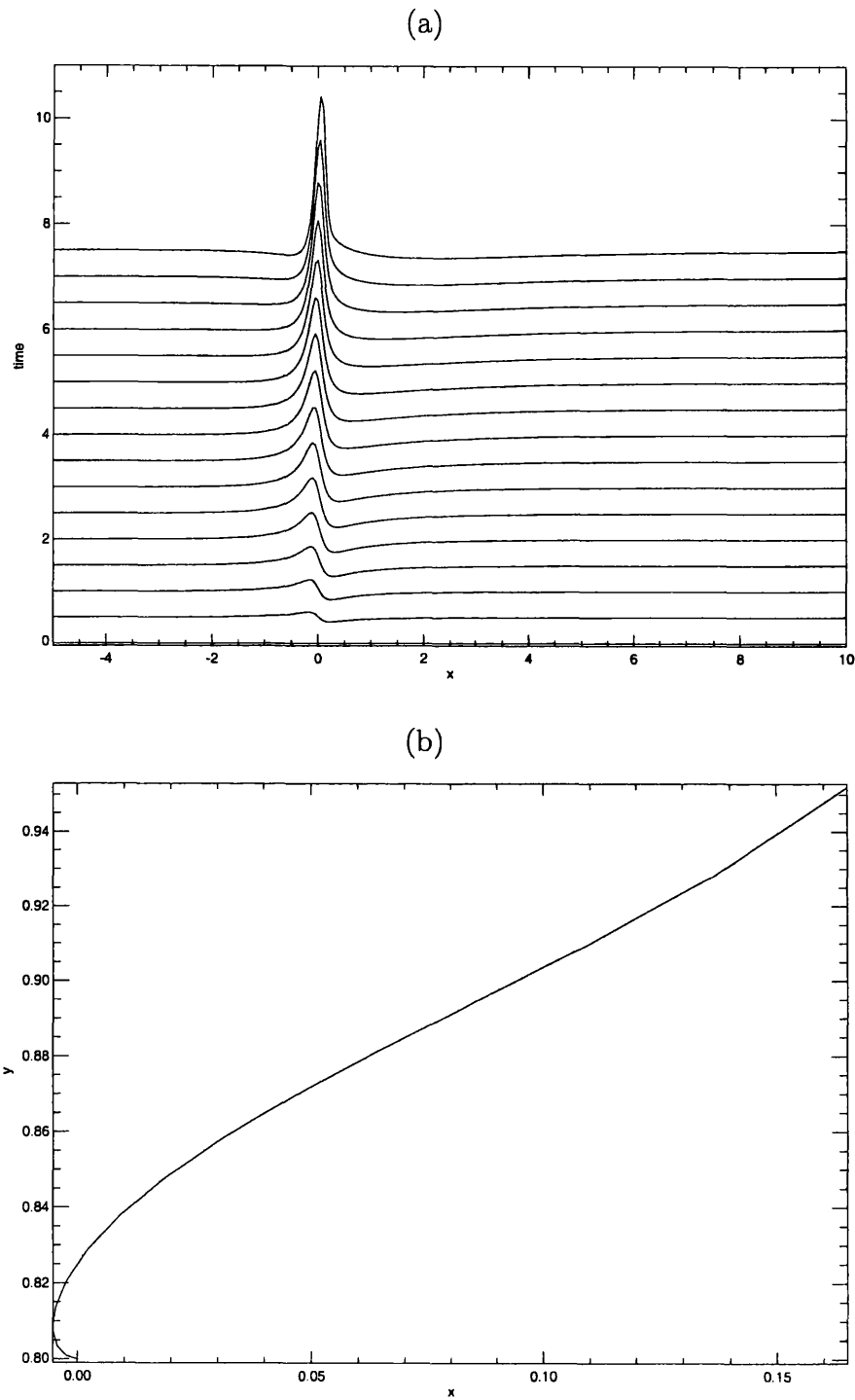
Figure 7.13: (a) The interface displacement for $y_0 = 0.8$ and $\Gamma = -0.5$, (b) the vortex trajectory.

Examining figure (7.16) for $y_0 = 0.5$ and $\Gamma = -1.5$, initially the vortex moves towards increasing x (influenced by wall image) and increasing y (growth of $|\eta|$, momentum conservation). As it nears the interface the pseudoimage effect becomes important and the vortex is pushed towards increasing x, reversing direction, the topographic waves disperse and so the vortex responds by drifting towards the wall. Now the effect of the wall image becomes important and the vortex changes direction again and moves towards increasing x, the wave oscillation at the point above the vortex starts its upward phase and so 'pulls' the vortex towards the interface and the cycle repeats. At strong forcing the constant drift due to the wall image is large enough to cause the distinctive, callipygian trajectories seen earlier and as the forcing becomes weaker the interplay described above is more easily seen. Note that the boustrophedonic motion in x still occurs at larger forcing but is 'hidden' by the stronger horizontal drift.

An analogous argument can be constructed for the cyclonic vortex cases, using figure (7.19) as a reference, the initial vortex motion is towards increasing x (due to the wall image effect as the topographic wave response is still forming) and also towards the wall (conservation of momentum due to the increasing response at the interface). As the interface displacement reaches its maximum the pseudoimage exerts a stronger influence and changes the vortex direction towards decreasing x but only briefly for as the wave oscillation begins its retardation phase, pulling the vortex away from the wall, the wall image influence regains control and changes the horizontal motion back towards increasing x. The cycle then repeats as the response at the interface above the vortex starts to grow in magnitude again. Again at stronger forcing these effects are less marked due to the larger, constant horizontal drift.

(a)

(b)
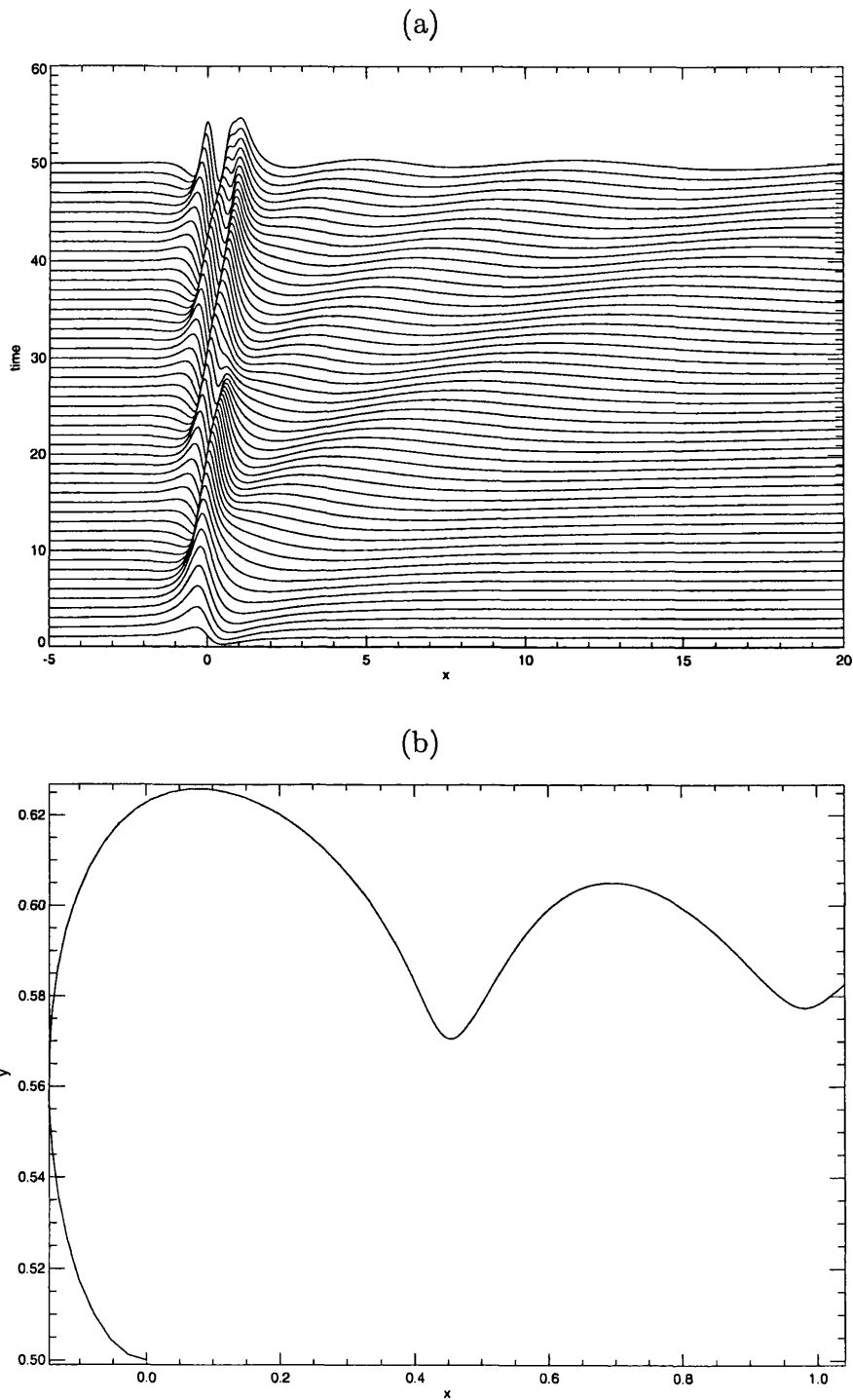
Figure 7.14: (a) The interface displacement for $y_0 = 0.5$ and $\Gamma = -3.5$, scaled by 2, (b) the vortex trajectory.

(a)

(b)
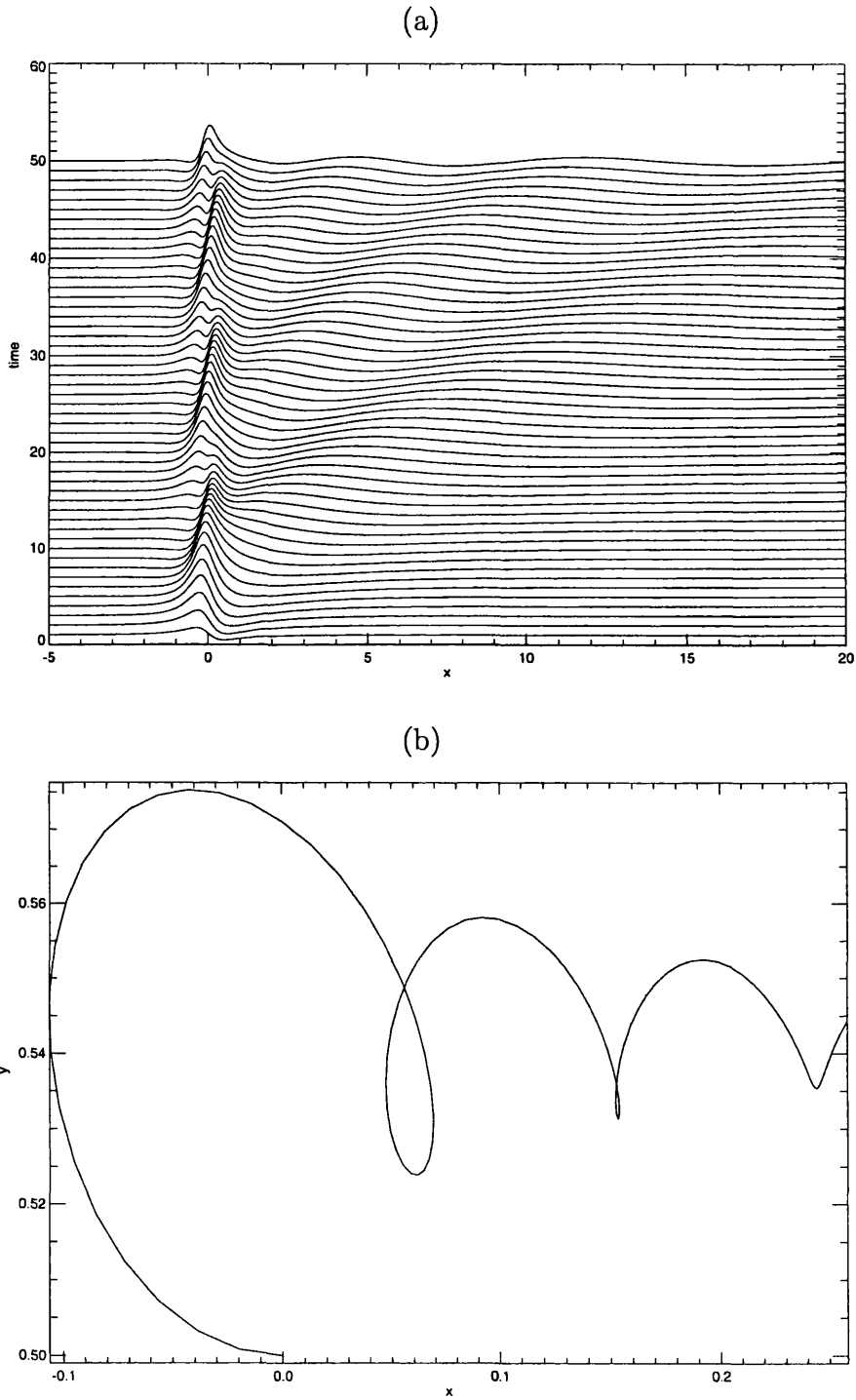
Figure 7.15: (a) The interface displacement for $y_0 = 0.5$ and $\Gamma = -2.5$, scaled by 2,

(b) the vortex trajectory.

(a)

(b)
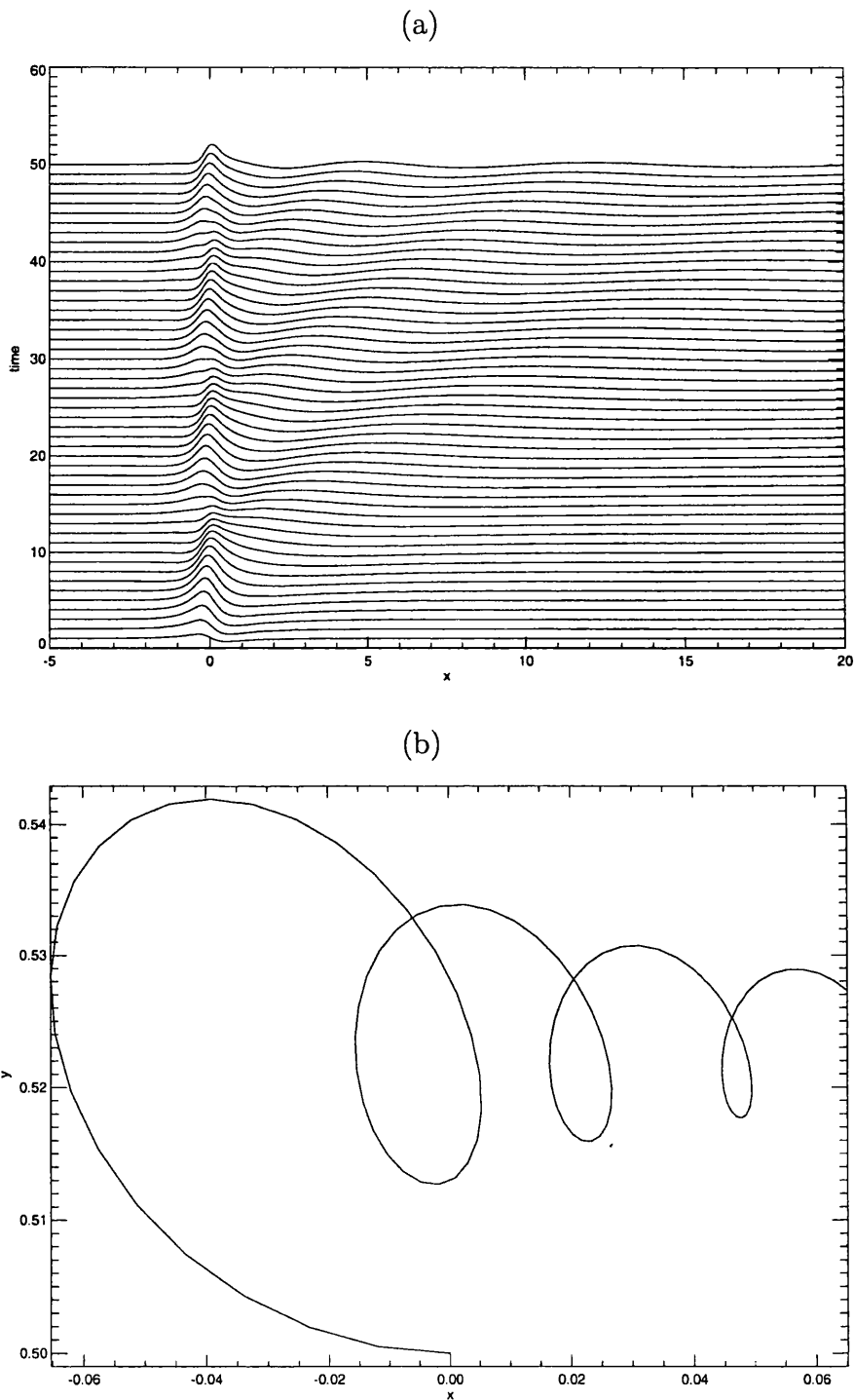
Figure 7.16: (a) The interface displacement for $y_0 = 0.5$ and $\Gamma = -1.5$, scaled by 2,

(b) the vortex trajectory.

(a)

(b)
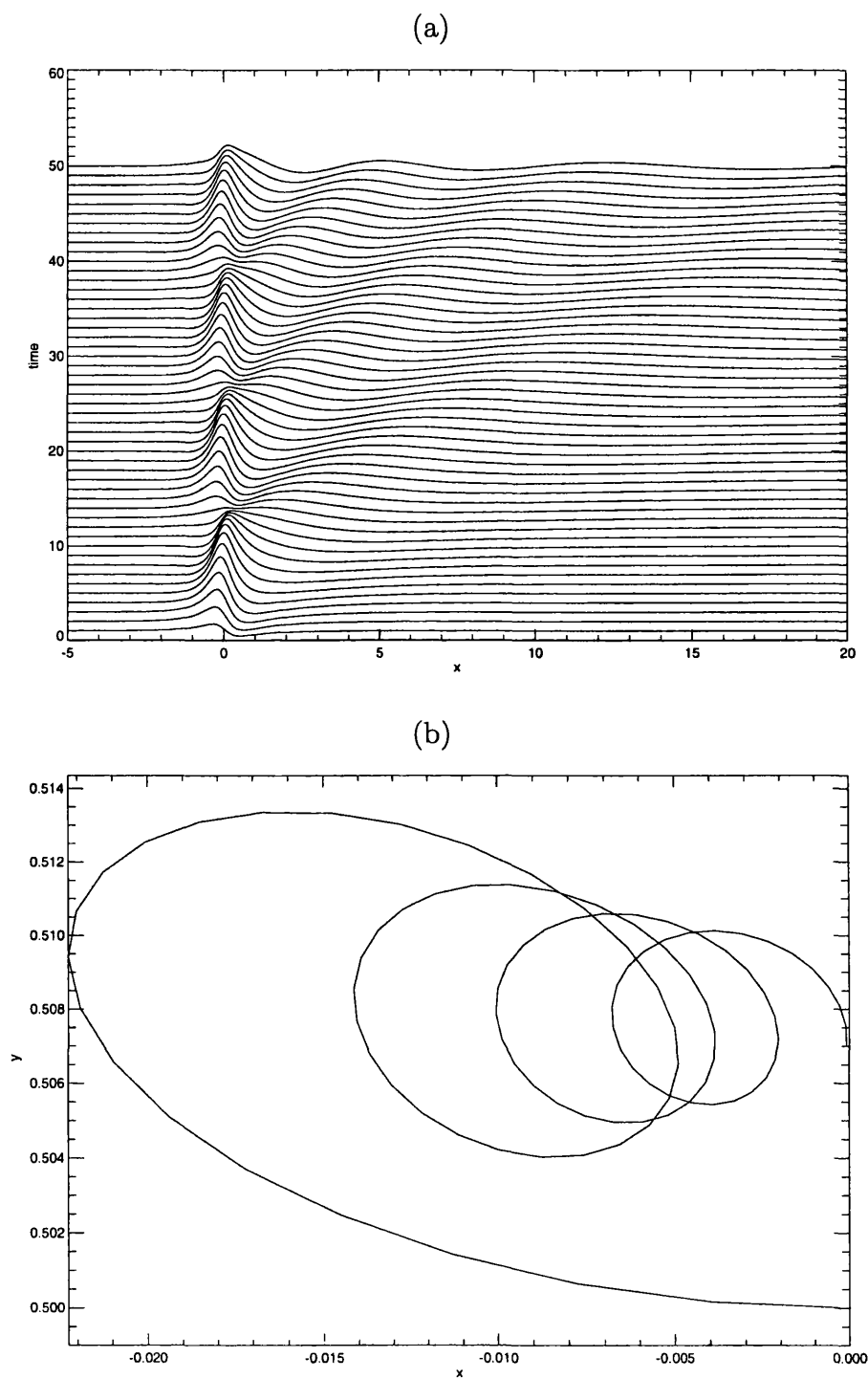
Figure 7.17: (a) The interface displacement for $y_0 = 0.5$ and $\Gamma = -0.5$, scaled by 10, (b) the vortex trajectory.

(a)

(b)
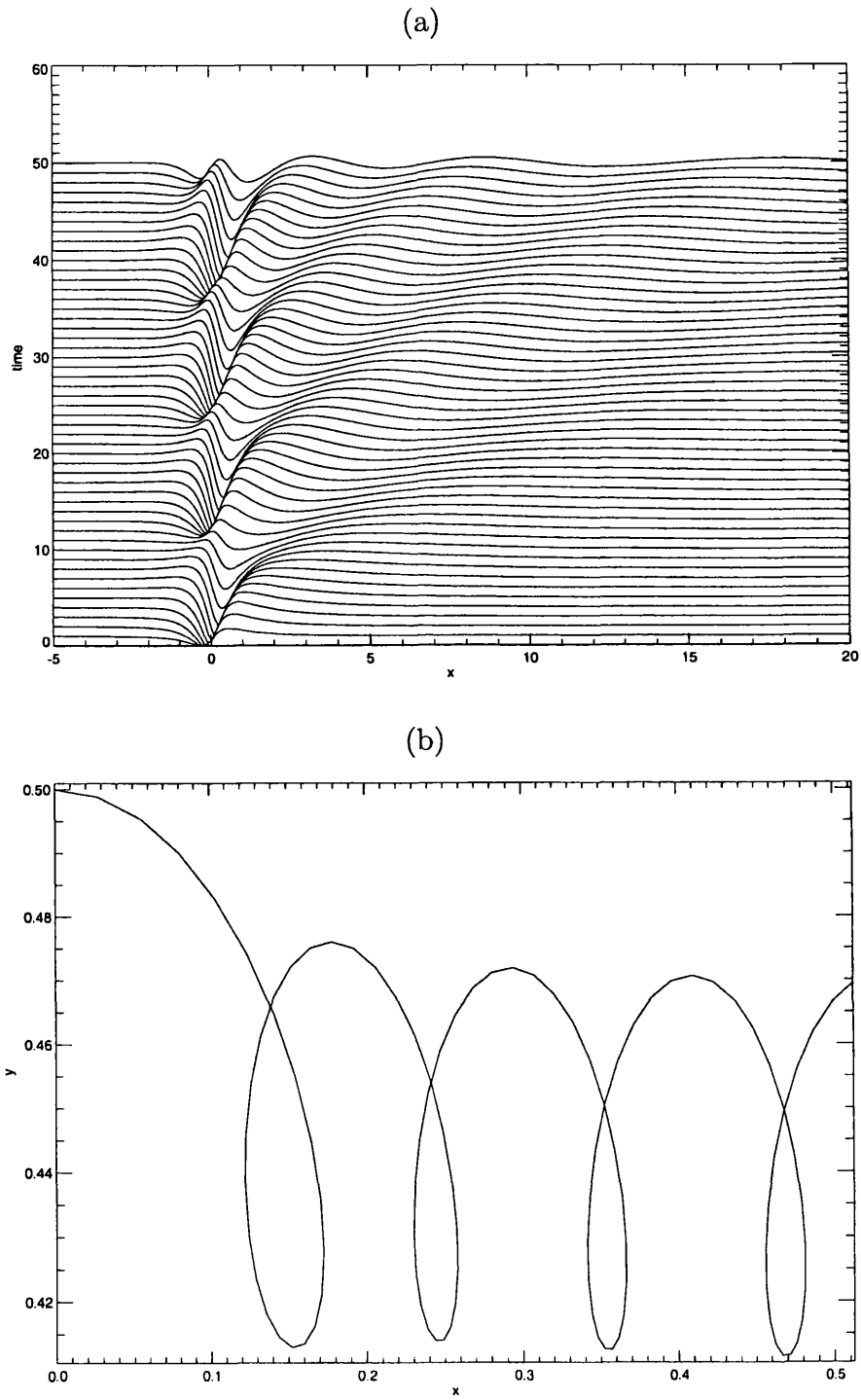
Figure 7.18: (a) The interface displacement for $y_0 = 0.5$ and $\Gamma = 3.5$, scaled by 2,

(b) the vortex trajectory.

(a)

(b)
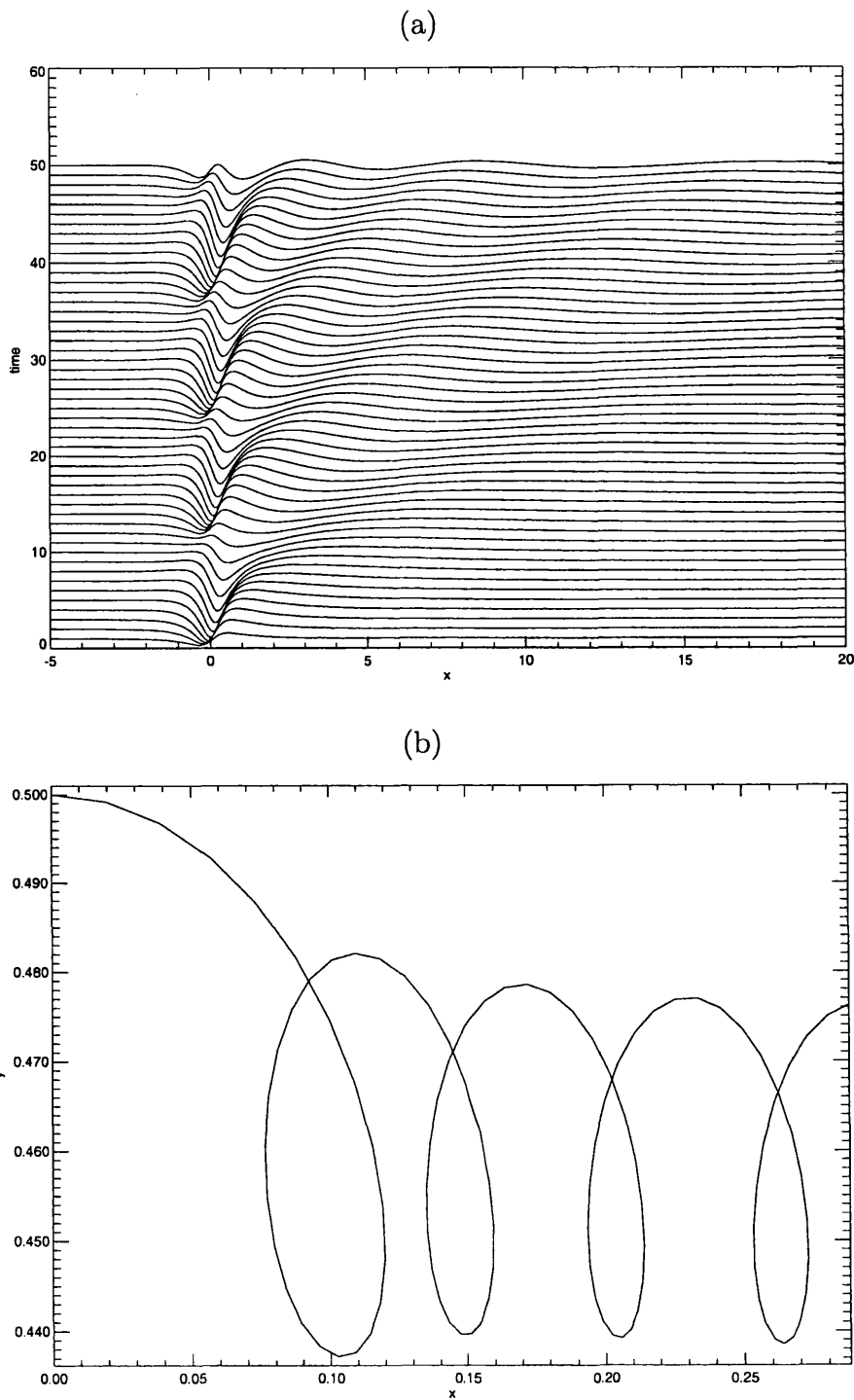
Figure 7.19: (a) The interface displacement for $y_0 = 0.5$ and $\Gamma = 2.5$, scaled by 2, (b) the vortex trajectory.

(a)

(b)
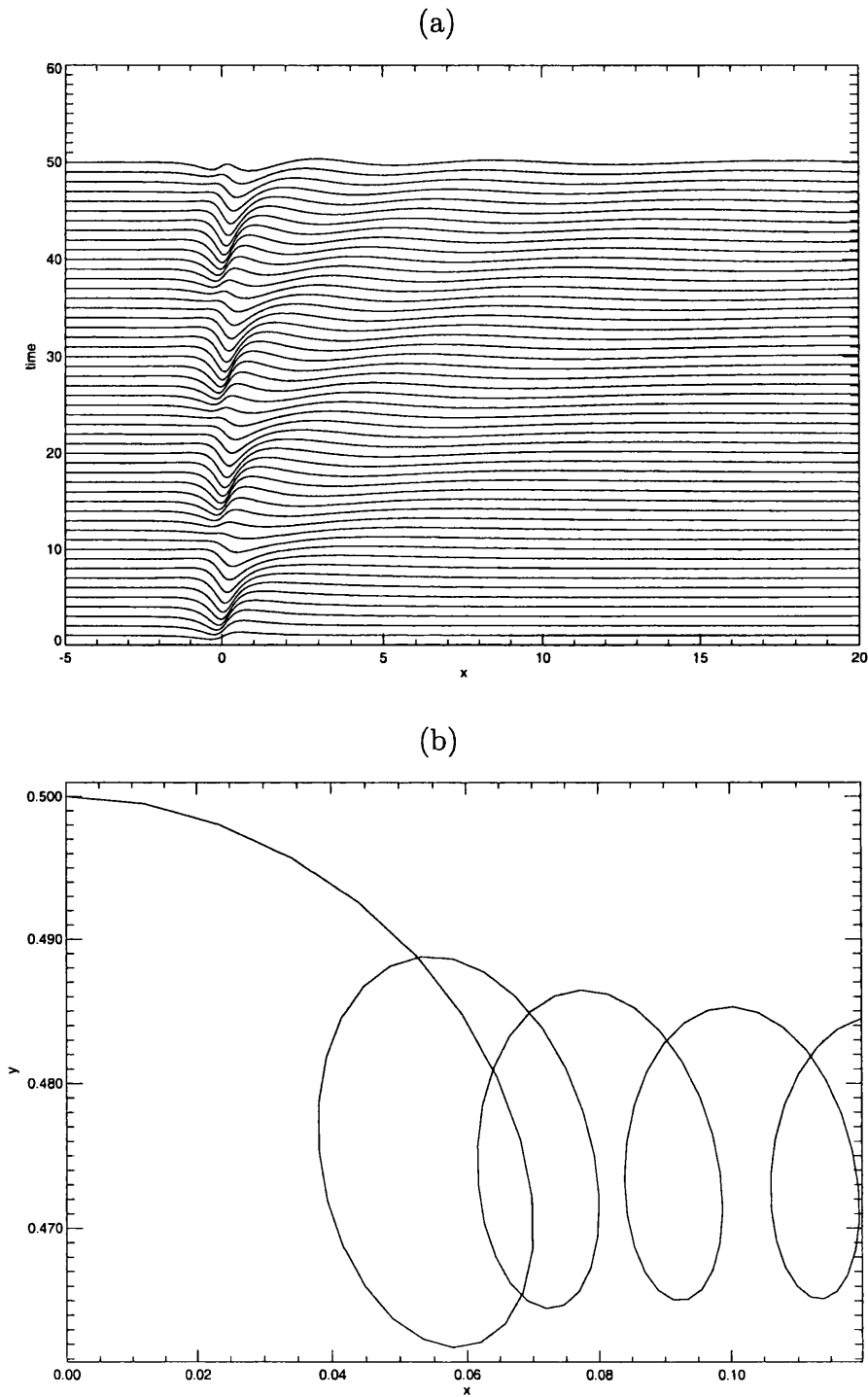
Figure 7.20: (a) The interface displacement for $y_0 = 0.5$ and $\Gamma = 1.5$, scaled by 2,

(b) the vortex trajectory.

(a)

(b)
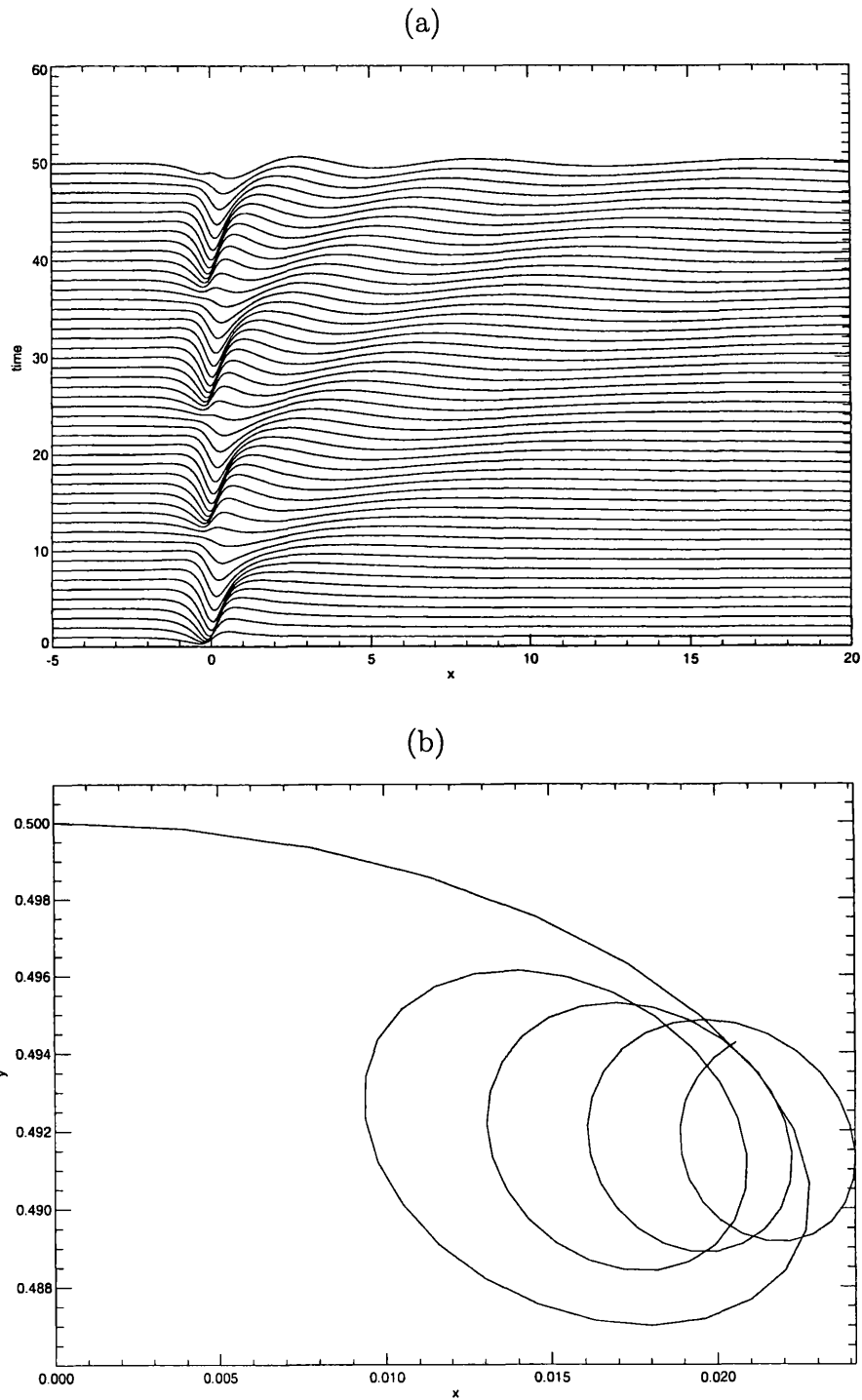
Figure 7.21: (a) The interface displacement for $y_0 = 0.5$ and $\Gamma = 0.5$, scaled by 10, (b) the vortex trajectory.

Case 3. $y_0 = 0.2$

This section shows the results for $y_0 = 0.2$ which is approaching the lower limit of $Y \sim O(1)$. Unsurprisingly the motion is dominated by the effect of the image vortex in the wall and all vortex trajectories show a much larger horizontal drift because of this.

Examining the anti-cyclonic case first, figure (7.22) shows the response for $y_0 = 0.2$ and $\Gamma = -3.5$. After initialisation the vortex oscillates for a short time but quickly moves away from the topographic wavetrain tail and settles down to a steady horizontal drift towards decreasing x which is due mainly to the vortex image in the wall; the pseudoimage only having a minor retarding effect on this drift. Note that the drift is still $O(\varepsilon)$, examining the plots an estimate of the drift speed is $U \approx 3/30$ which is exactly equal to $\varepsilon = 0.1$. Figure (7.23) shows the response at weaker forcing with $y_0 = 0.2$ and $\Gamma = -0.5$, the only differences are that the constant drift is smaller in magnitude and thus it will take longer for the system to reach a steady state.

Figures (7.24) and (7.25) show equivalent flow evolutions, vortex trajectories and errors for the cyclonic cases $\Gamma = 2.5$ and $\Gamma = 0.5$ respectively. The difference for the cyclonic vortex forcing is that the drift due to the image vortex is in the same direction as the topographic waves (namely towards increasing x) and so the pseudoimage can never escape from within the wavetrain and the vortex motion oscillates in y for a large time. The oscillations are decaying though and eventually a steady state will occur.

(a)

(b)
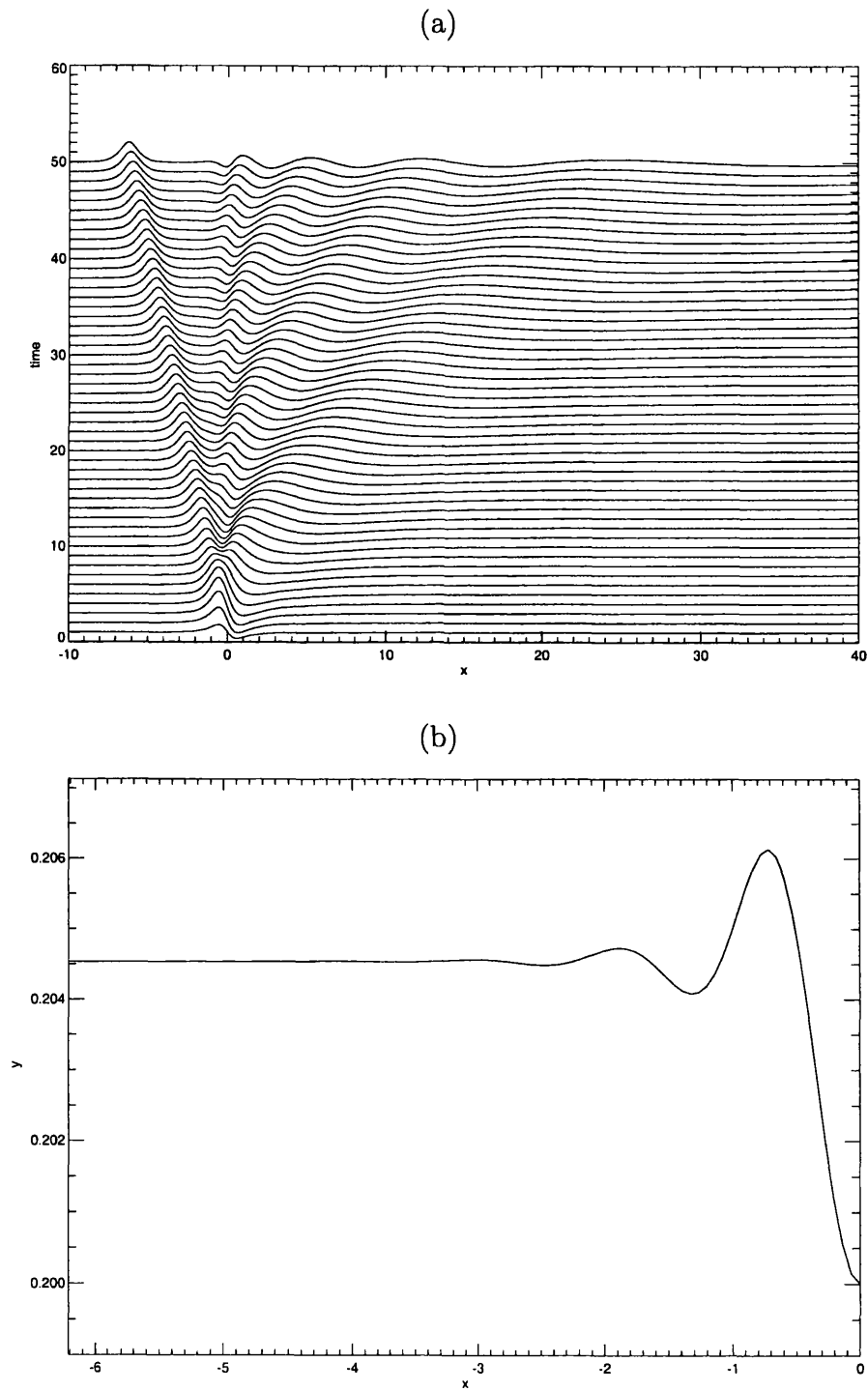
Figure 7.22: (a) The interface displacement for $y_0 = 0.2$ and $\Gamma = -3.5$, scaled by 5, (b) the vortex trajectory.

(a)

(b)
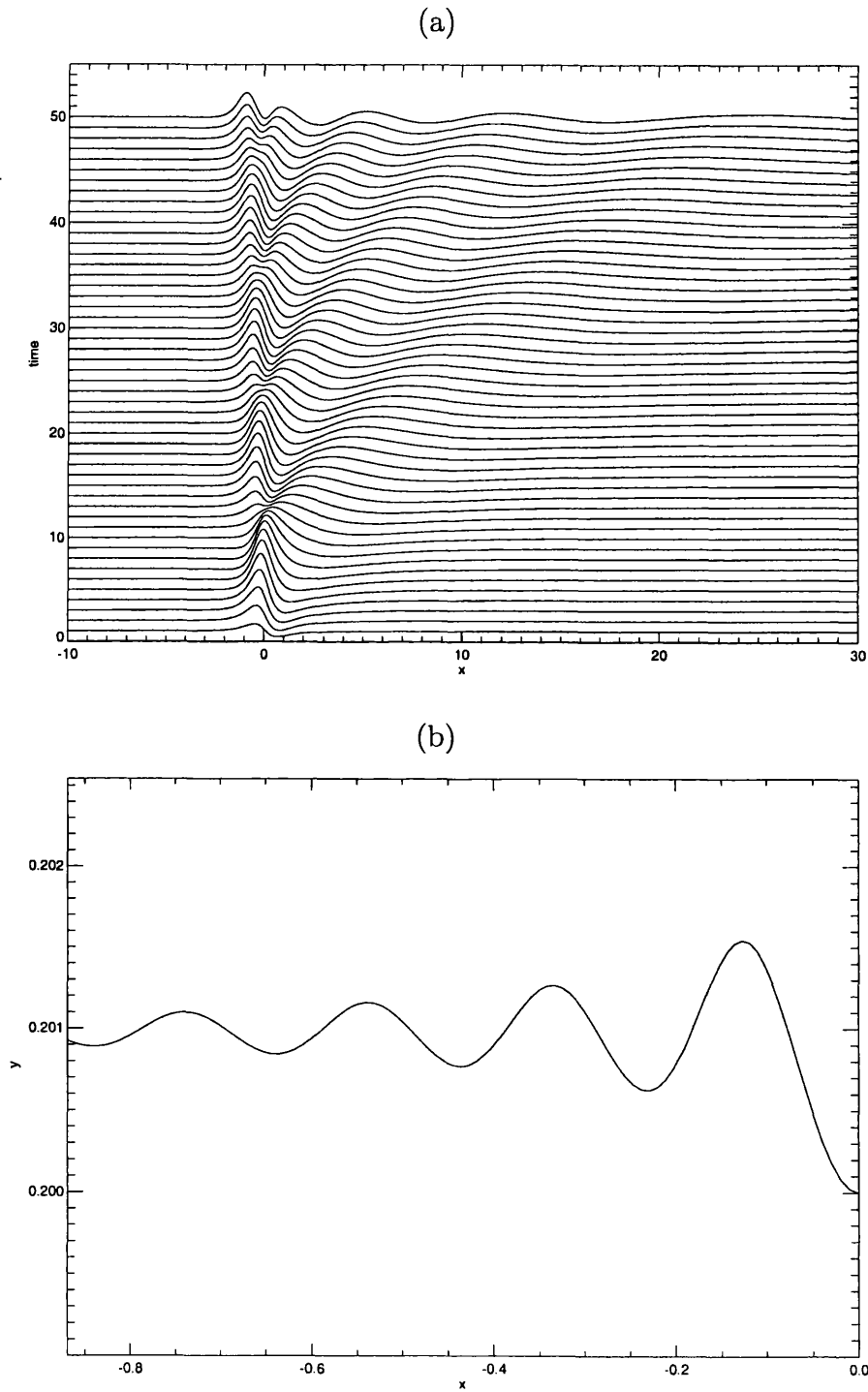
Figure 7.23: (a) The interface displacement for $y_0 = 0.2$ and $\Gamma = -0.5$, scaled by 30, (b) the vortex trajectory.

(a)

(b)
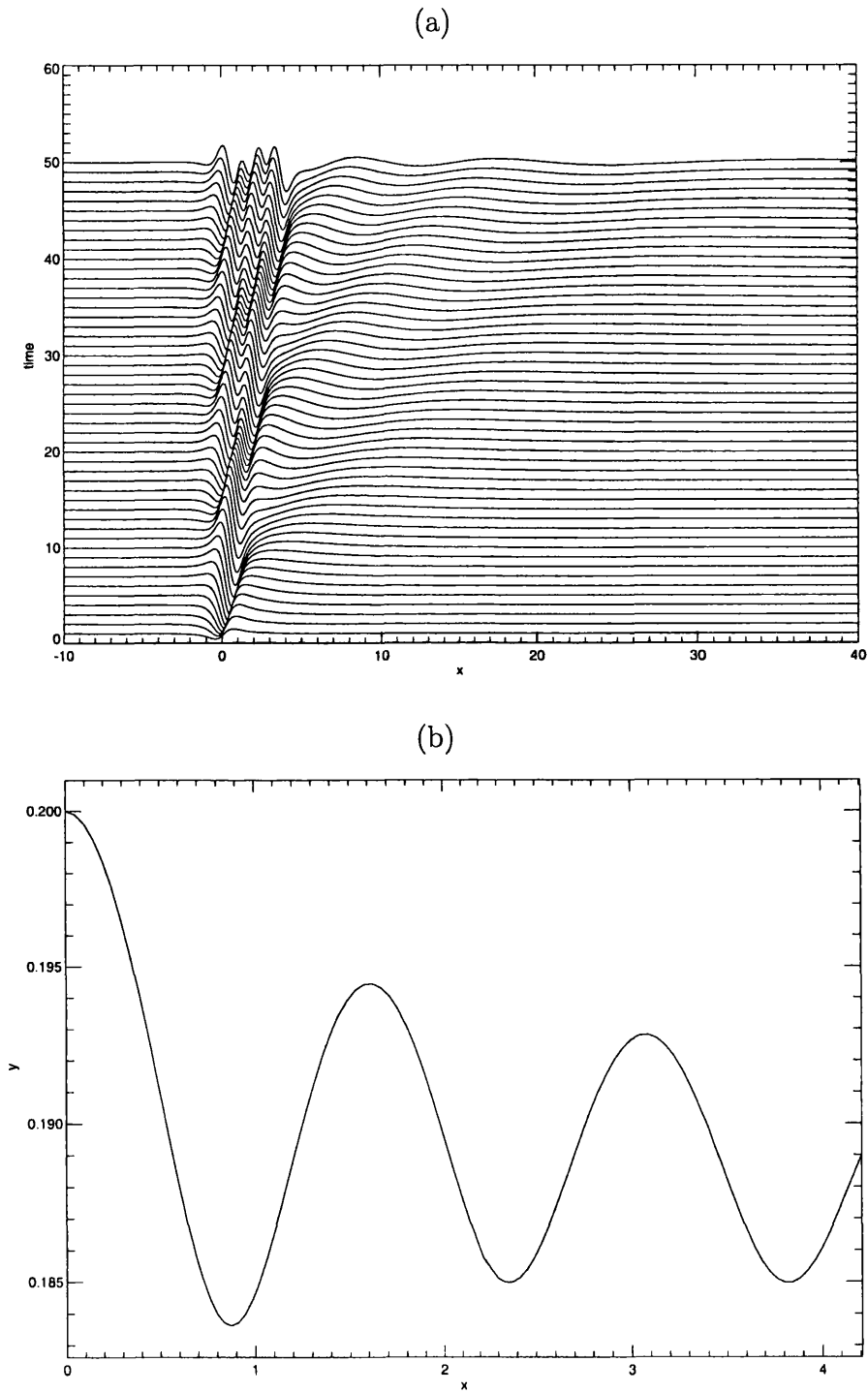
Figure 7.24: (a) The interface displacement for $y_0 = 0.2$ and $\Gamma = 2.5$, scaled by 5,

(b) the vortex trajectory.

(a)

(b)
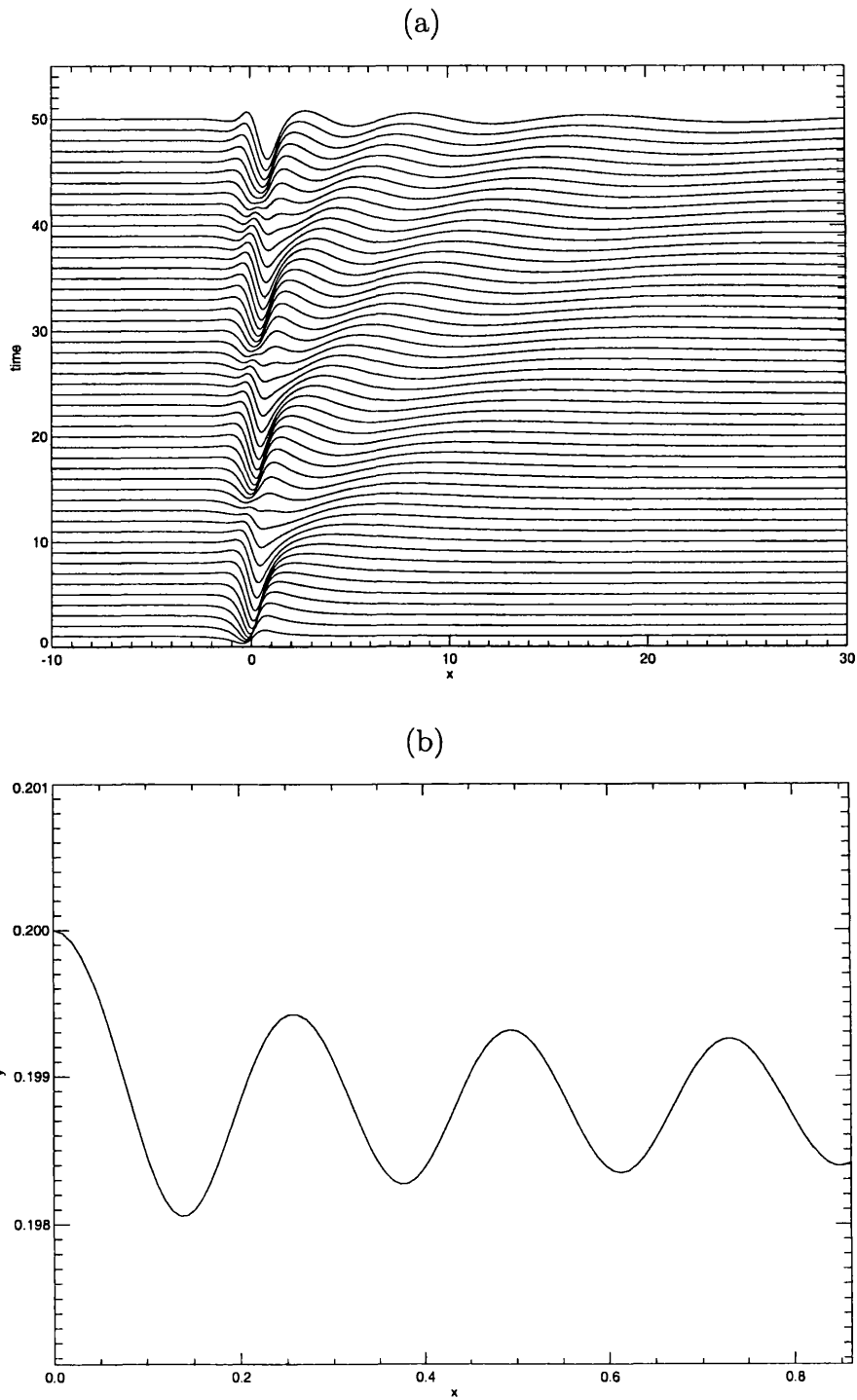
Figure 7.25: (a) The interface displacement for $y_0 = 0.2$ and $\Gamma = 0.5$, scaled by 30, (b) the vortex trajectory.

Summary

For the on-shelf cases shown above the vortex trajectories show that there is an interplay of influence between the vortex wall image and the vortex pseudoimage in the step. The motions of a vortex initialised close to the interface are dominated by the effect of the pseudoimage which induces a cyclonic/anti-cyclonic vortex towards decreasing/increasing x. However, conservation of momentum acts to pull an anti-cyclonic vortex towards the interface and so eventually nonlinear effects will become important. The opposite occurs for a cyclonic vortex which is pushed away and linear theory will be valid for large times.

For a vortex placed in the middle of the shelf the influences of the vortex wall image and vortex pseudoimage are equal but opposing in the direction of the velocity that they induce. This leads to the familiar looping vortex trajectories, the vortex never gets too close to the interface and so linear theory will remain valid.

When the vortex is placed close to the wall the vortex wall image dominates the motion causing cyclonic vortices to move towards increasing x and anti-cyclonic vortices towards decreasing x. Cyclonic/Anti-cyclonic vortices are pulled toward/away from the wall due to conservation of momentum. Anti-cyclones quickly reach a steady state as they move away from the topographic waves and do not interact with them, cyclonic vortices travel in the same direction as the waves and oscillate in y for longer times.

The next section looks at this last case in more detail.

7.5 $Y \sim O(\varepsilon)$.

This section is concerned with the linear response of the PV interface and vortex motions of a weak vortex that is initially placed very close to the wall. As was shown in chapter 3, the response at the PV interface lying along $y = 1$ is $O(\varepsilon^2)$ for a vortex of strength $O(\varepsilon)$. Even so, the closeness of the vortex to the wall creates a background, constant drift of $U \sim O(1)$ and this includes the possibility of a resonant interaction with the topographic waves that propagate along the interface also with $O(1)$ speeds. The purpose of this section is to examine cases which lead to steady state behavior, which in turn could lead to resonance and the breakdown of linear theory.

7.5.1 Derivation of Governing Equations

The streamfunction is written

$$\psi = \varepsilon^2 \psi_1. \tag{7.61}$$

Where ψ_1 is composed of a forcing term from the point vortex, Ψ and secondary motions, ϕ

$$\psi_1(x,y,t) = \phi(x,y,t) + \Psi(x - X(t), y - Y(t)). \tag{7.62}$$

The vortex is located at $(X(t), Y(t))$ where for $U = \Gamma/4\pi y_0$ and $y_0 = Y(0)/\varepsilon$ with $\Gamma, y_0 \sim O(1)$,

$$X \;=\; Ut + \varepsilon X_1(t) + \varepsilon^2 X_2 \ldots, \tag{7.63}$$

$$Y \;=\; \varepsilon y_0 + \varepsilon^2 Y_1(t) + \ldots. \tag{7.64}$$

Equations (3.44) give the higher order vortex velocities as

$$\frac{\mathrm{d}X_1}{\mathrm{d}t} = -\frac{\Gamma Y_1}{4\pi y_0^2}, \tag{7.65}$$

$$\frac{\mathrm{d}X_2}{\mathrm{d}t} = -\phi_y(X, Y), \tag{7.66}$$

$$\frac{\mathrm{d}Y_1}{\mathrm{d}t} = \phi_x(X, Y). \tag{7.67}$$

For this case at the step the vortex and its image are approximated to a dipole and so to $O(\varepsilon^2)$

$$\Psi(x - X(t), y) \simeq \frac{-\Gamma(y_0 + \varepsilon Y_1)y}{\pi((x - X)^2 + y^2)}. \tag{7.68}$$

Standard Fourier analysis reveals that the transform $\hat{\phi}$ of the secondary motions $\phi(x, y, t)$ in the region $0 < y < 1$ are given by

$$\hat{\phi} = 2B(t)\sinh(ky), \tag{7.69}$$

for some undetermined function $B(t)$. The second of the jump conditions given by (3.51) determines an evolution equation for the unknown function $B(t)$.

$$\frac{\mathrm{d}B}{\mathrm{d}t} + i\omega B = -\frac{i\hat{\Psi}(k, 1)}{2}e^{-ikX(t)-|k|}. \tag{7.70}$$

Now $\hat{\Psi}(k, 1)$ is defined

$$\hat{\Psi}(k, 1) = -\Gamma(y_0 + \varepsilon Y_1)e^{-|k|}. \tag{7.71}$$

The linearised kinematic condition relates the cross-step velocity at $y = 1$ to the interface displacement $\bar{\eta}$ (see figure (7.1)) through

$$\frac{\partial}{\partial t}\bar{\eta}(x, t) = \frac{\partial}{\partial x}\psi_1(x, 1, t). \tag{7.72}$$

Now $\bar{\eta} = 1 + \varepsilon^2 \eta(x, t)$ and writing (7.72) in Fourier space gives

$$\hat{\eta}_t = ik\hat{\psi}_1(k, 1, t). \tag{7.73}$$

Which can be written

$$\hat{\eta}_t = ik(\hat{\phi}(k, 1, t) + \hat{\Psi}(k, 1, t)e^{-ikX(t)}), \tag{7.74}$$

where $\hat{\phi}$ is given by (7.69) and $\hat{\Psi}$ by (7.71).

7.5.2 Momentum Conservation

As before, the momentum P in the x direction is given by the integral over space of the product of PV ζ and y

$$P = \int \zeta \, y \, dA. \tag{7.75}$$

The response at the interface is now $O(\varepsilon^2)$ and so $\bar{\eta} = 1 + \varepsilon^2 \eta$, putting this into (7.21) gives

$$P(t) = \varepsilon \Gamma Y(t) + \frac{\varepsilon^4}{2} \int_{-\infty}^{\infty} \eta^2 \, dx. \tag{7.76}$$

Note that the first term is in fact $O(\varepsilon^2)$ since $Y \sim O(\varepsilon)$. The error is still given by (7.23).

7.6   Linear Response for an On-Shelf vortex that is initially close to the Wall

7.6.1   Small Time Solution

As before, expand all variables dependent on t in a Taylor series up to $O(t^3)$. There is now an extra term in the equation of motion for $X(t)$,

$$
\begin{aligned}
X_1(t) &= X_{1a}t + X_{1b}t^2 + X_{1c}t^3 + \ldots, \\
X_2(t) &= X_{2a}t + X_{2b}t^2 + X_{2c}t^3 + \ldots, \\
Y_1(t) &= Y_{1a}t + Y_{1b}t^2 + Y_{1c}t^3 + \ldots, \\
B(t) &= B_1 t + B_2 t^2 + B_3 t^3 + \ldots, \\
\hat{\psi}(t) &= \hat{\psi}_1 t + \hat{\psi}_2 t^2 + \hat{\psi}_3 t^3 + \ldots, \\
\hat{\eta}(t) &= \hat{\eta}_1 t + \hat{\eta}_2 t^2 + \hat{\eta}_3 t^3 + \ldots
\end{aligned}
\tag{7.77}
$$

In a manner identical to the small-time analysis for $Y \sim O(1)$ the solution can be found and is

$$
B_1 = \frac{i\Gamma y_0}{2} e^{-2|k|},
\tag{7.78}
$$

$$
B_2 = -\frac{i}{2} B_1(\omega + kU),
\tag{7.79}
$$

$$
B_3 = \frac{y_0 B_1}{3}\left(\frac{\varepsilon}{2}\mathcal{F}(ik\hat{\phi}_1) - \frac{y_0 i k \varepsilon^2}{2}\mathcal{F}(\hat{\phi}_{1y}) + \frac{y_0 k^2 U^2}{2}\right).
\tag{7.80}
$$

The equations for the vortex center are

$$
X = Ut - \frac{\varepsilon^2}{2}\mathcal{F}(\hat{\phi}_{1y})t^2 - \left(\frac{\varepsilon\Gamma}{48\pi y_0^2}\mathcal{F}(ik\hat{\phi}_1) + \frac{\varepsilon^2}{3}\mathcal{F}(\hat{\phi}_{2y})\right)t^3,
\tag{7.81}
$$

$$
Y = \varepsilon y_0 + \frac{\varepsilon^2}{2}\mathcal{F}(ik\hat{\phi}_1)t^2 + \frac{\varepsilon^2}{3}\mathcal{F}(ik\hat{\phi}_2)t^3.
\tag{7.82}
$$

All of the inverse transforms shown above are to evaluated at $(Ut, \varepsilon y_0)$. The function $\hat{\phi}$ can be found by substitution of (7.78) - (7.80) into (7.69) and then $\hat{\eta}$ can be found using (7.74).

7.6.2 Results of Numerical Experiments

In order to maintain consistency with the previous chapters and also with chapter 8 the results of this section are shown in a frame of reference moving at the vortex drift speed $U = \Gamma/4\pi y_0$. All of the rest of the figures in this section are shown in this manner.

Again the results of this section fall into the three categories of supercritical $(U > 1)$, subcritical $(U < 1)$ and flow at criticality $(U = 1)$. However, unlike in chapter 3 the vortex is free to move consistent with the constraints of momentum conservation. The three cases are dealt with below.

Supercritical Flow

Figure (7.26) shows a typical example where the initial conditions are such that the equivalent, steadily propagating vortex would result in a supercritical response $(U = 1.3)$. In the modified dynamics that include the secondary motions of the vortex the results are not changed drastically for the case $U = 1.3$, $\kappa = 4$. After initialisation the response of the interface at the vortex is seen as a growing 'hump' of cyclonic (shallow to deep) fluid that travels with the vortex, this is the pseudoimage of the vortex in the interface. The first response of the vortex to this extra vortical fluid is to be pushed closer to the wall (c.f. section 7.2.2) and this happens on a short time interval (c. $t = 0 - 20$). This is in accordance to momentum conserva-

tion (7.76). As the vortex moves closer to the wall it speeds up in the horizontal direction and eventually a balance is reached consisting of the vortex drift due to its image in the wall plus its extra horizontal velocity due to the influence of the pseudoimage. The disturbance due to initialisation of the experiment is immediately washed downstream, forming a transient, dispersive wavetrain and does not play any further role in the dynamics. The vortex trajectory is shown in figure (7.27a) which is again plotted in a frame of reference moving with speed U (as are all the other trajectory plots in this section). The error for this experiment is shown in figure (7.27b) and averages out at approximately 4×10^{-8}. The role of conservation of momentum as elucidated in section 7.2.2 case 1 is all important and shows that as the transient downstream waves decay, the vortex-wave system will eventually reach a steady state consisting of the vortex/pseudoimage and vortex/image pair.

Figure (7.28) shows an experiment that is closer to resonance but still on the supercritical side ($U = 1.1$). Looking at the vortex trajectory (7.28b) it is immediately obvious that the vortex has been pushed much closer to the wall resulting in a greater horizontal drift and has therefore moved further in the horizontal in the same time interval. This is because the flow is near criticality and the response of the interface at the vortex is much stronger, resulting in a larger 'hump' of fluid. However the path is more gradual than figure (7.27b), the change in Y over time is smaller and this can be attributed to the fact that the wave disturbance downstream of the vortex has not totally removed itself from the region of the vortex, energy is still being fed to the waves and the vortex responds on a slower timescale. The indications are that the system will eventually reach a steady state as figure (7.28a) shows that the interface is flattening out downstream of the vortex. Before examining the resonant case the subcritical response is discussed.
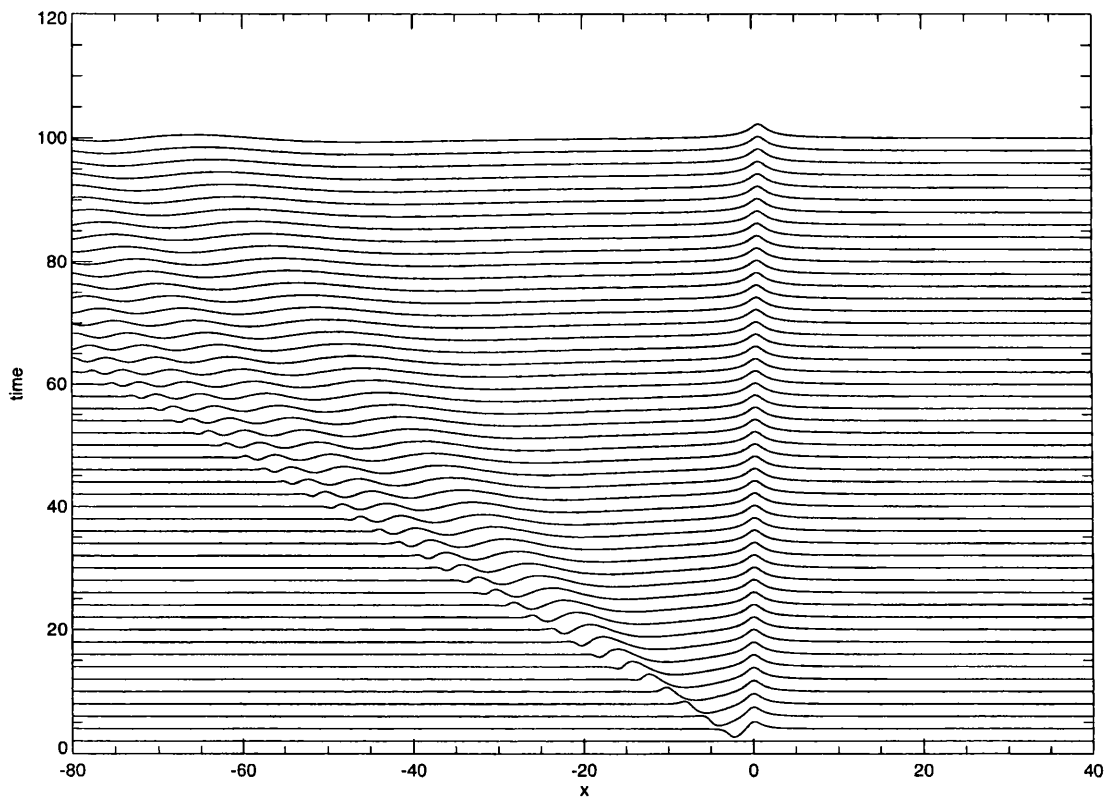
Figure 7.26: Flow for $U = 1.3$, $\kappa = 4$. The graph has been scaled by 5.
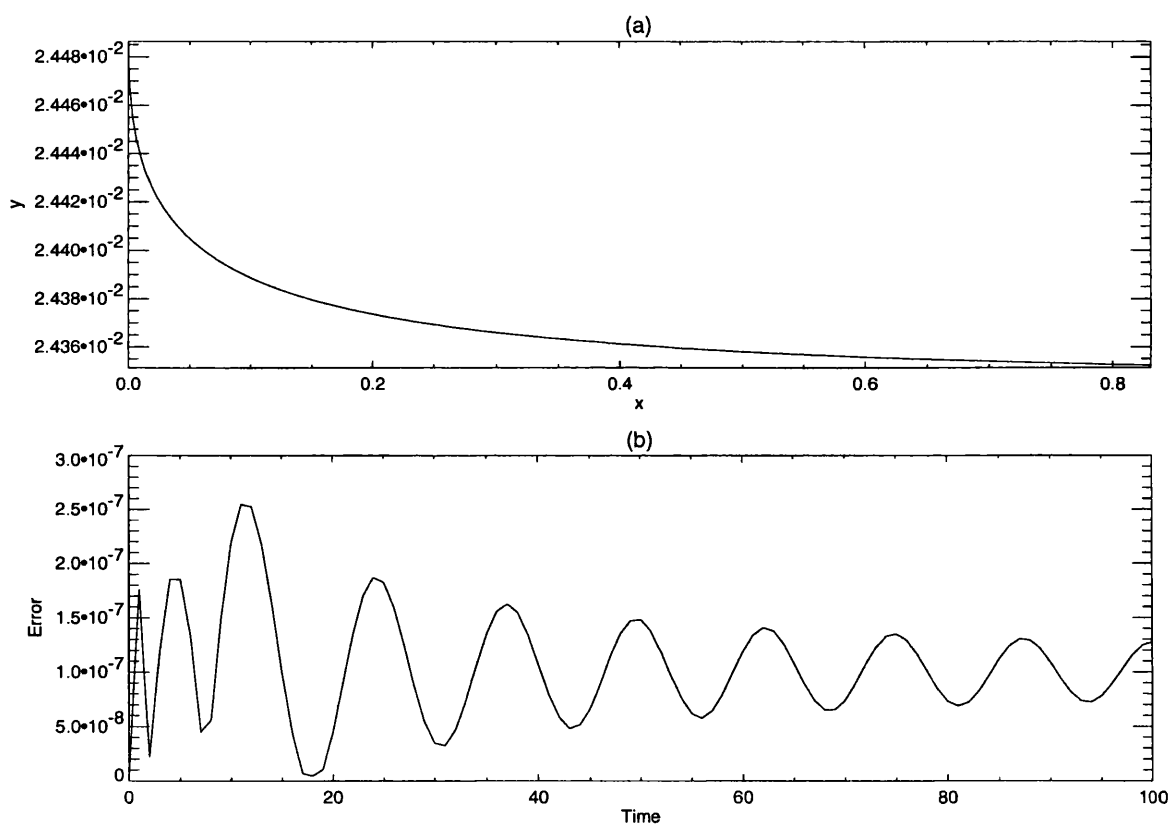
Figure 7.27: (a) Vortex trajectory and (b) error plot for $U = 1.3$, $\kappa = 4$.

(a)

(b)
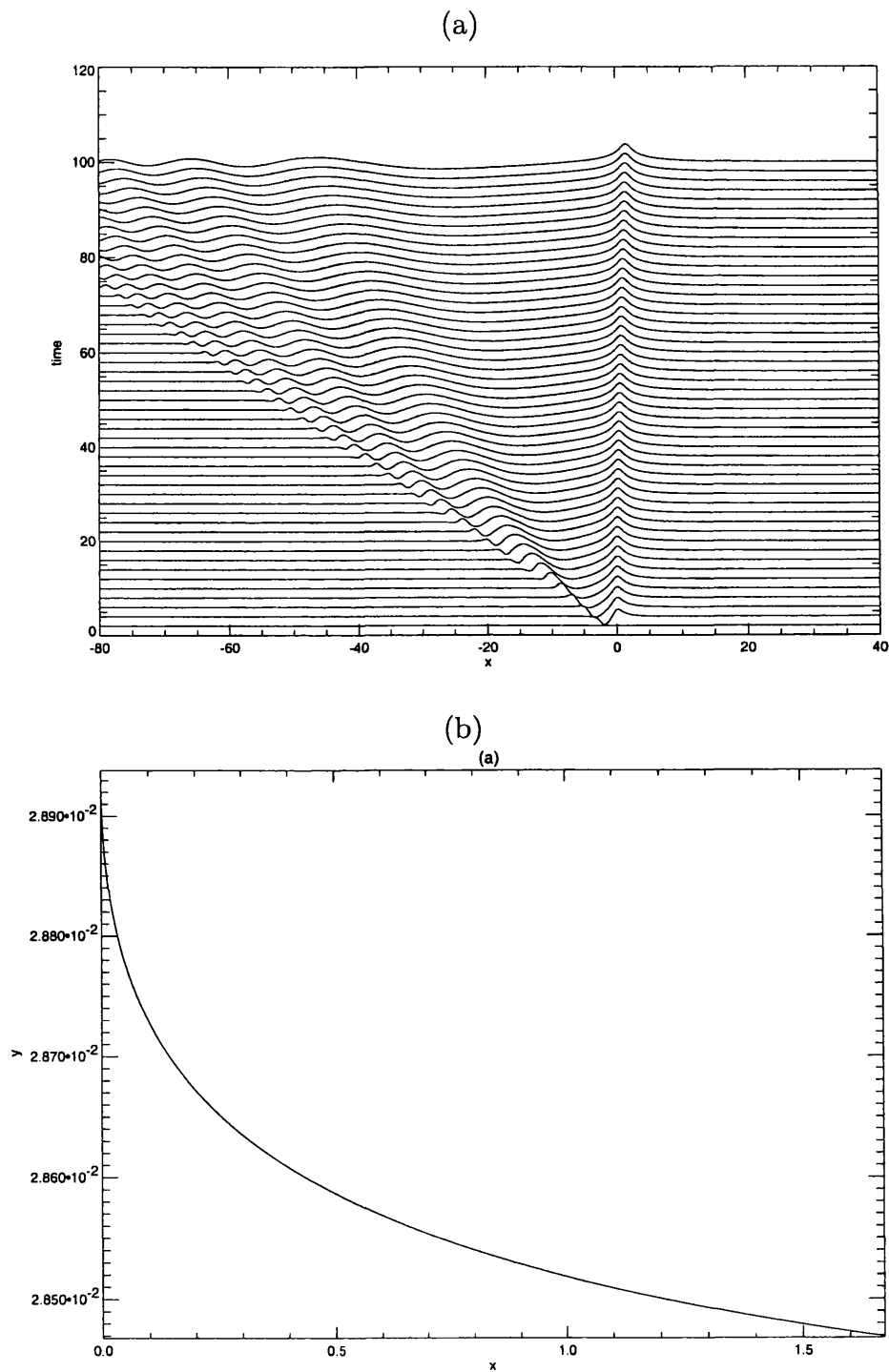
Figure 7.28: (a) The interface displacement for $U = 1.1$, $\kappa = 4$, scaled by 5, (b) the vortex trajectory.

Subcritical Flow

The results shown in figure (7.29) are for $U = -1$ and $\kappa = -4$ and the vortex trajectory is shown in figure (7.29b). As $U < 0$ the vortex is moving towards decreasing x and away from the waves as they can only travel in the opposite direction. As usual the initial response consists of a small disturbance of the interface that travels with the vortex and transient waves that, in this case, quickly move off ahead of the vortex. The initial response of the vortex to this disturbance is to move sharply away from the wall (c.f. section 7.2.2) and this happens on a much quicker timescale than the supercritical case. There is also not much associated change in the horizontal position of the vortex until the vortex reaches a suitable y position (approximately $y = 0.03$ in this case) at which point the weak effect of the pseudoimage above it propels the vortex ever so slightly towards increasing x. The main drift is still in the opposite direction though.

Figures (7.30) - (7.31) show the results for $U = 0.5$, 0.7 and $\kappa = 4$. In this region $0 < U < 1$ (and of course $U \sim O(1)$) the steady, linear version of chapter 3 describes a wavetrain that extends between the fastest wave, the longwave and the slowest (not traveling, or traveling at $-U$ in this frame of reference) and these were found by contour integration and application of Cauchy's Residue Theorem. Two poles contributed residues and these corresponded to the places where the phase velocity of the waves equaled the drift speed of the vortex. Here the region of the parameter space is the same and unsurprisingly the interface evolution is similar in structure. The vortex can no longer escape from the waves and remains in the middle of the wave train, with a large amplitude (when compared to the previous results) wavetrain downstream and longwaves of smaller amplitude upstream (see figure (7.30a)). Its motion consists of a gradual drift towards the wall in order to conserve

(a)

(b)
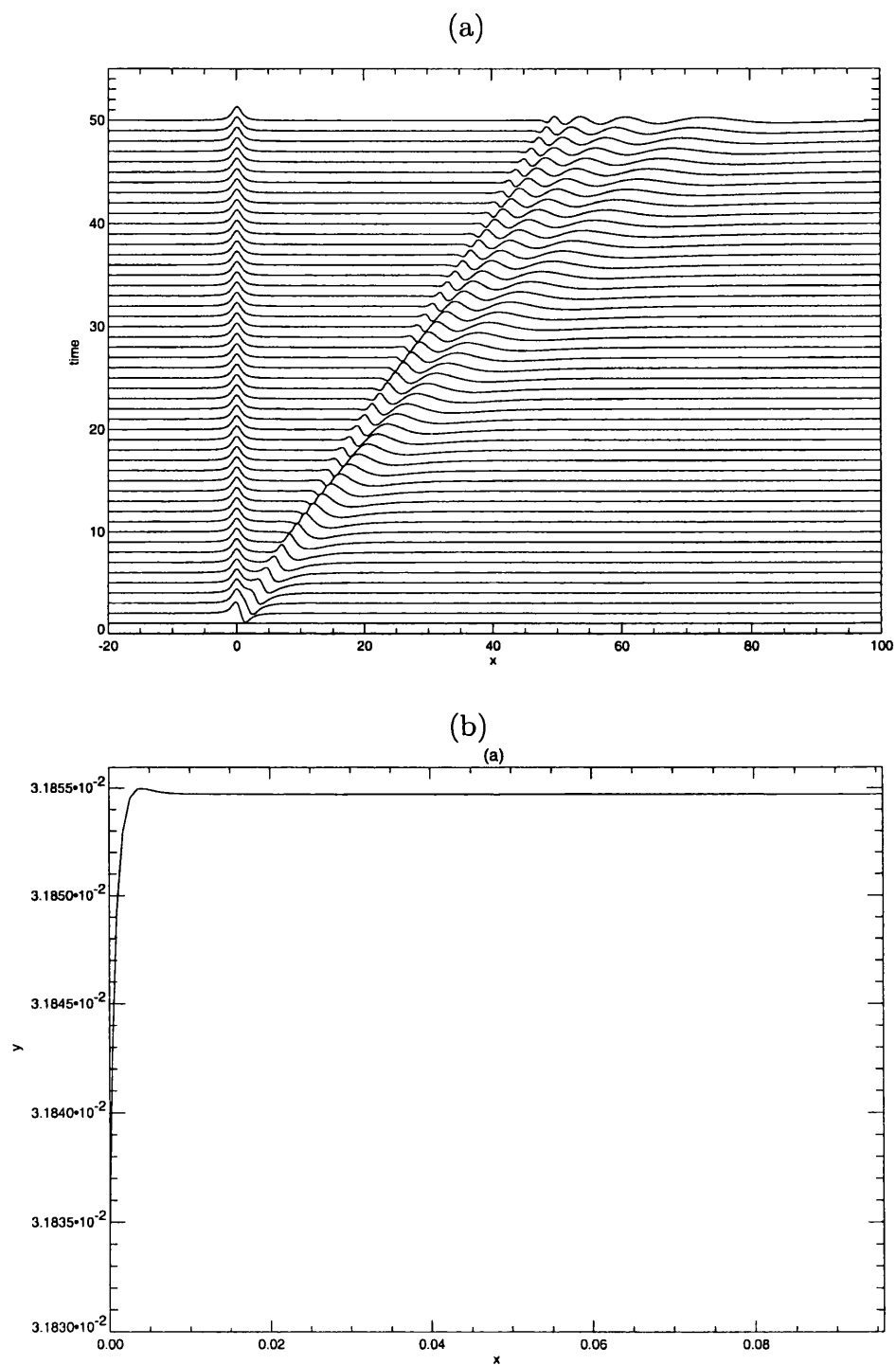
Figure 7.29: (a) The interface displacement for $U = -1$, $\kappa = -4$, scaled by 5, (b) the vortex trajectory.

momentum and an associated increase in its horizontal velocity due to the presence of the waves and its new proximity to its image in the wall.

Bell [1989] states that in this regime the vortex-wave interaction is 'unstable' and no steady state can form, this is due to the presence of the trailing lee waves. Any situation where a standing lee wave can form behind the vortex will mean that energy is continually being fed to the waves, this is manifested in the vortex trajectory as a continual drift in the y direction. This is illustrated in figures (7.32a) and (7.32b) where the integrations for $U = 0.5$, $\kappa = 4$ have been continued for longer times.

The implications of these results are that, for U, $\kappa > 0$, the vortex always gets initially pushed towards the wall which increases its horizontal speed (together with the effect of the interface displacements) and so it is natural to infer that the near-critical case will not result in an ever-growing response of the interface at the vortex but rather that the vortex will get pushed closer and closer to the wall, speeding up as it does so and then passing through criticality to the supercritical flow.

Resonant Flow

Figure (7.33) shows the near-resonant response with $U = 0.9$ and $\kappa = 4$. The question of whether linear resonance can occur is now in doubt as any growth/decline of the interface will compel the vortex to move towards or away from the wall. Bell [1989] describes any situation where there is a constant transfer of momentum from the vortex to the waves as an unstable interaction and will result in permanent unsteady motion. The near resonant case shown here is one such interaction, the parameters for the flow are $U = 0.9$, $\kappa = 4$ for times up to $t = 100$. The response of the interface is very similar to the steady case of chapter 3 however now the vortex can respond to the extra cyclonic PV generated above it by moving nearer

(a)

(b)
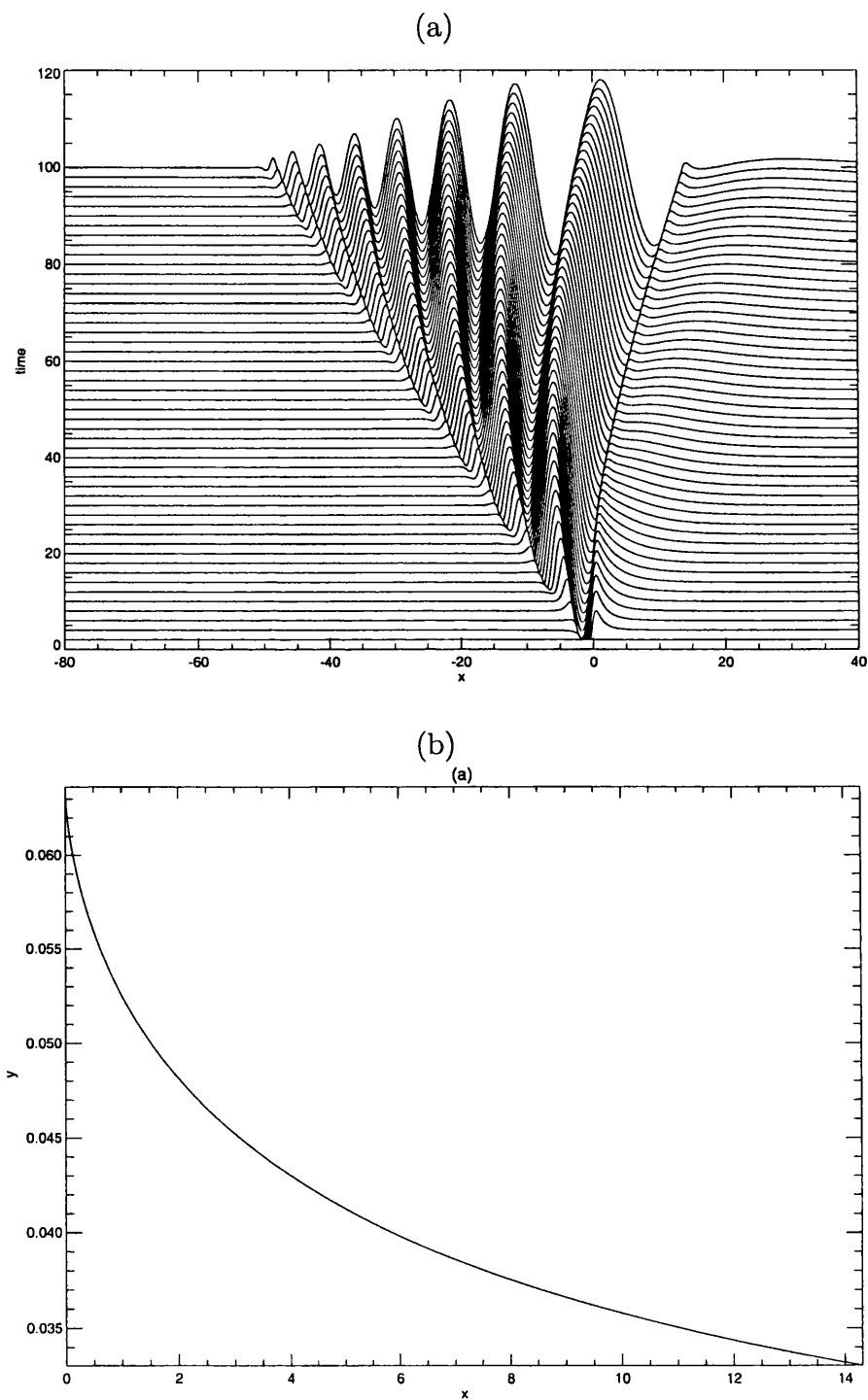
Figure 7.30: (a) The interface displacement for $U = 0.5$, $\kappa = 4$, scaled by 5, (b) the vortex trajectory.

(a)

(b)
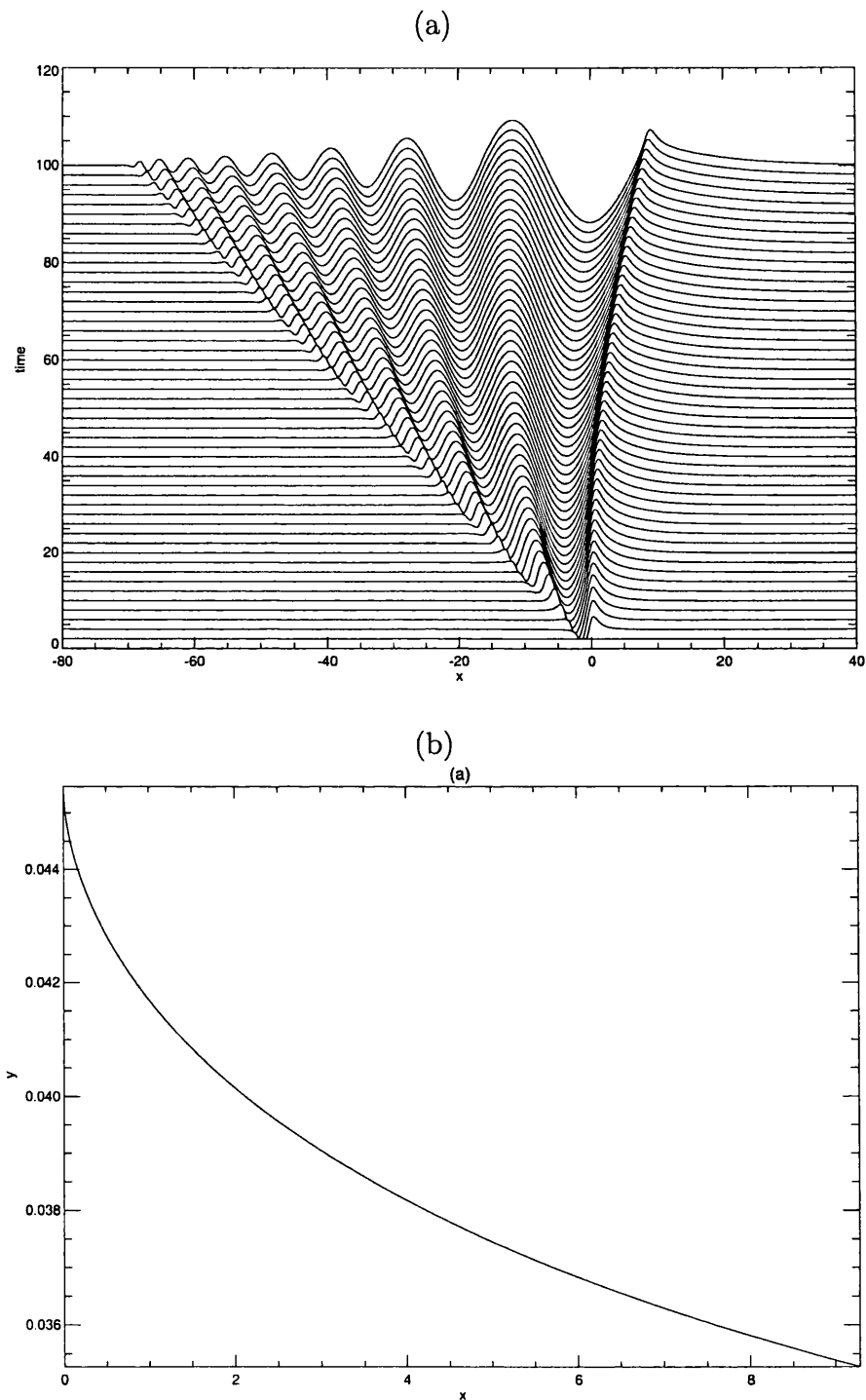
Figure 7.31: (a) The interface displacement for $U = 0.7$, $\kappa = 4$, scaled by 5, (b) the vortex trajectory.

(a)

(b)
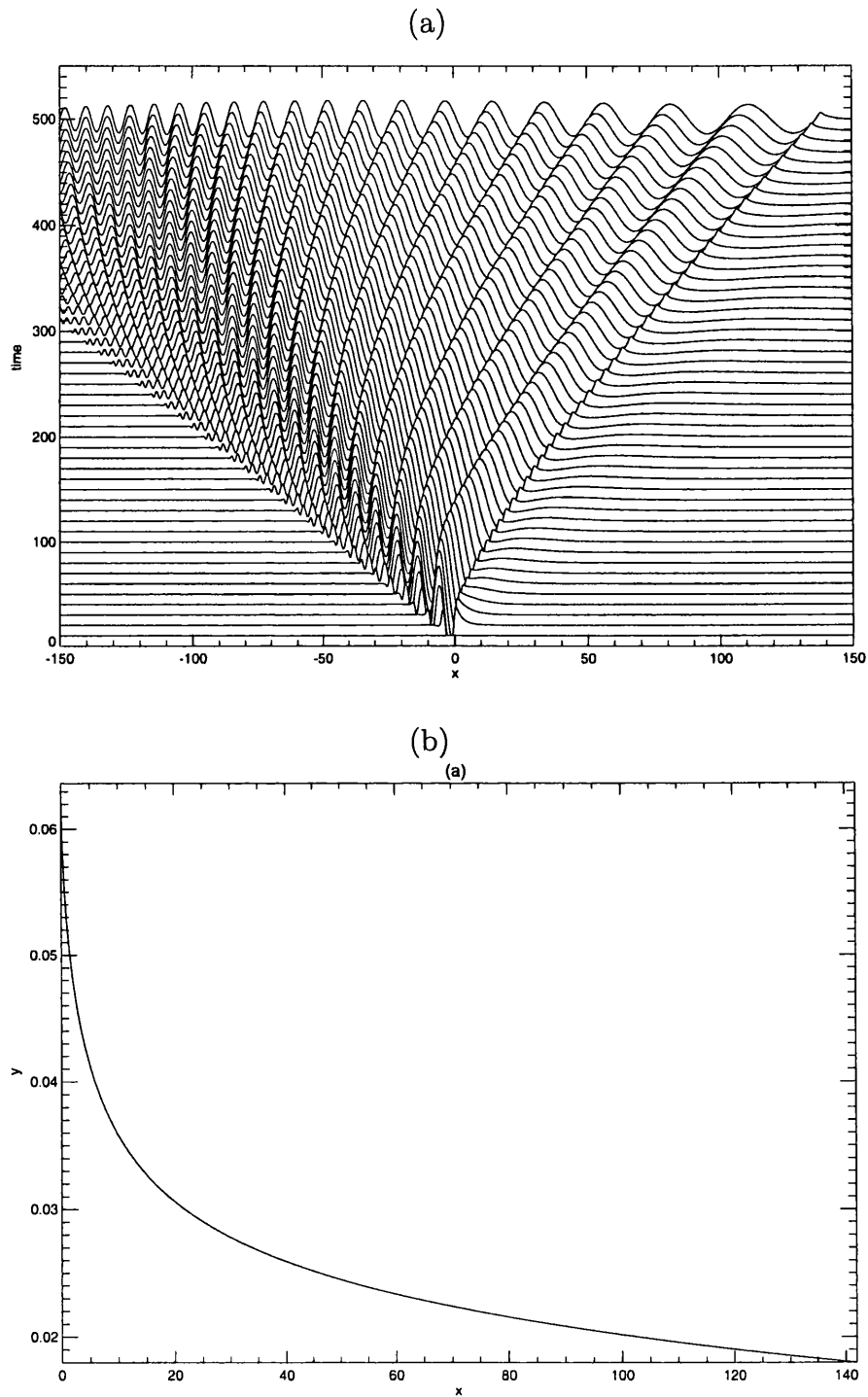
Figure 7.32: (a) The interface displacement for $U = 0.5$, $\kappa = 4$ integrated to a larger time, scaled by 10, (b) the vortex trajectory.

to the wall. The trajectory is shown in figure (7.33b) and it is quite clear that the vortex has not settled down to steady, horizontal motion with no variation in y. Figures (7.34a) and (7.34b) show the interface evolution, vortex trajectory and error for the 'resonant' case $U = 1$, $\kappa = 4$. Compared to figure (7.33b) the distance traveled horizontally is seen to have halved due to the fact that the change in y is smaller. This indicates that the effect of the waves at the vortex is smaller than for $U = 0.9$, indeed if the vortex is started at resonance $U = 1$ and then speeds up it then becomes the linear supercritical flow and resonance will not be achieved.

A longer integration for $U = 0.9$, $\kappa = 4$ is shown in Figures (7.35a) and (7.35b), this time ending at $t = 300$. The results show that the vortex does appear to reach a speed very close to $U = 1$, examining figure (7.35a) the change in χ of the wavefront over 100 time units from $t = 200 - 300$ is 1. However conservation of momentum will always ensure that any increase in wave amplitude will be complimented by the vortex moving towards the wall, thus speeding up in the horizontal implying that the near resonant or resonant cases will always pass into the supercritical state.

(a)

(b)
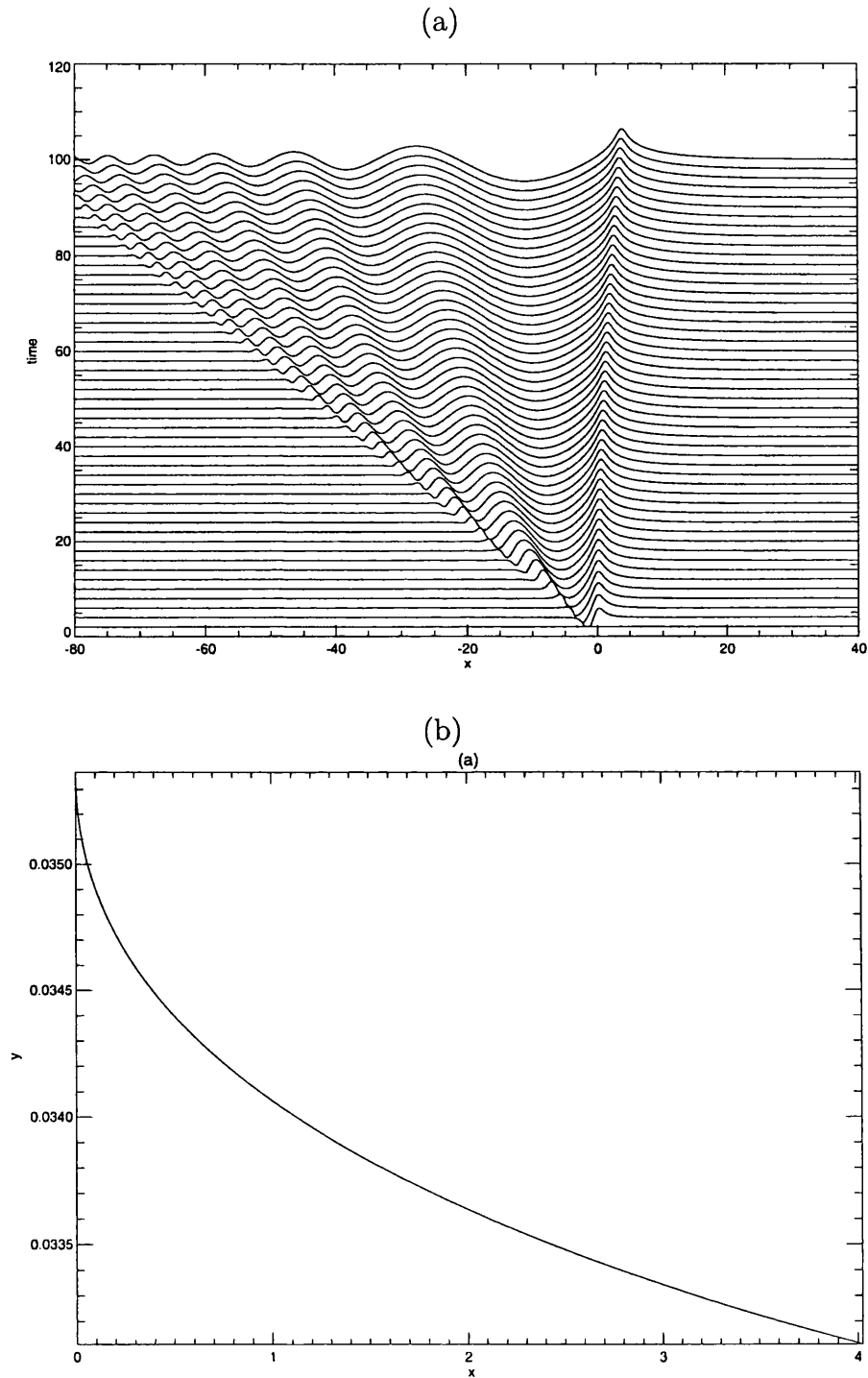
Figure 7.33: (a) The interface displacement for $U = 0.9$, $\kappa = 4$, scaled by 5, (b) the vortex trajectory.
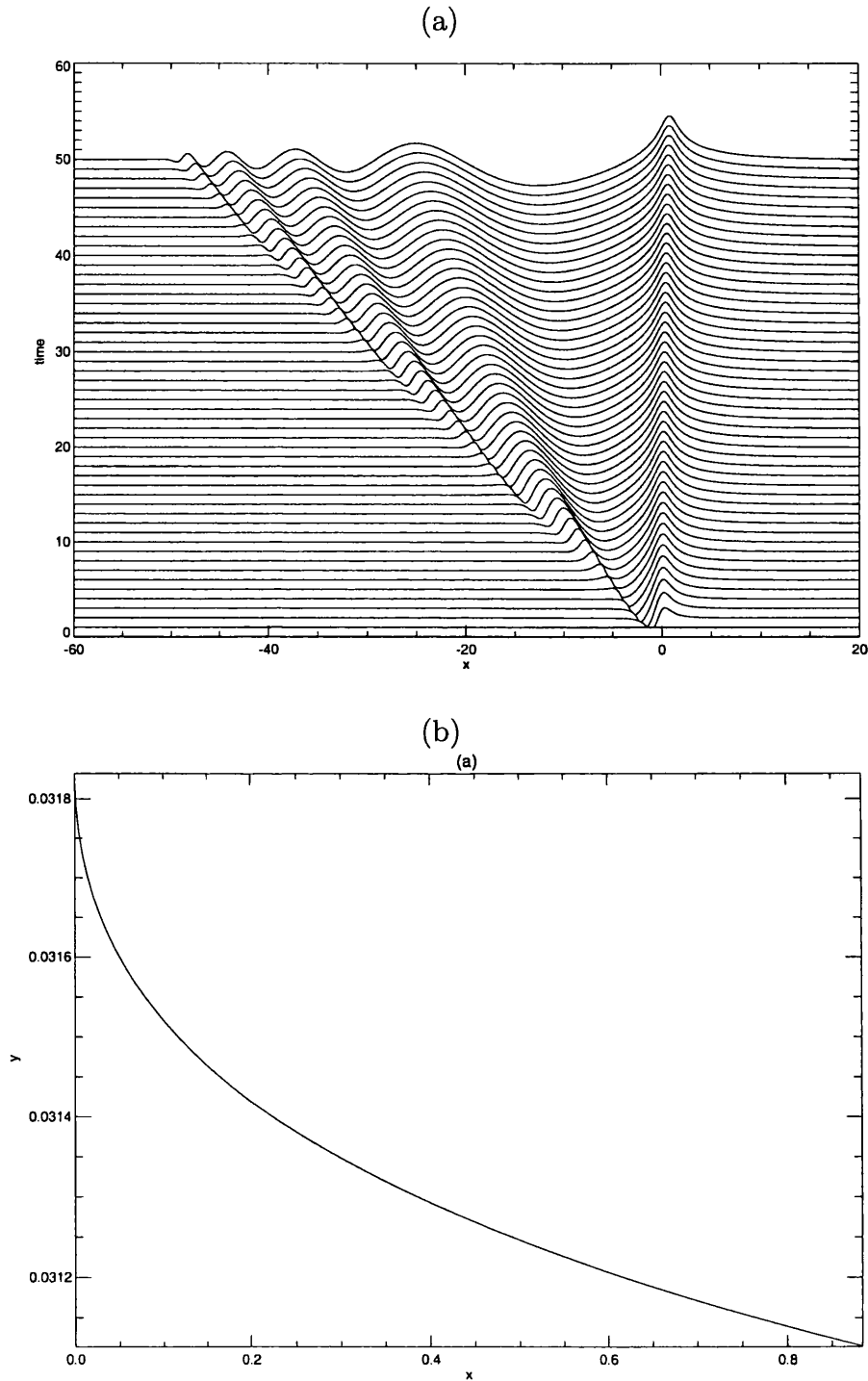
Figure 7.34: (a) The interface displacement for $U = 1$, $\kappa = 4$, scaled by 5, (b) the vortex trajectory.

(a)

(b)
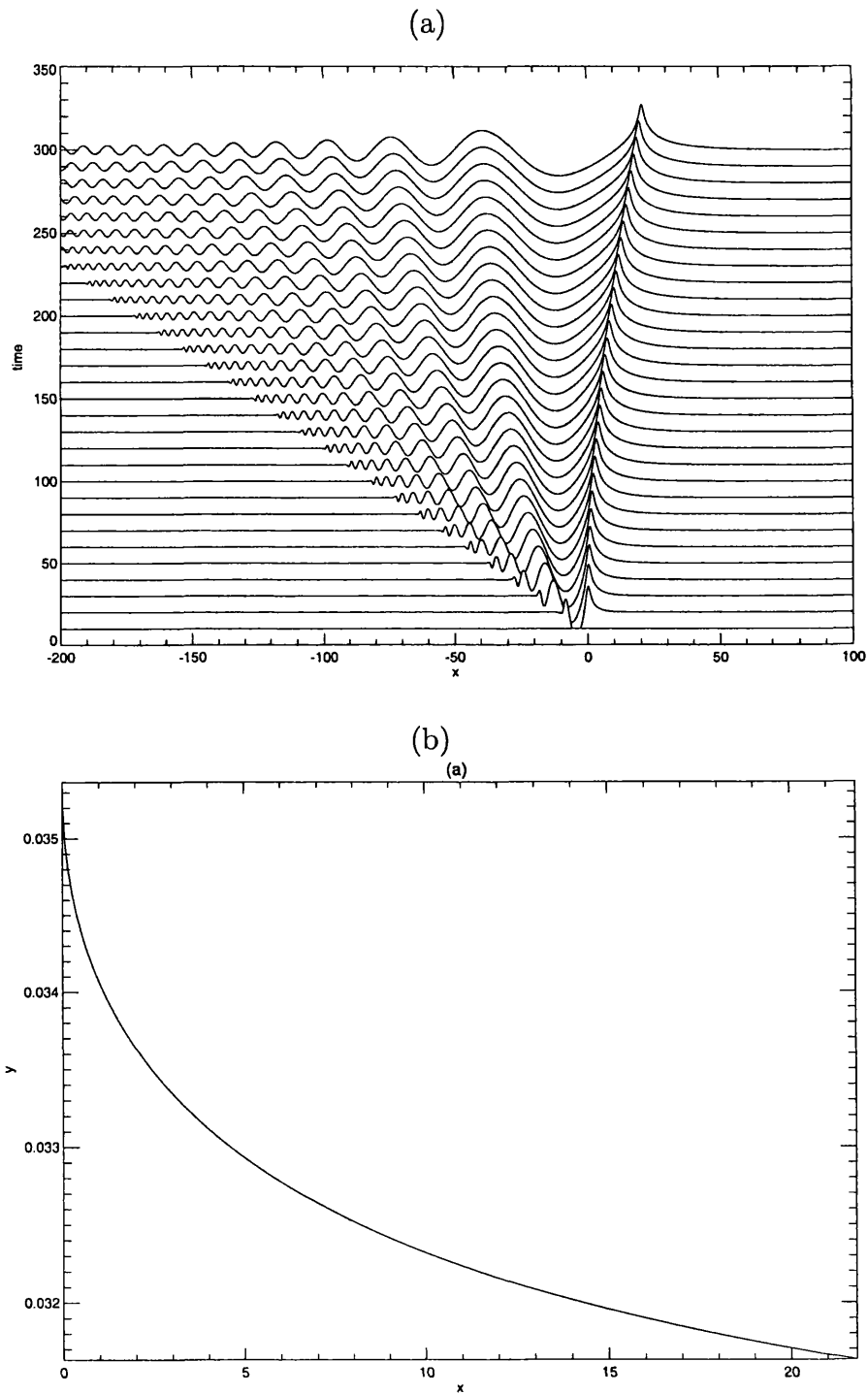
Figure 7.35: (a) The interface displacement for $U = 0.9$, $\kappa = 4$ for longer times, scaled by 20, (b) the vortex trajectory.
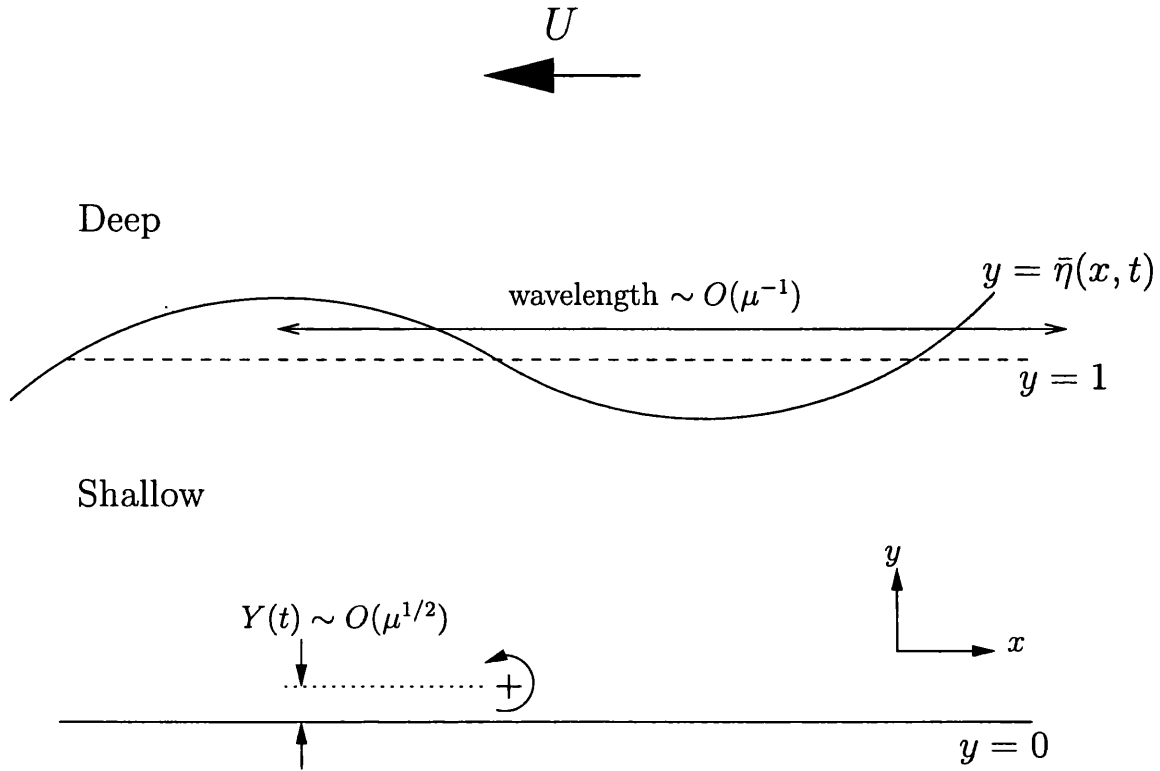
Figure 7.36: Schematic diagram for the derivation of the linear longwave problem.

7.7 The Linear Long-Wave Formulation.

In this section the velocity induced on the vortex by the interfacial waves is examined in the linear long-wave limit, this serves as a prelude to the next section where the same problem is examined for the weakly-nonlinear, long-wave case. The problem is set up as shown in figure (7.36) with a free stream U from right to left and the material contour separating the two regions of differing PV will be $\bar{\eta}(x, t)$. First, the y velocity due to the waves can be written as,

$$\frac{dY}{dt} = \frac{1}{2\pi} \int_{-\infty}^{\infty} \int_{1}^{\bar{\eta}} \left(\frac{x - \bar{x}}{(x - \bar{x})^2 + (y - \bar{y})^2} - \frac{x - \bar{x}}{(x - \bar{x})^2 + (y + \bar{y})^2} \right) d\bar{y} \, d\bar{x}. \qquad (7.83)$$

So for a vortex positioned at $(0, Y)$ this is

$$\frac{\mathrm{d}Y}{\mathrm{d}t}(0,Y) = \frac{1}{2\pi}\int_{-\infty}^{\infty}\int_{1}^{\bar{\eta}}(x-\bar{x})\Big(\frac{1}{\bar{x}^2+(Y-\bar{y})^2}-\frac{1}{\bar{x}^2+(Y+\bar{y})^2}\Big)\mathrm{d}\bar{y}\,\mathrm{d}\bar{x}. \quad (7.84)$$

The linear assumption is that the waves at the interface are small and so $Y \mp \bar{y} \simeq Y \mp 1$ and therefore

$$\frac{\mathrm{d}Y}{\mathrm{d}t}(0,Y) \simeq -\frac{1}{2\pi}\int_{-\infty}^{\infty}\bar{x}(\bar{\eta}(\bar{x})-1)\Big(\frac{1}{\bar{x}^2+(Y-1)^2}-\frac{1}{\bar{x}^2+(Y+1)^2}\Big)\mathrm{d}\bar{x}. \quad (7.85)$$

Now Y will always remain small and so

$$\frac{\mathrm{d}Y}{\mathrm{d}t}(0,Y) \simeq -\frac{1}{2\pi}\int_{-\infty}^{\infty}\frac{\bar{x}(\bar{\eta}(\bar{x})-1)}{\bar{x}^2+1}\Big((1-\frac{2Y}{\bar{x}^2+1})^{-1}-(1+\frac{2Y}{\bar{x}^2+1})^{-1}\Big)\mathrm{d}\bar{x}. \quad (7.86)$$

Using the binomial theorem this can be written as

$$\frac{\mathrm{d}Y}{\mathrm{d}t}(0,Y) \simeq -\frac{2Y}{\pi}\int_{-\infty}^{\infty}\frac{\bar{x}(\bar{\eta}(\bar{x})-1)}{(\bar{x}^2+1)^2}\mathrm{d}\bar{x}. \quad (7.87)$$

In the long-wave limit $\chi = \mu\bar{x}$ for μ small and so

$$\frac{\mathrm{d}Y}{\mathrm{d}t}(0,Y) \simeq -\frac{2Y}{\pi}\int_{-\infty}^{\infty}\frac{\mu^2\chi(\bar{\eta}(\chi/\mu)-1)}{(\chi^2+\mu^2)^2}\mathrm{d}\chi. \quad (7.88)$$

One of the delta-sequences is defined as

$$\pi\delta(\chi) = \lim_{\mu\to 0}\frac{\mu}{\mu^2+\chi^2}, \quad (7.89)$$

and so

$$\pi\delta_\chi(\chi) = \lim_{\mu\to 0}-\frac{2\mu\chi}{(\mu^2+\chi^2)^2}. \quad (7.90)$$

Therefore (7.88) can be expressed as a derivative of a delta function

$$\frac{\mathrm{d}Y}{\mathrm{d}t}(0,Y) \simeq \mu Y \int_{-\infty}^{\infty} \delta_\chi(\chi)(\bar{\eta}(\chi/\mu) - 1)\mathrm{d}\chi. \tag{7.91}$$

Using integration by parts and the sampling property of the delta function reveals that

$$\frac{\mathrm{d}Y}{\mathrm{d}t}(0,Y) \simeq -\mu Y \bar{\eta}_\chi(0), \tag{7.92}$$

so in the slow time variable $\tau = \mu^2 t$ and writing the interface displacement as $\bar{\eta} = 1 + \mu\Theta$ gives the linear long-wave approximation to the y velocity of the vortex as

$$\frac{\mathrm{d}Y}{\mathrm{d}\tau}(0,Y) \simeq -Y\Theta_\chi(0), \tag{7.93}$$

The analysis for the along-shore component of the vortex velocity is very similar, however since there are now contributions from the image vortex and the free stream then

$$\frac{\mathrm{d}X}{\mathrm{d}t} = -\frac{1}{2\pi}\int_{-\infty}^{\infty}\int_1^{1+\mu\Theta} \left(\frac{Y-\bar{y}}{\bar{x}^2 + (Y-\bar{y})^2} - \frac{Y+\bar{y}}{\bar{x}^2 + (Y+\bar{y})^2}\right)\mathrm{d}\bar{y}\,\mathrm{d}\bar{x} - \left(U - \frac{\Gamma}{4\pi Y}\right). \tag{7.94}$$

In the linear longwave limit this reduces to

$$\frac{\mathrm{d}X}{\mathrm{d}t}(0,Y) \simeq \frac{1}{\pi}\int_{-\infty}^{\infty}\frac{\mu^3\Theta(\chi/\mu)}{\chi^2 + \mu^2}\mathrm{d}\chi - \mu\left(U - \frac{\Gamma}{4\pi Y}\right). \tag{7.95}$$

Now using the delta-function representation of the integrand gives that

$$\frac{\mathrm{d}X}{\mathrm{d}t}(0,Y) \simeq \mu^2 \Theta(0) - \mu\left(U - \frac{\Gamma}{4\pi Y}\right). \tag{7.96}$$

So the linear longwave approximation for $\tau = \mu^2 t$ gives

$$\frac{\mathrm{d}X}{\mathrm{d}\tau}(0,Y) \simeq \Theta(0) - \frac{1}{\mu}\left(U - \frac{\Gamma}{4\pi Y}\right). \tag{7.97}$$

A physical interpretation of the dynamics described by (7.93) is shown in figure (7.37). The point vortex 'sees' the long interfacial wave as a tangent line Θ_χ and this is a slowly varying quantity with time. Looking at figure (7.37a), this shows the vortex as a cross with associated circulation situated near the wall. The gradient of the interface directly above the vortex is negative, this means that on the right hand side of the vortex, deep fluid has been drawn onto the shelf which has aroused secondary circulations (as shown by the clockwise arrow). The opposite has happened to the left of the vortex, shallow fluid has been pushed off the shelf creating anticlockwise circulations. The net effect is to 'pull' the vortex away from the wall and thus $\dot{Y} > 0$. Figure (b) shows the opposite case for which $\Theta_\chi > 0$, not only that but it also illustrates that the same argument will work when the arrangement is not so symmetrical. In this case fluid from the shallow side has been pulled over to the deep side but the change in circulation is stronger over to the right (as shown by a larger, anticlockwise arrow). The net effect is to push the vortex closer to the wall and therefore $\dot{Y} < 0$.

Figure (a)
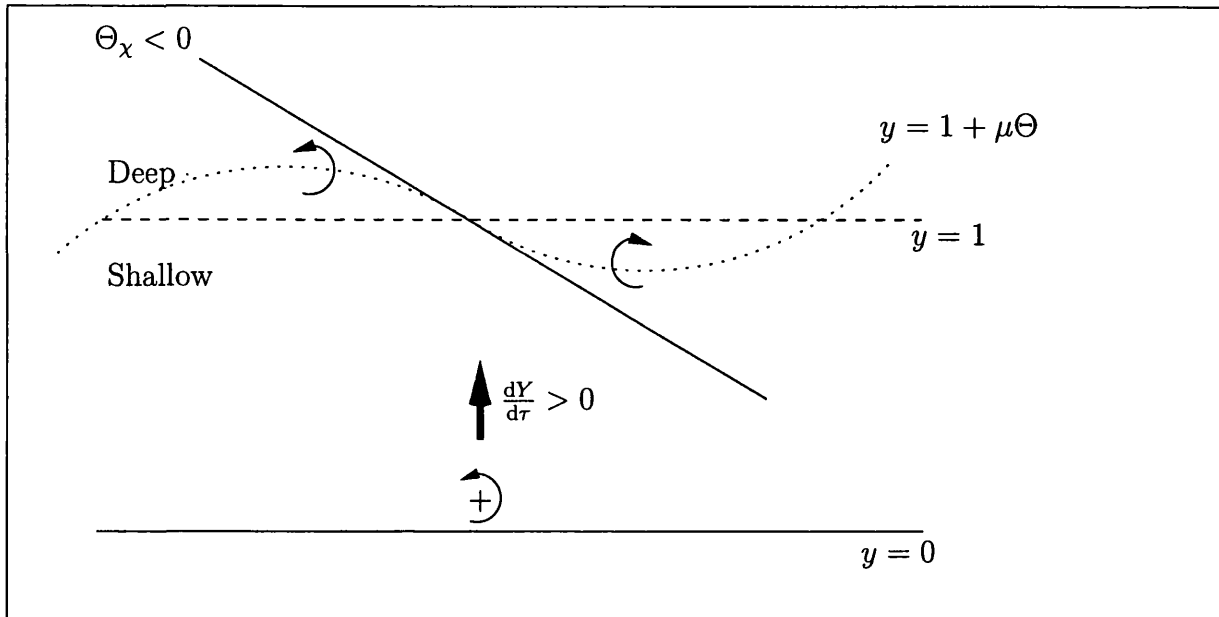
Figure (b)
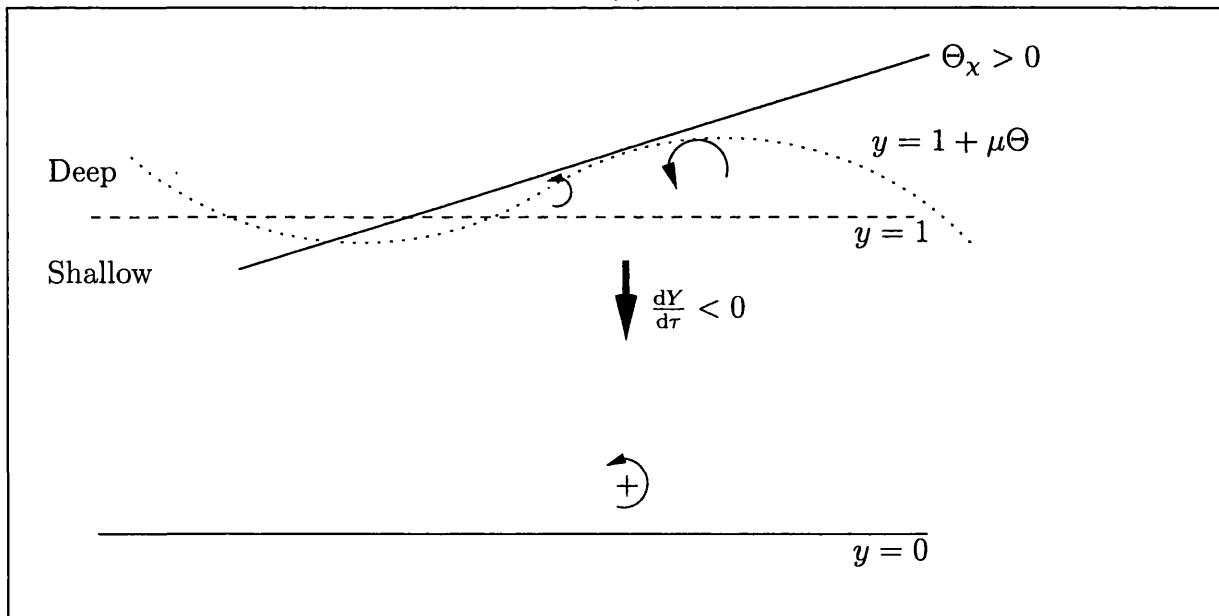
Figure 7.37: A physical interpretation of the influence of the slowly varying longwave on the motion of the vortex.

7.8 Discussion.

In this chapter the linear vortex-wave interactions were examined for three cases of initial placement of the vortex; first, the vortex was placed off-shelf, an order one distance from the wall; second, it was placed on-shelf but still an order one distance from the wall and third, it was placed an $O(\varepsilon)$ distance from the wall and approximated as a dipole.

For the first two cases a wide variety of vortex behaviors was found and the vortex motion and was governed primarily by the reaction to the pseudoimage in the interface and also conservation of momentum in the x direction. Conservation of momentum gave restrictions on the initial direction of the vortex motion and these were discussed and demonstrated numerically and error calculations based on this conservation law were derived and also demonstrated. The error was found to be between 10^{-6} and 10^{-8} for $\varepsilon = 0.1$. The interactions were classified according to which gave long term steady motions and which remained unsteady.

For the third case the role of the pseudoimage whilst being important in the initial stages of the vortex motion was at later times dominated by the action of the vortex image in the wall, this having the main effect on the horizontal drift speed of the vortex. The wave-vortex interaction complied with Bell's definition of unstable and stable interaction as the flows which resulted in a permanent lee wave train behind the vortex never settled to a steady state and the vortex continued to drift towards, or away, from the wall (dependent on the sign of its circulation).

The resonant case was also discussed and whilst flows with $U \approx 1$ did have large responses at the interface it was thought that they would not result in resonance in the long term as the vortex is always free to drift towards the wall, speeding up

as it does so, thus passing into the non-resonant regime. The unstable definition above also applies for the near resonant flows indicating also that the vortex will not reach a steady state and allow the interface to grow. However, the response at the interface does become reasonably large. Hence the weakly nonlinear, near-resonant response is studied in the next chapter.

The results shown here agree qualitatively with previous work in this field, namely the linear computations in Bell [1989] which also give rise to the distinctive, callipygian vortex trajectories (see Figure 9 in Bell [1989]). Also the fully nonlinear contour dynamic integrations in Dunn [1999] show that the initial drift of the vortex is well modeled by linear theory (see also Atassi [1998]) and that steady cases do occur for a wide range of parameter values for the weakly forced problem, he also stresses the importance of the pseudoimage in describing the flow evolution, however a fully nonlinear investigation of the case of weakly forced resonance at longwave speed unity is not pursued by Dunn [1999] as his work is primarily concerned with the response due to a moderate or intense vortex.

Chapter 8

Weakly Nonlinear Wave-Vortex Interactions.

8.1 Introduction

In this chapter, in contrast to chapter 4, the vortex is no longer constrained to move parallel to the wall at constant velocity but is free to respond to the presence of the weakly nonlinear waves. The waves in turn are forced by an unsteady term representing the moving vortex.

The system of equations governing the motion of the vortex and the evolution of the topographic waves is solved using a modified version of the method described in chapter 4 and the accuracy of the method is checked against its ability to conserve momentum in the x direction.

8.2 Derivation of Governing Equations

The coordinates of the vortex center are written $(X_0(t), Y_0(t))$ and the streamfunction is (in the usual notation)

$$\psi = \phi + Uy + \Psi. \tag{8.1}$$

The equations of motion for the vortex center are,

$$-\frac{\partial \psi}{\partial y}(X_0, Y_0) = \frac{dX_0}{dt}, \tag{8.2}$$

$$\frac{\partial \psi}{\partial x}(X_0, Y_0) = \frac{dY_0}{dt}. \tag{8.3}$$

In the slower timescale $\tau = \mu^2 t$ and on the long length scale $\chi = \mu x$ (8.2) and (8.3) become, for $\chi_0 = \mu X_0$,

$$-\frac{\partial \psi}{\partial y}(\chi_0, Y_0) = \mu \frac{d\chi_0}{d\tau}, \tag{8.4}$$

$$\frac{\partial \psi}{\partial \chi}(\chi_0, Y_0) = \mu \frac{dY_0}{d\tau}. \tag{8.5}$$

Equation (4.49) gives the expression for ϕ in the on-shelf region occupied by the vortex i.e.

$$\phi = \frac{1}{2}\Big((y-1)^2 H(y-1) - (y-Y)^2 H(y-Y)\Big) + (A + \mu^2 B)y$$

$$+\mu^2 \Big(\frac{Y_\chi^2}{2}(y-Y)^2 H(y-Y) - \frac{Y_{\chi\chi}}{6}(y-Y)^3 H(y-Y) - \frac{(A_{\chi\chi} + \mu^2 B_{\chi\chi})y^3}{6}\Big). \tag{8.6}$$

Therefore,

$$\frac{\partial \phi}{\partial y} = A + \mu^2 B - \frac{\mu^2 y^2}{2}(A_{xx} + \mu^2 B_{xx}) + (y - 1)H(y - 1) + C(Y, y)H(y - Y), \quad (8.7)$$

and

$$\frac{\partial \phi}{\partial \chi} = (A_\chi + \mu^2 B_\chi)y - \frac{\mu^2 y^3}{6}(A_{\chi\chi\chi} + \mu^2 B_{\chi\chi\chi}) + D(Y, y)H(y - Y), \quad (8.8)$$

where,

$$C(Y, y) = -(y - Y) + \mu^2 \left(Y_\chi^2 (y - Y) - \frac{Y_{\chi\chi}}{2}(y - Y)^2 \right), \quad (8.9)$$

$$D(Y, y) = (y - Y)Y_\chi - \mu^2 \left(Y_\chi^3 (y - Y) - \frac{3Y_\chi Y_{\chi\chi}}{2}(y - Y)^2 + \frac{Y_{\chi\chi\chi}}{6}(y - Y)^3 \right). (8.10)$$

There is no self-propagation of the vortex so, as before, the action of the image on the primary vortex Ψ_i, contributes to its velocity,

$$\Psi_i = -\frac{\Gamma}{4\pi}\{\log (\chi/\mu - \chi_0/\mu)^2 + (y + Y_0)^2\}. \quad (8.11)$$

Hence,

$$\frac{\partial \Psi_i}{\partial y}(\chi_0, Y_0) = -\frac{\Gamma}{4\pi Y_0}, \quad (8.12)$$

$$\frac{\partial \Psi_i}{\partial \chi}(\chi_0, Y_0) = 0. \quad (8.13)$$

Finally the motion of the vortex center due to the ψ field can be calculated from (8.1), (8.4), (8.5), (8.7), (8.8), (8.12) and (8.13) are

$$\mu \frac{\partial \chi_0}{\partial \tau} = -(A + \mu^2 B - \frac{\mu^2}{2} Y_0^2 (A_{xx} + \mu^2 B_{xx}) + U - \frac{\Gamma}{4\pi Y_0}), \qquad (8.14)$$

$$\mu \frac{\partial Y_0}{\partial \tau} = (A_x + \mu^2 B_x) Y_0 - \frac{\mu^2}{6} Y_0^3 (A_{xxx} + \mu^2 B_{xxx}). \qquad (8.15)$$

Equation (4.46) gives an expression for $A + \mu^2 B$ to $O(\mu^2)$ which is

$$A + \mu^2 B = -\mu \Theta + \mu^2 \mathbb{B}(\Theta) \qquad (8.16)$$

and hence (8.14) and (8.15) to leading order are,

$$\frac{\partial \chi_0}{\partial \tau} = \Theta\Big|_{\chi_0} - \frac{1}{\mu}\Big(U - \frac{\Gamma}{4\pi Y_0}\Big), \qquad (8.17)$$

$$\frac{\partial Y_0}{\partial \tau} = -\Theta_\chi\Big|_{\chi_0} Y_0, \qquad (8.18)$$

It is encouraging to note that these expressions are identical to (7.93) and (7.97), the results derived from linear longwave theory. Thus as far as the vortex propagation velocity is concerned, the linear and weakly nonlinear longwave theories give the same result. The difference will occur in the actual form of Θ and Θ_χ in (8.17) and (8.18). Equations(8.17) and (8.18) are to be solved in conjunction with the evolution equation,

$$\Theta_\tau - \Delta \Theta_\chi + \Theta \Theta_\chi (2 - H(\Theta)) - \mathbb{B}(\Theta_\chi) = -\frac{\Gamma Y_0}{\mu} \frac{\partial \Psi}{\partial \chi}, \qquad (8.19)$$

with the forcing term on the righthand-side of (8.19) now containing the feed-back terms $\chi_0(\tau), Y_0(\tau)$. As before, in the longwave limit Ψ to leading order is

$$\Psi = \frac{\mu/\pi}{\mu^2 + [\chi - \chi_0(\tau)]^2}, \tag{8.20}$$

which tends to a δ-function as $\mu \to 0$.

8.2.1 Small Time Solution

The three variables are expanded in powers of τ

$$\chi_0(\tau) = \chi_{01}\tau + \chi_{02}\tau^2 + \chi_{03}\tau^3 + \ldots, \tag{8.21}$$

$$Y_0(\tau) = Y_{00} + Y_{01}\tau + Y_{02}\tau^2 + Y_{03}\tau^3 + \ldots, \tag{8.22}$$

$$\hat{\Theta}(\tau) = \hat{\Theta}_1\tau + \hat{\Theta}_2\tau^2 + \hat{\Theta}_3\tau^3 + \ldots. \tag{8.23}$$

Substitution of (8.21) - (8.23) into (8.17) - (8.19) reveal that $\chi_{01} = \chi_{02} = Y_{01} = 0$ and

$$\chi_{03} = \frac{1}{3}\Theta_2\Big|_{\chi_0} - \frac{\Gamma Y_{02}}{4\pi Y_{00}\mu}, \tag{8.24}$$

$$Y_{02} = -\frac{1}{2}\Theta_1'\Big|_{\chi_0} Y_{00}, \tag{8.25}$$

$$Y_{03} = -\frac{1}{3}\Theta_2'\Big|_{\chi_0} Y_{00}, \tag{8.26}$$

here the dash represents differentiation with respect to χ. The small-time interface displacement is

$$\hat{\Theta}_1 = -\frac{\Gamma Y_{00}}{\mu}ike^{-\mu|k|}, \tag{8.27}$$

$$\hat{\Theta}_2 = \frac{ik}{2}\hat{\Theta}_1(\Delta + |k|), \tag{8.28}$$

$$\hat{\Theta}_3 = -\frac{1}{3}(k^2(\Delta + |k|)^2\frac{\hat{\Theta}_1}{2} + \mathcal{F}\Big\{\Theta\Theta'(2 - H(\Theta))\Big\} + \frac{\Gamma Y_{02}}{\mu}ike^{-\mu|k|}). \tag{8.29}$$

8.3 Momentum Conservation

The momentum P in the x direction is given by (7.21) and in the long length scale $\chi = \mu x$, for the long time scale $\tau = \mu^2 t$ and putting $\bar{\eta} = 1 + \mu\Theta$ this becomes

$$P(\tau) = \Gamma Y(\tau) + \frac{1}{2}\mu \int_{-\infty}^{\infty} \Theta^2 \, d\chi. \tag{8.30}$$

This quantity is constant over time τ. To see this explicitly, differentiate (8.30) with respect to τ to give

$$P_\tau = \Gamma Y_\tau(\tau) + \mu \int_{-\infty}^{\infty} \Theta\Theta_\tau \, d\chi. \tag{8.31}$$

Examining the integral term, substitute (8.19) for Θ_τ in the integrand giving

$$\Theta\Theta_\tau = \Delta\Theta\Theta_\chi - \Theta^2\Theta_\chi(2 - H(\Theta)) + \Theta\mathbb{B}(\Theta_\chi) - \frac{\Gamma Y}{\mu}\Theta\delta_\chi(\chi - \chi_0). \tag{8.32}$$

Assuming $\Theta \to 0$ as $|\chi| \to \infty$ the first three terms on the right-hand-side of (8.32) integrate to zero (see Appendix H) and using integration by parts on the last term gives

$$P_\tau = \Gamma Y_\tau(\tau) + \Gamma Y\Theta_\chi\Big|_{\text{vortex}}. \tag{8.33}$$

Finally substituting (8.18) into (8.33) gives

$$P_\tau = 0. \tag{8.34}$$

Therefore momentum is always conserved identically in the χ direction, when solving the coupled system of equations (8.17) - (8.19). This is used as a check on the performance of the numerical method.

8.4 The Numerical Method

The numerical method used for solving (8.17) - (8.19) is a simple extension of the numerical method used to solve (7.9), (7.11), (7.12) and (7.15) as described in chapter 7. Fourth-order Adams Bashforth methods are used to integrate (8.17) and (8.18) and the linearly implicit, multi-step methods described in chapter 5 are used for time-stepping the evolution equation (8.19). The deviations of the vortex motion from an $O(1)$ constant horizontal drift are decoupled from the evolution of the interface displacement and so at each time step either the vortex position is assumed constant (for time-stepping the interface equation (8.19)) or the interface is assumed to be stationary (for integrating (8.17) & (8.18)), at the next time-step the new values are used and so on. Before discussing the results of these numerical experiments the possible sources of error and ways of minimising them are discussed. The accuracy is determined through the method's ability to conserve momentum (i.e. (8.33))in the χ direction.

8.4.1 Sources of Error in the Numerical Method

The main source of error in the numerical method arises from the inability to accurately reproduce the δ_χ-function forcing, the key point being that *in the limit* $\mu \to 0$, the forcing term in the evolution equation (8.19) becomes

$$\frac{\partial \Psi}{\partial \chi} \to \delta_\chi. \tag{8.35}$$

However for finite μ the numerical representation of δ_χ is inaccurate. Fortunately the explicit form for Θ_τ given by (8.19) can be substituted into (8.31). Numerical integration across the computational domain should give zero and so each individual term can then be integrated to show where any errors are being produced. Three

example cases were calculated using different methods for representing the forcing and for calculating the response at the vortex, all the example cases had $\Delta = 0$, $\kappa = 2$ and $\mu = 0.1$ integrating from $\tau = 0$ to $\tau = 5$. The number of points used for discretising the problem was $n = 16384$ which for a maximum value $|\chi| = 200$ gave the highest wavenumber as $k_{max} \simeq 128$. The quantities

$$E_1(\tau) = \int_{-\infty}^{\infty} \left(\Delta\Theta\Theta_\chi - \Theta^2\Theta_\chi(2 - H(\Theta)) + \Theta\mathbb{B}(\Theta_\chi) \right) d\chi, \qquad (8.36)$$

and

$$E_2(\tau) = \Gamma Y_\tau - \frac{\Gamma Y}{\mu} \int_{-\infty}^{\infty} \Theta\delta_\chi(\chi - \chi_0) d\chi, \qquad (8.37)$$

were calculated plus the overall relative error $E(\tau)$ given by (7.23).

Case 1

In this case in the numerical method (see chapter 5 and chapter 7, section 7.2.1) the derivative of the δ-function was calculated in Fourier space and inverted using the FFT method. The quantity Θ_χ was calculated at the vortex using the sampling property of the δ-function but the response of the interface at the vortex was calculated using Trigonometric interpolation. The results are shown in figures (8.1) and (8.2). As can be seen from figure (8.1a) the dispersive and nonlinear terms of (8.19) do integrate to zero, for reference after time $\tau = 0.3$ the error $E_1 \simeq 10^{-10}$. Figure (8.1b) shows the error $E_2 \simeq 10^{-11}$, this means that the δ-function forcing is accurately being realised in Fourier space and that the sampling method using the δ-function works well. The overall error E is shown in figure (8.2), the steady increase in error could be attributed to the presence of higher and higher wavenumbers which would not be captured at this resolution and therefore cause errors. This is dealt with below in the section on increasing the resolution.

(a)
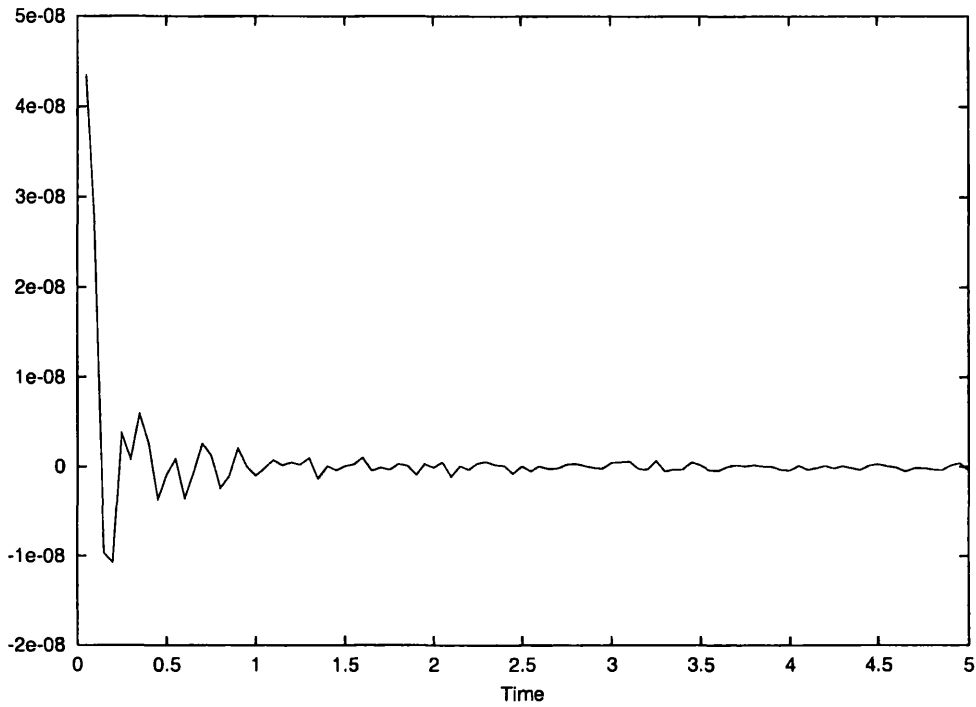
(b)
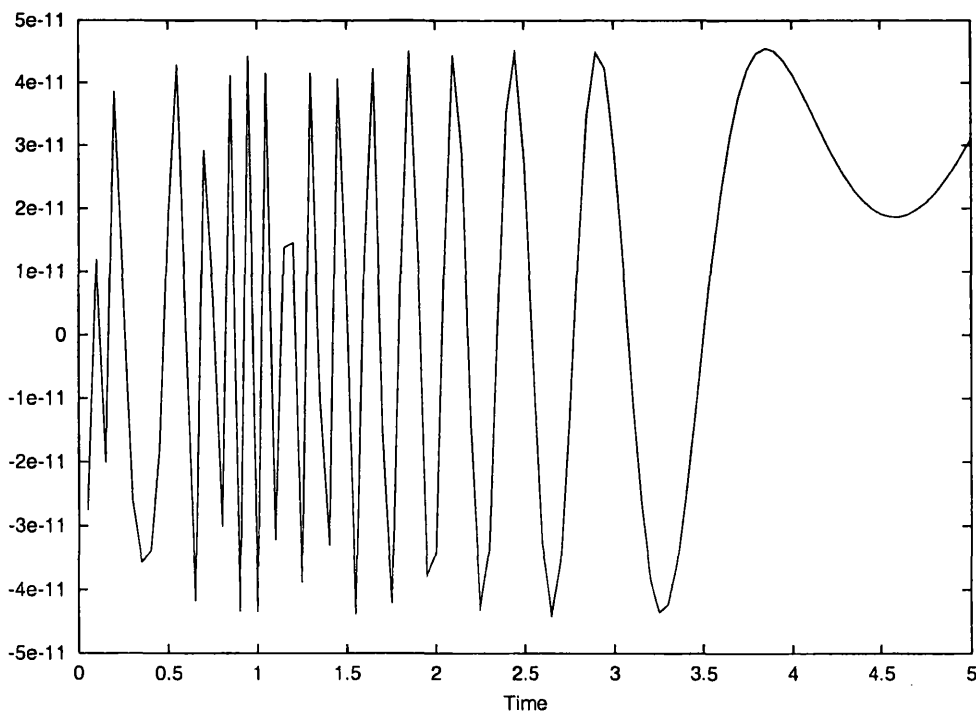
Figure 8.1: (a) Plot of the error E_1 against τ and (b) E_2 against τ for $\Delta = 0$ and

$\kappa = 2$ for Case 1.
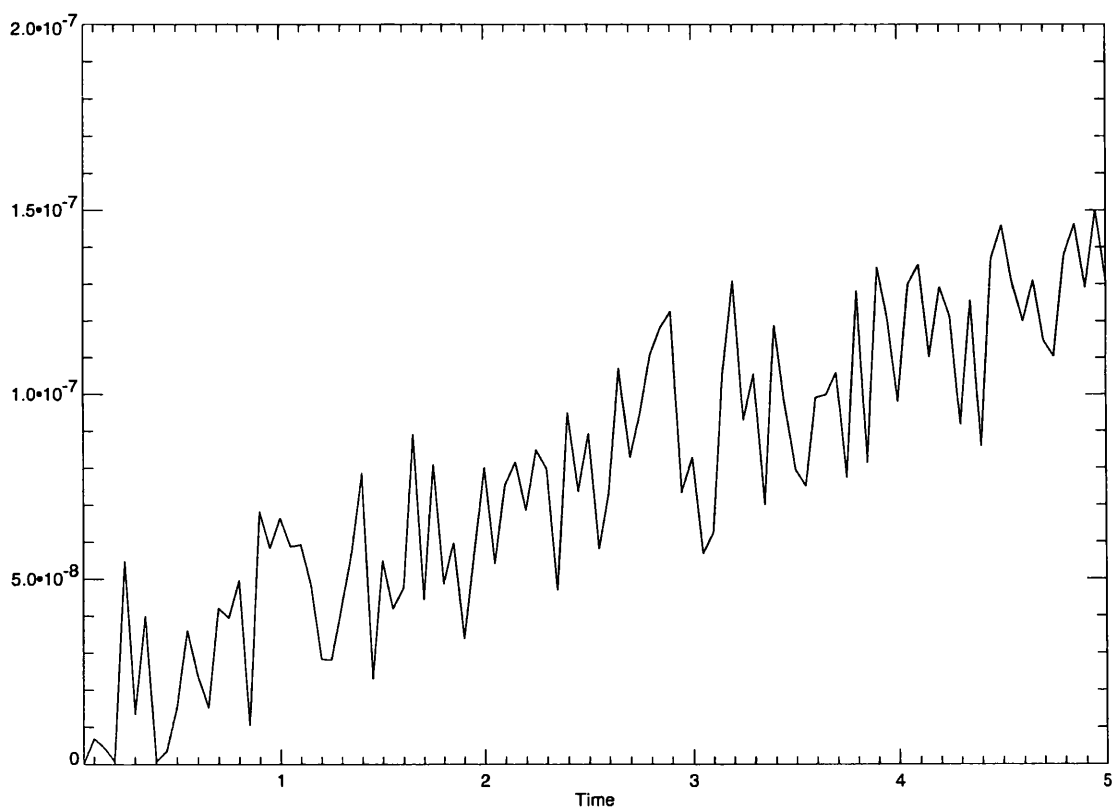
Figure 8.2: The error $E(\tau)$ for Case 1.

Case 2

This section is identical to Case 1 except that the δ-function derivative was calculated explicitly in real space, taking the derivative of (8.20) with respect to χ gives

$$\frac{\partial \Psi}{\partial \chi} = \frac{2\mu(\chi - \chi_0)/\pi}{(\mu^2 + [\chi - \chi_0(\tau)]^2)^2},\qquad (8.38)$$

and this was used in the right hand side of equation (8.19). The immediate consequence of this is that the error E_2 is identically zero as the two terms that form it are calculated in an identical manner. This means that E_2 is now not really testing anything, however the error E_1 is still satisfactory, as is the overall error E which does show that the method is accurate, but slightly less so than the previous case. The results are shown in figures (8.3) and (8.4).

Case 3

For this last case the δ-function derivative in E_2 was left in real space but both the quantities Θ and Θ_χ were calculated at the vortex using trigonometric interpolation (the method used to calculate ϕ and ϕ_x at the vortex in chapter 7). Figures (8.5) and (8.6) show the errors for this case. E_1 is satisfactorily close to zero as in the other cases, however now E_2 and E have got worse by many orders of magnitude. This does not mean that the trigonometric interpolation is inaccurate, indeed it was used in the chapter on the linear feedback problem to good effect with satisfactory errors being produced. Nor is it necessarily the case that the δ-function interpolation method is at fault as it results in good overall errors E for cases 1 and 2. The error in the conservation of momentum is really showing that the form of the equation of motion for Y_τ for finite μ which should read,

(a)
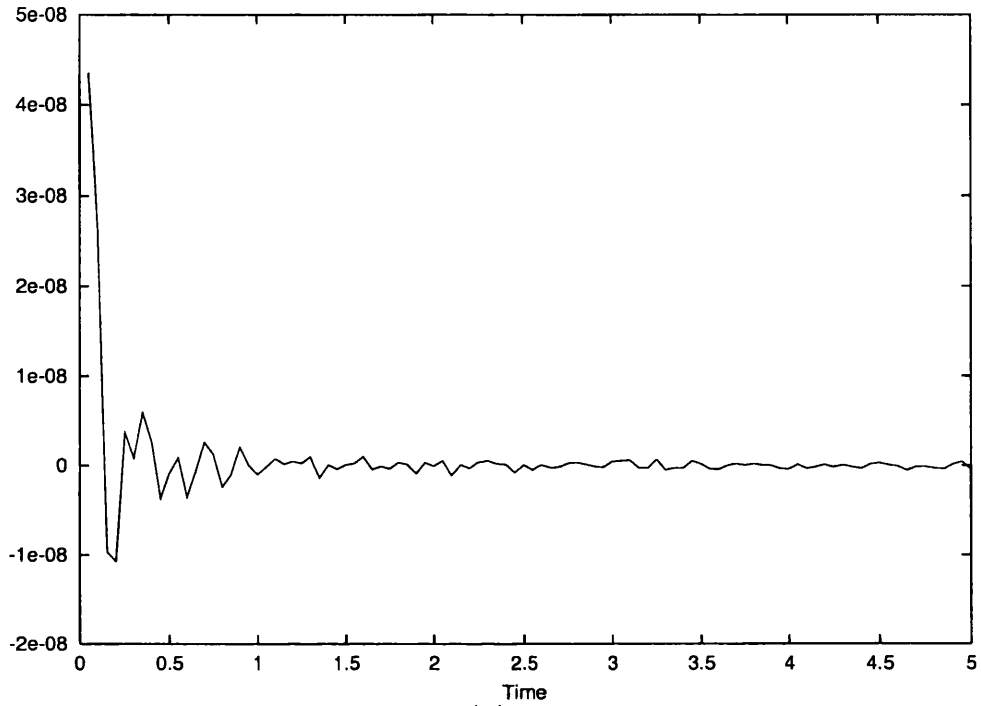
(b)
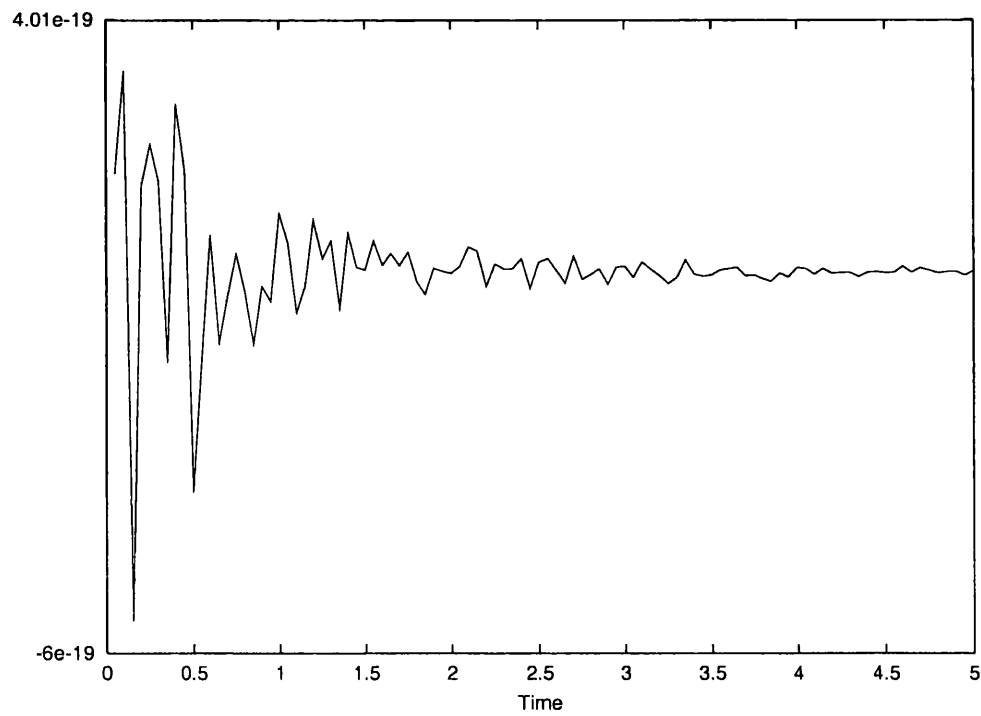
Figure 8.3: (a) Plot of the error E_1 against τ and (b) E_2 against τ for $\Delta = 0$ and $\kappa = 2$ for Case 2.
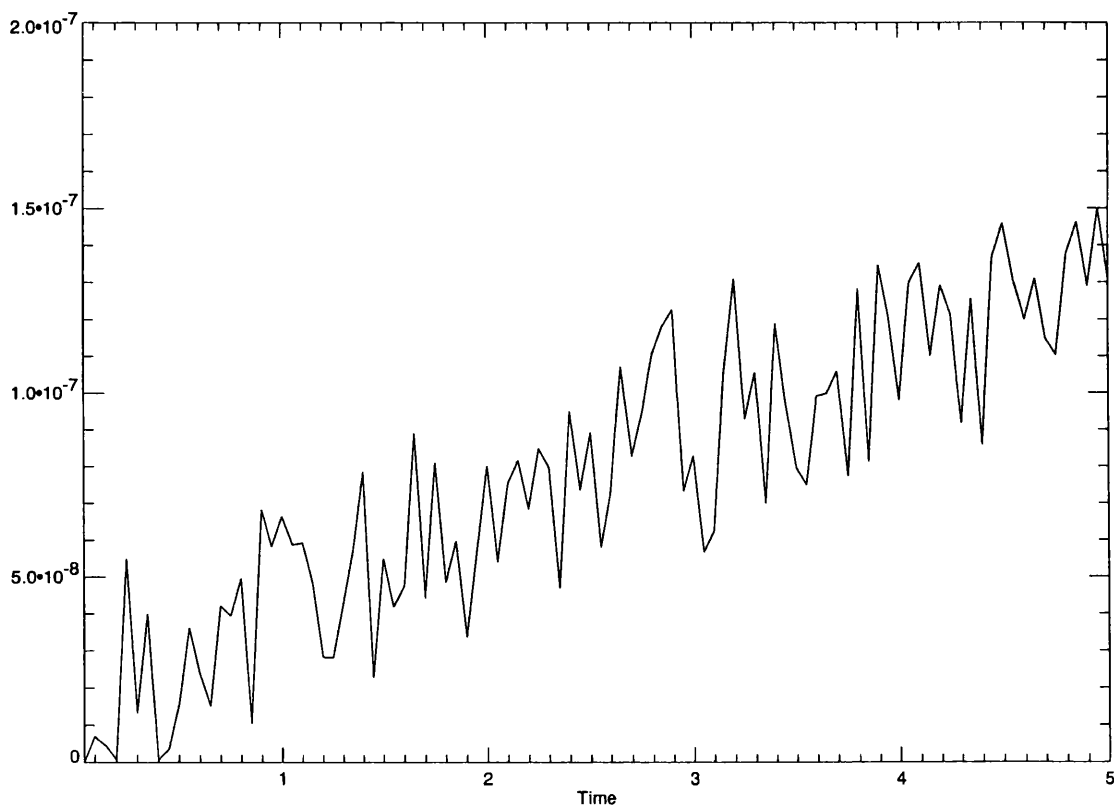
Figure 8.4: The error $E(\tau)$ for Case 2.

$$Y_\tau = Y(\tau) \int_{-\infty}^{\infty} \Theta \Psi_\chi \mathrm{d}\chi. \tag{8.39}$$

In the limit $\mu \to 0$ then $\Psi_\chi \to \delta_\chi$ and so $Y_\tau \to -Y\Theta_\chi$ (i.e. equation 8.18) calculated at the vortex. As has been mentioned in other studies (Bell [1989], Atassi et al. [1997], Dunn et al. [2000]) the important feature of a vortex reaction to the topographic waves is its movement in the y direction so it is equally important to make sure the method is calculating these dynamics correctly. From now on the method used will be that of case 1 as in tests it gave the lowest errors for $E(\tau)$, the overall error.

Changing the resolution.

Increasing the resolution should naturally make the error better and this is shown in figure (8.7) which shows the error $E_1 + E_2$ for the resolution *decreased* by half ($\mathrm{d}\chi$ is twice as big). This is to be compared to the errors shown in figure (8.1) for case 1, which, added together would be $\sim O(10^{-8})$ and less, the values of Δ and κ are unchanged as is the numerical method. Changing the spatial discretisation has effects on the numerical integrals in (8.31) and also on the δ-function integral for calculating Θ_χ at the vortex. There is also an associated change in wavenumber space with increased resolution but a decreased maximum wavenumber, the increased resolution means higher wavenumbers are realised, which is good, but the decrease in maximum wavenumber means that the forcing term of (8.19) will not be fully represented. It has been found that this is quite detrimental to the performance and overall error $E(\tau)$.

(a)
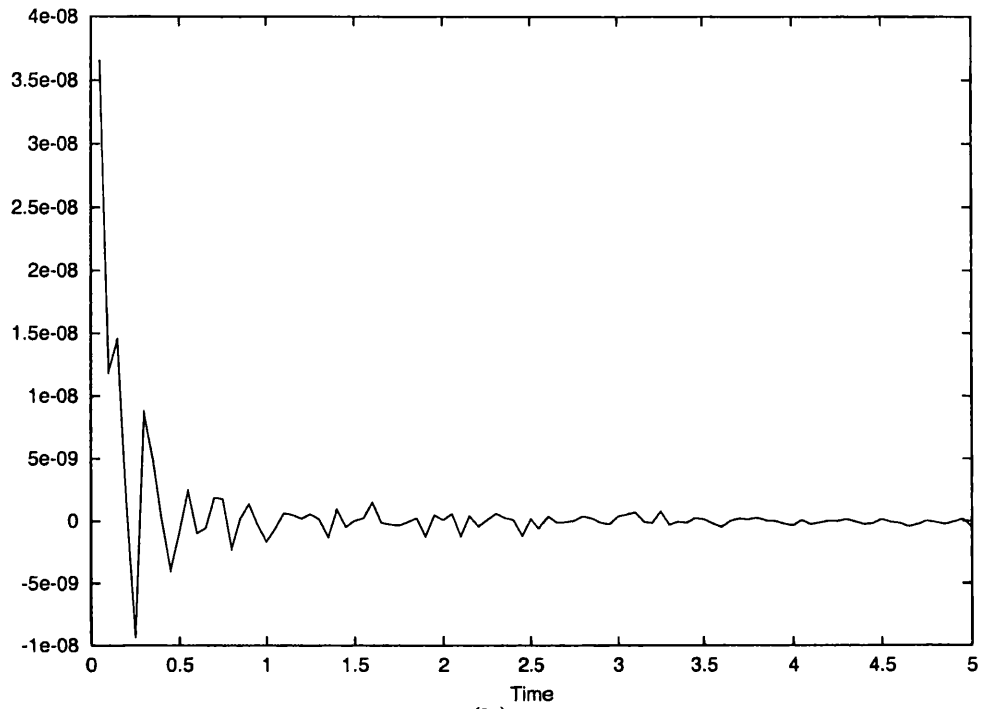
(b)
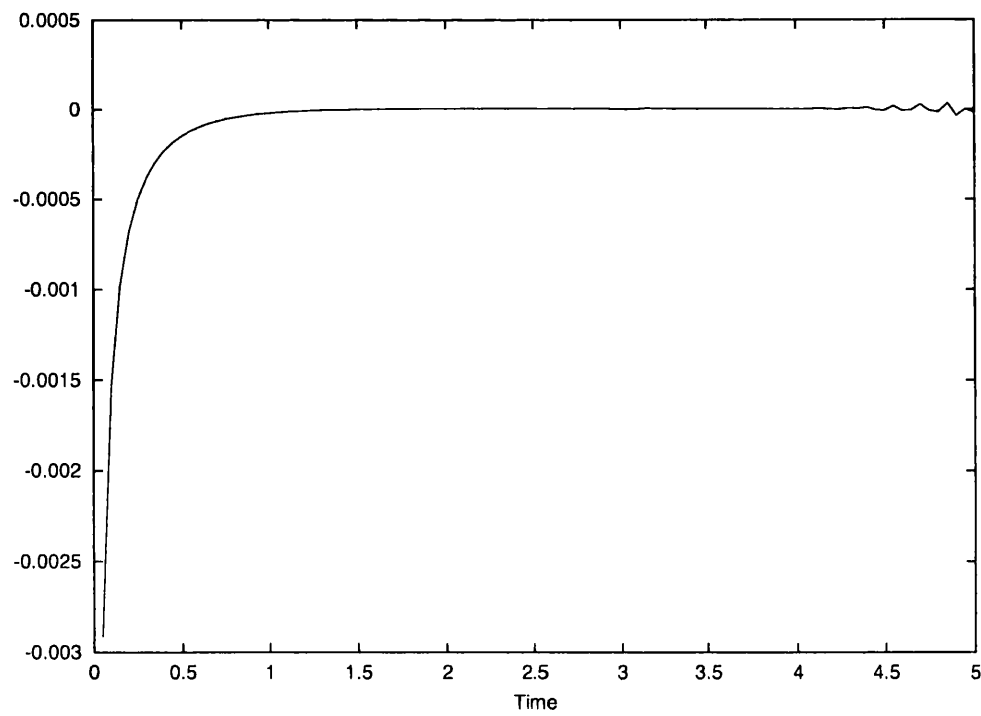
Figure 8.5: (a) Plot of the error E_1 against τ and (b) E_2 against τ for $\Delta = 0$ and $\kappa = 2$ for Case 3.
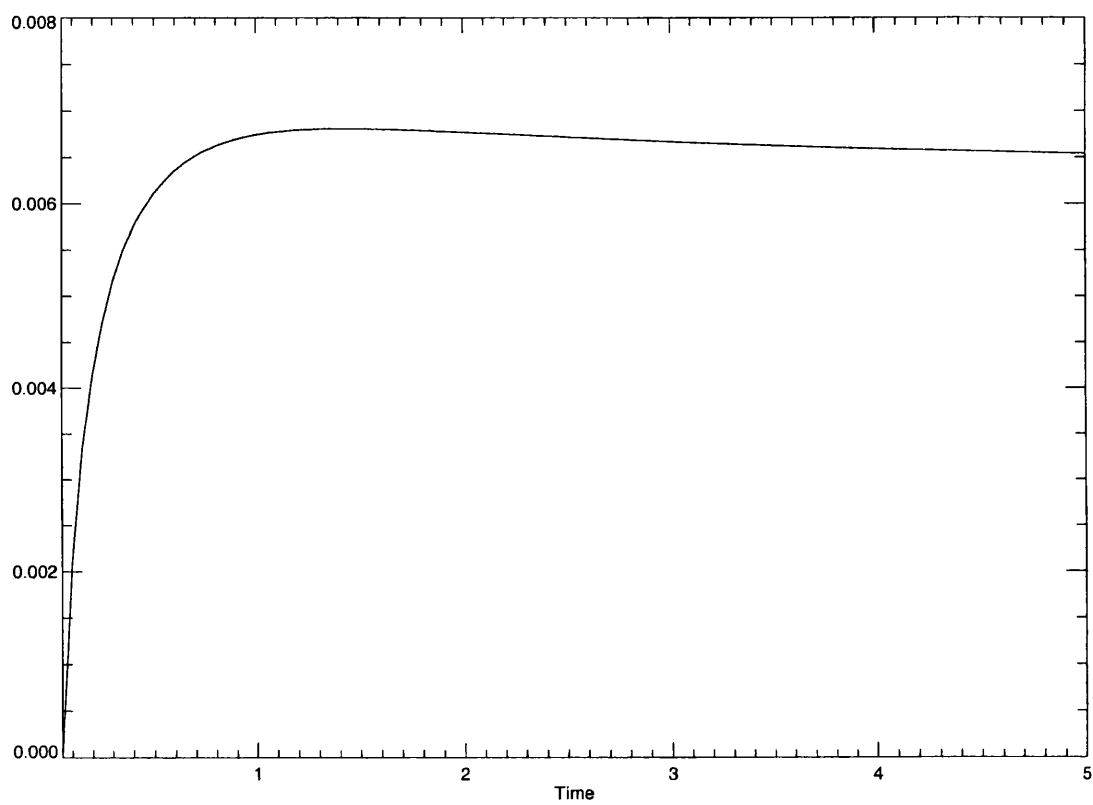
Figure 8.6: The error $E(\tau)$ for Case 3.
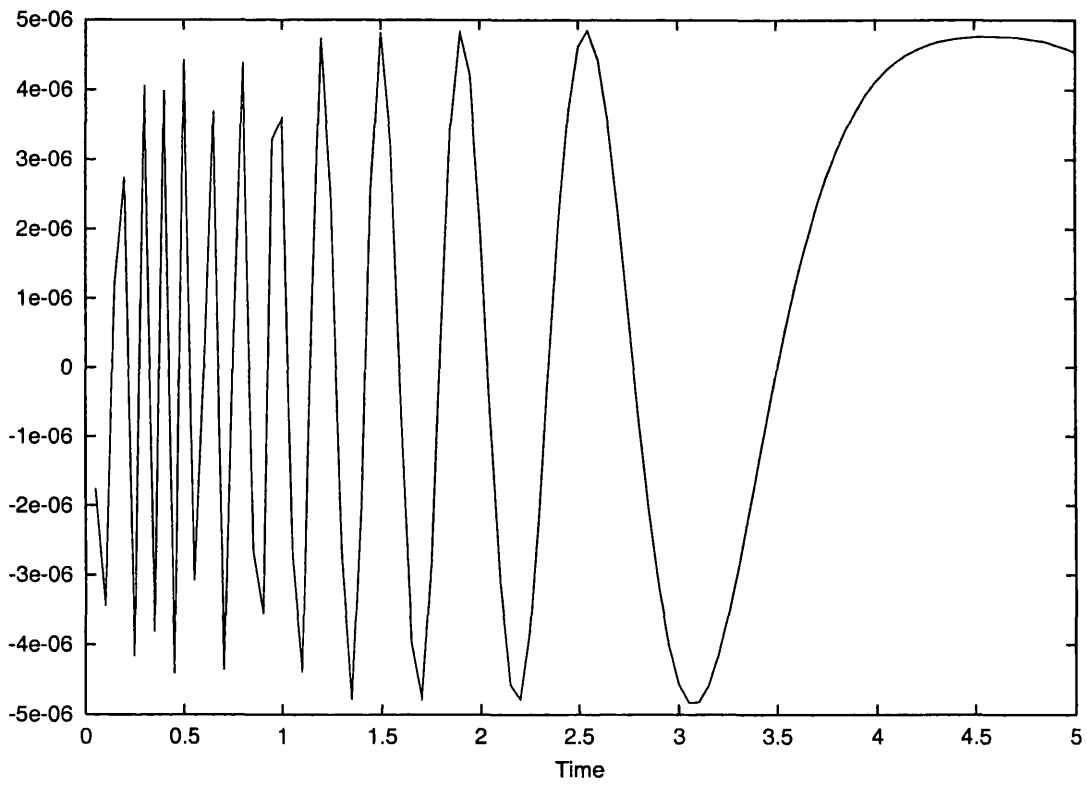
Figure 8.7: The error $E_1(\tau) + E_2(\tau)$ with decreased resolution in χ.
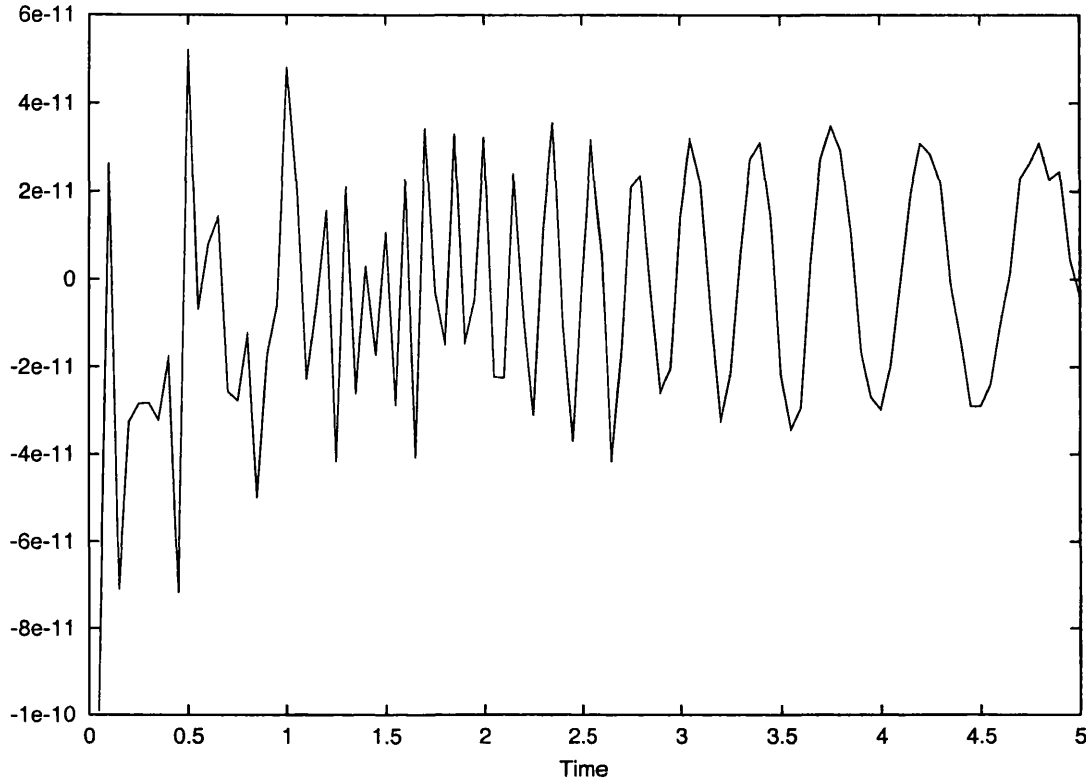
Figure 8.8: The error $E_1(\tau) + E_2(\tau)$ with $\mu = 0.05$.

Changing μ.

Since (8.18) is replaced by (8.39) in the actual system solved, the error $E_1 + E_2$ should improve as $\mu \to 0$ and hence also the overall error $E(\tau)$. Figure (8.8) shows a plot of $E_1 + E_2$ for $\mu = 0.05$ and this is also to be compared with figure (8.1) showing that the error $E_1 + E_2$ has decreased from $\sim 10^{-8}$ to $\sim 10^{-11}$. Decreasing μ should be done with care as a small change necessitates a larger maximum wavenumber (see figure (5.1)). The rest of the results in this section are with $\mu = 0.1$.

8.5 Results

Small κ

The weakly forced, small κ solutions are the weakly nonlinear analogies of the linear solutions shown in section 7.6.2. At this strength of forcing nonlinear effects are not apparent. Figure (8.9a) shows the response at the interface (scaled by 10) and (8.9b) shows the vortex trajectory and error for $\Delta = -2$ and $\kappa = 0.5$. The errors for the rest of the plots in this section did not get higher than $\sim O(10^{-7})$ and are not shown. Figure (8.9a) is very similar to the linear case with the initialisation of the vortex exciting a dispersive, nonlinear wavetrain to forming in the lee of the vortex (see figure (7.32)). The interface becomes permanently deformed above the vortex and this region of cyclonic PV acts to initially push the vortex towards the wall, this in turn causes the vortex to speed up in the horizontal. The vortex will continue to drift towards the wall due to the momentum flux from the vortex to the waves. However by the end of the experiment ($\tau = 20$) the vortex is seen to be breaking away from the lee waves and the response is becoming supercritical, this is confirmed by integrations for longer times and the vortex reaching a constant value of y.

Figures (8.10a) and (8.10b) show the response at a much more subcritical value of Δ ($\Delta = -6$) and $\kappa = 0.5$. Here the relationship between the vortex and the lee waves is unstable for the whole experiment, there is a continual flux of momentum from the vortex to the lee waves and as such, the vortex continues to drift towards the wall. As long as the waves continue to drain momentum away from the vortex it will carry on drifting towards the wall, this will make it accelerate (this is apparent in the curve of the leading wave front) and eventually may break away from the

wavetrain, however due to numerical limitations (the 'wrap-around' effect of the high wave numbers due to the finite computational domain) this cannot be shown for this case.

For $\Delta = -4$ and $\kappa = 0.5$ there are also very weak upstream propagating waves seen in figure (8.11a) with the corresponding trajectory in (8.11b). The plot has had to be scaled by 100 in order that the waves be seen. The presence of the upstream waves indicate another drain on the momentum of the vortex and so achieving a steady state for the long term seems doubtful.

Figure (8.12a) and (8.12b) show the case that, for a fixed vortex, leads to resonance (see chapter 4), the parameter values are $\Delta = 0$ and $\kappa = 0.5$. It can be seen that after initialisation the motion of the vortex toward the wall has caused it to speed up so that it is now in the supercritical regime. There is no interaction with the lee waves and the vortex has almost reached a steady state by $\tau = 20$. Hence the ability of the vortex to respond to wave radiation moves it closer to the wall and accelerates it, thus entering a supercritical state where no wave radiation takes place.

Large κ

At large κ (strong forcing) the vortex trajectory is initially determined by conservation of momentum resulting in a rapid drift towards the wall. This motion is then quickly dominated by the action of the image vortex in the wall which speeds up the vortex in the direction of increasing χ. In addition the effect of the pseudoimage (which is also anti-cyclonic) is also to increase the vortex speed. The vortex then propagates ahead from the leading wave and no further interaction between the vortex and waves occurs.

In all of the cases studied for a variety of strengths κ the above describes the vortex

(a)

(b)
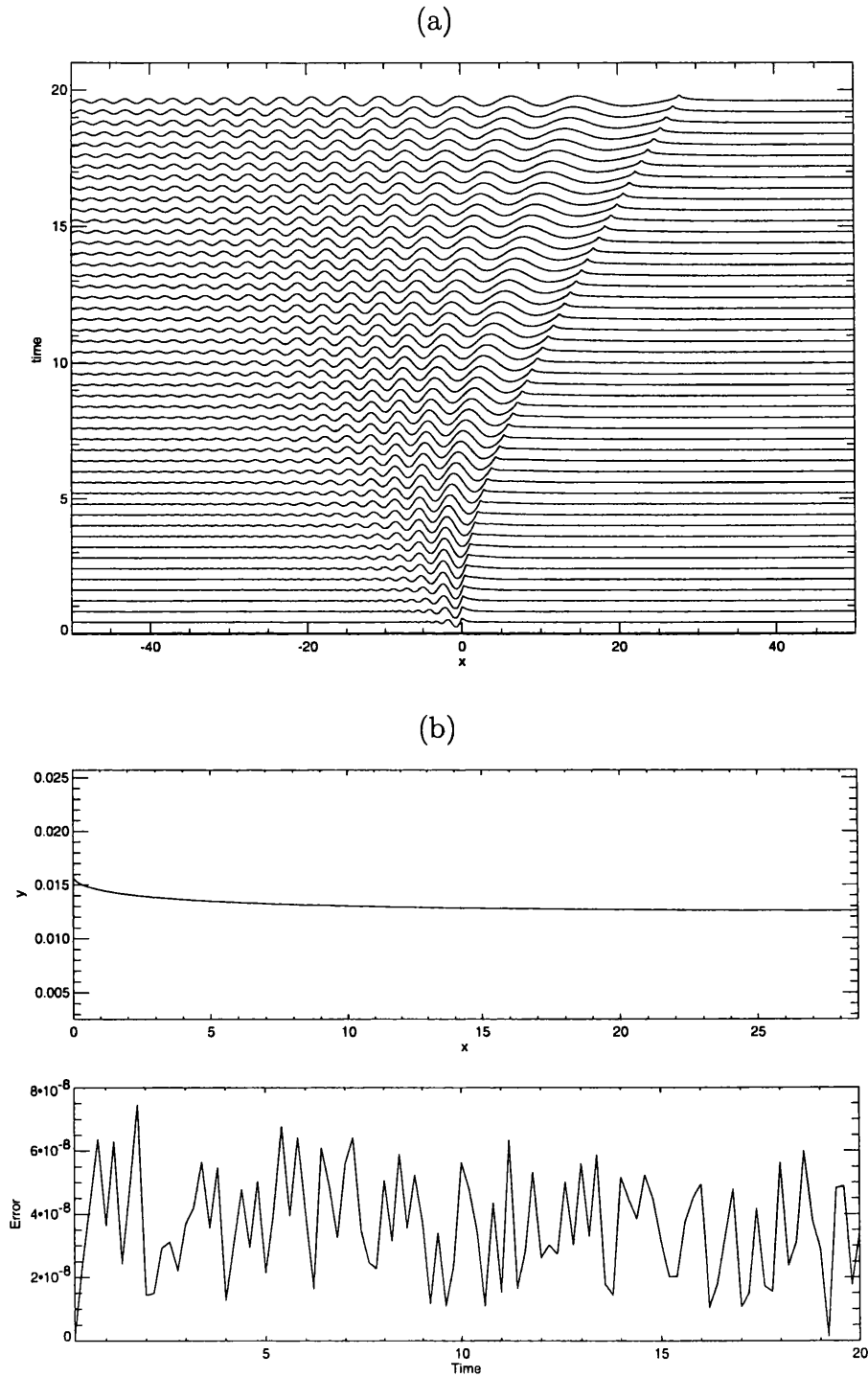
Figure 8.9: (a) The evolution of Θ for $\Delta = -2$ and $\kappa = 0.5$ (scaled by 10) and (b) The vortex trajectory and error plot E.

(a)

(b)
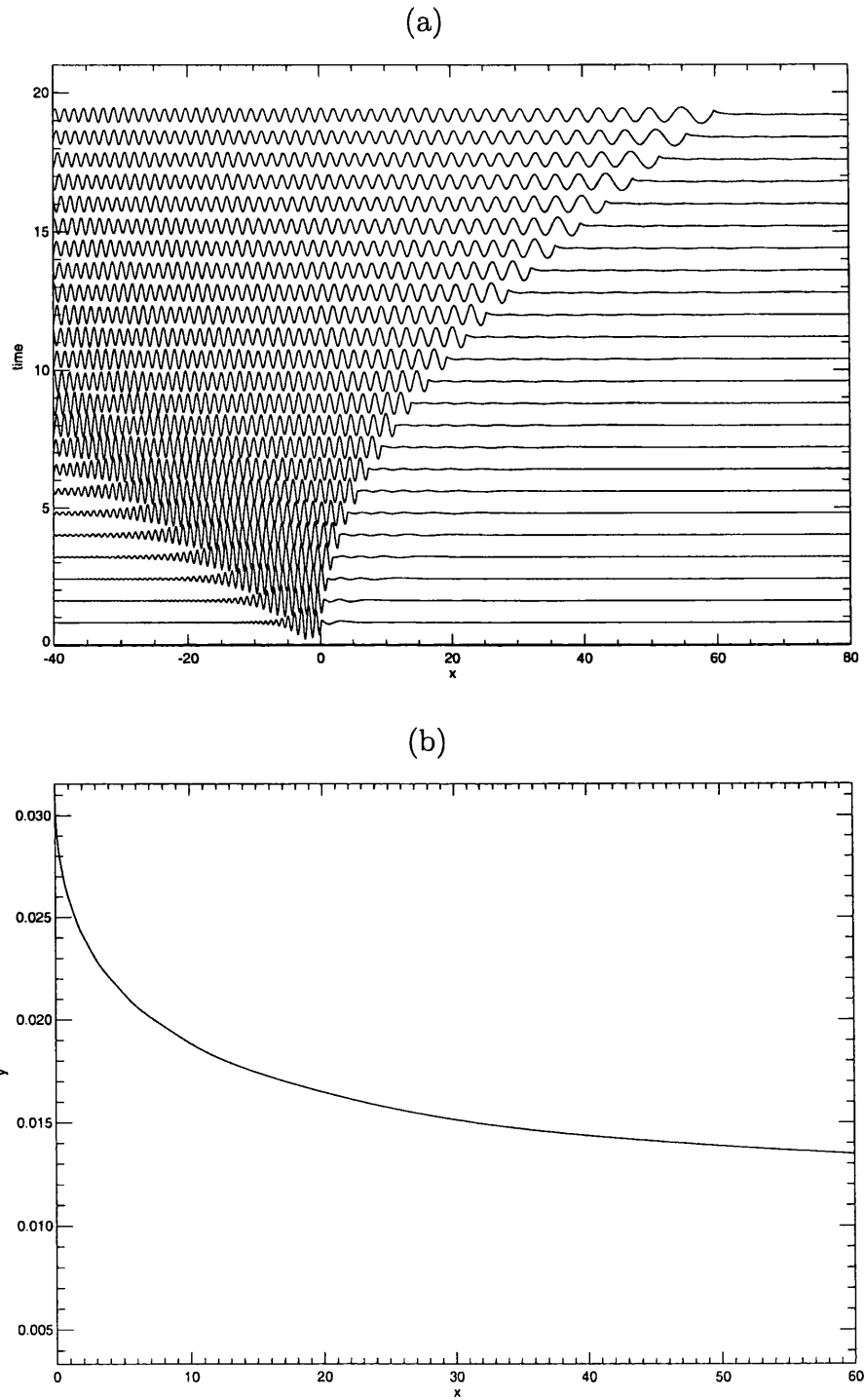
Figure 8.10: (a) The evolution of Θ for $\Delta = -6$ and $\kappa = 0.5$ (scaled by 10) and (b) The vortex trajectory.

(a)

(b)
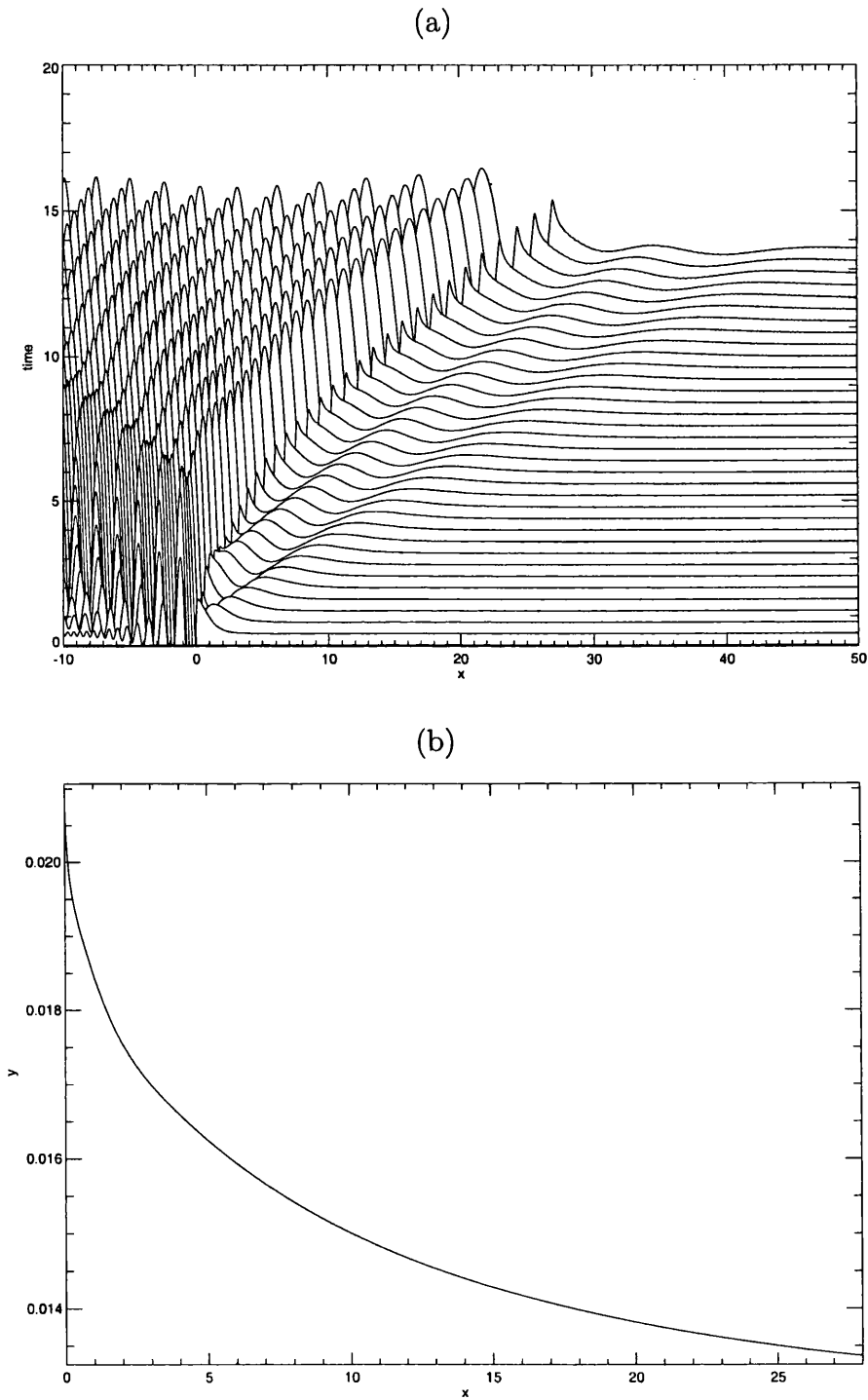
Figure 8.11: (a) A closer view of the evolution of Θ for $\Delta = -4$ and $\kappa = 0.5$ (scaled by 100) and (b) The vortex trajectory.

(a)

(b)
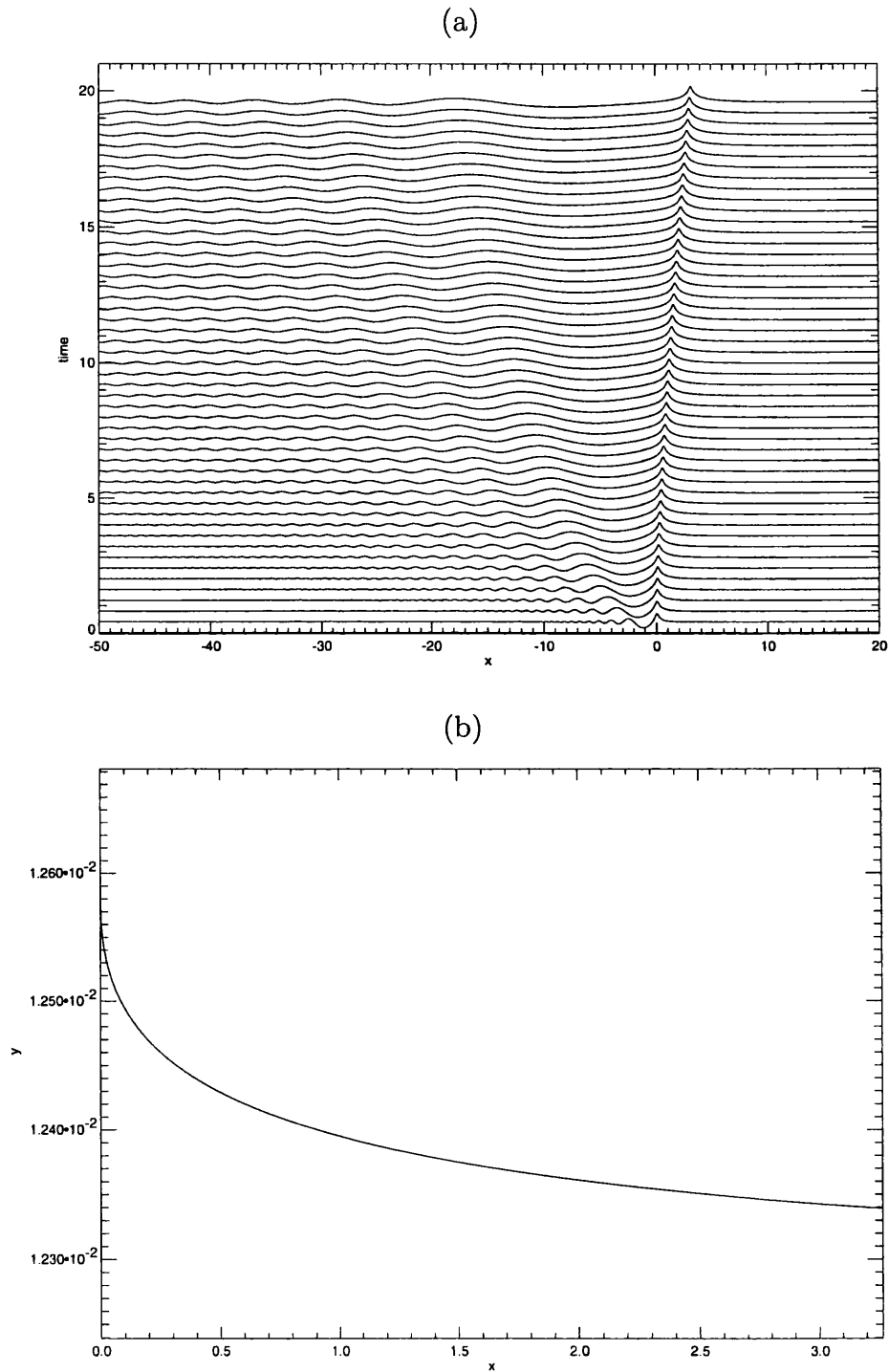
Figure 8.12: (a) The evolution of Θ for $\Delta = 0$ and $\kappa = 0.5$ (scaled by 30) and (b) The vortex trajectory.

evolution. The vortex wave system always approaches a steady state, namely a vortex propagating parallel to the will with no wave radiation. Some of the results are shown in figures (8.13)-(8.16). The first is for $\Delta = -2$ and $\kappa = 3$, figure (8.13a) shows the interface evolution and (8.13b) the trajectory. Recall that in this frame of reference the speed with which it is traveling towards increasing χ is against the drift speed U which is present in the streamfunction, and so is quite strong indeed.

Figures (8.14) and (8.15) show the responses for $\Delta = -4$ and $\Delta = -6$ respectively and $\kappa = 3.5$ in both. Even this far into the subcritical regime the vortex still speeds up enough to escape ahead of the wavetrain i.e. it eventually becomes supercritical.

Figure (8.16) shows the case for $\Delta = 0$ and $\kappa = 3.5$, which again is clearly another example of the vortex getting sufficiently close to the wall for the motion to become supercritical.

(a)

(b)
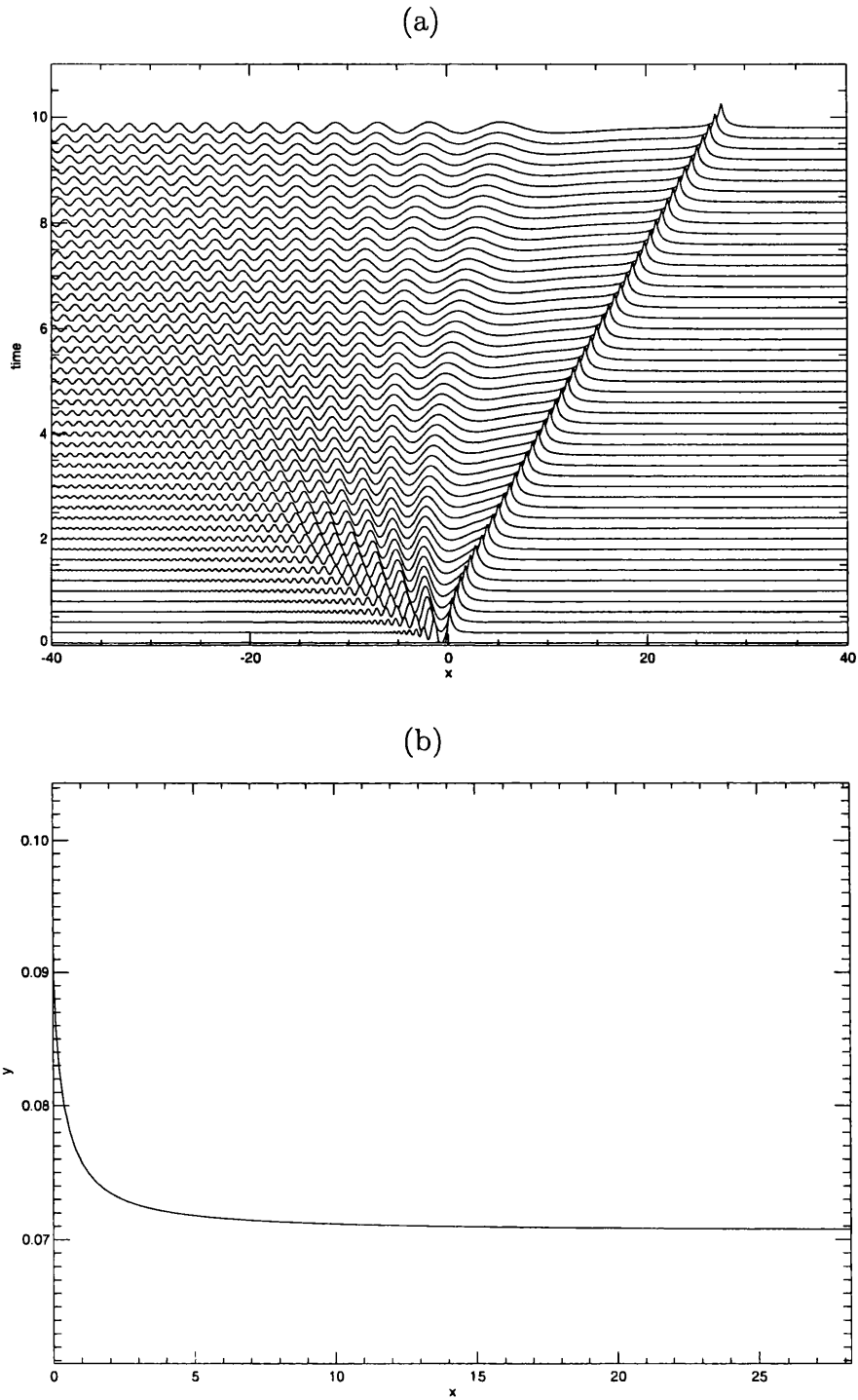
Figure 8.13: (a) The evolution of Θ for $\Delta = -2$ and $\kappa = 3$ and (b) The vortex trajectory.

(a)

(b)
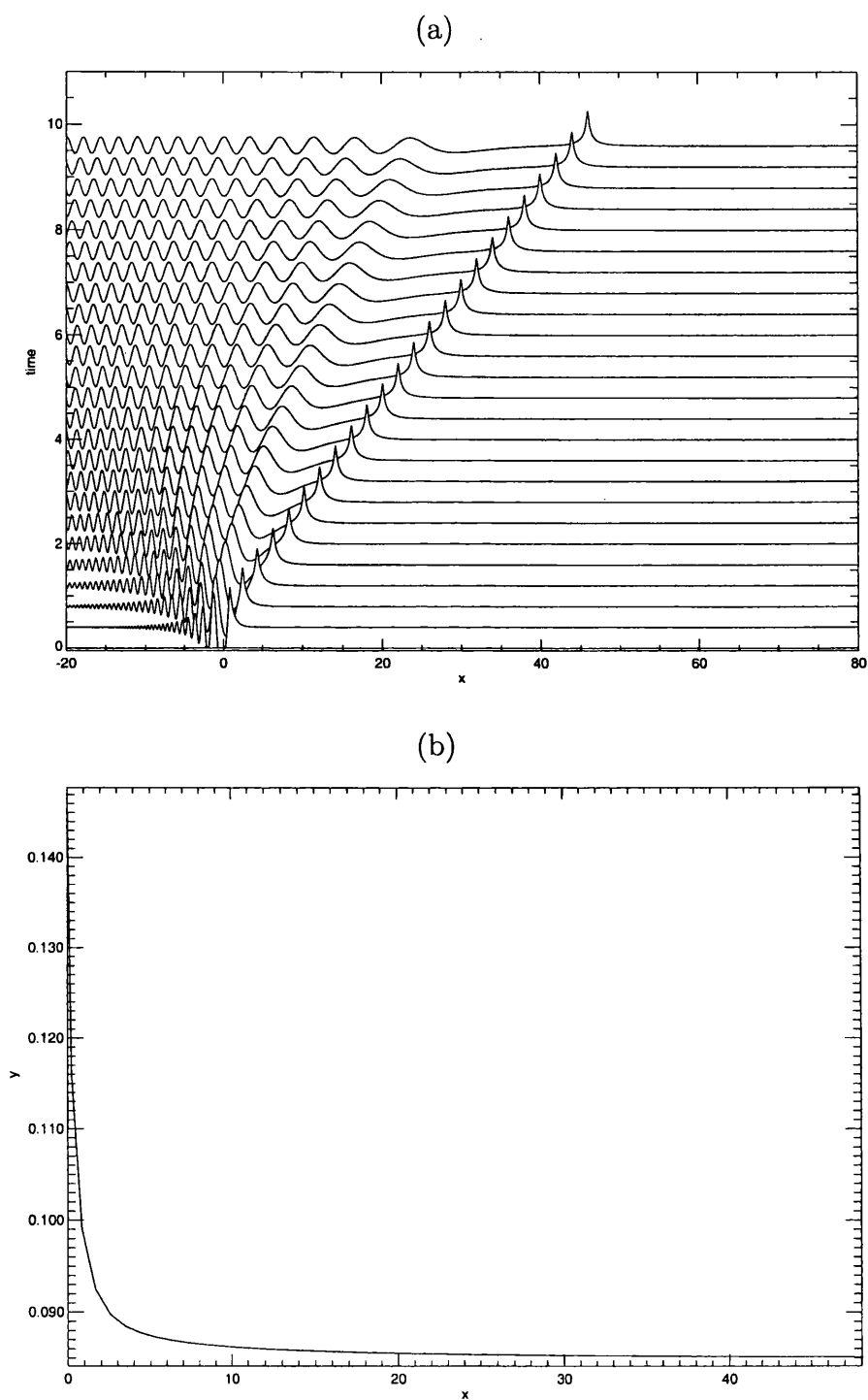
Figure 8.14: (a) The evolution of Θ for $\Delta = -4$ and $\kappa = 3.5$ and (b) The vortex trajectory.

(a)

(b)
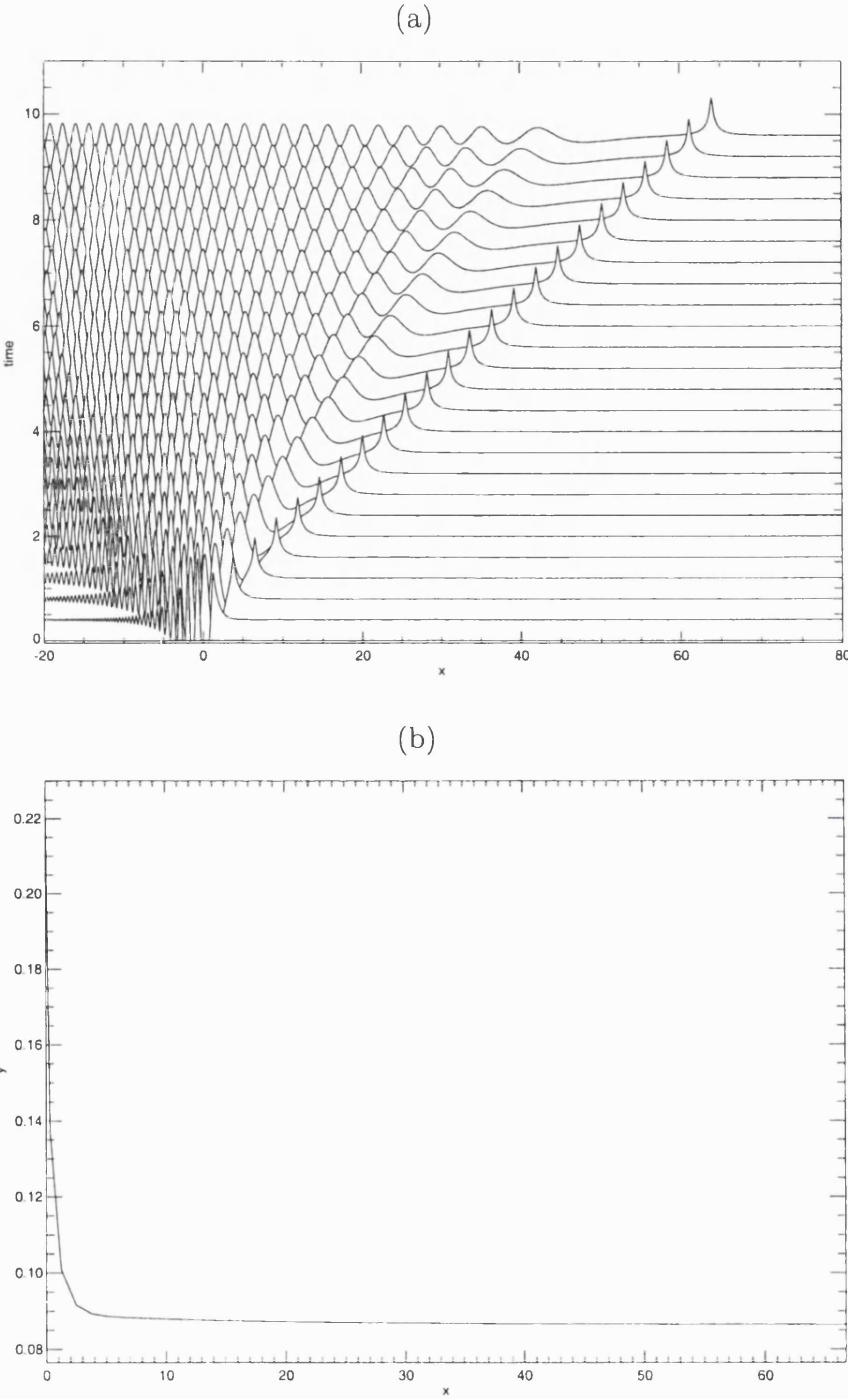
Figure 8.15: (a) The evolution of Θ for $\Delta = -6$ and $\kappa = 3.5$ and (b) The vortex trajectory.

(a)

(b)
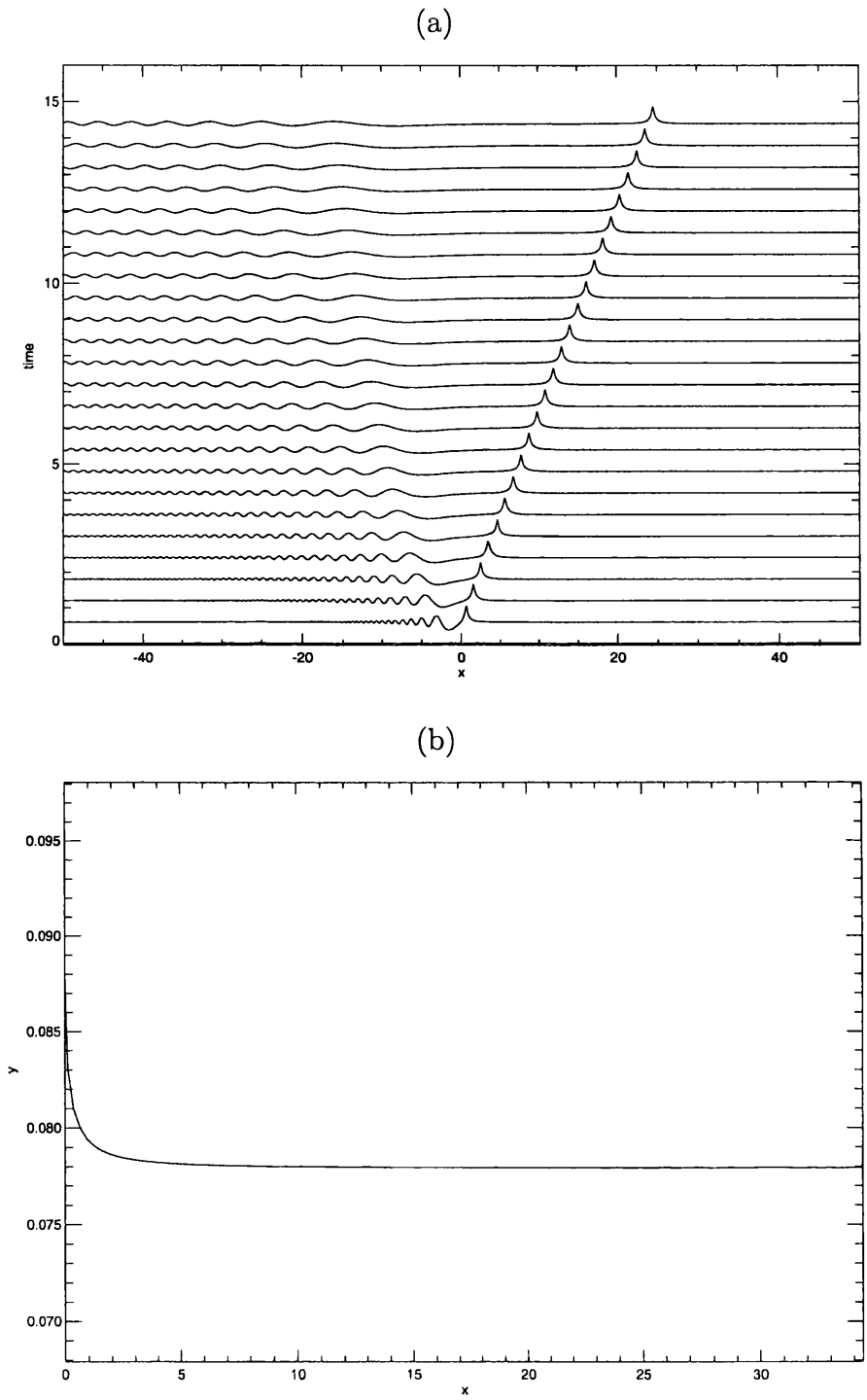
Figure 8.16: (a) The evolution of Θ for $\Delta = 0$ and $\kappa = 3.5$ and (b) The vortex trajectory.

8.6 Discussion.

In this chapter the interaction of a vortex and weakly nonlinear topographic waves was examined for a variety of vortex strengths and initial positions. At weak vortex strengths (small κ) the vortex motion and topographic wave dynamics were very similar to the equivalent linear responses. The initial value problem resulted in steady states for situations where the vortex was free to travel ahead of the topographic wavetrain and in cases where this wasn't so (subcritical flow) the vortex responded with a continual drift towards the wall.

At stronger forcing the motion was dominated by the image of the vortex in the wall and not by topographic wave generation. Initially, in order to conserve momentum in the χ-direction, Bell [1989], the vortex is pushed towards the wall, this change in y causes the vortex to speed up and at these values of κ this is quite significant. The vortex reaches a steady state consisting of a non-radiating steady flow in the horizontal direction as its new proximity to its image has caused it to propagate far away from the topographic wavefront. All of the resulting flows for these large values of κ eventually become supercritical and the various nonlinear wave effects shown in chapter 4 arising from the waves interacting with a steady vortex are not seen.

The conservation of momentum was used as a tool for checking the accuracy of the numerical method and error plots were given for each experiment shown. For most the error was $\approx 10^{-8}$ with $\mu = 0.1$. The sources of error in applying this numerical method were also discussed and methods for improving were given.

These results are in keeping with past work relating to this situation i.e. Bell [1989], Atassi et al. [1997], Dunn [1999] and they also show that for the most part,

in this freely evolving vortex case, linear theory is a good approximation. The results of chapter 4, whilst being unrealistic in the sense that the vortex is not allowed to move, may be applicable to a situation whereby the vortex has reached a steady state consisting of constant horizontal drift and the pseudoimage response at the interface (as seen above) which is then perturbed in some manner (either in strength or position). This would obviously result in topographic wave generation at the interface with the waves and vortex would react in a more nonlinear fashion and some of the behavior described in chapter 4 may be observed.

8.7   APPENDIX H: The terms of equation (8.32) that integrate to zero.

Note that

$$\int_{-\infty}^{\infty}\left[\Delta\Theta\Theta_\chi - \Theta^2\Theta_\chi(2 - H(\Theta))\right]\mathrm{d}\chi = \left[\frac{\Delta\Theta^2}{2} - \frac{\Theta^3}{3}(2 - H(\Theta))\right]_{-\infty}^{\infty}, \qquad \text{(H-1)}$$

which is zero as $\Theta \to 0$ for $|\chi| \to \infty$.

The equivalent BDA dispersive term is less straightforward to show it integrates to zero. First, begin with Parseval's theorem, which states that for two functions f and g and their respective Fourier transforms $\hat{f}$ and $\hat{g}$ (and with the complex conjugate of a function being denoted by a star i.e. conjugate(f) = f^*), that

$$\int_{-\infty}^{\infty} \hat{f}\,\hat{g}^*\mathrm{d}k = \int_{-\infty}^{\infty} f\,g^*\mathrm{d}\chi. \qquad \text{(H-2)}$$

Now Θ and $\mathbb{B}(\Theta_\chi)$ are both real functions of χ, τ and so taking the conjugate

$$\Theta^* = \Theta,$$
$$[\mathbb{B}(\Theta_\chi)]^* = \mathbb{B}(\Theta_\chi). \qquad \text{(H-3)}$$

So applying Parseval's Theorem one way gives

$$\int_{-\infty}^{\infty}\Theta^*\,\mathbb{B}(\Theta_\chi)\mathrm{d}\chi = \int_{-\infty}^{\infty}\hat{\Theta}^*ik|k|\hat{\Theta}\,\mathrm{d}k, \qquad \text{(H-4)}$$

and the other way gives

$$\int_{-\infty}^{\infty}\Theta\,[\mathbb{B}(\Theta_\chi)]^*\mathrm{d}\chi = \int_{-\infty}^{\infty}\hat{\Theta}(ik|k|\hat{\Theta})^*\,\mathrm{d}k. \qquad \text{(H-5)}$$

Equations (H-4) and (H-5) are equal by virtue of (H-3) and

$$i\hat{\Theta}^* = -(i\hat{\Theta})^*, \qquad \text{(H-6)}$$

gives from (H-4) and (H-5)

$$\int_{-\infty}^{\infty} 2ik|k|\hat{\Theta}\hat{\Theta}^{*} \, \mathrm{d}k = 0. \tag{H-7}$$

Using Parseval's Theorem again implies that

$$\int_{-\infty}^{\infty} \Theta \, \mathbb{B}(\Theta_{\chi}) \, \mathrm{d}\chi = 0. \tag{H-8}$$

Chapter 9

Conclusions.

The interaction of a point vortex and topographic waves near coastal topography has been studied in both the linear and weakly nonlinear limits as a simple paradigm for coastally propagating vortex dynamics.

Firstly the general problem was formulated and then linearised for small disturbances. The leading order problem was studied which consisted of a fixed (in a particular reference frame) vortex exciting topographic waves at the interface between two regions of differing PV. Long time asymptotic solutions were found for the linear waves and these showed that eventually the PV interface acts like a 'wall', so a vortex on-shelf eventually becomes identical to a vortex in a channel and a vortex off-shelf becomes a vortex near a wall. These long time steady states were described analytically and found using FFT numerical inversions and show that the pseudoimage description of weak vortex dynamics is very apt.

The special case of an on-shelf cyclonic vortex very close to the wall can lead to a resonant interaction and this was studied in the linear and weakly nonlinear limits. The weakly nonlinear behavior in this region was explored numerically and found to

263

be qualitatively similar to flow regimes described in Clarke and Johnson [1996a,b] even though the scalings used in deriving the weakly nonlinear governing wave equation shrunk the vortex forcing to a δ-function derivative, the wave equation was of the BDA type and forced by the δ-function derivative. Examples were given showing normal supercritical and subcritical flows; blocked, everywhere unsteady subcritical flows; transition, steady downstream subcritical flows and resonant flows with upstream traveling solitary waves. A summary, regime diagram showed how these different flow types related to each other with regards to strength of the vortex and closeness to resonance.

The final section of the thesis then looked at the higher order vortex motions as the ability of the vortex to respond to the deforming interface is a very important concept. Two threads ran through this analysis and discussion; the role of the vortex image in the wall compared with the role of the vortex pseudoimage in the interface, this was important in determining the underlying background drift of the vortex and also the higher order motions of the vortex in the along-shore direction; second was the conservation of momentum in the x direction which determines the off-shore motion of the vortex and was also used as a general error test of the numerical method. Implicit in discussions about momentum flux between the vortex and the waves is Bell's notion of *stable* and *unstable* vortex-wave systems. An unstable system occurs when a trailing, permanent wavetrain forms behind the vortex and continually drains the vortex of momentum (stable is when this doesn't occur and the vortex can move ahead or behind the wavetrain), this concept is important as it means that the vortex will continue to drift in the y direction unless it can 'escape' from the wavetrain. This can lead to the breakdown of the linear theory if say, the vortex gets pushed across the interface or in the case of an on-shelf cyclonic vortex

close to the wall, the vortex always gets pushed nearer to the wall speeding up as it does so and preventing any resonant interactions.

This was found to be a problem in the weakly nonlinear investigations of this problem. An unfortunate situation arises for this case in that for small values of the nondimensional forcing strength κ the vortex can be made to stay within reach of the topographic lee waves, however the forcing is not strong enough to conjure nonlinear behavior. However, at stronger forcing where nonlinear effects become important the vortex rushes off ahead of the lee waves and does not interact with them, at stronger forcing the problem always becomes supercritical and none of the other nonlinear behavior seen for the stationary vortex was observed. This is interesting as it is saying that the near-resonant vortex response to wave radiation is that it will always reach a steady state through conservation of momentum

9.1 Further Work:

One important extension to this work would be an investigation into the fully nonlinear behavior of the wave-vortex interactions near resonance. This would have to be done numerically using contour dynamical integrations, the results of this thesis could then be checked against the fully nonlinear results to see how accurately linear and weakly nonlinear theory describes the motions of the waves and vortex. In Dunn [1999] this has been done for a divergent, barotropic point vortex in the presence of coastal topography, however that work was more concerned with modeling the effects due to a moderate or intense vortex. For the weak vortex an example of resonance was given with the parameter values (using the notation of this thesis) $h = 0.3$ and $y_0 = 1.67$ with $\varepsilon = 0.1$, so the topographic longwave speed is 0.3, res-

onance can then be achieved when the vortex is placed off-shelf as the background drift due to the image vortex in the wall could still be $U = 0.3 \sim O(\varepsilon)$. Unfortunately the case with $h = 1$ meaning that resonance can only occur if $y_0 \sim O(\varepsilon)$ was not shown. Setting the shelf to be close to the wall changes the wave dynamics too as the interfacial waves become less and less dispersive and the problem becomes similar to that studied in Atassi et al. [1997]. So to reiterate, the problem of a weak vortex initially placed an $O(\varepsilon)$ distance from the wall should be calculated using contour dynamics to compare results with this thesis.

Another interesting extension of this study would be that of the equivalent problem but set in a rotating channel geometry. This problem would be bounded in the off-shore direction which implies that the governing equation for the interface evolution would be of the KdV-type, (the $\mathbb{B}$ operator occurs for semi-infinite domains) and would have the form

$$\Theta_\tau - \Delta\Theta_\chi + \Theta\Theta_\chi N(\text{sgn}(\Theta)) + \lambda\Theta_{\chi\chi\chi} = -\kappa\delta_\chi(\chi), \qquad (9.1)$$

where $\Delta \sim O(1)$ is the detuning parameter, $N(\text{sgn}(\Theta))$ is some coefficient dependent on the sign of Θ, $\lambda \sim O(1)$ is a fixed constant dependent on the ratio of the shelf width and channel width and $\kappa \sim O(1)$ is the nondimensional strength of the vortex.

Following Clarke and Johnson [1999] and Johnson and Clarke [1999], the steady version of (9.1) can be integrated immediately to give

$$G(\Theta_0) - G(\Theta) + \lambda\Theta_{\chi\chi} = -\kappa\delta(\chi), \qquad (9.2)$$

where

$$G(\Theta) = -\Delta\Theta + \frac{\Theta^2}{2}N, \qquad (9.3)$$

and Θ_0 is the value of the interface far upstream. In steady flow this is assumed to be constant and non-negative. It is also assumed that far upstream the derivatives of Θ are zero. At the origin the interface displacement Θ is assumed to be continuous but its derivative is not. Integrating (9.2) from $(-\varepsilon, \varepsilon)$ where $0 < \varepsilon \ll 1$ gives

$$\int_{-\varepsilon}^{\varepsilon} \Big(G(\Theta_0) - G(\Theta) \Big) \mathrm{d}\chi + \lambda[\Theta_\chi] = -\kappa. \tag{9.4}$$

As $\varepsilon \to 0$ the integral term vanishes as the integrand is continuous and the jump condition at the origin is

$$[\Theta_\chi] = -\frac{\kappa}{\lambda}. \tag{9.5}$$

Away from the origin (9.2) can be written

$$G(\Theta_0) - G(\Theta) + \lambda\Theta_{\chi\chi} = 0. \tag{9.6}$$

Multiplying (9.6) by θ_χ and integrating once with respect to χ gives the 'energy' equation

$$V(\Theta) + \frac{\lambda}{2}\Theta_\chi^2 = E, \tag{9.7}$$

for some constant E and the 'potential' V is given by

$$V(\Theta) = \Theta G(\Theta_0) + \frac{\Delta\Theta^2}{2} + \frac{N\Theta^3}{6}, \tag{9.8}$$

so in an analogous manner to Clarke and Johnson [1999] and Johnson and Clarke [1999] the energy equation (9.7) can be plotted as contours of fixed E in (Θ, Θ_χ) space. This renders the descriptions of various flow regimes (supercritical, subcritical

and blocked etc) as heteroclinic and homoclinic orbits in (Θ, Θ_χ) space, with the jump in derivative at the vortex described by condition (9.5).

Acknowledgements

Bibliography

T.R. Akylas. On the excitation of long nonlinear water waves by a moving pressure distribution. *J.Fluid Mech*, 141:455–466, 1984.

M. Allison. Icarus, 1990.

M. Allison, D.A. Godfrey, and R.F. Beebe. A wave dynamical interpretation of Saturn's polar hexagon. *Science*, 247, 1990.

O.V. Atassi. Analytical and numerical study of the nonlinear interaction between a point vortex and a wall-bounded shear layer. *J.Fluid Mech*, 373:155–192, 1998.

O.V. Atassi, A.J. Bernoff, and S. Lichter. The interaction of a point vortex with a wall-bounded vortex layer. *J.Fluid Mech*, 343:169–195, 1997.

P.G. Baines. *Topographic effects in Stratified Flows*. Cam. Univ. Press, 1995.

G.I. Bell. Interaction between vortices and waves in a simple model of geophysical flow. *Phys.Fluid.A.*, 2:575–586, 1989.

C.M. Bender and S.A. Orszag. *Advanced mathematical methods for scientists and engineers*. McGraw-Hill, 1978.

T. Benjamin. Internal waves of permanent form in fluids of great depth. *J. Fluid Mech*, 29:559–592, 1967.

E.O. Brigham. *The fast Fourier transform.* Prentice-Hall, 1973.

R. Camassa and D.D. Holm. An integrable shallow water equation with peaked solitons. *Phys. Rev. Lett.*, 71:1661–1664, 1993.

C. Canuto, M.Y. Hussaini, A. Quarteroni, and T.A. Zang. *Spectral methods in fluid dynamics.* Springer-Verlag, Berlin, 1988.

G.F. Carnevale, O.U. Velasco Fuentes, and P. Orlandi. Inviscid dipole-vortex rebound from a wall or coast. *J. Fluid Mech.*, 351:75–103, 1997.

S.R. Clarke and R.H.J. Grimshaw. The effect of weak shear on finite-amplitude internal solitary waves. *J. Fluid Mech.*, 395:125–159, 1999.

S.R. Clarke and E.R. Johnson. Topographically forced long waves on a sheared coastal current. part 1. The weakly nonlinear response. *J.Fluid Mech*, 343:131–151, 1996a.

S.R. Clarke and E.R. Johnson. Topographically forced long waves on a sheared coastal current. part 2. Finite-amplitude waves. *J.Fluid Mech*, 343:153–168, 1996b.

S.R. Clarke and E.R. Johnson. Finite-amplitude topographic Rossby waves in a channel. *Phys.Fluids*, 11:107–120, 1999.

S.R. Clarke and E.R. Johnson. The weakly nonlinear limit of forced Rossby waves in a stepped channel. *Proc. R. Soc. Lond. A*, 457:2361–2378, 2001.

S.L. Cole. Transient waves produced by flow past a bump. *Wave Motion*, 7:579–587, 1985.

J.W. Cooley and J.W. Tukey. An algorithm for the machine calculation of complex Fourier series. *Mathematics of Computation*, 19:297–301, 1965.

B. Cushman-Roisin and B. Tang. Geostrophic turbulence and emergence of eddies beyond the radius of deformation. *J. Phys. Oceanogr.*, 20:97–113, 1990.

R. Davies and A. Acrivos. Solitary internal waves in deep water. *J. Fluid Mech*, 29: 593–607, 1967.

P.G. Drazin and R.S. Johnson. *Solitons: An Introduction.* Cambridge University Press, 1989.

T.A. Driscoll and B. Fornberg. A padé-based algorithm for overcoming the Gibbs phenomenon. *Numerical Algorithms*, 26:77–92, 2001.

D.G. Dritschel. Contour surgery: a topological reconnection scheme for extended contour integrations using contour dynamics. *J. Comput. Phys.*, 77:240–266, 1988.

D.C. Dunn. *Vortex interactions with topographic features in geophysical fluid dynamics.* PhD thesis, University College London, 1999.

D.C. Dunn, N.R. McDonald, and E.R. Johnson. The motion of a singular vortex near an escarpment. *J. Fluid Mech*, 448:335–365, 2000.

G.R. Flierl. Rossby wave radiation from a strongly nonlinear warm eddy. *J. Phys. Oceanogr.*, 14, 1984.

G.R. Flierl and K. Haines. The decay of modons due to Rossby wave radiation. *Phys. Fluids*, 6, 1994.

A.S. Fokas and B. Fuchssteiner. Symplectic structures, their bäcklund transformations and hereditary symmetries. *Physica*, 4:47–66, 1981.

B. Fornberg. A fast spectral algorithm for nonlinear wave equations with linear dispersion. *J. Comp. Phys*, 155:456–467, 1999.

C.E. Fröberg. *Introduction to numerical analysis.* Addison-Wesley, 1970.

A.E. Gill. The hydraulics of rotating channel flow. *J.Fluid Mech,* 80:641–671, 1977.

I.S. Gradshteyn and I.M. Rhysik. *Tables of Integrals, Series and Products.* Academic Press, 1980.

A.E. Green and P.M. Naghdi. A derivation of equations for wave propagation in water of variable depth. *J. Fluid Mech.,* 78:237–246, 1976.

R. Grimshaw. Resonant forcing of barotropic coastally trapped waves. *J. Phys. Oceanog.,* 17:54–65, 1987.

R. Grimshaw, E. Pelinovsky, and O. Poloukhina. Higher-order Korteweg-de Vries models for internal solitary waves in a stratified shear flow with a free surface. *Nonlin. Processes in Geo. Phys.,* 9:221–235, 2002.

R. Grimshaw and Z. Yi. Finite-amplitude long waves on coastal currents. *J. Phys. Oceanog.,* 20:3–18, 1990.

R.H.J. Grimshaw and N. Smyth. Resonant flow of a stratified fluid over topography. *J. Fluid Mech.,* 169:429–464, 1986.

E. Hairer and G. Wanning. *Solving ordinary differential equations II: Stiff and differential-algebraic Problems.* Springer-Verlag, Berlin, 2 edition, 1996.

P.H. Haynes, E.R. Johnson, and R.G. Hurst. A simple model of Rossby-wave hydraulic behaviour. *J.Fluid Mech,* 253:359–384, 1993.

N.G. Hogg and H.M. Stommel. The heton, an elementary interaction between discrete baroclinic geostrophic vorticies, and its implications concerning eddy heat-flow. *Proc. R. Soc. Lon. A,* 397:1–20, 1985.

E.R. Johnson. Topographic waves and the evolution of coastal currents. *J. Fluid Mech.*, 160:499–509, 1985.

E.R. Johnson and S.R. Clarke. Dispersive effects in Rossby-wave hydraulics. *J.Fluid Mech*, 401:27 – 54, 1999.

E.R. Johnson and S.R. Clarke. Rossby wave hydraulics. *Annu. Rev. Fluid Mech*, 33:207–230, 2001.

R.S. Johnson. Camassa-Holm, Korteweg-de Vries and related models for water waves. *J. Fluid Mech.*, 455:63–82, 2002.

G.K. Korotaev and A.B. Fedotov. Dynamics of an isolated barotropic eddy on a β-plane. *J.Fluid Mech.*, 264, 1994.

G.A. Lawrence. The hydraulics of steady two-layer flow over a fixed obstacle. *J.Fluid Mech*, 254:605–633, 1993.

Sir M.J. Lighthill. *Waves in Fluids*. Cambridge University Press, 1974.

P. Malanotte-Rizzoli. Boundary-forced nonlinear planetary radiation. *J. Phys. Oceanogr.*, 14:1032–1046, 1984.

N.R. McDonald. The decay of cyclonic eddies by rossby wave radiation. *J.Fluid Mech.*, 361:237–252, 1998a.

N.R. McDonald. Motion of an intense vortex near topography. *J.Fluid Mech*, 367:359–377, 1998b.

M.E. McIntyre. The stratospheric polar vortex and sub-vortex: fluid dynamics and midlatitude ozone loss. *Phil. Trans. R. Soc. Lon. A*, 352:227–240, 1995.

J.C. McWilliams. Submesoscale coherent vorticies in the ocean. *Rev. Geophys.*, 23: 165–182, 1985.

NASA. Gravity recovery and climate experiment (GRACE). NASA/JPL/University of Texas' Center for Space Research/GeoForschungsZentrum (GFZ) Potsdam, 2003.

M.V. Nezlin and G.G. Sutyrin. Problems of simulation of large long-lived vorticies in the atmospheres of the giant planets (Jupiter, Saturn, Neptune). *Surveys Geophys.*, 15:63–99, 1994.

H. Ono. Algebraic solitary waves in stratified fluids. *J. Phys. Soc. Japan.*, 39, 1975.

A. Patoine and T. Warn. The interaction of long, quasi-steady baroclinic waves with topography. *J. Atmos. Sci.*, 39:1018–1025, 1982.

J. Pedlosky. *Geophysical Fluid Dynamics.* Springer, 1979.

L. Pratt and L. Armi. Hydraulic control of flows with nonuniform potential vorticity. *J. Phys. Oceanogr*, 17:2016–2029, 1987.

L. Pratt and P.A. Lundberg. Hydraulics of rotating strait and sill flow. *Ann. Rev. Fluid Mech*, 23:81–106, 1991.

G.M. Reznik and R. Grimshaw. Ageostrophic dynamics of an intense localized vortex on a β-plane. *J. Fluid Mech.*, 443:351–376, 2001.

G.M. Reznik, R. Grimshaw, and E.S. Benilov. On the long-term evolution of an intense localized divergent vortex on the beta-plane. *J.Fluid Mech*, 422:249–280, 2000.

C.G. Rossby. On the dynamics of certain types of blocking waves. *J. Chin. Geophys. Soc.*, 2:1–13, 1949.

M.E. Stern. Hydraulically critical rotating flow. *Phys. Fluids*, 15:2062–2064, 1972.

M.E. Stern. Blocking an inviscid shear flow. *J.Fluid Mech*, 227:449–472, 1991.

M.E. Stern and G.R. Flierl. On the interaction of a vortex with a shear flow. *J.Geo.Res*, 92:10733–10744, 1987.

L.A. Stomovsky, H.E. Revercomb, R.J. Krauss, and V.E. Suorni. J. Geophys. Res., 1983.

G.B. Whitham. *Linear and nonlinear waves.* Wiley, 1974.

A. Woods. The topographic control of planetary-scale flow. *J. Fluid Mech*, 247: 603–621, 1993.